Non-Radial Pulsation in Early-Type Stars

Richard Henry Denny Townsend

Thesis submitted for the Degree of Doctor of Philosophy

UNIVERSITY
COLLEGE LONDON

May 1997

ProQuest Number: 10046202

All rights reserved

INFORMATION TO ALL USERS
The quality of this reproduction is dependent upon the quality of the copy submitted.

In the unlikely event that the author did not send a complete manuscript
and there are missing pages, these will be noted. Also, if material had to be removed,
a note will indicate the deletion.

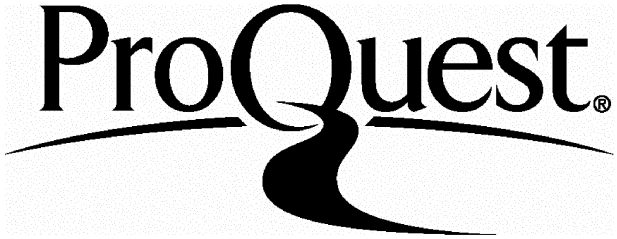

ProQuest 10046202

Published by ProQuest LLC(2016). Copyright of the Dissertation is held by the Author.

All rights reserved.
This work is protected against unauthorized copying under Title 17, United States Code.
Microform Edition © ProQuest LLC.

ProQuest LLC
789 East Eisenhower Parkway
P.O. Box 1346
Ann Arbor, MI 48106-1346

Typeset (July 31, 1997) in Times Roman using the LaTeX 2_ε document preparation system.

Abstract

A comprehensive study of pulsation in early-type (O and B) stars is undertaken. Starting with the equations of hydrodynamics, expressions governing adiabatic, non-radial pulsation in such stars are derived, along with complementary formulations of the boundary conditions suitable for solution of the equations. Two types of structure models are presented, one simplistic and the other more physically realistic, and a discussion of various techniques currently used for solution of the pulsation equations is applied to the latter type of models.

Such solution demonstrates that early-type main-sequence stars can be expected to be vibrationally unstable towards an opacity-driven excitation mechanism; furthermore, a consideration of the boundary conditions in such stars shows that some types of pulsation will be associated with trans-photospheric wave leakage through the stellar surface, possibly accounting for the wind variability observed in these systems.

The interaction between rotation and pulsation is investigated in some depth, with a discussion of two different techniques for approaching the problem. It is demonstrated that rotation leads to the introduction of both convective and quasi-toroidal pulsation, and, furthermore, that it will serve to confine pulsation activity towards equatorial regions. The emphasis throughout the discussion is placed on the numerical implementation of current theories.

All theoretical developments are combined in a pair of computer codes which model the line-profile variations of stars undergoing non-radial pulsation. The implementation of these models is discussed, with particular emphasis on the spectral-synthesis approach adopted, and they are compared with similar codes developed by other authors. The models are used to investigate some basic aspects of line-profile variability, with a discussion of the mechanisms behind the phenomenon, and a consideration of a number of issues which have previously been overlooked in the field; in particular, the possibility that a star may exhibit line-profile variability, but no ostensible photometric variability, is demonstrated, and the observational consequences of the trans-photospheric wave leakage previously mentioned are examined.

To Marianne

Acknowledgements

Firstly, I would like to thank Ian Howarth for all the support and advice he has given me over the duration of my PhD. His patience with my never-ending pestering rivals that of a sloth on valium, and the breadth and depth of his knowledge parallels that of Deep Thought (after it was switched on, of course). I am also indebted to the members (both active, retired and honorary) of the A25 society: to Keith for his knowledge of stellar spectra and philosophical pontification, to Andy for his encouragement and xpilot expertise, to Kaj for his lava-lamp and 12-round revolver, and to Matt D, Matt S, Rachel and Dave for their episodic rants, intermissions and cups of tea. Furthermore, I am eternally grateful to both Myron Smith and Stan Owocki for their endless wisdom, and to Daniel Schaerer for the provision (and explanation) of his most excellent models.

Thanks must also go to Jon and Jack for riding shotgun with the Aubergine Cavalry, and to Leajam, Shivers and Alison, for providing essential supporting fire. Additionally, I consider myself blessed with the ULO crowd — Emma, Tammay, Chris, Darren, Gabby, Mike, Claire and Rich — for stopping me from working at just the right times, and making sure that my closing year at UCL was the best.

Finally, I would like to thank Marianne, for both her love and support over my time at Oxford and UCL, for teaching me that yellow Smarties always taste the best, and for showing me that

Barn's burnt down —
now
I can see the moon.

Masahide

I met a traveller from an antique land
Who said: 'Two vast and trunkless legs of stone
Stand in the desert. Near them, on the sand,
Half sunk, a shattered visage lies, whose frown,
And wrinkled lip, and sneer of cold command,
Tell that its sculptor well those passions read
Which yet survive, stamped on these lifeless things,
The hand that mocked them and the heart that fed.
And on the pedestal these words appear —
"My name is Ozymandias, king of kings:
Look on my works, ye Mighty, and despair!"
Nothing beside remains. Round the decay
Of that colossal wreck, boundless and bare
The lone and level sands stretch far away.'

Percy Bysshe Shelley (*Ozymandias*)

Contents

List of Figures

List of Tables

Chapter 1

Introduction

1.1 Historical Background

The fundamental nomenclature with which the astronomer describes stellar systems, from the Greek Bayer letters and Latin constellation names to the more recent spectral classification designators of Morgan *et al.* (1943), owes its existence to an underlying fact about the physical nature of stars, namely that the majority stars are, in essence, *stable* objects. This stability is the principal reason why a given star may be observed, studied and classified on a constant footing over time-scales of days, years, and, indeed, centuries. However, it has long been known that some classes of stars exhibit a periodic variability in their brightness, even though their time-averaged properties may share the same constancy of non-variable systems.

In the majority of cases, this periodic variability, which can show typical time-scales varying from seconds to years, has been attributed to some manifestation of stellar pulsation, whereby the plasma throughout the star oscillates with some definite frequency. These oscillatory displacements generate temperature perturbations through the progressive compression and rarefaction of the plasma, which, when combined with changes in the stellar radius, lead to the observed periodic variability in brightness. Up until the middle of this century, almost all observations of such variability were thought to arise from the action of *radial* pulsation, whereby points at a given stellar radius all oscillate with the same phase. Theoretical models of radial pulsation predict that a star will oscillate at either a definite 'fundamental' frequency, or in one of a number of discrete overtones, in much the same way as a vibrating string (see Cox (1980) for a comprehensive review). These models have proven extremely successful in accounting for the variability of whole classes of stars, such as the RR Lyrae and classical (δ) Cepheid pulsators; indeed, the success with the latter has enabled them to be used as 'standard candles' in the calibration of the intergalactic distance scale, through the existence of a period-luminosity relationship.

However, some observations of variable stars have shown that their periodic brightness changes

occur at frequencies smaller than the fundamental frequency predicted by models, thus proving difficult to reconcile with radial pulsation theory. It was Ledoux (1951) who first suggested that such observations could be due to *non-radial* pulsation, whereby points at a given stellar radius do not share the same oscillation phase. Whilst the theory of non-radial pulsation, hereinafter NRP, was actually developed by Thomson (1863), before the corresponding radial-pulsation theory, it was not really considered actively until Ledoux (1951) demonstrated that it could account for the anomalously long variability period of β Canis Majoris (which could not be explained in terms of a radial pulsation model).

Subsequent studies of stellar variability have suggested that NRP manifests itself right across the Hertzprung-Russell diagram, ranging from the β Cepheid and δ Scuti pulsators to the variable DA White Dwarfs and the Sun itself; Unno *et al.* (1989) present a comprehensive review of these different classes of non-radial pulsators. The ground-breaking discovery of the 'five-minute' oscillations in the Sun by Leighton *et al.* (1962) has led to the emergence of the field of helioseismology, whereby observations of many non-radial pulsation modes have been used to infer certain physical properties throughout the entire solar interior. As a tool to probe this interior, helioseismology can offer unparalleled insights into stellar structure and evolution; it is therefore logical to generalize its application to all non-radially pulsating stars, leading to the newly-emergent field of asteroseismology.

The application of asteroseismology to early-type (O and B) stars is of particular interest since these stars account for 70% of the luminous matter in galaxies (even though their incidence by number is as low as 1%). They are the principal method by which many nucleosynthesized elements are dispersed to form the interstellar medium, and their large intrinsic luminosities render them attractive as 'standard candles' to complement classical Cepheid pulsators in the calibration of the intergalactic distance scale; accordingly, a better understanding of such stars is of relevance to many branches of astrophysics, in addition to the study of stellar structure and evolution.

The topic of this thesis, therefore, is an 'applied-theoretical' study of NRP in early-type stars. Whilst a purely theoretical treatment of pulsation in such stars is of scientific interest, it only has real value when confronted with current observations, so that theories may be tested and the diagnostic potential of NRP be exploited. Accordingly, the emphasis of the thesis is a review, refinement and unification of current pulsation theories, and, perhaps more importantly, a discussion of issues which arise when these theories are implemented to generate observationally-verifiable predictions. The following section presents a brief overview of research in the field, whilst the subsequent section discusses the structural layout of the thesis.

1.2 Non-Radial Pulsation in Early-Type Stars

The study of NRP in early-type stars began with the seminal work of Ledoux (1951), who demonstrated that the long period ($\approx$ 50 hours) of the variable star β CMa could be explained in terms

of a beating phenomenon between two pulsation modes of similar frequency. Subsequent investigations have shown that a number of early-type stars exhibit similar variability; these stars appear to be confined to a narrow region of the Hertzprung-Russell (HR) diagram, with spectral types between B0.5 and B2, and luminosity classes between III and IV (Unno *et al.* 1989). The fact that many of these so-called β Cepheid stars (named after their prototype) exhibit large radial velocity variations has been used by some authors (*e.g.*, Smith 1977) to argue that they all pulsate with a dominant radial mode which beats with non-radial modes of smaller amplitudes; this point, however, still remains the subject of some debate.

The effects of non-radial pulsation on spectral line profiles was first considered by Osaki (1971), who demonstrated that such pulsation will introduce periodic changes in line equivalent widths, depths and asymmetries. Searches for such line-profile variations, hereinafter lpv, in stars other than the β Cepheid class remained inconclusive until Smith & Karp (1976) reported the widespread incidence of small-amplitude lpv in sharp-lined O8 to B5 stars. Subsequent work by Smith (1977), based on the predictions of Osaki (1971), demonstrated that these lpv can be successfully modelled by NRP, suggesting that pulsation in early-type stars is not just confined to the narrow β Cepheid region of the HR diagram. Further progress in modelling the lpv of such stars with NRP (*e.g.*, Smith 1978; Buta & Smith 1979; Smith 1981) led to the establishment of a new class of early-type non-radial pulsators (Smith *et al.* 1984); these 53 Per variables (again named after their prototype) appear to be distinct from β Cepheid stars, in that they exhibit neither large radial velocity variations, nor variability periods which are stable over long time-scales, and, furthermore, are distributed over a wider region of the HR diagram.

One defining characteristic of 53 Per stars is that they exhibit narrow spectral lines, indicating an absence of significant broadening due to rotation. The first detection of periodic lpv in a broad-line early-type star was made by Walker *et al.* (1979), who observed discrete, narrow absorption and emission features travelling from blue to red in the rotationally-broadened O9.5V star ζ Ophiuchi. The authors suggested that these lpv were generated by the migration across the stellar disk of discrete 'spot' features. However, Vogt & Penrod (1983), in their seminal treatment, demonstrated that the variability observed in ζ Oph was inconsistent with either spot or co-rotating 'spoke' models, and showed that the lpv could be successfully modelled with NRP in the form of waves travelling across the surface of the star. Subsequent observations of many other broad-line early-type stars has shown that the incidence of such lpv appears to be high (*e.g.*, Baade 1984; Gies & Kullavanijaya 1988; Stagg *et al.* 1988; Reid *et al.* 1993; Hahula 1993; Fullerton *et al.* 1996), leading to the introduction of a second (broad-line) class of line-profile variable early-type stars, usually termed ζ Oph variables. As with the 53 Per (narrow-line) variables, these stars are spread across both O and B spectral types, and occur in luminosity classes ranging from I (*e.g.*, ζ Pup— Reid & Howarth 1996) through to V (*e.g.*, HD93521— Howarth & Reid 1993).

For NRP to be excited in any star, there must be some mechanism by which energy is converted from thermal to vibrational forms. Such excitation mechanisms remain somewhat of a mystery in

line-profile-variable early-type stars; whilst pulsation in β Cepheid systems can be attributed to an opacity-driven mechanism (*e.g.*, Cox *et al.* 1992), similar to that present in classical (δ) Cepheids, the search still continues for a suitable excitation mechanism in both 53 Per and ζ Oph pulsators (see §5.5 for some interesting results in this area). In this sense, therefore, there remains much scope for progress in the study of such stars; it is for this reason that the work in this thesis, whilst remaining quite general in some areas, is focused on these two classes of early-type non-radial pulsators.

1.3 Thesis Overview

The work presented herein begins in the following chapter with a review of the basic theory behind non-radial pulsation. The equations which govern pulsation are derived under certain assumptions, generally valid in early-type stars, and a preliminary discussion of their characteristics is undertaken. These equations are then transformed into a form suitable for numerical solution; however, before such solution can be accomplished, the restrictions on pulsation at the stellar origin and surface must be examined. These restrictions, usually termed boundary conditions, are discussed in Chapter 3, which examines two different approaches to the problem. The possibility of wave leakage through the stellar surface is introduced, and an investigation of the effects of NRP on the photosphere is undertaken.

With the mathematical framework of NRP laid down, Chapter 4 presents two sets of stellar structure models suitable for investigation from a pulsation standpoint. The first of these sets, the polytropic models, are primarily considered for historical and implementation reasons, whilst the second, the *CoStar* models, are based on state-of-the-art stellar structure calculations. As with the majority of the thesis, the emphasis in this chapter is on implementation issues, in particular transforming the *CoStar* models into a form suitable for pulsation analyses.

Chapter 5 uses the results of preceding chapters to solve the pulsation equations for the *CoStar* models. Both semi-analytical and numerical solution techniques are considered, with a particular emphasis on the implementation and application of the latter. The vibrational stability of the *CoStar* models is discussed, as are more general stability issues, and the concept of wave leakage is further developed by investigating its implications for the models considered.

An investigation of pulsation in early-type stars, in particular the broad-line ζ Oph-variable class, would be incomplete without a discussion of the interaction between pulsation and rotation. Accordingly, Chapter 6 presents an in-depth investigation of this issue, examining and contrasting the different approaches currently used to tackle the problem, and, as before, examining particular issues which arise when implementing these approaches. Of all chapters presented, this is the largest, principally due to the sheer complexity and richness of results which the treatment of rota-

tion introduces, but also due to the fact that the effects of rotation on pulsation have been somewhat neglected by many authors in the field.

As was indicated in §1.1, theoretical studies of NRP are of little value unless they are used to produce models which may be directly compared with observations. In the case of 53 Per and ζ Oph pulsators, analyses are primarily spectroscopic, in the form of observations of lpv, and it is for this reason that Chapter 7 presents a number of models which combine the results of preceding chapters to generate synthetic time-resolved spectra for early-type stars undergoing NRP. These models are discussed in some depth, as are the more general issues of lpv modelling, and some preliminary calculations are presented; the emphasis of the chapter is on the broader aspects of pulsation-generated lpv, rather than on application of the models to specific cases, in line with the more theoretical and implementational bias of the thesis. Whilst this bias means that there are no specific results which stand out for discussion in a concluding section, Chapter 8 summarizes the general findings of the thesis, and looks back over the work undertaken, with an emphasis on possible improvements which could be implemented. The future direction of the study of pulsation in early-type stars is discussed, and areas especially in need of further investigation are highlighted.

On a final note, the reader is encouraged to peruse Appendix G, which contains a list of all mathematical symbols used throughout the work; this list should ensure that little confusion can arise over the meaning of symbols, some of which are multiply defined.

Chapter 2

The Basic Theory

2.1 Introduction

As was indicated in the preceding chapter, the fact that the majority of stars are amenable to some form of long-term classification indicates that they possess an underlying stability. Interestingly enough, it is this stability which is responsible, in part, for the existence of stellar pulsation. To demonstrate this, it is useful to consider in greater detail the various forms which stellar stability may take.

At its most fundamental level, stellar stability may be split into two basic types, namely, dynamical and thermal. Dynamical stability is usually encapsulated by the assumption of hydrostatic equilibrium, whereby the gravitational, pressure and external forces on each element of stellar plasma sum to zero when the star is in its equilibrium state. Any perturbations to this equilibrium state lead to an adjustment of the stellar structure, which returns the star to equilibrium over the typical time-scale $\tau_{\rm dyn}$ of the free-fall time,

$$\tau_{\rm dyn} = \sqrt{\frac{R^3}{GM}}, \tag{2.1}$$

where R is the stellar radius, M the mass, and G the gravitational constant. In almost all stars, this time-scale is of the order of minutes or hours; thus, they spend the majority of their lifetimes in a state of dynamical stability (convection is a specialized form of local dynamical instability, and will be discussed briefly in later sections).

In contrast, the time-scale over which major changes to the thermal configuration of a star can occur is of the order of millions of years. Hydrostatic equilibrium may be assumed over such periods, and, as a consequence, perturbations to the thermal energy of the star over much shorter time-scales are compensated for by corresponding changes to its gravitational energy store (*e.g.*, Schwarzchild 1965), maintaining the thermal equilibrium. Notable exceptions to this are cases

such as degenerate thermonuclear ignition (nova-like outbursts and the helium flash); however, thermal stability is rapidly restored after such events. Longer-term thermal instabilities, usually termed secular instability, are usually not relevant to non-radial pulsation (Unno *et al.* 1989); although chemically inhomogeneous zones within stars *may* lead to non-radial secular instability, Gabriel & Noels (1976), Rosenbluth & Bahcall (1973) and Saio *et al.* (1980) have demonstrated that for the case of low-mass stars this does not occur, and is unlikely in the majority of stars. Rapid rotation may also lead to secular instability, but only for stars with a very low degree of central condensation, such as neutron stars (Managan 1986); accordingly, such instabilities will not be discussed further here.

The prevalence of dynamical stability in stars indicates the existence of some form of restoring force, which maintains the state of hydrostatic equilibrium; it is precisely this restoring force which is responsible for oscillations in stars. When an element of stellar material is perturbed from its equilibrium position, the dynamical restoring force will return it back to this position; however, the exchange between potential and kinetic energy will generally cause the element to overshoot the equilibrium point time and time again, and it will enter into a state of oscillation. The specifics of this oscillation will be determined by the nature of the dynamical restoring force, which will in turn depend on the structure and composition of the star; it is for this reason that the discipline of asteroseismology, discussed in Chapter 1, enables inferences on internal stellar structure to be made from observations of pulsation-originated variability.

In this chapter, the basic equations governing non-radial pulsation in stars are derived. This derivation closely parallels that given by Unno *et al.* (1989), with the introduction of a number of simplifications applicable to pulsation in early-type stars. In particular, the assumption of adiabacity is used throughout, whereby any heat transfer between adjacent elements of stellar material over a pulsation cycle is neglected. Many authors have used this approximation (*e.g.*, Dziembowski 1971; Osaki & Hansen 1973; Buta & Smith 1979; Boury *et al.* 1980; Brassard *et al.* 1989; Kovacs 1990), since it allows great simplifications to be made to the formalism of stellar pulsation theory; however, it entails a notable drawback. Since the mechanisms responsible for the self-excitation of free stellar pulsations rely on heat transfer between vibrational and thermal energy forms (*e.g.*, Kato 1966; Osaki 1974; Gabriel *et al.* 1975; Shibahashi & Osaki 1976; Stellingwerf 1978; Cox *et al.* 1992; Glatzel 1994), the non-adiabatic processes by which they operate cannot be properly studied within the strictures of the adiabatic approximation. However, if this approximation is a good one, it *is* still possible to obtain insight into pulsation excitation using the quasi-adiabatic stability analysis introduced by Osaki & Hansen (1973) (see §5.5).

In any case, the response of a star to a given perturbation (however it arises) may still be investigated within the adiabatic approximation; in the following sections, therefore, the basic equations of adiabatic, linear non-radial pulsations are derived from the equations of hydrodynamics, and

their local behaviour is studied.

2.2 Equations of Hydrodynamics

The fundamental equations which govern the pulsation characteristics of stars are those of hydrodynamics. These equations represent the generalization of basic physical laws from single or few-particle systems to continuum (fluid) systems, such as stellar plasmas. The derivation of these equations is left to publications on fluid mechanics (*e.g.*, Eckart 1960), since it is their application which is of interest herein.

In their most compact form, the equations of hydrodynamics may be expressed in terms of conservation laws for mass, momentum and energy (*e.g.*, Unno *et al.* 1989). Within the adiabatic approximation, the hydrodynamical energy equation need not be considered; furthermore, simplifications to the two remaining equations may be made by neglecting forces external to the star, such as gravitational interactions in binary systems, and also electromagnetic forces. The latter is justified in the case of early-type stars due to the lack of observational evidence for significant ordered magnetic fields in such systems (Barker 1986). Additionally, viscous forces are usually small and unimportant in the stellar interior, and therefore may be neglected (Unno *et al.* 1989).

The interaction between pulsation and convection presents difficulties due to the continued absence of a sound theory of convection (*e.g.*, Gabriel *et al.* 1975); however, convection in early-type stars is primarily restricted to the thermonuclear core regions, and it is unlikely that it will have any serious impact on pulsation confined to stellar envelopes. Accordingly, explicit treatment of convection is passed over herein, although rotationally-stabilized convective pulsation is discussed briefly in §6.7.2.

With these simplifications, the relevant equations of hydrodynamics, written in terms of conservation laws for mass and momentum, are given by

$$\frac{\partial \rho}{\partial t} + \nabla \cdot (\rho \mathbf{v}) = 0 \tag{2.2}$$

and

$$\rho \left(\frac{\partial}{\partial t} + \mathbf{v} \cdot \nabla \right) \mathbf{v} = -\nabla p - \rho \nabla \Phi \tag{2.3}$$

respectively, where ρ denotes the density, $\mathbf{v}$ the local fluid velocity, p the (scalar) pressure and Φ the gravitational potential. The parenthetical differential operator on the left-hand side of the latter equation is usually termed the material, or convective, time-derivative, since it represents the temporal rate-of-change of a quantity as measured in the co-moving reference frame of a constant-mass fluid parcel.

These hydrodynamical equations do not form a closed system in the mathematical sense, and an additional equation is required to enable solution, namely Poisson's equation,

$$\nabla^2\Phi = 4\pi G\rho, \tag{2.4}$$

which relates the gravitational potential Φ to the matter distribution ρ through the gravitational constant G. In the full non-adiabatic formalism, where heat transfers between fluid parcels are considered, supplementary equations are required to describe energy transport and the physical characteristics of the stellar plasma; however, these equations are not required herein. It is for this reason that the adiabatic approximation is so useful, since pulsation may be studied in systems where such supplementary equations cannot be formulated, such as polytropic stellar models (§4.2).

The equations governing the equilibrium state of a non-rotating star may be obtained by setting all time derivatives and velocity fields to zero in the hydrodynamical equations (including the neglected energy equation) and combining them with the supplementary equations discussed above. The resulting system may be solved for all variables throughout the star to create stellar structure models; the calculation of such models constitutes a whole branch of astrophysics in itself, and is left to dedicated publications (*e.g.*, Schwarzchild 1965; Chandrasekhar 1967; Kippenhahn & Weigert 1990).

2.3 Equations of Pulsation

To obtain the equations governing linear, non-radial pulsation in stars, the equations presented in the preceding section are subjected to perturbations, assumed to be small enough that second- and higher-order terms may be neglected. These perturbations are usually discussed from the standpoint of two complementary paradigms, the Eulerian model and the Lagrangian model.

In the Lagrangian model, the perturbations to a given variable are expressed in terms of the change in that variable experienced by a given constant-mass fluid parcel. The Lagrangian perturbation δf to a variable f may be written as

$$\delta f(\mathbf{r}) = f(\mathbf{r}) - f_0(\mathbf{r}_0), \tag{2.5}$$

where f_0 is the value of the variable prior to the perturbation, and $\mathbf{r}$ and $\mathbf{r}_0$ are the perturbed and unperturbed position vectors respectively *of the same fluid parcel.* It is important to note that in the Lagrangian model, the position vector $\mathbf{r}$ is a dependent variable, whilst $\mathbf{r}_0$ is an independent variable used to label which fluid parcel is under scrutiny. This model is primarily of use in the treatment of the pulsation boundary conditions (Chapter 3), since the surface of a star is not defined in a spatial sense (*i.e.*, fixed radius), but rather as the locus of all fluid parcels which lie on the outer boundary.

The Eulerian model, in contrast, is concerned with perturbations which occur at a fixed spatial position. The Eulerian perturbation f' to the same variable f is accordingly given by

$$f'(\mathbf{r}) = f(\mathbf{r}) - f_0(\mathbf{r}), \tag{2.6}$$

where, again, f_0 is the unperturbed value of the variable. In the calculation of this perturbation, it is the position vector $\mathbf{r}$ which is held constant; the fluid parcel at $\mathbf{r}$ in the perturbed and unperturbed states is different. The Eulerian paradigm is the more useful of the two models in constructing the equations of pulsation, since $\mathbf{r}$ remains the independent variable throughout.

The Lagrangian and Eulerian perturbations are related to first order in displacement $\boldsymbol{\xi}$ by

$$\delta f(\mathbf{r}, t) = f'(\mathbf{r}, t) + \boldsymbol{\xi} \cdot \nabla f_0(\mathbf{r}) \tag{2.7}$$

(*e.g.*, Cox 1980; Unno *et al.* 1989), where $\boldsymbol{\xi}$ is given by

$$\boldsymbol{\xi} = \mathbf{r} - \mathbf{r}_0. \tag{2.8}$$

It is important to note that $\boldsymbol{\xi}$ is neither an Eulerian nor a Lagrangian quantity; rather, it is the underlying variable which connects the two models together. The time-derivatives $\partial/\partial t$ and d/dt, corresponding to the Eulerian and Lagrangian models respectively, are related by

$$\frac{d}{dt} = \frac{\partial}{\partial t} + \mathbf{v} \cdot \nabla \tag{2.9}$$

where $\mathbf{v}$ is the fluid velocity; the Lagrangian time-derivative, written in the form of a full differential to underline the dependent nature of $\mathbf{r}$ in the Lagrangian model, can be recognized as the material derivative mentioned in the preceding section. Unno *et al.* (1989) demonstrate that when the unperturbed state is static ($\mathbf{v}_0 = 0$), the Lagrangian and Eulerian time derivatives are equal and lead to the identity

$$\delta \mathbf{v} \equiv \frac{d\boldsymbol{\xi}}{dt} = \mathbf{v}' \equiv \frac{\partial \boldsymbol{\xi}}{\partial t}. \tag{2.10}$$

Since $\mathbf{v}'$ is the only velocity field present in a non-rotating star (neglecting convection), is is usual to write it simply as $\mathbf{v}$.

With the two perturbation models discussed, derivation of the equations of linear, non-radial pulsation proceeds by taking the Eulerian perturbation of equations (2.2), (2.3) and (2.4). Linearization is achieved by discarding all second and higher-order perturbation terms, remembering that the fluid velocity $\mathbf{v}$ is itself a first-order quantity, and that equilibrium quantities are time-independent. This linearization is valid if the perturbations are small, and is used to render the pulsation equations tractable; non-linear pulsation is a highly non-trivial problem, even in the radial case, and is left to more in-depth studies (*e.g.*, Stellingwerf 1980; Dappen & Perdang 1985;

Fadeyev & Lynas-Gray 1996). The resulting linearized pulsation equations are then

$$\frac{\partial \rho'}{\partial t} + \nabla \cdot (\rho \mathbf{v}) = 0, \tag{2.11}$$

$$\rho \frac{\partial \mathbf{v}}{\partial t} = -\nabla p' - \rho' \nabla \Phi - \rho \nabla \Phi' \tag{2.12}$$

and

$$\nabla^2 \Phi' = 4\pi G \rho', \tag{2.13}$$

where primed quantities represent Eulerian perturbations, and the corresponding unprimed quantities denote equilibrium quantities. These three differential equations form a general mathematical description of pulsation in non-rotating stars. Since all coefficients in the equations relate only to equilibrium quantities, a separation of variables into spatial and temporal components may be effected. This leads to some general perturbed variable $f'(\mathbf{r}, t)$ being expressed in terms of spatial and temporal parts of the form

$$f'(\mathbf{r}, t) = f'(\mathbf{r}) \exp(\mathrm{i}\sigma t), \tag{2.14}$$

where σ is the pulsation frequency, and i the imaginary unit. With such a time-dependence assumed, equations (2.11)-(2.13) may be rewritten as

$$\rho' + \nabla \cdot (\rho \boldsymbol{\xi}) = 0, \tag{2.15}$$

$$-\rho \sigma^2 \boldsymbol{\xi} = -\nabla p' - \rho' \nabla \Phi - \rho \nabla \Phi' \tag{2.16}$$

and

$$\nabla^2 \Phi' = 4\pi G \rho' \tag{2.17}$$

where the substitution $\mathbf{v} \equiv \mathrm{i}\sigma\boldsymbol{\xi}$ has been made. All perturbed variables in equations (2.15)–(2.17) are now functions of only the spatial coordinate $\mathbf{r}$.

These three expressions may be simplified by splitting the mass and momentum equations into radial and horizontal parts, and then eliminating the horizontal displacement vector $\boldsymbol{\xi}_h = (0, \xi_\theta, \xi_\phi)$. Further simplifications may also be achieved by combining the thermodynamic relation for an adiabatic change,

$$\frac{\delta \rho}{\rho} = \frac{1}{\Gamma_1} \frac{\delta p}{p}, \tag{2.18}$$

where

$$\Gamma_1 = \left(\frac{\partial \ln p}{\partial \ln \rho} \right)_S, \tag{2.19}$$

with equation (2.7), to give the expression

$$\frac{\rho'}{\rho} = \frac{1}{\Gamma_1}\frac{p'}{p} - A\xi_r. \tag{2.20}$$

The (scalar) quantity ξ_r is the radial displacement perturbation, and A is the Schwarzchild discriminant introduced by Ledoux & Walraven (1958); it distinguishes between regions of convective stability ($A < 0$) and instability ($A > 0$), and is given by

$$A = \frac{d\ln\rho}{dr} - \frac{1}{\Gamma_1}\frac{d\ln p}{dr} \tag{2.21}$$

Equation (2.20) may be used to eliminate ρ' from the three adiabatic pulsation equations; Unno *et al.* (1989) use this procedure (although in a more general, non-adiabatic form) to re-write the pulsation equations in a scalar form, obtaining

$$\frac{1}{\rho}\left(\frac{\partial}{\partial r} + \frac{\rho g}{\Gamma_1 \rho}\right)\rho' - (\sigma^2 + gA)\xi_r + \frac{\partial \Phi'}{\partial r} = 0, \tag{2.22}$$

$$\frac{1}{r^2}\frac{\partial}{\partial r}(r^2\xi_r) + \frac{1}{\Gamma_1}\frac{d\ln p}{dr}\xi_r + \left(\frac{\rho}{\Gamma_1 p} + \frac{\nabla_h^2}{\sigma^2}\right)\frac{p'}{\rho} + \frac{1}{\sigma^2}\nabla_h^2\Phi' = 0 \tag{2.23}$$

and

$$\left(\frac{1}{r^2}\frac{\partial}{\partial r}r^2\frac{\partial}{\partial r} + \nabla_h^2\right)\Phi' - 4\pi G\rho\left(\frac{p'}{\Gamma_1 p} - A\xi_r\right) = 0, \tag{2.24}$$

where g is the gravitational acceleration. The differential operator $r^2\nabla_h^2$, sometimes termed the *Legendrian* (*e.g.*, Cox 1980), is given by

$$r^2\nabla_h^2 = \frac{1}{\sin^2\theta}\left[\sin\theta\frac{\partial}{\partial\theta}\left(\sin\theta\frac{\partial}{\partial\theta}\right) + \frac{\partial^2}{\partial^2\phi}\right], \tag{2.25}$$

and is discussed in the following section. Solution of equations (2.22)–(2.24) gives values for ξ_r, p' and Φ' throughout the star; ρ' may then be recovered using equation (2.20), and the horizontal displacement vector $\boldsymbol{\xi}_h$ is calculated from

$$-\sigma^2\boldsymbol{\xi}_h + \nabla_h\left(\frac{p'}{\rho} + \Phi'\right) = 0, \tag{2.26}$$

where ∇_h is the horizontal component of the gradient operator in spherical polar coordinates,

$$\nabla_h = \left(0, \frac{1}{r}\frac{\partial}{\partial\theta}, \frac{1}{r\sin\theta}\frac{\partial}{\partial\phi}\right). \tag{2.27}$$

2.4 Angular Dependencies

The equations of adiabatic, non-radial pulsation presented in the preceding section are partial differential equations, with the independent variables being the usual spherical polar coordinates (r, θ, ϕ).

Inspection of expressions (2.22)–(2.24) shows that the *only* angular (*i.e.*, $\theta - \phi$ dependent) operator present in these pulsation equations, whether it be differential or multiplicative in the sense of an angle-dependent coefficient, is the Legendrian operator $r^2\nabla_h^2$, given by (2.25). The significance of this is that a separation of variables may be achieved, in such a way that the dependent variables ξ, p' and Φ' share the *same* angular dependence. If this dependence is represented by $Y(\theta, \phi)$, then this function must satisfy the equation

$$(r^2\nabla_h^2 + \chi)Y(\theta, \phi) = 0, \tag{2.28}$$

where χ is a constant introduced in the separation. This equation must be solved subject both to the regularity conditions that $Y(\theta, \phi)$ is well-behaved and finite over the region $0 \leq \theta \leq \pi$ and $0 \leq \phi \leq 2\pi$, and to the boundary condition that $Y(\theta, \phi)$ is periodic over $\Delta\phi = 2\pi$. These conditions are imposed since only physically realistic, single-valued solutions are of interest; their consequence is that equation (2.28) is an eigenvalue problem and can only be solved for certain values of χ. The solutions are the eigenfunctions $Y_l^m(\theta, \phi)$ of the Legendrian operator, known as the *spherical harmonics* of azimuthal order m and harmonic degree l (*e.g.*, Abramowitz & Stegun 1964). The spherical harmonics are usually written in terms of the associated Legendre polynomials $P_l^m(\cos\theta)$ (*e.g.*, Arfken 1970), so that

$$Y_l^m(\theta, \phi) = (-1)^{(m+|m|)/2}\sqrt{\frac{2l+1}{4\pi}\frac{(l-|m|)!}{(l+|m|)!}}P_l^{|m|}(\cos\theta)\exp(im\phi), \tag{2.29}$$

where l and m are integers restricted such that $l \geq 0$ and $-l \leq m \leq l$; these restrictions are consequences of the regularity and boundary conditions discussed above. The normalization of the spherical harmonics is chosen so that they form an complete orthonormal set over the surface of a sphere (*e.g.*, Arfken 1970); that is,

$$\int_{\phi=0}^{2\pi}\int_{\theta=0}^{\pi} Y_l^m(\theta, \phi)Y_{l'}^{m'}(\theta, \phi)\sin\theta\, d\theta\, d\phi = \delta_{m,m'}\delta_{l,l'}, \tag{2.30}$$

where $\delta_{i,j}$ is the Kronecker delta. Expressions for the associated Legendre polynomials $P_l^m(\cos\theta)$ can be found in Appendix B; in general, they can be written as products between an $(l-|m|)$th degree polynomial in $\cos(\theta)$ and a term $\sin^{|m|}\theta$. Note that the explicit form of $P_l^m(\cos\theta)$ varies from author to author, especially in the choice of sign, and should be inspected closely in comparisons between different works.

The sign specified in expression (2.29) is somewhat arbitrary, since equation (2.28) is linear and homogeneous. This particular form has been chosen to conform to the so-called Condon-Shortley phase convention, since most representations of the recurrence relations (*e.g.*, Abramowitz & Stegun 1964) and group-theory properties (*e.g.*, Tinkham 1964) satisfied by the spherical harmonics assume such a convention. The explicit form of the phase term in expression (2.29) differs from that of Arfken (1970), and exemplifies the caveat regarding the form of $P_l^m(\cos\theta)$ used.

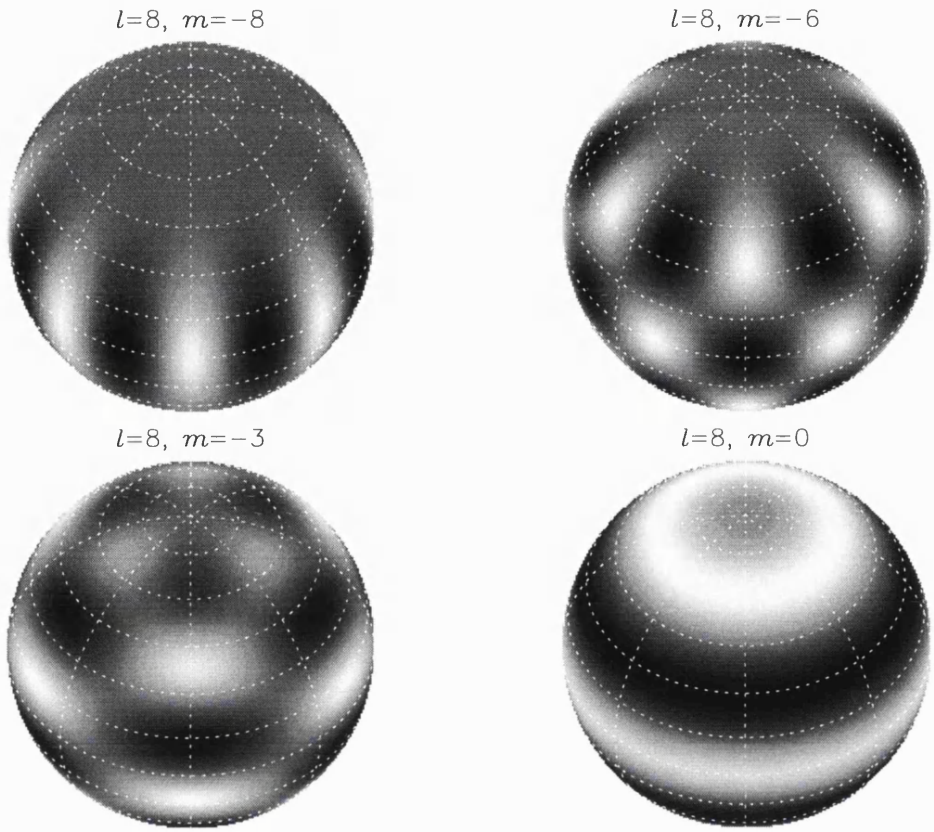

Figure 2.1: The spherical harmonics $Y_l^m(\theta, \phi)$ plotted over the surface of a sphere for $l = 8$ and $-m = 8, 6, 3, 0$. The $m = -8$ harmonic is termed *sectoral*, the $m = 0$ harmonic *zonal*, and the other harmonics *tesseral*.

Figure 2.1 illustrates the morphology of these spherical harmonics over the surface of a sphere, for a harmonic degree l of 8 and various values of azimuthal order m. Harmonics with $m = 0$ are constant along rings of constant colatitude θ, and are known as *zonal*, whilst those with $|m| = l$ consist of segments of alternating sign arrayed around the equator, and are known as *sectoral*; other harmonics are usually termed *tesseral*. Sectoral and tesseral modes have a zero amplitude at the poles (since $\sin\theta = 0$ there), whilst zonal modes have a polar amplitude of $\pm\sqrt{(2l+1)/2\pi}$. All modes possess l nodal lines over the surface of the sphere, along which their values are identically zero; these nodal lines divide the surface of the star into $2|m|(l - |m| + 1)$ separate regions if $m \neq 0$, and into $(l + 1)$ regions otherwise. Of the l nodal lines, m are spaced equally in azimuth ϕ as loci of constant longitude, and the remaining $(l - |m|)$ form loci of constant colatitude θ parallel to the equatorial plane. Furthermore, modes of even $(l - |m|)$ have even parity (symmetry) about the equator, whilst those of odd $(l - |m|)$ possess odd parity (antisymmetry) about the equator.

The eigenvalues corresponding to the eigenfunctions Y_l^m are given by

$$r^2\nabla_h^2 Y_l^m(\theta,\phi) = l(l+1)Y_l^m(\theta,\phi) \tag{2.31}$$

so the separation constant χ in equation (2.28) is constrained to take the value $-l(l+1)$. With the angular dependence of the perturbed variables thus elucidated, they may now be written in the form

$$\xi_r(r,\theta,\phi,t) = \xi_r(r)Y_l^m(\theta,\phi)\exp(\mathrm{i}\sigma t), \tag{2.32}$$

$$p'(r,\theta,\phi,t) = p'(r)Y_l^m(\theta,\phi)\exp(\mathrm{i}\sigma t) \tag{2.33}$$

and

$$\Phi'(r,\theta,\phi,t) = \Phi'(r)Y_l^m(\theta,\phi)\exp(\mathrm{i}\sigma t). \tag{2.34}$$

Substitution of these expressions into the adiabatic pulsation equations (2.22)–(2.24), with the use of equation (2.31) and a subsequent division by the common factor Y_l^m, leads to equations for the radial parts $f(r)$ of the perturbed variables, namely

$$\frac{1}{\rho}\left(\frac{d}{dr}+\frac{\rho g}{\Gamma_1 p}\right)\rho' - (\sigma^2+gA)\xi_r + \frac{d\Phi'}{dr} = 0 \tag{2.35}$$

$$\frac{1}{r^2}\frac{d}{dr}(r^2\xi_r) + \frac{1}{\Gamma_1}\frac{d\ln p}{dr}\xi_r + \left(\frac{\rho}{\Gamma_1 p} - \frac{l(l+1)}{\sigma^2 r^2}\right)\frac{p'}{\rho} - \frac{l(l+1)}{\sigma^2 r^2}\Phi' = 0 \tag{2.36}$$

and

$$\left(\frac{1}{r^2}\frac{d}{dr}r^2\frac{d}{dr} - \frac{l(l+1)}{r^2}\right)\Phi' - 4\pi G\rho\left(\frac{p'}{\Gamma_1 p} - A\xi_r\right) = 0, \tag{2.37}$$

where now ξ_r, p' and Φ' are used to denote $\xi_r(r)$, $p'(r)$ and $\Phi'(r)$ respectively; little confusion can arise with this shorthand notation. Since the coefficients in these equations change by many orders of magnitude throughout stellar interiors, solution of the equations is usually preceded by transforming the variables into dimensionless quantities whose magnitude is of order unity; Dziembowski (1971) first presented such a formulation, and this approach will be discussed in section §2.6.

2.5 Local Wave Properties

It is instructive to investigate the local behaviour of the pulsation equations (2.35)–(2.37) derived above. This can be achieved using a technique akin to the WKBJ method of solving differential equations (Coulson & Jeffrey 1977), namely assuming that the equation coefficients are constant over suitably short distance scales. With such an assumption, all three pulsation equations may be solved using wave functions of the form

$$f(r) = \exp(ik_r r), \tag{2.38}$$

where the radial wavenumber k_r is given by

$$k_r^2 = \frac{(\sigma^2 - L_l^2)(\sigma^2 - N^2)}{c^2\sigma^2}. \tag{2.39}$$

This expression introduces two characteristic frequencies L_l and N, the Lamb and Brunt-Väisälä frequencies respectively, given by

$$L_l^2 = \frac{l(l+1)c^2}{r^2} \tag{2.40}$$

and

$$N^2 = -gA, \tag{2.41}$$

where c, the adiabatic sound speed, is given for an ideal gas by

$$c^2 = \frac{\Gamma_1 p}{\rho}. \tag{2.42}$$

Equation (2.39) is essentially a dispersion relation governing the local behaviour of pulsation. In regions where $\sigma^2 > (L_l^2, N^2)$ or $\sigma^2 < (L_l^2, N^2)$, k_r is real, and the pulsation has the characteristics of travelling waves; such regions are known as *propagative* zones. In contrast, areas where $L_l^2 < \sigma^2 < N^2$ or $N^2 < \sigma^2 < L_l^2$ possess an imaginary k_r (*i.e.*, $k_r^2 < 0$), and the pulsation amplitude in such *evanescent* zones grows or decays exponentially with radius.

Evanescent zones usually occur at stellar boundaries, and serve to reflect pulsation waves propagating outwards from the interior; this reflection leads to the establishment of standing waves in the stellar interior (Cox 1980). In some cases, however, a 'tunneling' effect through surface evanescent zones may lead to wave propagation in the wind regions; Unno *et al.* (1989) introduced the possibility of such a phenomenon, and it is discussed in greater detail in §3.5.

The existence of two cutoff frequencies L_l and N in the dispersion equation is indicative of the two types of non-radial pulsation which may occur in stars. The Lamb frequency L_l is associated with pulsation where the principal restoring force is pressure (known as p-mode pulsation); this restoring force is the only one operative in radially-pulsating systems, and is the same as that of normal acoustic sound waves. In contrast, the Brunt-Väisälä frequency N is unique to non-radial pulsation, in that the restoring force associated with it results from the buoyancy discrepancy of a displaced fluid parcel relative to surrounding stellar material. This restoring force can only operate in stratified media; such stratifications of stellar material occur as a consequence of the gravitational field, and pulsation with such a restoring force is accordingly known as gravity (g-mode) pulsation. A fuller discussion of the physical significance of the Brunt-Väisälä frequency is given in Appendix A.

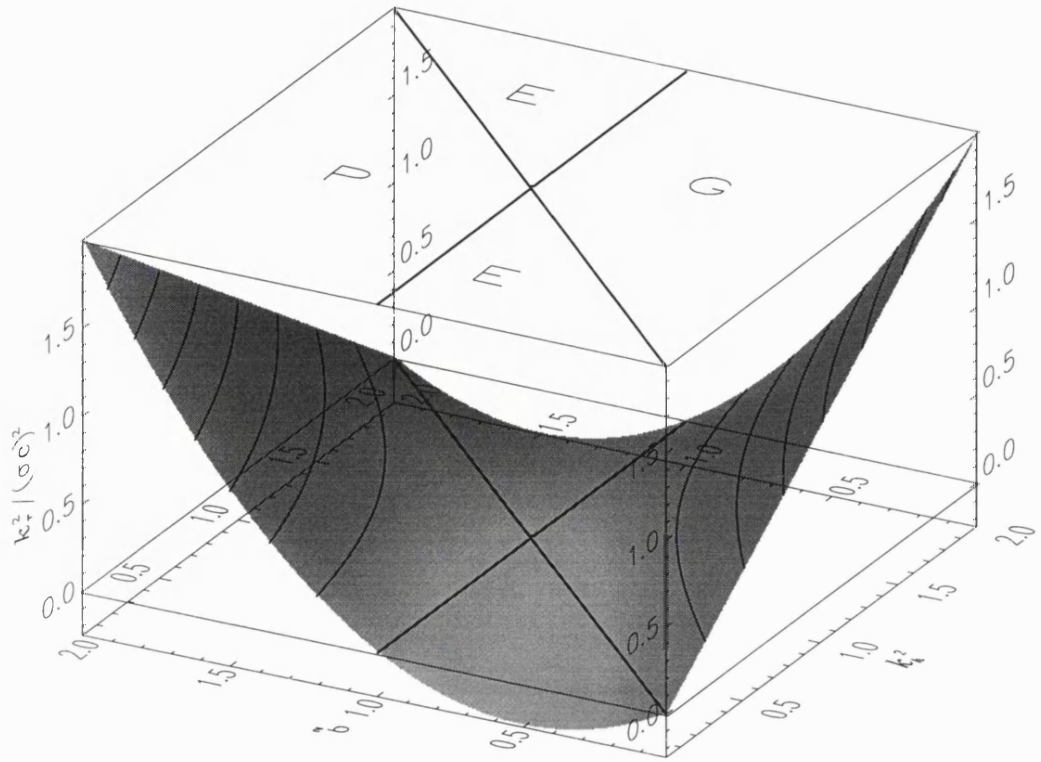

Figure 2.2: The two-dimensional dispersion relation for the typical values of $N^2 = 1$ and $L_l^2 = 1$, showing the quantity k_r^2/σ^2c^2 as a function of σ^2 and k_h^2. The curved lines on the surface represent contours of constant k_r^2/σ^2c^2, bold contours marking the $k_r = 0$ loci. k_r^2 is positive in the p-mode (P) and g-mode (G) propagation regions, and negative in the evanescent (E) regions.

Unno *et al.* (1989) found it useful to express the Lamb frequency L_l in terms of the horizontal wavenumber k_h, where

$$k_h^2 = \frac{l(l+1)}{r^2} = \frac{L_l^2}{c^2}, \tag{2.43}$$

since there are l nodal lines across the stellar surface at radius r, and $l(l+1)$ appears rather than l^2 to account for the spherical geometry. Figure 2.2 shows the two-dimensional dispersion relation, plotting k_r^2/σ^2c^2 as a function of σ^2 and k_h^2 for the typical values of $N^2 = 1$ and $L_l^2 = 1$. The lines $\sigma = c^2k_h^2$ and $\sigma = N^2$, where k_r is identically zero, are drawn in bold, and the regions where p-mode, g-mode and evanescent wave propagation occur are labelled 'P', 'G' and 'E' respectively. It is apparent that g-modes are usually associated with low frequencies, and p-modes with higher frequencies, with the varieties separated by evanescent zones.

Dispersion diagrams have proven very useful in the study of solar oscillations, since they have

allowed the distinction to be made between convective granulation (which typically falls in the evanescent regions of the diagram), and non-radial pulsation (*e.g.*, Frazier 1968). However, such diagrams are of quantitative use only in systems where the horizontal wavenumber k_h may be directly measured; since, unfortunately, this is not possible for early-type stars, dispersion diagrams are really of use only as tools for the *qualitative* understanding of pulsation in such systems.

2.6 The Dimensionless Formulation

Dziembowski (1971) presented a useful formulation of the pulsation equations (2.35)–(2.37) which allows all variables to be expressed as dimensionless quantities. This representation has been adopted by many authors (*e.g.*, Osaki & Hansen 1973; Buta & Smith 1979; Cox 1980; Saio 1980; Unno *et al.* 1989; Lee & Saio 1990); its usefulness lies in the fact that most dimensionless variables possess a similar order of magnitude (near unity), and thus may be used in numerical computations without serious loss of accuracy. Furthermore, it allows a direct comparison of pulsation phenomena between stars with disparate physical characteristics, by removing all references to quantities such as radius and mass (which vary greatly between, *e.g.*, white dwarfs and supergiants).

The dimensionless formulation revolves around writing the dependent variables ξ_r, p' and Φ' in terms of three new variables y_1, y_2 and y_3, given by Dziembowski (1971) as

$$y_1 = \frac{\xi_r}{r}, \tag{2.44}$$

$$y_2 = \frac{1}{gr}\left(\frac{p'}{\rho} + \Phi'\right) \tag{2.45}$$

and

$$y_3 = \frac{1}{gr}\Phi'. \tag{2.46}$$

Furthermore, it useful to introduce a fourth dependent variable

$$y_4 = \frac{1}{g}\frac{d\Phi'}{dr}, \tag{2.47}$$

which allows the reduction of the second-order differential equation (2.37) equation to two first-order equations. With the dimensionless variables so defined, the pulsation equations (2.22)–(2.37) may be written in the form

$$x\frac{dy_1}{dx} = (V_g - 3)y_1 + \left[\frac{l(l+1)}{c_1\omega^2} - V_g\right] y_2 + V_g y_3, \tag{2.48}$$

$$x\frac{dy_2}{dx} = (c_1\omega^2 - A^\star)y_1 + (A^\star - U + 1)y_2 - A^\star y_3, \tag{2.49}$$

$$x\frac{dy_3}{dx} = (1 - U)y_3 + y_4 \tag{2.50}$$

and

$$x\frac{dy_4}{dx} = UA^\star y_1 + UV_g y_2 + \left[l(l+1) - UV_g\right] y_3 - Uy_4, \tag{2.51}$$

where the independent variable is now $x \equiv r/R$. The 'dimensionless structure variables' $V \equiv \Gamma_1 V_g$ and U are homology-invariant quantities which originate from the study of polytropic and isothermal gas spheres (Chandrasekhar 1967); in terms of the usual physical variables, they are given by

$$V = -\frac{d\ln p}{d\ln r} = \frac{gr\rho}{p} \tag{2.52}$$

and

$$U = \frac{d\ln M_r}{d\ln r} = \frac{4\pi\rho r^3}{M_r}, \tag{2.53}$$

where M_r is the mass contained within radius r. The other two structure variables, $A^\star$ and c_1, are defined by

$$c_1 = (r/R)^3/(M_r/M) \tag{2.54}$$

and

$$A^\star = -rA, \tag{2.55}$$

so that $A^\star$ is the dimensionless form of the Schwarzchild discriminant A. Furthermore, the dimensionless frequency ω is defined through

$$\omega^2 = \frac{\sigma^2 R^3}{GM}. \tag{2.56}$$

With all of the variables in Dziembowski's (1971) formulation so defined, it can be seen that the equations of linear, adiabatic, non-radial pulsation (2.48)–(2.51) are four first-order, linear, homogeneous, coupled differential equations. Simultaneous solution of these equations will accordingly lead to four arbitrary constants of integration; these constants are usually encapsulated by algebraic boundary conditions enforced at the stellar origin and surface. The boundary conditions are the topic of discussion in the following chapter, whilst the final two sections of this chapter briefly consider a couple of areas which merit attention at this point.

2.7 The Cowling Approximation

Cowling (1941) introduced a very useful approximation which simplifies the basic pulsation equations greatly. The approximation revolves around neglecting any perturbations to the gravitational potential Φ; this is justified by the fact that, in non-radial pulsation with harmonic degree $l \gtrsim 2$, the

contribution to the gravitational potential perturbation from one part of the star is largely cancelled by contributions from others. The use of the approximation is equivalent to setting the dimensionless variables y_3 and y_4 to zero; an inspection of equations (2.50) and (2.51) shows that such a procedure will not lead to serious error if the variable U is suitably small over the region of interest. However, it should be pointed out the cancellation discussed herein is not particularly complete for modes with $l \lesssim 2$, and the Cowling approximation may be in error in such cases. The approximation is generally of use in simplifying theoretical treatments; for instance, it is used extensively in Chapter 6.

2.8 Time-independent Toroidal Modes

In addition to the usual time-dependent solutions to the pulsation equations discussed in this chapter, there exists a class of trivial solutions known as toroidal modes. These solutions may be found by setting the pulsation frequency σ and scalar variables p', ρ' and Φ' to zero, but assuming that time-independent velocity fields remain. Then, equation (2.12) vanishes, and equation (2.11) is written as

$$\mathbf{v} \cdot \nabla\rho + \rho\nabla \cdot \mathbf{v} = 0. \tag{2.57}$$

In a spherically-symmetric star, $\nabla\rho$ is radial everywhere; accordingly, this equation may be solved with a radial velocity v_r of zero, and a horizontal velocity $\mathbf{v}_h$ subject to the requirement that

$$\nabla_h \cdot \mathbf{v}_h = 0. \tag{2.58}$$

This is equivalent to the requirement that

$$\mathbf{v}_h = \nabla_h \times [f(r, \theta, \phi)\mathbf{e}_r], \tag{2.59}$$

where $f(r, \theta, \phi)$ is some completely arbitrary function, and $\mathbf{e}_r$ is the unit vector in the radial direction. It is usual to express the angular dependence of $f(r, \theta, \phi)$ in terms of the spherical harmonics used previously,

$$f(r, \theta, \phi) = f(r)Y_l^m(\theta, \phi), \tag{2.60}$$

so that the toroidal mode with harmonic degree l and azimuthal order m is characterized by the velocity field

$$\mathbf{v}_{l,m} = f(r)\nabla_h \times \left[Y_l^m(\theta, \phi)\mathbf{e}_r\right]. \tag{2.61}$$

These toroidal modes correspond to steady-state eddy motions over spherical surfaces. All time-independent stellar velocity fields can be written in terms of such modes; for instance, low-amplitude solid-body rotation is equivalent to an $l = 1$, $m = 0$ mode with $f(r) \propto r$. Toroidal modes

are generally of little interest in the context of stellar variability, and are not considered again until §6.7.3, when it is demonstrated that, in rotating stars, they exhibit an oscillatory behaviour which may generate observable variability.

Chapter 3

The Boundary Conditions

3.1 Introduction

The formulation of the pulsation equations presented in Chapter 2 describes the response of a star to a small, oscillatory perturbation. The equations, however, are an incomplete description of stellar pulsation without the inclusion of algebraic relations between the dependent variables at both the surface and the origin; these so-called boundary conditions are encapsulations of the constants of integration which result from solution of the pulsation equations, and are required to complete the theoretical description of a pulsating star. In the past, some authors have somewhat overlooked the importance of boundary conditions; this may be unwarranted, since their specific form can make gross changes to the solutions of the pulsation equations. Furthermore, and perhaps more importantly, the outer boundary of a pulsating star is the region which observational data probe, and thus a proper treatment of this boundary is essential if there is to be any real opportunity to successfully model stellar pulsation (Chapter 7). Accordingly, this chapter discusses the pulsation boundary conditions in some depth.

3.2 Dziembowski's formulation

3.2.1 Introduction

Dziembowski (1971) has presented a seminal formulation of the boundary conditions pertinent to linear, adiabatic, non-radial pulsation, in terms of the dimensionless variables introduced in §2.6. In his treatment, two boundary conditions are applied at the origin, and two at the stellar surface; however, noting that these conditions are essentially abstract entities whose position is selected on the basis of mathematical expediency, there are some cases where it is useful to move the outer boundary into trans-photospheric regions (see §3.5). In any case, most reformulations of the boundary

conditions mirror the underlying form of those presented by Dziembowski (1971); since this original treatment is somewhat terse, the four boundary conditions are derived in full in the following two subsections.

3.2.2 The Inner Boundary Conditions

Near the stellar origin, the dimensionless structure variables introduced in §2.6 have limiting values given by

$$\left.\begin{array}{rcl} U & \longrightarrow & 3 + O(x^2) \\ V_g & \longrightarrow & 0 + O(x^2) \\ A^\star & \longrightarrow & 0 + O(x^2) \end{array}\right\} \quad \text{as } x \longrightarrow 0, \tag{3.1}$$

where $O(x^2)$ denotes terms of order x^2 and higher, and the quantity c_1 approaches a central value which depends on the particular details of the star. These limits may be used to reduce equations (2.48) and (2.49) to linear differential equations with *constant* coefficients,

$$x\frac{dy_1}{dx} = -3y_1 + \frac{l(l+1)}{c_1\omega^2}y_2 \tag{3.2}$$

and

$$x\frac{dy_2}{dx} = c_1\omega^2 y_1 - 2y_2. \tag{3.3}$$

Eliminating y_2 from these expressions leads to a second-order differential equation for y_1 near the centre,

$$x^2\frac{d^2y_1}{dx^2} + 6x\frac{dy_1}{dx} + [6 - l(l+1)]\,y_1 = 0, \tag{3.4}$$

which may be solved using functions of the form $y_1 = x^\lambda$. The characteristic equation corresponding to this differential equation is

$$\lambda^2 + 5\lambda + [6 - l(l+1)] = 0, \tag{3.5}$$

giving $\lambda = l-2$ or $\lambda = -l-3$. The latter of these solutions is discarded, since it diverges as $x \to 0$, whilst the former gives

$$y_1 \sim x^{l-2} \quad \text{as } x \longrightarrow 0, \tag{3.6}$$

Substituting this expression into equation (3.2) leads to an algebraic relation between y_1 and y_2 at the stellar origin,

$$(l-2)y_1 = -3y_1 + \frac{l(l+1)}{c_1\omega^2}y_2, \tag{3.7}$$

which may be simplified to give the inner 'mechanical' boundary condition as

$$c_1\omega^2 y_1 - l y_2 = 0. \tag{3.8}$$

Equations (2.50) and (2.51) may be reduced in a similar manner to

$$x\frac{dy_3}{dx} = -2y_3 + y_4 \tag{3.9}$$

and

$$x\frac{dy_4}{dx} = l(l+1)y_3 - 3y_4 \tag{3.10}$$

near the origin, which lead to a second-order differential equation for y_3 of

$$x^2\frac{d^2y_3}{dx^2} + 6x\frac{dy_3}{dx} + [6 - l(l+1)]y_3 = 0. \tag{3.11}$$

This is essentially the same as equation (3.4), so, again,

$$y_3 \sim x^{l-2} \quad \text{as } x \longrightarrow 0, \tag{3.12}$$

giving the inner 'potential' boundary condition as

$$l y_3 - y_4 = 0. \tag{3.13}$$

This completes the boundary condition formulation for the core. The assumption that the dimensionless stellar structure variables reach limiting values at the centre of the star may be justified by noting that a non-rotating star has complete inversion symmetry through the origin; hence, the derivations presented herein are quite general.

3.2.3 The Outer Boundary Conditions

The boundary conditions applied at the stellar surface are derived in much the same way as those in the preceding subsection. The dimensionless structure variables at this surface are given by

$$\left.\begin{array}{rcl} U & \longrightarrow & 0 \\ c_1 & \longrightarrow & 1 \end{array}\right\} \quad \text{as } x \longrightarrow 1, \tag{3.14}$$

where $A^\star$ and V_g are assumed to approach values dependent on the surface details. As before, equations (2.50) and (2.51) are reduced to

$$x\frac{dy_3}{dx} = y_3 + y_4 \tag{3.15}$$

and

$$x\frac{dy_4}{dx} = l(l+1)y_3 \tag{3.16}$$

near the surface, and y_4 is eliminated from these expressions to give

$$y_3 \sim x^{-l} \quad \text{as } x \longrightarrow 1, \tag{3.17}$$

where the $y_3 \sim x^{l+1}$ solution has been discarded, since it diverges with increasing x. The outer potential boundary condition is therefore found to be

$$(l+1)y_3 + y_4 = 0. \tag{3.18}$$

The other boundary condition, the outer mechanical condition, governs how the surface responds physically to pulsation perturbations, and is somewhat more difficult to obtain using the procedure outlined above. Baker & Kippenhahn (1965) derived the mechanical boundary condition for radial pulsation by assuming an (infinite) isothermal atmosphere, and requiring that the pulsation amplitude did not diverge with increasing radius. Dziembowski (1971) presented the corresponding boundary condition pertinent to non-radial pulsation, obtained using a similar method, but did not supply the actual derivation; however, Cox (1980), with a more explicit and somewhat different treatment, obtained the same results. The derivation presented herein uses a combination of the methods of Baker & Kippenhahn (1965), Dziembowski (1971) and Cox (1980).

As $x \rightarrow 1$ at the outer boundary, it is reasonable to require that the quantity $\delta p/p$ limits at a constant, finite value, even if p becomes vanishingly small (Cox 1980), so that the stellar surface is not seriously disrupted. Accordingly, equations (2.7) and (2.44)–(2.46) may be used to write the Lagrangian pressure perturbation δp as

$$\frac{\delta p}{p} = p' + \boldsymbol{\xi} \cdot \nabla p = V\left(y_2 - y_1 - y_3\right), \tag{3.19}$$

so that the requirement on $\delta p/p$ is expressed by

$$\frac{d}{dx}\left[V\left(y_2 - y_1 - y_3\right)\right] = 0 \quad \text{as } x \longrightarrow 1. \tag{3.20}$$

If it is assumed that the atmosphere contains negligible mass, and that it is both isothermal and homogeneous near the outer boundary, then the derivative of V will be given by

$$\frac{dV}{dx} = -\frac{V}{x}. \tag{3.21}$$

Combining this expression with equation (3.20), and using equations (2.48)–(2.50) to eliminate the derivatives of y_1, y_2 and y_3, the mechanical boundary condition at $x = 1$ may be written (after dividing through by V) as

$$\left(V_g + A^\star - \omega^2 - 4\right) y_1 + \left[\frac{l(l+1)}{\omega^2} - V_g - A^\star\right] y_2 + \left(V_g + A^\star\right) y_3 + y_4 = 0. \tag{3.22}$$

This expression may be further simplified by noting that, for an chemically homogeneous isothermal atmosphere, the dimensionless Schwarzchild discriminant $A^\star$ is given by

$$A^\star = V_g\left(\Gamma_1 - 1\right); \tag{3.23}$$

substitution of this expression into equation (3.22) allows the elimination of all $A^\star$ terms, leading to

$$\left(V - 4 - \omega^2\right) y_1 + \left[\frac{l(l+1)}{\omega^2} - V\right] y_2 + (V - l - 1) y_3 = 0, \tag{3.24}$$

where $\Gamma_1 V_g$ has been replaced by V, and the outer potential boundary condition (3.18) has been used to eliminate y_4. Since V is typically very large at the stellar surface, this expression may be simplified by discarding all terms higher than first order in V^{-1}, leading to the final expression for the outer mechanical boundary condition, hereinafter the Δ-boundary,

$$\left\{1 + \frac{1}{V}\left[\frac{l(l+1)}{\omega^2} - 4 - \omega^2\right]\right\} y_1 - y_2 + \left\{1 + \frac{1}{V}\left[\frac{l(l+1)}{\omega^2} - l - 1\right]\right\} y_3 = 0. \tag{3.25}$$

In the limit that the surface pressure vanishes, $V \to \infty$, and this expression reduces to the so-called 'zero' boundary condition, hereinafter the Z-boundary,

$$y_1 - y_2 + y_3 = 0, \tag{3.26}$$

which is equivalent to the requirement that $\delta p = 0$ at the surface. Equation (3.25), the Δ-boundary, constitutes the fourth and final boundary condition in Dziembowski's (1971) formulation; however, the normalization of the pulsation equations remains arbitrary at this point. A specification of this normalization effectively constitutes a fifth boundary condition, and will be discussed in the following section.

In the derivation of the Δ-boundary, no particular requirements of adiabacity were made, so the treatment is applicable to non-adiabatic pulsation as well as the adiabatic pulsation considered in the preceding chapter. The assumption of an isothermal atmosphere, used both to calculate the derivative of V, and to eliminate $A^\star$, is not as restrictive as it might seem; any atmosphere can be piecewise divided into isothermal regions, and the requirement of isothermality need only apply to the layer actually at the outer boundary. Note, though, that the assumption of isothermality *does* require that there is mass above the outer boundary; otherwise the surface pressure must be zero, and the Δ-boundary just reduces to the Z-boundary. Possibly the greatest source of error in the modelling of pulsation at the outer boundary, however, is a lack of data concerning the behaviour of $A^\star$ and V at the surface. In some stars, particularly those with well-developed stellar winds, the notional boundary assigned at some optical depth is not necessarily related to the actual mass boundary of the star; in such cases, a proper treatment should model the outer boundary with a less restrictive approach. Unno *et al.* (1989) presented such a treatment, and it is discussed in further detail in §3.4, whilst §3.6 examines some of the observational consequences of the outer boundary conditions derived above.

3.3 The Eigenfrequencies

Inspection of both the pulsation equations (2.48)–(2.51), and the boundary conditions derived in the preceding two sections, shows that they are all linear and homogeneous in the pulsation variables; that is, every term in the expressions is first-order in y_i for $i = 1, \ldots, 4$. A consequence of this is that the normalization of any solution, consistent with the boundary conditions, is completely arbitrary. The necessary specification of this normalization constitutes an additional boundary condition, supplementing the four already found; it is usually most convenient to set this fifth condition as

$$y_1 = 1 \quad \text{at } x = 1, \tag{3.27}$$

which specifies the radial displacement amplitude ξ_r at the surface (*e.g.*, Dziembowski 1971; Osaki & Hansen 1973; Saio & Cox 1980; Unno *et al.* 1989). The unrealistically large value of ξ_r given by such a normalizations is not important, since the pulsation equations are linear, and any solutions found may be scaled to more realistic amplitudes. Note that there exist some cases, such as modes which are confined to the stellar core and have a negligible amplitude at the surface, where it is more useful to apply this normalization at the origin.

The addition of this supplementary boundary condition to the four pulsation equations means that the pulsation problem is over-specified (in the mathematical sense), and solutions can be found only for certain values of the pulsation frequency ω; in this sense, ω should be considered an eigenvalue, and accordingly is termed the *eigenfrequency* of pulsation. Solution of the four pulsation is then an eigenvalue problem, with an implicit fifth equation complementing the supplementary boundary condition

$$\frac{d\omega}{dx} = 0. \tag{3.28}$$

This expression indicates that ω may vary from solution to solution, but remains constant over the whole star for a given solution; furthermore, the eigenvalue nature of ω means that stars may pulsate in only a discrete spectrum of modes, each associated with a unique set of functions $y_1(r), \ldots, y_4(r)$ which constitute the stellar pulsation eigenfunctions. Typically, eigenfunctions with $\omega^2 \lesssim 10$ show characteristics of g-mode pulsation, whilst those with $\omega^2 \gtrsim 10$ show the characteristics of p-mode pulsation (see §4.3.4); Unno *et al.* (1989) have demonstrated that these eigenfunctions form a complete orthonormal set, and therefore that any arbitrary pulsation may be expressed in terms of a combination of these normal modes.

For each value of the harmonic degree l appearing in the pulsation equations, there exists an infinite set of discrete values which the eigenfrequency ω can assume. Notional labels are usually

assigned to each of these modes by specifying the number of nodes (excluding the origin) occurring in $y_1(r)$ between the centre and the surface; this labelling is discussed in greater detail in Chapter 5. The absence of the azimuthal order m from the equations means that, for non-rotating stars, there is a $(2m+1)$-fold degeneracy in the eigenfrequency for each value of l; this degeneracy is lifted in rotating stars (see Chapter 6) by the action of the coriolis force, in a manner akin to the Zeeman effect of atomic physics.

On a final point, it can be noted that it is ω^2, as opposed to ω itself, which appears throughout the pulsation equations; it is therefore more useful to consider the former as the eigenvalue of the equations, since they are then bi-linear in this variable. Accordingly, the discussion in the remainder of the chapter, and in subsequent chapters, adopts this approach.

3.4 Unno's Formulation

3.4.1 Introduction

Unno *et al.* (1989) have presented a compact and elegant derivation of the boundary conditions, which leads to the same results as Dziembowski's (1971) formulation for three of the boundary conditions (equations (3.8), (3.13) and (3.18)), but a different result for the outer mechanical boundary condition, which is generally less restrictive. In essence, this derivation (Unno *et al.* 1989, §18.1) is equivalent to that given in §3.2, in that it solves the four simultaneous constant-coefficient differential equations at the inner and outer boundaries by eliminating variables between the equations; however, it uses a matrix eigenvalue technique to perform the elimination, which allows the outer mechanical condition to be derived under very few assumptions, in contrast to the requirements of isothermality and chemical homogeneity imposed in §3.2. The following subsection reviews the derivation, whilst subsequent subsections consider some of the consequences of this more realistic boundary condition, including the possibility of wave leakage through the stellar surface.

3.4.2 The Outer Mechanical Boundary Condition

As before, the differential equations at the outer boundary are solved using functions of the form x^λ, but in this case λ is found from the the eigenvalues of the matrix

$$\mathbf{b} = \begin{pmatrix} V_g - 3 & l(l+1)/\omega^2 - V_g & V_g & 0 \\ \omega^2 - A^\star & 1 + A^\star & -A^\star & 0 \\ 0 & 0 & 1 & 1 \\ 0 & 0 & l(l+1) & 0 \end{pmatrix}, \tag{3.29}$$

where the element $\mathbf{b}_{ij}$ is the coefficient of y_j in the differential equation for y_i. The eigenvalues are given by

$$\lambda_1 = -l, \tag{3.30}$$

$$\lambda_2 = l + 1 \tag{3.31}$$

and

$$\lambda_\pm = \frac{1}{2}[(V_g + A^\star - 2) \pm \gamma^{1/2}], \tag{3.32}$$

where the discriminant γ is defined as

$$\gamma = (A^\star - V_g + 4)^2 + 4[l(l+1)/\omega^2 - V_g](\omega^2 - A^\star). \tag{3.33}$$

The solution corresponding to λ_2 is discarded, since it diverges with increasing x, and that corresponding to λ_1 leads to the outer potential boundary condition (3.18), derived previously in §3.2.

The remaining solutions $\lambda_\pm$ are the ones associated with Unno *et al.*'s (1989) formulation of the outer mechanical boundary condition, hereinafter termed the Υ-boundary; the sign in expression (3.32) is chosen so that the energy density of the pulsation does not grow exponentially with increasing radius. The eigenvectors of $\mathbf{b}$ corresponding to the $\lambda_\pm$ eigenvalues are used to derive the Υ-boundary as

$$\frac{\lambda_- - \mathbf{b}_{11}}{\mathbf{b}_{12}} y_1 - y_2 - \left[\frac{\alpha_1(\lambda_- - \mathbf{b}_{11})}{\mathbf{b}_{12}} - \alpha_2\right] y_3 = 0 \tag{3.34}$$

(Unno *et al.* 1989), where the coefficients α_1 and α_2 are given by[1]

$$\alpha_1 = \frac{\mathbf{b}_{12}\mathbf{b}_{23} - \mathbf{b}_{13}(\mathbf{b}_{22} + l)}{(\mathbf{b}_{11} + l)(\mathbf{b}_{22} + l) - \mathbf{b}_{12}\mathbf{b}_{21}} \tag{3.35}$$

and

$$\alpha_2 = \frac{\mathbf{b}_{21}\mathbf{b}_{13} - \mathbf{b}_{23}(\mathbf{b}_{11} + l)}{(\mathbf{b}_{11} + l)(\mathbf{b}_{22} + l) - \mathbf{b}_{12}\mathbf{b}_{21}} \tag{3.36}$$

These expressions are derived under the assumption that there is no wave energy incident from above the outer boundary; this assumption may be invalid in some cases, and is discussed in further detail in §3.5.

Inspection of expression (3.33) shows that, for certain values of ω^2, γ can assume negative values; in such cases, $\lambda_\pm$ is complex, and the solutions at the outer boundary represent progressive waves. In contrast, when γ is positive, $\lambda_\pm$ is real, and the solutions correspond to evanescent waves;

[1] (Unno *et al.* 1989) have a typographical error in their expression [18.38] for α_2.

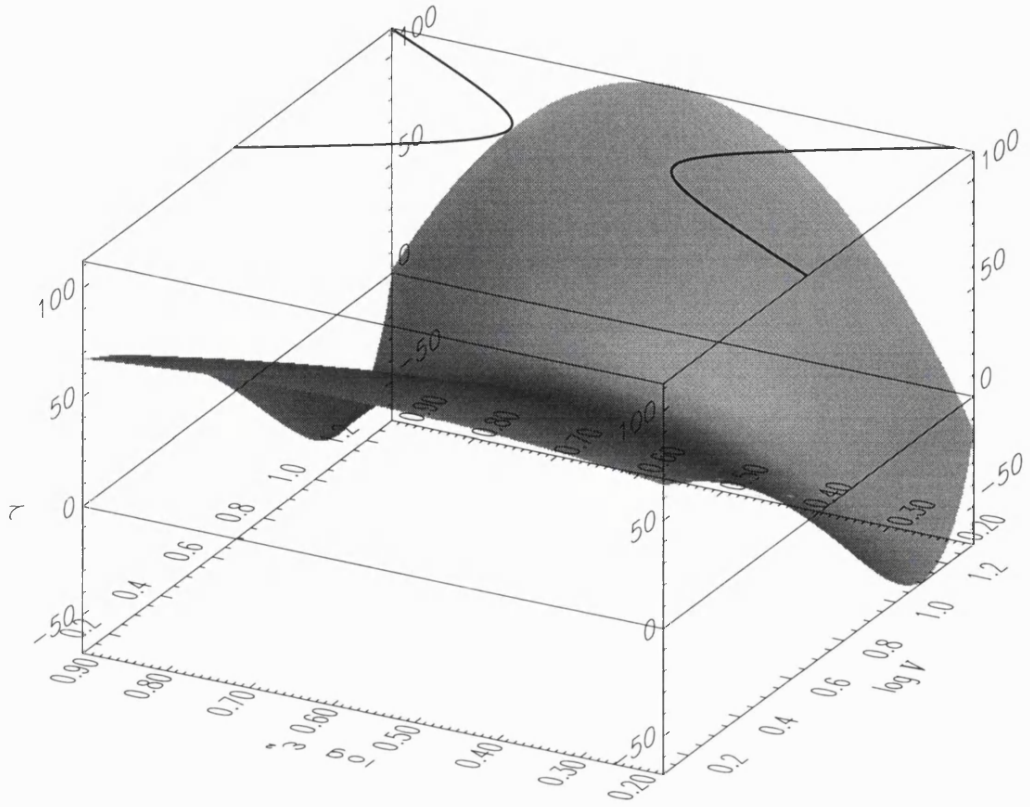

Figure 3.1: The discriminant γ plotted as a function of ω^2 and V. Regions where $\gamma > 0$ represent evanescent pulsation at the outer boundary, whilst those with $\gamma < 0$ are associated with wave leakage through this boundary The two critical frequencies $\omega_{c_1}^2$ and $\omega_{c_2}^2$, at which $\gamma = 0$, are shown as contours above the surface.

these two types of pulsation at the outer boundary are separated from one another by the roots of the equation $\gamma = 0$, which defines two critical frequencies ω_{c_1} and ω_{c_2} (Unno *et al.* 1989) such that $\gamma > 0$ if $\omega_{c_1}^2 < \omega^2 < \omega_{c_2}^2$.

Figure 3.1 illustrates γ as a function of ω^2 and V, using the typical value of $l = 4$. For the purposes of calculating the figure, the $A^\star$ term appearing in equation (3.33) has been (temporarily) eliminated in favour of V using equation (3.23), with a canonical value of $\Gamma_1 = 5/3$; this allows both easy visualisation of the functional behaviour of γ, and a simple comparison with the Δ-boundary, but is not at all necessary for the derivation of the Υ-boundary. It is apparent from inspection of this figure that, as $V \to (0, \infty)$, the two critical frequencies approach the limiting values $\omega_{c_1}^2 \to 0$ and $\omega_{c_2}^2 \to \infty$. In such cases, the pulsation is evanescent at the outer boundary for *any* pulsation mode, and no progressive-wave boundary can exist. Models which require that the pressure goes to zero

at the outer boundary (such as the Z-boundary) will behave in such a limiting manner; they should therefore be treated with caution, since they totally disallow one type of pulsation (progressive-wave) at this boundary.

The following two subsections further investigate the progressive and evanescent outer boundaries discussed above; particular attention is paid to the differences between them and the Δ-boundary presented in §3.2.3, and to wave leakage through the stellar surface which may occur at a progressive boundary.

3.4.3 Reflective Boundaries

In the case where $\gamma > 0$, $\lambda_{\pm}$ is real, and the pulsation at the outer boundary is evanescent; the negative branch of $\lambda_{\pm}$ must then be chosen to ensure that the energy density, which varies as $x^{\pm\sqrt{\gamma}}$, decays with increasing radius. This evanescent boundary represents a region where wave propagation cannot occur (§2.5); any waves incident on the boundary from the interior are totally reflected, and no wave leakage can occur into regions outside the star. Since the Brunt-Väisälä and Lamb frequencies limit to zero and infinity respectively at the stellar origin, and therefore the pulsation is evanescent there also, standing waves will be established throughout the star, which will continue to pulsate indefinitely at a constant amplitude (in the absence of any excitation or damping mechanism), due to the confinement of wave energy in the system.

In the case where $V \to \infty$ at the outer boundary, expression (3.34) reduces to the Z-boundary, as mentioned above. In more realistic cases, where V is finite, it is useful to compare the Υ-boundary with the Δ-boundary discussed in §3.2 (which also corresponds to an evanescent outer boundary), to investigate under what conditions, and by how much, they differ. To accomplish this, the value of the dimensionless pressure perturbation y_2 at the surface was calculated as a function of ω^2 and V, using the expressions for both the Δ-boundary and the Υ-boundary; as before, $A^\star$ was eliminated from equation (3.33) using equation (3.23). The normalization presented in §3.3 was used to establish the value of y_1, whilst the Cowling approximation allowed the further elimination of y_3. Figure 3.2 illustrates the difference between the two values y_2^{Δ} (Δ-boundary) and y_2^{Υ} (Υ-boundary); where the plotting of the surface has been suppressed in regions where $\gamma < 0$, since such areas do not correspond to an evanescent (reflective) boundary.

Inspection of this surface shows that, for suitably large values of V, the assumptions made in the derivation of the Δ-boundary do not appear to introduce serious errors with respect to the (presumably more accurate) results of the Υ-boundary. However, at smaller values of V, the discrepancies between the two boundary conditions become increasingly significant; furthermore, as ω^2 approaches either of the critical frequencies $\omega_{c_1}^2$ or ω_{c_2}, the Δ-boundary begins to break down, and loses validity completely once these frequencies are reached. This breakdown will usually not occur in the photosphere of a real star, since V is typically very large there; however, V can assume

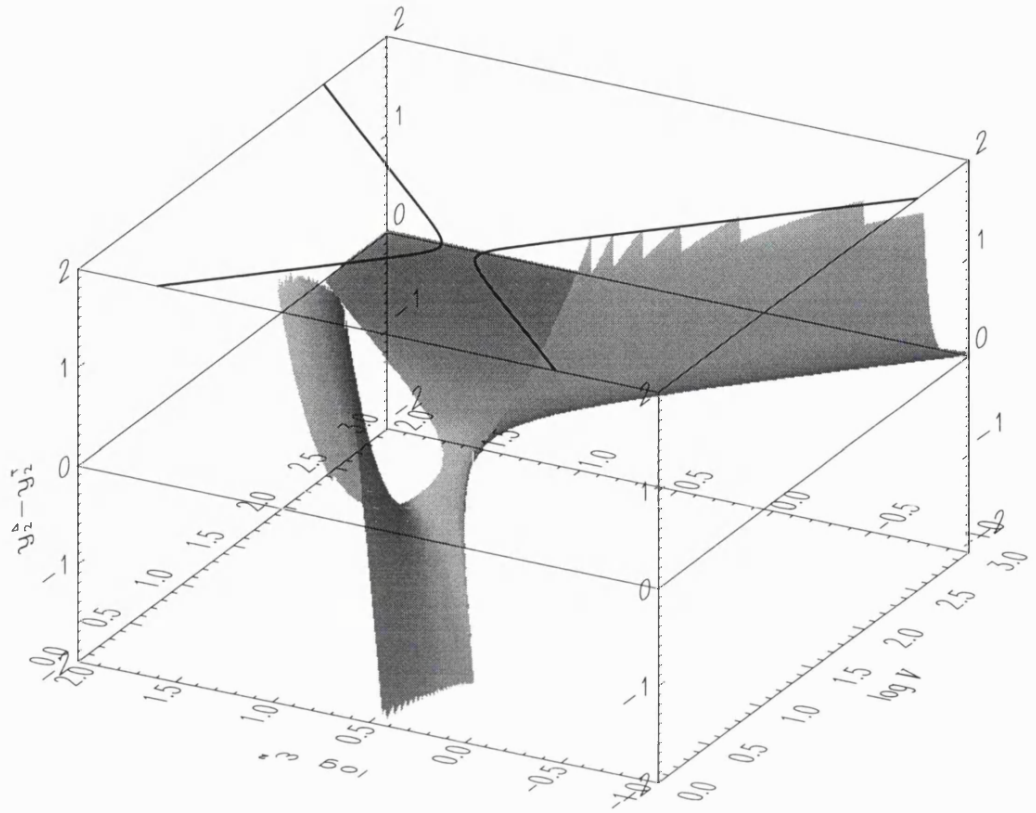

Figure 3.2: The difference between the surface values of y_2^{Δ} and y_2^{Υ}, calculated assuming the Δ-boundary and the Υ-boundary respectively, plotted as a function of ω^2 and V. The plotting of the surface has been suppressed in regions where $\gamma < 0$, whilst the contours above the surface mark the $\gamma = 0$ critical frequencies $\omega_{c_1}^2$ and $\omega_{c_2}^2$.

much smaller values in trans-photospheric zones (see §3.5), and in such cases it is essential to use the Υ-boundary formulation.

3.4.4 Progressive Boundaries

In contrast to the reflective boundary discussed above, the cases where $\omega^2 < \omega_{c_1}^2$ or $\omega^2 > \omega_{c_2}^2$ lead to negative values of γ; consequently, the eigenvalues $\lambda_{\pm}$ are complex, and the dependent variables at the outer boundary vary like

$$y_i(x) \sim x^{\lambda_{\pm}} \sim \exp\left(\pm \mathrm{i}\sqrt{|\gamma|}\ln x\right), \tag{3.37}$$

which, when combined with a temporal dependence of $\exp(\mathrm{i}\sigma t)$, describes the propagation of dispersive progressive waves. The boundary condition associated with these waves is given by equa-

tion (3.34), with the complex $\lambda_\pm$ as

$$\lambda_\pm = 1/2 \left[(V_g + A^\star - 2) \pm \mathrm{i}\sqrt{|\gamma|} \right]. \tag{3.38}$$

Again, the sign of $\lambda_\pm$ is chosen so that the energy density of the waves does not grow exponentially with increasing radius.

The criterion $\gamma < 0$ for progressive waves at the outer boundary can be somewhat misleading. Noting that the boundary condition (3.34) for such waves requires that the dependent variables y_i be complex throughout the entire star, it can be seen that solution of the pulsation equations can only be accomplished if ω, too, is complex. This in turn requires that γ be complex, and in such cases the inequality $\gamma < 0$ ceases to have any meaning. It is therefore possible to predict when the outer boundary is reflective (since γ is real and the inequality $\gamma > 0$ is meaningful), but not, paradoxically, when it is progressive, for the reasons given. In practice, however, this state of affairs rarely presents problems, since the iterative methods for solution of the pulsation equations presented in Chapter 5 ensure that convergence occurs only towards self-consistent solutions.

When the eigenfrequency ω is complex, the pulsation will have a time dependence which varies as

$$y_i(t) \sim \exp(-\sigma_i t) \exp(\mathrm{i}\sigma_r t), \tag{3.39}$$

where σ_r and σ_i denote the real and imaginary parts, respectively, of the dimensioned pulsation frequency σ, demonstrating that the pulsation amplitude will grow or decay exponentially with time. This time dependence arises as a consequence of the progressive-wave pulsation at the outer boundary; since such waves correspond to energy leakage through this boundary, the amplitude of pulsation must change with time to ensure that energy is conserved. The assumption that no wave energy is incident from above the boundary requires that the sign of σ_i be positive in any physically realistic solution, so that the pulsation amplitudes decay with time as energy is lost into regions above the boundary.

It can now be seen that, for pulsation modes with $\omega^2 < \omega_{c_1}^2$ or $\omega^2 > \omega_{c_2}^2$, the outer boundary is unable to reflect completely waves incident from the stellar interior, and a fraction of the wave energy will leak through the surface; if the pulsation amplitude throughout the star is to remain the same over time, there must be a suitable source of energy within the stellar interior to compensate for this loss. The following section looks into this wave leakage in greater detail, with a particular emphasis on the behaviour of progressive waves in stars with winds.

3.5 Wave Leakage

The introduction of the concept of wave leakage in the preceding section naturally raises questions concerning the behaviour of pulsation above the outer boundary. If it is assumed that the dimen-

sionless structure variables remain at their outer-boundary values, then the wave propagation in trans-photospheric regions will be identical to that at the outer boundary (equation (3.37)). However, this assumption of physical homogeneity above the boundary is somewhat simplistic; both V and $A^\star$ invariably change above the (nominal) stellar surface, especially for systems with well-developed winds.

This departure from the assumed situation has important ramifications for trans-photospheric wave propagation; for instance, consider a system in which γ is negative at the outer boundary, but progressively increases with increasing radius until, at some point above the boundary, it acquires a positive value. In such cases, all pulsation above this turning point will be evanescent, and any waves which leak through the outer boundary will subsequently be reflected back towards the boundary; the assumption that no wave energy is incident from above the boundary is therefore violated. To resolve this difficulty, the location of the outer boundary must be relocated at a point above which the sign of γ does not change, so that the character of the pulsation above this point is always either propagative or evanescent. This relocation is possible because, in the context of pulsation, the outer boundary is a mathematical construct, and need not actually correspond to the photosphere of the star.

In contrast, systems may also exist where γ is positive at the outer boundary, but assumes negative values at large radii. In these cases, there will be a degree of energy leakage through the evanescent barrier and out into the propagative zone, in a manner analogous to quantum-mechanical tunneling. Again, the boundary conditions derived do not correctly model such phenomena, and the outer boundary must be relocated. Such cases have particular relevance to the study of early-type stars, in which pulsation is invariably evanescent ($\gamma > 0$) in the photosphere, but may become propagative ($\gamma < 0$) further out in the wind which many of these stars possess. Cranmer (1996) has modelled a one-dimensional wind subject to a periodic perturbation at the base, and found that, for p-modes above some cutoff frequency, wave propagation readily occurs. This propagation is assisted both by the input of wave group velocity from the co-moving local reference frame in the sub-sonic regions, and by the relatively slow decay of the wind density ($\sim r^{-2}$) in the super-sonic regions.

Unfortunately, a proper approach which unifies pulsation in the stellar interior with this wind-wave propagation lies well beyond the treatments presented in this chapter. The presence of a wind significantly modifies the hydrodynamical pulsation equations through the introduction of an underlying velocity field; furthermore, the linearization procedure use in the derivation of these equations will be seriously in error in wind regions where non-linear shock phenomena are known to occur. Whilst a proper treatment of these issues cannot be undertaken herein, certain qualitative statements may still be made about the behaviour of pulsation in systems with stellar winds; it is, of course, imperative that these statements are not taken out of the very limited theoretical context

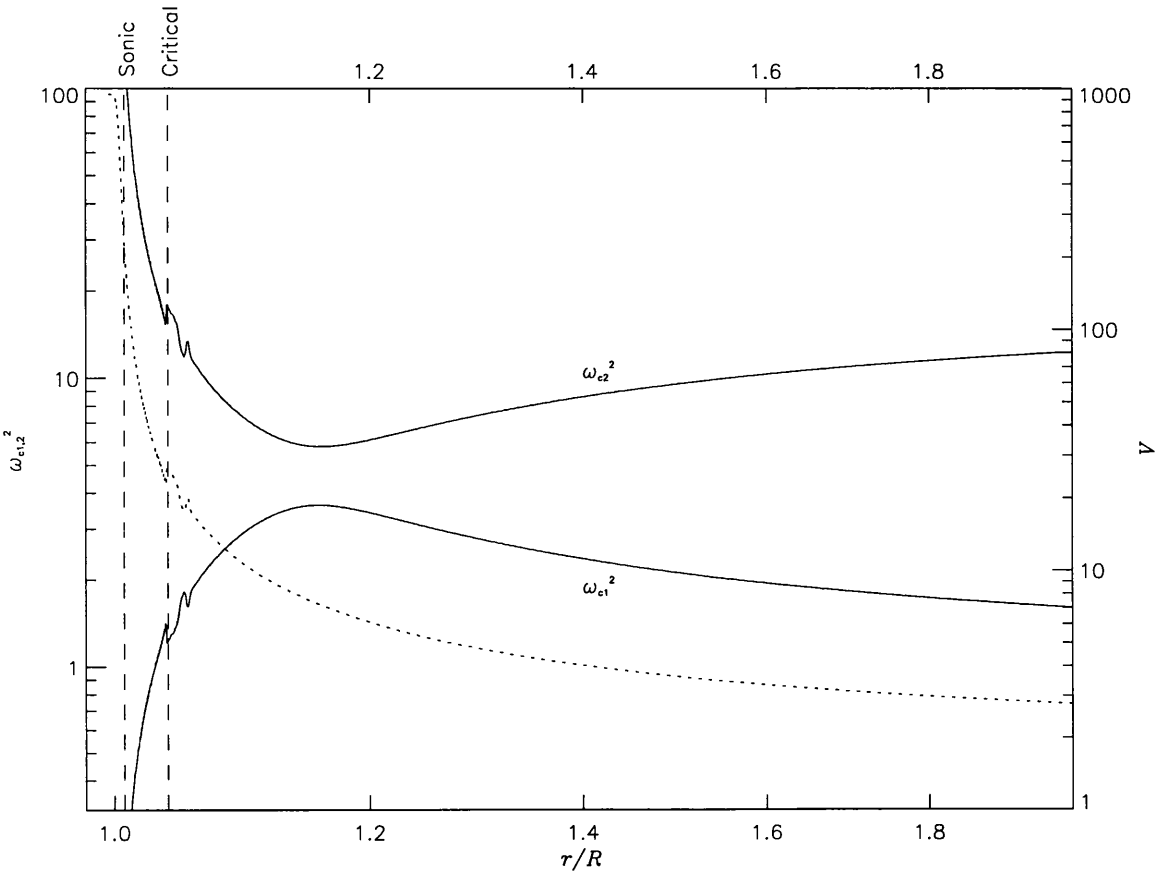

Figure 3.3: The critical frequencies $\omega_{c_2}^2$ and $\omega_{c_1}^2$ (solid) and the dimensionless structure variable V (dotted), plotted as a function of r/R for an MCAK wind model (Pauldrach *et al.* 1986). The dashed vertical lines show the locations of the sonic and critical points.

in which they are made.

Keeping this point in mind, it is useful to investigate the behaviour of the critical frequencies ω_{c_1} and ω_{c_2} throughout stellar winds; formally, they retain significance only in static media, but useful insights may still be gleaned by examining their behaviour in a qualitative manner. To accomplish this, physical parameters throughout a typical wind were calculated using a code provided by Howarth (personal communication), which implements the model described by Pauldrach *et al.* (1986); this model is a modification of the seminal CAK treatment presented by Castor *et al.* (1975), who considered a radiatively-driven wind in the Sobolev (1960) and point-source approximations. The modifications account for both the finite size of the stellar disk, and for rotation; even though the Sobolev approximation is retained, Pauldrach *et al.* (1986) demonstrated that the results produced by their modified CAK model (MCAK) are in good agreement with a more complete treatment which calculates the line force from detailed radiative-transfer solutions.

Using this MCAK code, therefore, the density structure of the wind was calculated for a star with a mass M_r, radius R and surface temperature T of 19 $M_\odot$, 9 $R_\odot$ and 35,000 K respectively, and an equatorial rotation velocity of 400 km s^{-1}; these parameters correspond loosely to those of the O9.5V pulsator HD 93521 (*e.g.*, Howarth & Reid 1993; Massa 1995). With the assumption of isothermality throughout this wind (Pauldrach *et al.* 1986), and taking Γ_1 to be 5/3 in equation (3.23), V and $A^\star$ were evaluated with the expressions

$$V = \frac{3}{2}A^\star = -\frac{d\ln\rho}{d\ln r}, \tag{3.40}$$

which enabled the critical frequencies to be calculated throughout the wind using equation (3.33). Figure 3.3 shows the results of these calculations, plotting both V and the critical frequencies as a function of radius.

Once the wind has reached its terminal velocity v_∞, the hydrostatic pressure must vanish for mass to be conserved; this accounts for the rapid decay of V above the stellar surface observed in the figure. The corresponding critical frequencies approach one another sharply at $r \approx 1.18R$, and then monotonically diverge to zero and infinity as $r \to \infty$. With the usual interpretation of these frequencies, it would appear that *all* waves leaking through the photosphere will propagate out to some (finite) radius, above which $\omega_{c_1}^2 < \omega^2 < \omega_{c_2}^2$ everywhere, and subsequently be reflected back; however, this is not necessarily the case. Owocki & Rybicki (1986) have demonstrated that, for a line-absorption driven wind, no wave above the sonic point r_s can ever propagate to smaller radii; the waves are continually swept outwards by the supersonic flow.

Accordingly, it is more likely to be the case that if any wave energy reaches the sonic point, it will be permanently lost from the star, no matter what the behaviour of the critical frequencies above this point is. The leakage will include energy associated with evanescent waves, since they will acquire a propagative character at r_s due to the underlying super-sonic flow of the wind; however, it is probable that the degree of leakage will be small in such cases, due to the thickness of the evanescent zone (at least $r_s - R$) through which they have had to tunnel. This zone will be somewhat thinner for waves which become propagative below the sonic point, and the degree of leakage will be correspondingly higher. At this point, it should again be emphasized that these predictions are based on the simplest of theories, and should be treated with the caution that they are due.

A consequence of wave leakage from a star, in whatever form, is that the the photospheric radius and pressure perturbations, ξ_r and p' respectively, will be neither in phase nor anti-phase with one another, but instead possess a relative phase displacement determined by the degree of leakage; this phenomenon is demonstrated in §5.6. It has important ramifications for the formation of lpv, since both the temperature perturbations and the horizontal displacements in the stellar photosphere depend on the pressure perturbations, as will be shown in the following section. In general,

phase displacements due to leakage will lead to a time-averaged wavelength asymmetry in the amplitude of photospheric lpv; such an asymmetry could be employed as an observational diagnostic for wave leakage, in principle allowing a connection between pulsation and wind variability to be proven. Such a possibility is considered in greater detail in §7.5.9, although the broader aspects of wind-wave propagation are not discussed further.

3.6 Perturbations at the Stellar Surface

It is important to appreciate that the outer boundary conditions derived in §§3.2 and 3.4 possess a significance beyond completing the mathematical description of pulsation, in that they relate the pulsation perturbations at the *visible* surface of the star. These perturbations are responsible for both line-profile and photometric variability, and, accordingly, this section derives suitable expressions for them, using the boundary conditions found previously.

In the limit of vanishing surface pressure, and under the Cowling approximation (§2.7), the Z-boundary (equation (3.26)) may be used to relate y_1 and y_2 in the photosphere by

$$y_2 = y_1. \tag{3.41}$$

Combining this expression with equations (2.26), (2.44) and (2.45), the horizontal displacement perturbation is given by

$$\boldsymbol{\xi}_h = k\left(0, \frac{\partial}{\partial\theta}, \frac{1}{\sin\theta}\frac{\partial}{\partial\phi}\right)\xi_r, \tag{3.42}$$

where $k \equiv \omega^{-2}$. Recalling from equation (2.32) that the angular dependence of ξ_r is given by the spherical harmonics $Y_l^m(\theta, \phi)$, the pulsation velocity fields $\mathbf{v}$ at the stellar surface will have the form

$$\mathbf{v} = V_0\left(1, k\frac{\partial}{\partial\theta}, \frac{k}{\sin\theta}\frac{\partial}{\partial\phi}\right)Y_l^m(\theta, \phi), \tag{3.43}$$

where V_0 sets the amplitude of the fields.

It is evident from examination of this expression that g-modes, which typically have $\omega^2 \lesssim 10$, generally possess surface velocity fields dominated by horizontal eddy motions, whilst p-modes, with $\omega^2 \gtrsim 10$, will be dominated by radial velocity fields. Along with a determination of the value of ω from observations of σ, a study of the comparative amplitudes of radial and horizontal velocity fields can indicate whether the pulsation has p- or g-mode characteristics.

The Δ-boundary can be used to obtain an expression for the pulsation-induced temperature variations at the stellar surface (Buta & Smith 1979). In the adiabatic approximation, these temperature variations arise from pressure perturbations through the relation

$$\frac{\delta T}{T} = \nabla_{\rm ad}\frac{\delta p}{p}, \tag{3.44}$$

where the adiabatic temperature gradient is given by

$$\nabla_{\rm ad} = \left(\frac{d\ln T}{d\ln p}\right)_S . \tag{3.45}$$

The Lagrangian pressure perturbation is found from equations (3.19) and (3.25) to be

$$\frac{\delta p}{p} = V\left(y_2 - y_1 - y_3\right) = \left[\frac{l(l+1)}{\omega^2} - 4 - \omega^2\right] y_1 + \left[\frac{l(l+1)}{\omega^2} - l - 1\right] y_3, \tag{3.46}$$

so that the temperature variations are given by

$$\frac{\delta T}{T} = \nabla_{\rm ad}\left\{\left[\frac{l(l+1)}{\omega^2} - 4 - \omega^2\right] y_1 + \left[\frac{l(l+1)}{\omega^2} - l - 1\right] y_3\right\}. \tag{3.47}$$

Within the Cowling approximation, this reduces to the form found initially by Buta & Smith (1979), namely

$$\frac{\delta T}{T} = \nabla_{\rm ad}\left[\frac{l(l+1)}{\omega^2} - 4 - \omega^2\right]\frac{\xi_r}{r}. \tag{3.48}$$

This expression has been used by a number of authors to calculate the temperature variations in models of pulsation-induced line-profile variability (*e.g.*, Lee & Saio 1990; Gies 1991; Lee *et al.* 1992*a*). However, the assumptions made in its derivation may be somewhat in error; in particular, the use of the Δ-boundary, with the limitations discussed in §3.2, may prove to be too inaccurate to model temperature variations in real systems reliably. This problem may, of course, be rectified by using the less restrictive Υ-boundary discussed in §3.4.

The requirement that the pulsation is adiabatic at the stellar surface, for the derivation of expression (3.48), is also problematical. In the photosphere, the thermal diffusion time-scale is typically quite small when compared to interior values; consequently, significant heat transfer occurs between adjacent fluid parcels, and the pulsation should be considered non-adiabatic. To estimate the degree of non-adiabacity, it is useful to introduce the transition frequency ω_t

$$\omega_t = \frac{\tau_{\rm dyn}}{\tau_{\rm th}}, \tag{3.49}$$

where the dynamical time-scale $\tau_{\rm dyn}$ was discussed in §2.1; the thermal diffusion time-scale $\tau_{\rm th}$ is given by

$$\tau_{\rm th} = \frac{4\pi r^3 \rho c_p T}{L_r}, \tag{3.50}$$

where c_p is the specific heat per unit mass at constant pressure, and L_r the luminosity at radius r. Non-adiabatic effects become appreciable in regions where ω_t exceeds the pulsation frequency ω (Unno *et al.* 1989, §26.1); such non-adiabatic zones typically occur near the stellar surface where the heat capacity c_p becomes small, and are separated from the adiabatic interior by a transition region at $\omega/\omega_t \sim 1$. The location of the transition region for a mode of a given frequency is deeper

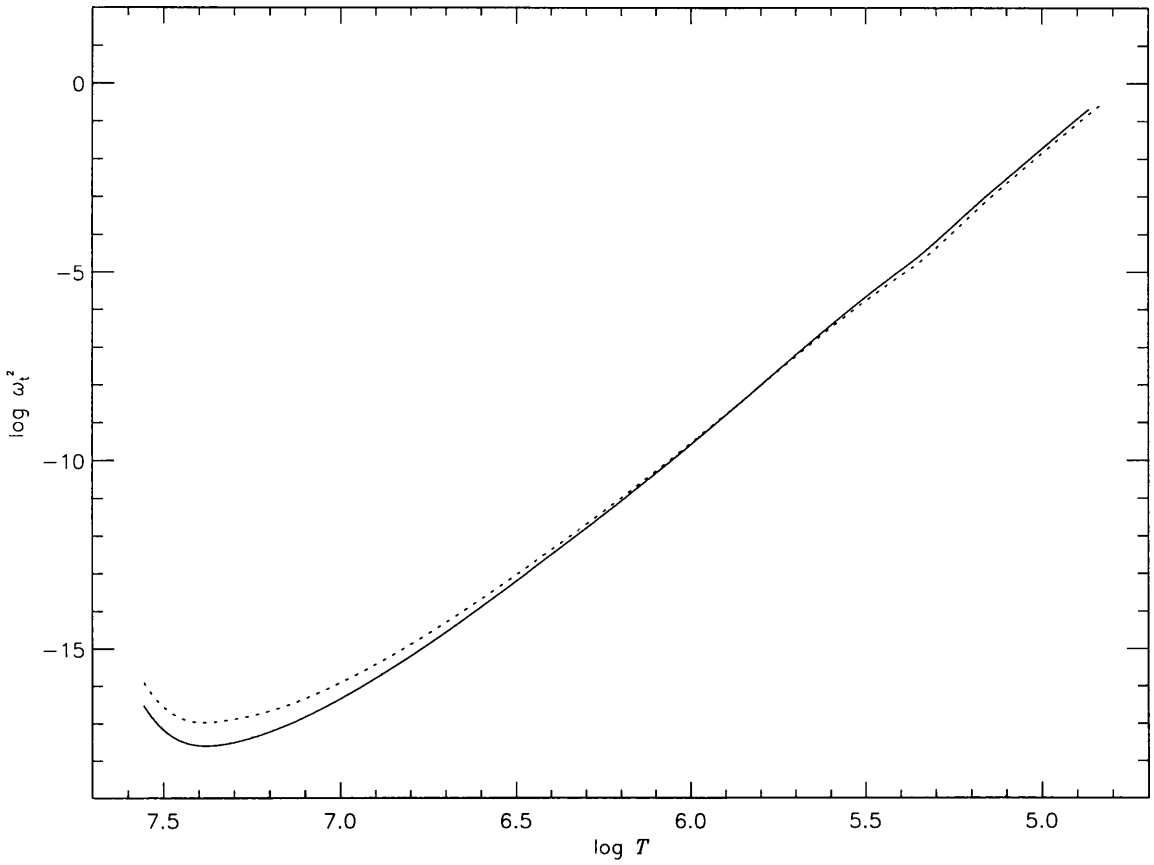

Figure 3.4: The non-adiabatic transition frequency ω_t^2 as a function of temperature in the interiors of *CoStar* models 6 (solid) and 151 (dotted). The pulsation becomes appreciably non-adiabatic in regions where ω_t exceeds the pulsation frequency ω.

both in high-mass stars, due to the proportionality of $\tau_{\rm th}$ to the mass-to-luminosity ratio (Unno *et al.* 1989), and for low-frequency pulsation, due to the longer time-scales available for thermal transfer between adjacent fluid parcels. It is apparent from examination of expression (3.50) that, for a star whose temperature and pressure approach zero at the surface, the assumption of adiabacity in the photosphere will always be invalid. Figure 3.4 illustrates the transition frequency ω_t^2 as a function of T for more realistic cases, the two *CoStar* stellar structure models discussed in Chapter 4; these models terminate at the base of the atmosphere. It is apparent that, in the case of p-modes ($\omega^2 \gtrsim 10$), the pulsation will be adiabatic right up to the base of the atmosphere, and presumably through into the atmosphere as well, whereas for low-frequency g-modes ($\omega^2 \lesssim 0.1$), the pulsation becomes appreciably non-adiabatic within the interior. Expression (3.48) may be seriously in error for such modes, and its use as portmanteau expression for all photospheric temperature perturbations in pulsation models (*e.g.*, Buta & Smith 1979; Lee *et al.* 1992*a*; Gies 1996) is questionable. However, it remains of use in the study of low-frequency modes as a measure of the maximum amplitude of temperature variations $(\delta T/T)_{\rm max}$, since the introduction of non-adiabacity

is unlikely to enhance the temperature perturbations of adiabatic pulsation. Furthermore, as figure 3.4 shows, it is still valid (within the context of the other assumptions in its derivation) in the case of higher-frequency modes ($\omega^2 \gtrsim 0.1$).

With this discussion of the pulsation boundary conditions complete, along with the investigation of some of their consequences, the following chapter looks into the calculation of stellar-structure models suitable for use in solving the pulsation equations.

Chapter 4

The Structure Models

4.1 Introduction

In the preceding chapters, the basic equations of linear, adiabatic, non-radial pulsation have been derived, along with the boundary conditions necessary for their complete solution. All of these equations depend on the explicit structure of the star in which they describe pulsation; accordingly, this chapter presents two classes of stellar-structure models, broadly pertinent to early-type stars, which are used extensively in later chapters for solution of the pulsation equations. The first of these classes, the polytropic models, are much-simplified mathematical constructs which originate from the earliest studies of stellar structure. Although the calculation of these models involves many assumptions, and, in general, they are poor representations of real stars, they do retain enough basic stellar astrophysics to be useful in pulsation studies. The polytropic models, discussed in §4.2, are included herein primarily for the sake of completeness, since they posses a certain degree of historical relevance, and were also used extensively in the testing of the numerical codes presented in Chapter 5.

The other class of models presented are based on the stellar structure and evolution calculations of Schaerer (1995). These calculations combine advances in stellar-structure theory with recent developments in physical data, such as the opacity tabulations of Rogers & Iglesias (1992), to yield comprehensive, and presumably accurate, models of stars over a range of masses and compositions. Two such models were obtained for the purposes of examining their pulsation characteristics; these so-called *CoStar* models 6 and 151 are discussed in §4.3.

It should be pointed out that the main emphasis of this chapter is a discussion of the approach used to calculate the dimensionless structure variables $A^\star$, V, c_1 and U from the 'raw' stellar structures. In this respect, this chapter is oriented more towards numerical implementation, as opposed to theoretical discussion. A consideration of the underlying physics behind the structure models (in

particular, the *CoStar* models) is not really pertinent here, and is left to more specific works (*e.g.*, Schwarzchild 1965; Chandrasekhar 1967; Kippenhahn & Weigert 1990).

4.2 The Polytropic Models

4.2.1 Introduction

Polytropes are a class of simplified stellar-structure models which were first used in considering the gravitational equilibrium of a homogeneous gaseous configuration (Lane 1870; Ritter 1878; Thomson 1887). Many authors have used polytropic models for qualitative studies of stellar pulsation (*e.g.*, Scuflaire 1974; Saio 1980), since these models retain the general features of true stellar structures whilst having a simplicity which allows both ease of mathematical manipulation, and also a high degree of physical insight. In this section, the basic equations of polytropic models are used to derive expressions for the dimensionless structure variables introduced in §2.6.

The origins of polytropic theory lie in the consideration of a gravitationally-bound gaseous system, maintained at equilibrium by some form of mixing which satisfies the thermodynamic relation

$$dQ = cdT, \tag{4.1}$$

where dQ is the heat supplied in the mixing towards equilibrium, dT is the corresponding temperature change, and c is some generalized specific heat which is assumed to remain constant throughout the mixing process. With this assumption, it can be shown that, for an ideal gas, the pressure and density obey relations of the form

$$\rho = \lambda\vartheta^{\eta} \tag{4.2}$$

and

$$p = K\lambda^{1+1/\eta}\vartheta^{\eta+1} \tag{4.3}$$

(*e.g.*, Chandrasekhar 1967), where ϑ is some variable which parameterizes the density structure of the star. The constants λ and K fix the density and temperature scales respectively, and η, the polytropic index, depends on the value assigned to the heat capacity c . These two equations, with appropriate choices of λ, K and η, can be used to describe the run of variables over restricted regions of real stellar structures, and thus constitute useful parameterizations. In the most generalized case, however, the assumption is made that an individual polytropic parameterization characterises the complete stellar structure; such models are known as *complete polytropes*, and are the principal type used in studies of stellar pulsation. For such complete polytropes, Chandrasekhar (1967) demonstrated that the central condensation of the star is a monotonically increasing function of the

polytropic index η; this dependence allows η to be used to construct basic evolutionary sequences (Scuflaire 1974), since the central condensation of most stars increases monotonically with time.

Equations (4.2) and (4.3) can be substituted into the equations of hydrostatic equilibrium and mass conservation, to yield the *Lane-Emden* equation (*e.g.*, Chandrasekhar 1967), a second-order differential equation for ϑ of the form

$$\frac{1}{\alpha}\frac{d}{d\alpha}\left(\alpha^2\frac{d\vartheta}{d\alpha}\right) = -\vartheta^\eta, \tag{4.4}$$

where the independent variable α is defined in terms of the radius r by

$$r = \left[\frac{(\eta+1)K}{4\pi G}\lambda^{1/\eta-1}\right]^{1/2}\alpha. \tag{4.5}$$

The arbitrary normalization that λ equals the central density ρ_c leads to the boundary condition

$$\left.\begin{array}{rcl} \vartheta & \longrightarrow & 1 \\ \frac{d\vartheta}{d\alpha} & \longrightarrow & 0 \end{array}\right\} \quad \text{as } \alpha \longrightarrow 0. \tag{4.6}$$

Analytical solutions to the Lane-Emden equation have long been known for the cases of $\eta = 0$, 1 and 5. In other cases (remembering that η need not be integral), it is useful to split the Lane-Emden equation into two first-order equations,

$$\frac{d\tilde{\vartheta}}{d\alpha} = -\alpha^2\vartheta^\eta \tag{4.7}$$

and

$$\frac{d\vartheta}{d\alpha} = \frac{\tilde{\vartheta}}{\alpha^2}, \tag{4.8}$$

where

$$\tilde{\vartheta} \equiv -\alpha^2\frac{d\vartheta}{d\alpha}. \tag{4.9}$$

These two equations may be solved via numerical integration; a Bulirsch-Stoer technique with adaptive step-sizes (Press *et al.* 1992) was used herein to perform this integration. Since the equations are numerically ill-conditioned at $\alpha = 0$ (*i.e.*, containing expressions of the form 0/0), a polynomial expansion around the origin was used to initiate the integration process.

The solution of the Lane-Emden equation is terminated when $\vartheta = 0$, since it becomes complex for $\vartheta < 0$, and only real solutions are of physical interest. The point $\alpha = \alpha_s$ where $\vartheta = 0$ represents the surface of the star, and is a monotonically-increasing function of η. For polytropes with $\eta \geq 5$, $\alpha_s \to \infty$, and the star is of infinite extent; an isothermal star in hydrostatic equilibrium ($\eta \to \infty$) is one such case.

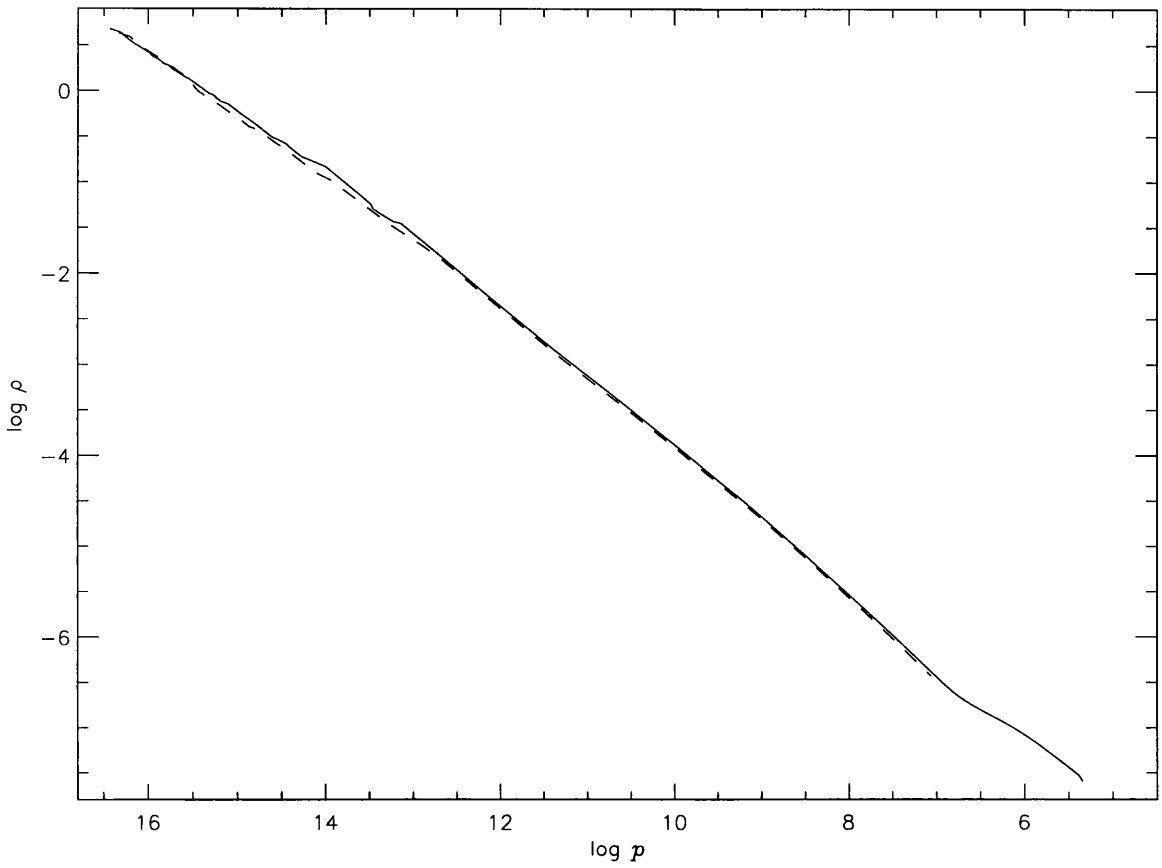

Figure 4.1: *CoStar* models 6 (solid) and 151 (dashed) plotted in the $\log p$–$\log \rho$ plane. The close approximation of the models to a straight line demonstrates that, at least for the pressure and density, the *CoStar* models are well approximated by polytropes.

To investigate how well real stars are modelled by polytropes, figure 4.1 shows a plot in the $\log p$–$\log \rho$ plane of the two *CoStar* models discussed in §4.3. For a true polytropic model, this plot would result in a straight line with a gradient $\eta/(\eta+1)$; the results of fitting such a straight line to the *CoStar* models, using a least-squares model, are summarized in table 4.1. The table specifies the fit parameters and the value of η inferred from β, the fitted line gradient. It is evident that the *CoStar* models can be represented to a surprisingly high degree of accuracy by single polytropes of index $\eta \approx 3$. Model 151 has a polytropic index slightly larger than that of model 6 because it is the more evolved of the two, and will have a correspondingly greater central condensation (Scuflaire 1974).

These results tend to support the suggestion made previously that polytropic models are useful for qualitative investigations of stellar pulsation. However, one caveat about this polytropic fitting should be raised; whilst the relationship between pressure and density in real stellar models may be represented well by a polytrope, it does not follow that all of the other variables in the stellar interior are similarly well represented. In particular, any variations of the adiabatic exponent Γ_1 throughout the star are not accounted for in polytropic models. For truly quantitative investigation

Table 4.1: The parameters obtained from fitting *CoStar* models 6 and 151 with a least-squares straight line of the form $\log\rho = \alpha+\beta\log p$; the polytropic index η associated with the fits was calculated from $\beta = \eta/(\eta+1)$. All errors quoted are to a 68% confidence level.

Model Number	α	β	η
6	0.798 ± 0.008	0.746 ± 0.002	2.94 ± 0.01
151	0.721 ± 0.006	0.752 ± 0.001	3.04 ± 0.01

of pulsation, the *CoStar* models presented in the following section (or their equivalents) must be used. The remainder of this section is concerned with the calculation of the dimensionless structure variables (§2.6) from the solutions of the Lane-Emden equation.

4.2.2 The Polytropic Dimensionless Variables

Using the equations given by Chandrasekhar (1967), which relate the solutions of the Lane-Emden equation to internal stellar quantities, expressions may be derived for the dimensionless structure variables in terms of the Lane-Emden function ϑ. This derivation begins by considering the expression for V given in equation (2.52), namely

$$V = -\frac{d\ln p}{d\ln r}.$$

Substituting the polytropic relations (4.2) and (4.3) into this expression yields

$$V = -\frac{(\eta+1)}{\alpha\vartheta}\tilde{\vartheta}. \tag{4.10}$$

The corresponding polytropic expression for the dimensionless Schwarzchild discriminant $A^\star$ can be obtained by writing it in the form

$$A^\star = V\left(\frac{d\ln\rho}{d\ln p} - \frac{1}{\Gamma_1}\right); \tag{4.11}$$

since the differential evaluates to $(1 + 1/\eta)$ in a polytropic configuration, this reduces to

$$A^\star = -\frac{(\eta+1)}{\alpha\vartheta}\tilde{\vartheta}\left(\frac{\eta+1}{\eta} - \frac{1}{\Gamma_1}\right), \tag{4.12}$$

where equation (4.10) has been used to eliminate V. The polytropic mass relation

$$M_r = -4\pi\left[\frac{(\eta+1)K}{4\pi G}\right]^{3/2}\lambda^{(3-\eta)/2\eta}\tilde{\vartheta} \tag{4.13}$$

may be used to eliminate M_r from equation (2.54), so that the polytropic expression for c_1 becomes

$$c_1 = (\alpha/\alpha_S)^3/(\tilde{\vartheta}/\tilde{\vartheta}_S). \tag{4.14}$$

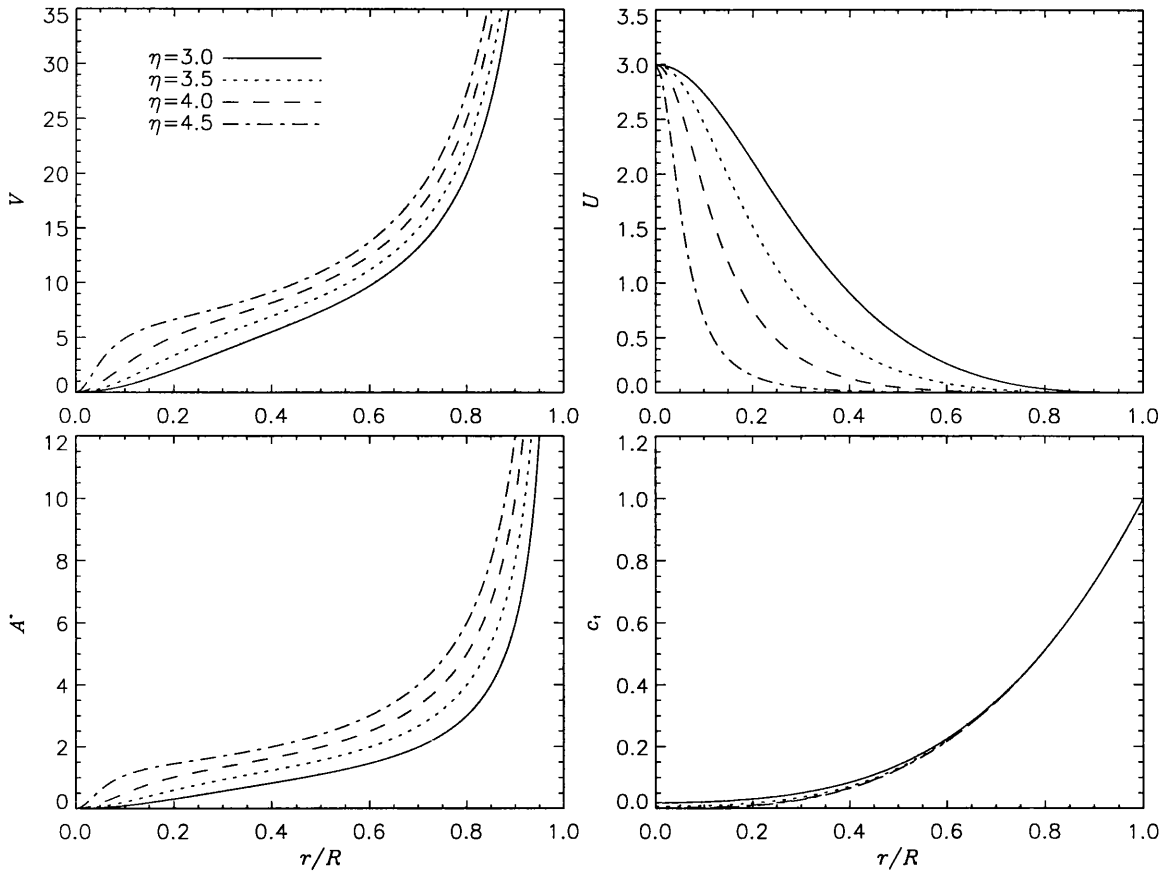

Figure 4.2: The dimensionless variables V, U, $A^\star$ and c_1 as a function of r/R for polytropic models of index $\eta = 3, 3.5, 4$ and 4.5. For all models, the adiabatic exponent Γ_1 was taken to be 5/3.

The mass relation may also be combined with equation (2.53) to obtain

$$U = -\frac{\alpha}{\tilde{\vartheta}} \frac{d\tilde{\vartheta}}{d\alpha}, \tag{4.15}$$

which is further simplified using equation (4.8) to

$$U = -\frac{\alpha^3 \vartheta^\eta}{\tilde{\vartheta}}. \tag{4.16}$$

A consideration of these expressions leads to a number of conclusions about the use of polytropes in pulsation studies. Inspection of equations (4.10), (4.12), (4.14) and (4.15) shows that a given polytropic model, expressed in terms of the dimensionless variables, is a function only of η and the adiabatic exponent Γ_1. This property is responsible, in part, for the popularity of polytropic pulsation models, since they are characterized by so few free parameters.

Another important point, which certainly merits attention, is that for $\eta < \Gamma_1/(\Gamma_1 - 1)$, $A^\star$ is negative throughout the entire star. In such cases, the star will (formally) be in a state of complete convection, and any pulsation will be evanescent in nature (§2.5). For a canonical value of

$\Gamma_1 = 5/3$, this lower boundary on η lies at $\eta = 2.5$; in practice, therefore, most authors study only models with $\eta \gtrsim 3$ (*e.g.*, Scuflaire 1974; Saio 1980).

Figure 4.2 illustrates the run of the variables V, U, $A^\star$ and c_1 throughout a star, for the polytropic indices $\eta = 3$, 3.5, 4 and 4.5, and an adiabatic exponent Γ_1 of 5/3. Of note is the divergence of both V and $A^\star$ to infinity as the stellar surface is approached; this behaviour occurs due to the fact that, in any polytropic model, the pressure and density limit to zero at the stellar surface. Another point worth remarking on is the strong dependence of the form of U on the polytropic index η. Since U is essentially a measure of the density at a point in terms of the mean density interior to that point, its behaviour highlights the fact that η is a monotonic function of the degree of central condensation in a model, as mentioned previously. On a final note, it can be observed that the behaviour of all four dimensionless variables at both the stellar origin and the surface is in accordance with equations (3.1) and (3.14) presented in Chapter 3.

As was mentioned in the introduction, these polytropic models are included here primarily for the sake of completeness; they were used extensively for calculations before the *CoStar* models were available, and their simple nature rendered them very useful in checking the accuracy of the numerical codes presented in Chapter 5. However, the *CoStar* models, discussed in the following section, effectively render the polytropic models obsolete; consequently, the latter will be considered again only briefly.

4.3 The *CoStar* Models

4.3.1 Introduction

The *CoStar* models, presented by Schaerer (1995), represent one of the first attempts to calculate 'Complete Stellar Models' (hence the name) which consistently treat the stellar interior, photosphere and wind. The equations used in their calculation assume full spherical geometry, and permit non-zero bulk velocities for the modelling of mass outflows. Atmospheres are treated in detailed non-LTE statistical equilibrium; radiative transfer is modelled within the Sobolev (1960) approximation, and line-blanketing is included using the method of Schmutz *et al.* (1991). The physical data for the calculations are derived from the recent OPAL opacity calculations of Rogers & Iglesias (1992), and an equation of state is adopted from Schaerer (1991) and Schaller *et al.* (1992).

For the purposes of pulsation studies, two of these *CoStar* models, labelled 6 and 151, were provided by Schaerer (personal communication); the physical parameters of these models are summarized in table 4.2. Both of the models come from a $20M_\odot$ evolutionary track; model 6 is ZAMS, whilst model 151 is a slightly evolved main-sequence star. The physical parameters of the models (apart from, perhaps, the helium abundances) appear to loosely correspond to those of the O9.5V pulsator HD 93521 (*e.g.*, Howarth & Reid 1993; Massa 1995), suggesting that a study of their

Table 4.2: The physical parameters of *CoStar* models 6 and 151. X and Y are the usual hydrogen and helium surface abundances (by mass) respectively; X_c is the core hydrogen abundance.

Model	$\frac{M}{M_\odot}$	$\log T_{\rm eff}$ [K]	$\log \frac{L}{L_\odot}$	$\log g$ [cm s^{-2}]	$\frac{R}{R_\odot}$	X	X_c	Y
6	20.00	4.556	4.664	4.236	5.700	0.680	0.678	0.300
151	19.60	4.523	4.767	4.011	7.313	0.680	0.478	0.300

pulsation characteristics is highly relevant.

Both models were obtained as ASCII text files which tabulate the physical parameters throughout the star; the following two subsections discuss the procedure used to read these files, and obtain relevant pulsation data from the information contained within them, whilst §4.3.4 investigates the general pulsation characteristics of the models.

4.3.2 Reading the *CoStar* Model Files

The *CoStar* ASCII text files consist of three sections, describing the atmosphere, envelope and core, respectively; the atmosphere is taken down to a Rosseland-mean optical depth of 20, whilst the envelope terminates at a point interior to which the hydrogen/helium ionization is complete. In addition to the actual tabulation of variables, the files contain extensive comment lines to aid human readability; tables 4.3 and 4.4 document all of the (pertinent) variables specified by the files in the core and envelope respectively, along with the corresponding names assigned to them in the comment lines. These names are adopted herein to represent the actual numerical value of a variable as specified by the *CoStar* files; this procedure helps to highlight the distinction between the quantities specified by the *CoStar* model files, with their limited information and numerical precision, and those of the underlying theoretical star which the *CoStar* files model. The meaning of variables not previously introduced is specified in the tables; the majority of these new variables are not really necessary for calculations performed in the adiabatic approximation, but do have a use in the quasi-adiabatic stability analysis undertaken in §5.5.

Initially, the *CoStar* model files were edited by hand to remove comment lines and introduce markers to denote the core/envelope and envelope/atmosphere boundaries (since the file format is different in each of the three regions). However, this proved time-consuming and error-prone; accordingly, a code, hereinafter REAPER, was devised to read 'raw' *CoStar* files and place all pertinent data in comprehensive arrays. In the atmosphere, the radius r is defined to be constant, which precludes its use in any pulsation study where r is the independent variable; accordingly, REAPER

discards all atmospheric information, and begins reading information at a grid point in the envelope where r begins to change (this typically occurs within two grid points of the envelope/atmosphere boundary). Since the set of variables defined throughout the models was not uniform (with some variables defined in the envelope but not in the core, and *vice versa*), supplementary calculations were required within REAPER to ensure that all data were complete over the entire star. In particular, the adiabatic exponents Γ_1, Γ_2 and Γ_3 were evaluated in the core using

$$\Gamma_1 = \frac{1}{\alpha - \nabla_{\rm ad}\delta}, \tag{4.17}$$

$$\Gamma_2 = \frac{1}{1 - \nabla_{\rm ad}} \tag{4.18}$$

and

$$\Gamma_3 = \frac{\nabla_{\rm ad}}{\alpha - \nabla_{\rm ad}\delta} + 1. \tag{4.19}$$

These expressions were derived from equations for the exponents given by Unno *et al.* (1989); each expression consists only of variables which *are* defined in the core regions of the *CoStar* models (*i.e.*, ALPHA, DELTA and ADIM). Calculation of the mean molecular weight μ in the core was accomplished by recalling that the core is formally defined to be the region of complete hydrogen/helium ionization. This means that μ will be given by

$$\frac{1}{\mu} = 2X + \frac{3}{4}Y + \frac{1}{2}(1 - X - Y), \tag{4.20}$$

where, again, X and Y *are* defined in the core. The mean weight $1/2$ assigned to the metals (and their electrons) has been adopted from the value given by Unno *et al.* (1989); it may be in error, but the metallicity is generally small in models with only small degrees of evolution, and so any errors in VMY, the calculated value of μ, will be correspondingly small.

The core values of the pressure scale height ∇_r and the 'pressure scale mass' ∇_{M_r} are found in a corresponding simple manner; the equations of hydrostatic equilibrium and mass conservation give

$$\nabla_r = -\frac{pr}{GM_r\rho} \tag{4.21}$$

and

$$\nabla_{M_r} = \frac{4\pi\rho r^3}{M_r}\nabla_r. \tag{4.22}$$

For some calculations, a value for the specific heat at constant pressure, c_p, is also required. This is actually specified in the model envelopes, but is expressed in rather arcane units, so it is easier to evaluate it from the thermodynamic relation

$$c_p = \frac{p\delta}{\nabla_{\rm ad}\rho T}. \tag{4.23}$$

Table 4.3: The variables defined in the envelope region of the *CoStar* stellar-structure files. The *CoStar* names of the variables, along with their meaning, are given; κ is the opacity, μ the mean molecular weight, and β the ratio of gas pressure to total pressure.

Name	Variable	Name	Variable
UVLPT	$\log p$	RHP	$\alpha \equiv \left(\frac{\partial \ln \rho}{\partial \ln p}\right)_T$
VLRO	$\log \rho$	RHT	$-\delta \equiv \left(\frac{\partial \ln \rho}{\partial \ln T}\right)_p$
VLT	$\log T$	VLKA	κ
VLM	$\log M_r$	VKAT	$\kappa_T \equiv \left(\frac{\partial \ln \kappa}{\partial \ln T}\right)_p$
VLR	$\log r$	VKAP	$\kappa_p \equiv \left(\frac{\partial \ln \kappa}{\partial \ln p}\right)_T$
		VMY	μ
GAMMA1	Γ_1	VMYT	$\mu_T \equiv \left(\frac{\partial \ln \mu}{\partial \ln T}\right)_p$
GAMMA2	$\Gamma_2 \equiv 1/(1-\nabla_{\rm ad})$	VMYP	$\mu_p \equiv \left(\frac{\partial \ln \mu}{\partial \ln p}\right)_T$
GAMMA3	$\Gamma_3 \equiv \left(\frac{\partial \ln T}{\partial \ln \rho}\right)_S + 1$	BETA	$\beta \equiv p_{\rm gas}/p$
GRAR	$\nabla_r \equiv \left(\frac{d \ln r}{d \ln p}\right)$	GRAM	$\nabla_{M_r} \equiv \left(\frac{d \ln M_r}{d \ln p}\right)$
GRAT	$\nabla \equiv \left(\frac{d \ln T}{d \ln p}\right)$	VNA	$\nabla_{\rm ad}$

The discriminant ZENSI, which takes positive values in convective zones and negative values otherwise, is not specified in the envelope, but may trivially be assigned appropriate values there, since the envelope convective zones are marked in the *CoStar* files by text comments.

When the arrays initialized by REAPER were used to calculate the dimensionless structure variables over the *CoStar* models, a number of numerical difficulties were encountered. These difficulties invariably revolved around the evaluation of numerical derivatives from low-precision data. Whilst the derivatives appearing in the definitions of V and U (equations (2.52) and (2.53) respectively) do not present problems, since these quantities posses equivalent algebraic expressions, the dimensionless Schwarzchild discriminant $A^\star$ is particularly difficult to evaluate without the introduction of a large degree of numerical noise. The following subsection discusses the procedure adopted herein to surmount this problem.

4.3.3 Calculating the *CoStar* Brunt-Väisälä Frequency

The problems encountered in the evaluation of $A^\star$ arise from its dependence on the Brunt-Väisälä frequency N, through

$$A^\star = \frac{rN^2}{g} = \frac{1}{\Gamma_1}\frac{d \ln p}{d \ln r} - \frac{d \ln \rho}{d \ln r}; \tag{4.24}$$

Table 4.4: The variables defined in the core region of the *CoStar* stellar-structure files. The *CoStar* names of the variables, along with their meaning, are given; κ is the opacity, ϵ the nuclear energy generation rate, and β the ratio of gas pressure to total pressure. X and Y are the hydrogen and helium mass fractions respectively, and the discriminant ZENSI is greater than zero in convective zones.

Name	Variable	Name	Variable
VM	M_r/M	ALPHA	$\alpha \equiv \left(\frac{\partial \ln \rho}{\partial \ln p}\right)_T$
P	$\log p$	DELTA	$\delta \equiv -\left(\frac{\partial \ln \rho}{\partial \ln T}\right)_p$
T	$\log T$	BETA	$\beta \equiv p_{\rm gas}/p$
R	$\log r$	EPS	ϵ
VL	L_r/L	EPSP	$\epsilon_p \equiv \left(\frac{\partial \ln \epsilon}{\partial \ln p}\right)_T$
RH	$\log \rho$	EPST	$\epsilon_T \equiv \left(\frac{\partial \ln \epsilon}{\partial \ln T}\right)_p$
ADIM	$\nabla_{\rm ad}$	CAPP	$\kappa_p \equiv \left(\frac{\partial \ln \kappa}{\partial \ln p}\right)_T$
X	X	CAPT	$\kappa_T \equiv \left(\frac{\partial \ln \kappa}{\partial \ln T}\right)_p$
Y	Y	ZENSI	—

whilst the two derivatives on the right-hand side of this expression may be large, their difference, especially in convective zones, can be very small. Furthermore, whilst the pressure derivative may be found from the values of ∇_r, the corresponding density derivative is not specified in the *CoStar* models, and must be calculated numerically. These two factors lead to a large degree of numerical noise in the calculated values of both N^2 and $A^\star$, as is demonstrated in figure 4.3, which plots N^2 as a function of radius in *CoStar* models 6 and 151 (N^2 is plotted rather than $A^\star$ since it is the more natural variable for qualitative pulsation studies). It is apparent that, especially throughout the core regions, the numerical noise in N^2 is totally unacceptable.

A number of approaches were adopted in an attempt to eliminate this noise, from median filtering the values of N^2, to fitting the pressure and density with a cubic spline and obtaining analytical derivatives from the spline fit. However, although a number of these methods were found to reduce the noise to some extent, none led to its elimination at an acceptable level. The reasons for this failure lie in the low numerical precision (typically, only 5 significant figures) of the *CoStar* model files (presumably, the actual *CoStar* calculations were performed at higher precision and then truncated for tabulation); accordingly, a completely different approach is required for the calculation of both N^2 and $A^\star$.

Brassard *et al.* (1989) experienced similar numerical difficulties in the calculation of the Brunt-

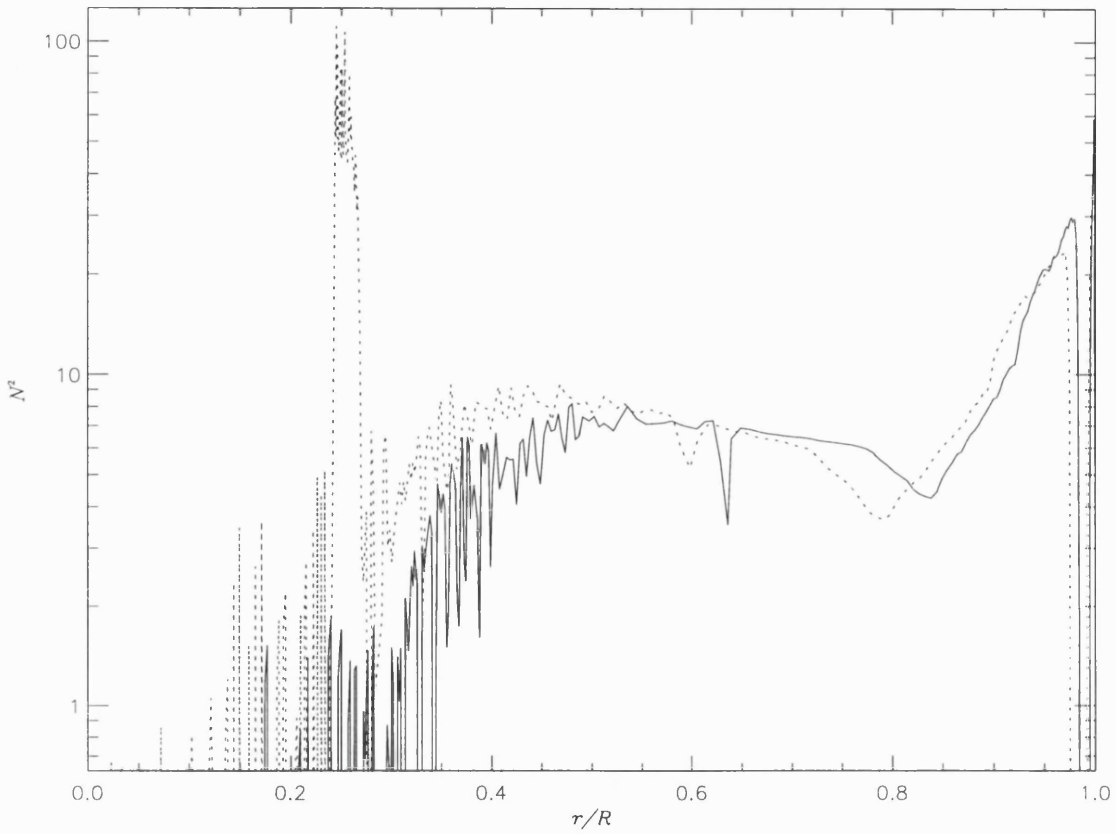

Figure 4.3: The square of the Brunt-Väisälä frequency N, in units of GM/R^3, plotted as a function of r/R for *CoStar* models 6 (solid) and 151 (dotted) — values calculated using numerical derivatives for the density scale height. Note the large amount of numerical noise in the calculated function, especially at small radii.

Väisälä frequency, whilst studying the properties of variable DA white-dwarf stars. They found that the degenerate nature of the white-dwarf plasma led to very small values of N^2, and encountered numerical noise equivalent to that discussed above. Their approach for solving this problem revolved around writing the Brunt-Väisälä frequency in a form dependent on thermodynamic rather than mechanical quantities, namely

$$N^2 = \frac{gV}{r}\left[(\nabla_{\rm ad} - \nabla)\delta + \sum_{i=1}^{l-1} \frac{d\ln X_i}{d\ln p}\left(\frac{\partial \ln p}{\partial \ln X_i}\right)_{T,p}\right], \tag{4.25}$$

where X_i denotes the mass fraction of the ith element present in the star (and there assumed to be l such elements). Brassard *et al.* (1989) deemed this expression useful since δ (introduced in table 4.3) is typically close to zero in degenerate matter (Unno *et al.* 1989), and hence, if the summation term in the expression is temporarily neglected, any numerical noise in $(\nabla_{\rm ad} - \nabla)$ will lead to only small degrees of noise in the calculated value of N^2.

In the context the *CoStar* models, this expression is useful for slightly less fundamental reasons. Even in regions where N^2 is very small, δ assumes moderate values, and so the noise introduced by the $(\nabla_{\rm ad} - \nabla)$ term would still appear to be problematical, especially in convective zones. However, it is a reasonable assumption that the degree of super-adiabacity in a convective zone is negligibly small, and accordingly the term $(\nabla_{\rm ad} - \nabla)$ may be set identically to zero in such regions. Convective zones are tagged in the *CoStar* model files with positive values of the ZENSI variable, so an implementation of this procedure is trivial. Outside convective zones, the $(\nabla_{\rm ad} - \nabla)$ term differs appreciably from zero, and does not require numerical differentiation for its calculation (since both $\nabla_{\rm ad}$ and ∇ are specified in the model files); accordingly, it introduces very little numerical noise in the calculated value of N^2.

The only remaining source of noise in N^2 is the summation term in equation (4.25), which is non-zero in zones of varying chemical composition. It would appear that there is insufficient thermodynamic information in the *CoStar* model files to calculate values for this summation, let alone ensure that these values are sufficiently noise-free. However, Unno *et al.* (1989) demonstrated that, in regions of complete ionization, the summation term may be written

$$\sum_{i=1}^{I-1} \frac{d\ln X_i}{d\ln p} \left(\frac{\partial \ln p}{\partial \ln X_i} \right)_{T,p} = \nabla_\mu \equiv \frac{d\ln \mu}{d\ln p}. \tag{4.26}$$

This expression cannot be used in the partially-ionized envelope regions of the *CoStar* models; fortunately, though, these regions are chemically homogeneous, and so the summation term will be identically zero throughout. In contrast, this expression *is* valid in the completely ionized core regions (which can be chemically inhomogeneous). Calculation of ∇_μ must proceed via numerical differentiation, since it is not specified anywhere in the *CoStar* model files; this will introduce a degree of noise, but, as it turns out, surprisingly little, since ∇_μ is non-zero only in the molecular-weight-gradient zones surrounding the convective cores of evolved models. Thus, the values of $A^\star$ throughout the *CoStar* models may be calculated using

$$A^\star = V\nabla_\mu \tag{4.27}$$

in the convective (ZENSI > 0) core regions,

$$A^\star = V\left[(\nabla_{\rm ad} - \nabla)\delta + \nabla_\mu\right] \tag{4.28}$$

in the radiative (ZENSI < 0) core regions, and

$$A^\star = V\left[\delta(\nabla_{\rm ad} - \nabla)\right] \tag{4.29}$$

in the radiative envelope regions ($A^\star$ will be zero in convective envelope regions). Evaluation of the product $V\nabla_\mu$ is best accomplished by numerically calculating the full space derivative of μ.

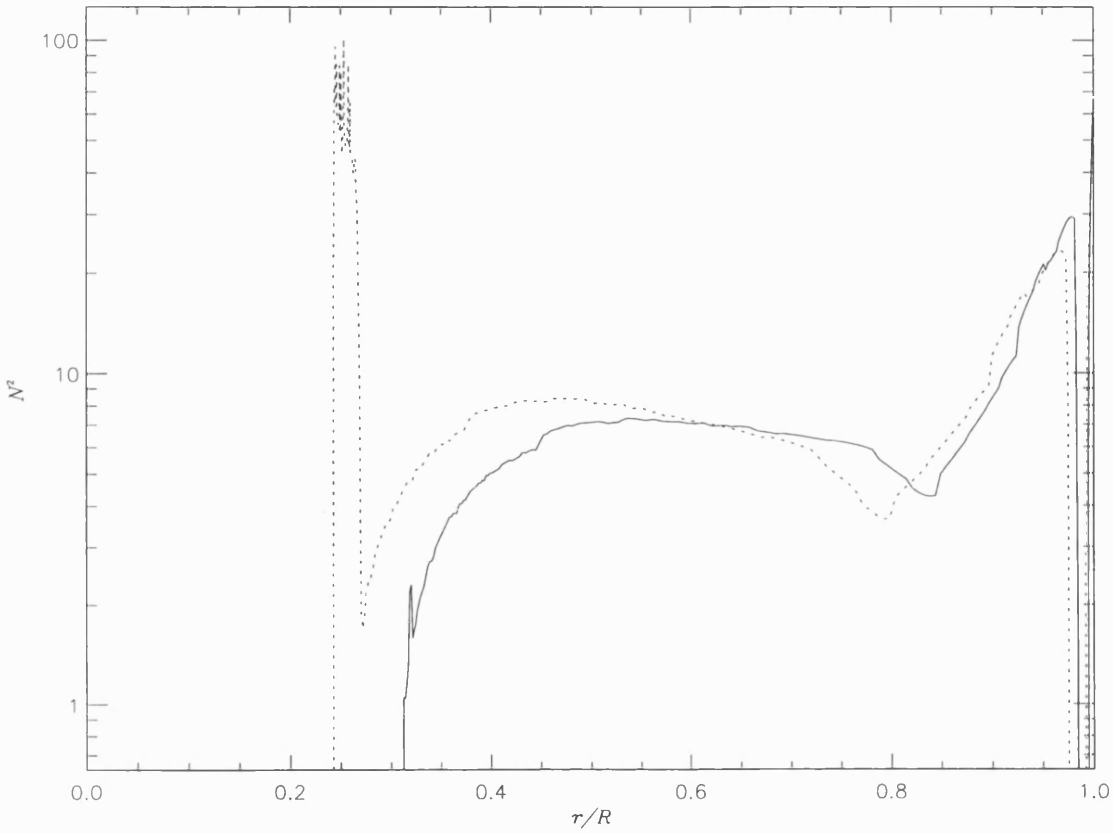

Figure 4.4: The square of the Brunt-Väisälä frequency N, in units of GM/R^3, plotted as a function of r/R for *CoStar* models 6 (solid) and 151 (dotted) — values calculated using the formulation of Brassard *et al.* (1989). Observe that there is numerical noise remaining only in the region of varying composition outside the core of model 151.

Figure 4.4 shows N^2 as a function of radius, calculated using the above procedure, for models 6 and 151. It is apparent that the noise has been all but eliminated from N^2; the only region which still presents problems is the molecular-weight-gradient zone just outside the convective core of model 151. This residual noise can easily be suppressed by applying a sliding 7-point median filter to the calculated values; figure 4.5 shows that such an approach reliably eliminates almost all of the remaining noise in N^2.

4.3.4 The *CoStar* Dimensionless Variables

The calculation of V, U and c_1 is considerably simpler than that of $A^\star$, and does not require any discussion. The computed values of these variables, along with those of $A^\star$, are illustrated as a function of radius in Fig 4.6 for models 6 and 151. As with the polytropic models, the behaviour

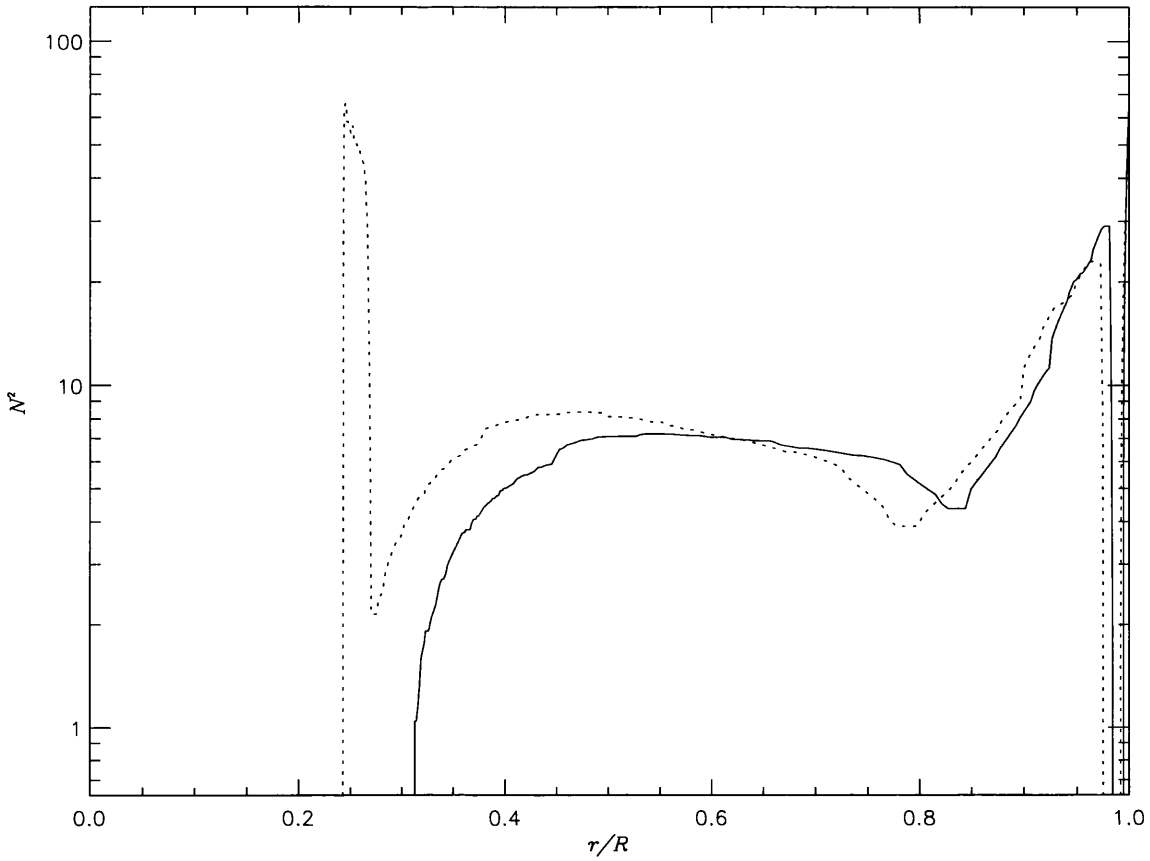

Figure 4.5: The square of the Brunt-Väisälä frequency N, in units of GM/R^3, plotted as a function of r/R for *CoStar* models 6 (solid) and 151 (dotted) — values calculated using the formulation of Brassard *et al.* (1989) and then smoothed using a sliding median filter. Observe that the numerical noise has all but been eliminated.

of the the variables at the stellar origin and surface is in agreement with equations (3.1) and (3.14) of §3.2. However, a comparison of this figure with figure 4.2 shows that, whilst the behaviour of the dimensionless variables in the *CoStar* models is broadly the same as that for the polytropic models presented previously, $A^\star$ shows considerably more structure in the former than in the latter.

This structure is particularly apparent at $r/R \sim 0.25$ for model 151, where the gradient in the mean molecular weight around the convective core leads to a characteristic trapezoidal spike in $A^\star$. This gradient also leads to the noticeable 'kink' in U for the same model, highlighting the caveat mentioned in §4.2.1 concerning representing the *CoStar* models with polytropes.

Whilst a quantitative investigation of the pulsation characteristics pertinent to the *CoStar* models is left to the following chapter, it is useful at this stage to examine the more qualitative aspects of the models through the use of propagation diagrams. These are essentially plots of the Lamb and

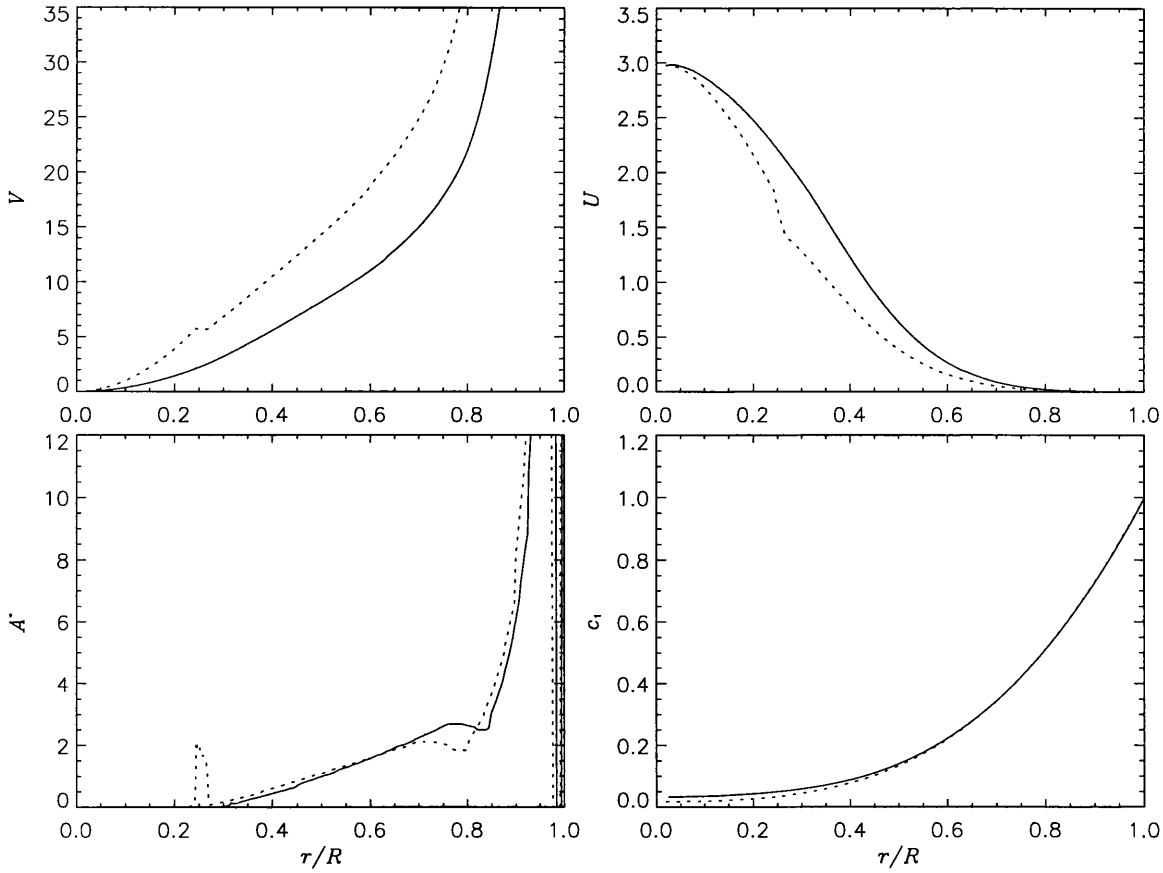

Figure 4.6: The dimensionless variables V, $A^\star$, c_1 and V as a function of r/R for *CoStar* models 6 (solid) and 151 (dotted).

Brunt-Väisälä frequencies as a function of radius; recalling from §2.5 that these frequencies represent the cutoffs for p- and g-mode pulsation respectively, propagation diagrams are useful tools for investigating the characteristics of a mode of given frequency throughout the star. Accordingly, figure 4.7 shows the propagation diagrams for the two *CoStar* models; since it is ω^2 which appears in the dimensionless pulsation equations, all frequencies have been plotted as their squares. The regions corresponding to p- and g-mode propagation have been hatched, whilst the evanescent zones have been left blank. A value of 2 was adopted for l in the evaluation of the Lamb frequency (equation (2.40)).

The propagation diagrams for the two models share the same broad characteristics; the Lamb frequency decreases monotonically with increasing radius due to the decrease in both the temperature and in $1/r^2$. The behaviour of the Brunt-Väisälä frequency is somewhat more complicated; recalling from equations (4.24) that

$$N^2 = \frac{g}{r} A^\star,$$

it can be seen that competition between $A^\star$ and the factor g/r, which generally increase and de-

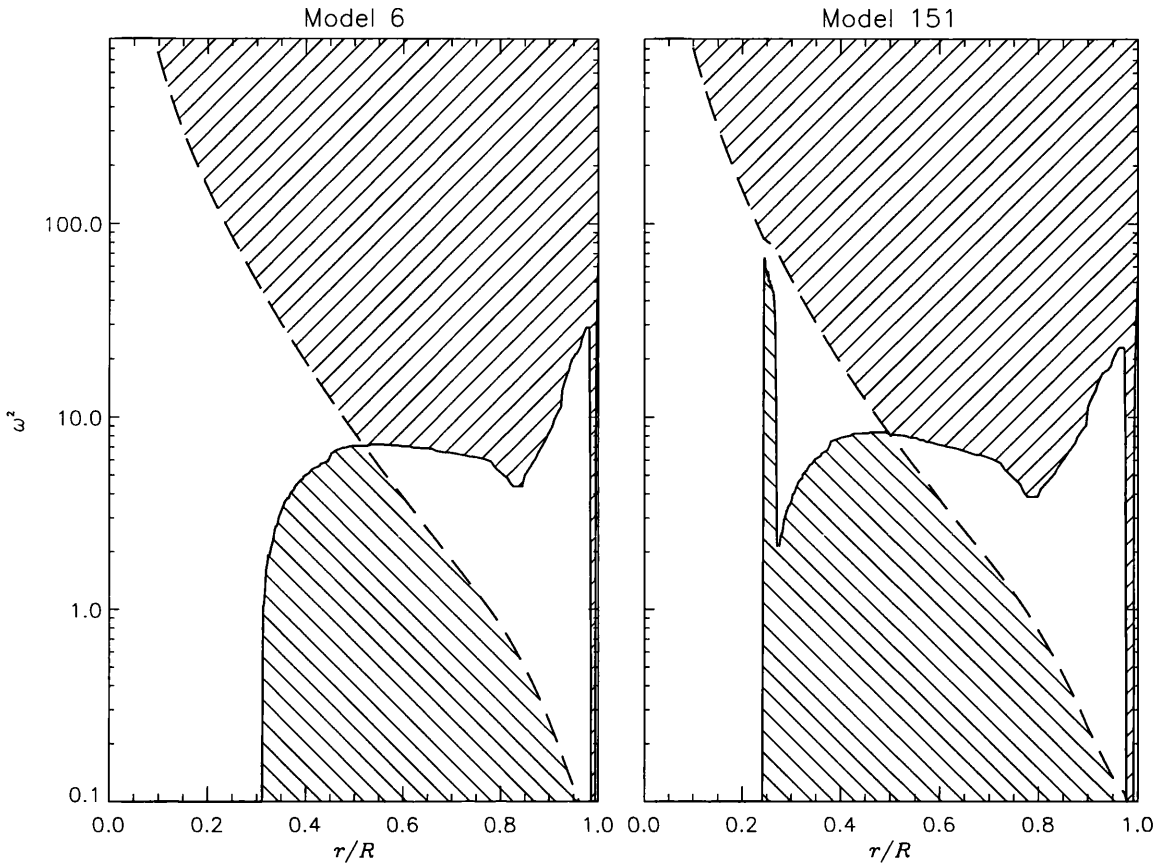

Figure 4.7: The $l = 2$ propagation diagrams for *CoStar* models 6 and 151. The squares of the Brunt-Väisälä (solid) and Lamb (dashed) frequencies, in units of GM/R^3, are plotted as functions of r/R; areas hatched (/) and (\) mark regions where p- and g-mode pulsation respectively can occur.

crease with increasing radius respectively, leads to the characteristic double inflection around $0.3 \lesssim r/R \lesssim 0.8$. Below $r \lesssim 0.3$, N^2 assumes negative values due to the presence of the core convection zone, and all normal wave propagation is suppressed (although convective modes may exist, as is demonstrated in §6.7.2). The thin sub-photospheric convection zone at $r \sim 0.95$ also leads to negative values of N^2; this zone occurs due to the presence of a helium ionization region.

Both diagrams show that the p- and g-mode propagation zones are, generally, well separated, with the former occurring at high frequencies ($\omega^2 \gtrsim 10$), and the latter at low ones ($\omega^2 \lesssim 10$). Furthermore, the p-zone is primarily confined to the stellar envelope, although it does extend into the core at high frequencies, whilst the g-zone typically starts at the core boundary (for the reasons mentioned above), and extends up to the outer envelope for the lower-frequency modes. The conspicuous trapezoidal spike in the Brunt-Väisälä frequency of model 151, due to the molecular-weight-gradient zone discussed previously, can lead to the existence of mixed-character modes which are propagative in both the outer envelope (p-mode) and just outside the core (g-mode).

Osaki (1975) has considered such core-envelope resonances extensively, although for the case of more evolved models with thicker molecular-weight-gradient zones. Kato (1966) suggested that if the temperature gradient in such zones is super-adiabatic (such that $\nabla > \nabla_{ad}$) but the molecular-weight gradient suppresses convection, any oscillation in these 'semi-convective' zones will grow with time (*i.e.*, the pulsation is unstable); this excitation mechanism is considered in greater detail in §5.5. In the case of the *CoStar* models, the molecular-weight-gradient-zone in model 151 is sub-adiabatic, and, accordingly, Kato's (1966) excitation mechanism is unlikely to be effective in this star. However, it should be noted that stellar rotation can lead to the existence of semi-convective zones which allow similar excitation mechanisms to operate; this possibility is discussed in greater detail in §6.7.2.

With the two *CoStar* models presented and discussed, it is now appropriate to investigate how they will actually respond when the equations of pulsation pertinent to them are solved. This is accomplished in the following chapter, which initially looks into techniques for solving the equations, and then applies these techniques to the models.

Chapter 5

Solving the Pulsation Equations

5.1 Introduction

The theories and results presented in the preceding chapters represent a complete description of linear, adiabatic non-radial pulsation, from the four differential equations and corresponding boundary conditions describing the behaviour of the pulsation, to the *CoStar* models which provide the 'input data' for pulsation studies. This chapter is concerned with the solution of the pulsation equations, to yield the eigenfrequencies and eigenfunctions which form the set of normal modes in which a star may pulsate.

Historically, two principal approaches have been used to solve the pulsation equations: a semi-analytical technique known as the asymptotic method (Tassoul 1980), and the direct or indirect numerical integration of the equations themselves. The former approach is generally applicable in cases where $\omega^2 \ll 1$ or $\omega^2 \gg 1$, and leads to simple, closed expressions for the pulsation eigenfrequencies. The latter, in contrast, is applicable to pulsation at any frequency, subject to numerical accuracy limitations, although correspondingly simple expressions for the eigenfrequencies do not exist.

The following two sections present these approaches, with an overview of the results of the former and the implementation issues of the latter, and a discussion and comparison of the particular advantages and limitations inherent in them. Subsequent sections apply the numerical approach to the *CoStar* models discussed in the preceding chapter, to probe manner in which these model stars will pulsate, and the chapter is concluded with a brief consideration of the driving mechanisms responsible for the excitation of pulsation. There do exist other techniques for solution of the pulsation equations, in particular variational approaches (Clement 1981; Clement 1984; Clement 1986; Clement 1989), which have proven useful, but the discussion herein is restricted to the two main approaches mentioned.

5.2 The Asymptotic Technique

5.2.1 Introduction

The asymptotic technique, extensively developed by Tassoul (1980), is a semi-analytical approach to solving the pulsation equations which is applicable in the limiting cases of $\omega^2 \ll 1$ and $\omega^2 \gg 1$. In these limits, the equations tend to systems of the Sturm-Liouville type (Arfken 1970), and may be solved using WKBJ methods (Coulson & Jeffrey 1977); after various transformations of the dependent variables, and under the Cowling approximation, solutions are constructed piecewise using Airy functions of the first and second kinds (Unno *et al.* 1989). These functions are fitted at transition points where, generally, the nature of the pulsation switches from propagative to evanescent, and *vice versa*.

Whilst the semi-analytical asymptotic expressions for the pulsation eigenfunctions are somewhat complicated, and will not be reproduced here, the corresponding expressions for the eigenfrequencies posses a surprising simplicity for both p- and g-modes. Since it is these eigenfrequencies which are directly observable through time-resolved spectroscopy or photometry, these expressions are presented and discussed in the following two subsections.

5.2.2 p-Mode Eigenfrequencies

Using the asymptotic technique, Tassoul (1980) demonstrated that the eigenfrequencies σ of p-modes with harmonic degree l may be written, for suitably small l, as

$$\sigma \int_0^R \frac{1}{c} dr = \left(2n + l + \eta_e + \frac{1}{2}\right) \frac{\pi}{2} + \frac{1}{\sigma} V_{io} + O\left(\frac{1}{\sigma^2}\right). \tag{5.1}$$

Here, V_{io} is some constant, and η_e is the effective polytropic index (§4.2) at the surface of the star. The radial order n is a positive integer which enumerates the number of nodes in ξ_r and p' in the radial direction. For simple stellar structures, n may be used to label different modes uniquely, in much the same way as l and m; however, there are some cases where this labelling is degenerate, and other schemes must be used (see §5.4.3). At suitably high frequencies, the above expression reduces to the first-order result

$$\sigma_{n,l} = \frac{(2n + l + \eta_e + 1/2)\,\pi/2}{\int_0^R c^{-1} dr}, \tag{5.2}$$

where the n and l subscripts on σ now indicate its functional dependence on these quantities. This expression has been derived under the assumption that the p-mode propagation zone extends from the stellar origin to the surface; an inspection of figure 4.7 shows that this assumption is valid only for high-frequency modes ($\omega^2 \gg 1$). The absence of the azimuthal order m from this equation highlights the fact that, for non-rotating stars, the pulsation frequencies are independent of m.

One important result implied by equation (5.2) is that, at high enough frequencies, the pulsation frequency spectrum of modes of the same l will show uniform spacing; that is,

$$\sigma_{n+1,l} - \sigma_{n,l} = \Delta\sigma_l, \tag{5.3}$$

where $\Delta\sigma_l$ is a constant independent of n. This result has been supported by observations of the five-minute oscillation periods in the sun (*e.g.*, Duvall *et al.* 1988), which show the distinct constant frequency spacing expected; a measurement of the magnitude of this spacing immediately gives information on the sound speed throughout the sun, through the integral appearing in equation (5.2). Observations of p-mode pulsation in other systems have shown similar results (*e.g.*, Edmonds *et al.* 1992); these observations are made possible by the fact that, although there is too little power in individual modes to render them detectable, modes associated with (n, l) and $(n + \alpha, l - 2\alpha)$, for integral α, share the same frequencies and will thus contribute together to give an observable period.

In addition to the information contained in the magnitude of the frequency spacings, measurements of the departures of observed frequencies from the behaviour dictated by equation (5.2) lead to more detailed information on the internal stellar structure (*e.g.*, Guenther 1994). Unfortunately, these techniques require data of both extremely high quality and coverage, and so are primarily of importance in the study of the sun and local stars, of which none are the early-type stars considered herein. Accordingly, the information content of p-mode frequency observations will not be considered any further, and the discussion moves on in the following subsection to the asymptotic treatment of g-modes.

5.2.3 g-Mode Eigenfrequencies

The application of the asymptotic technique to g-modes is somewhat more complicated than it is to p-modes; this is because of the non-monotonic behaviour of the Brunt-Väisälä frequency with respect to radius, mentioned in §4.3.4. For g-modes which are propagative from the origin out to a radius r_1, and evanescent from thence onwards, Tassoul (1980) derived the expression for the eigenfrequencies, in a first approximation, as

$$\sigma_{n,l} = \frac{\sqrt{l(l+1)}}{(2n + l - 1/2)\pi/2} \int_0^{r_1} \frac{|N|}{r} dr, \tag{5.4}$$

where, as before, n is the number of radial nodes in ξ_r and p'. In contrast, for g-modes which are evanescent out to a radius r_1, and propagative from thence onwards, the eigenfrequencies are given by

$$\sigma_{n,l} = \frac{\sqrt{l(l+1)}}{(2n + \eta_e)\pi/2} \int_{r_1}^{R} \frac{|N|}{r} dr, \tag{5.5}$$

Table 5.1: The basic parameters for pulsation modes in some early-type stars; the dimensionless frequencies ω_c have been calculated in the co-rotating frame of reference (see §6.1) using rotation-rate data when available, and estimated otherwise. References refer to the values for the observed period Π.

Star		$M/M_\odot$	$R/R_\odot$	Π (Hours)	ω_c^2	Reference
HD 36512	v Ori	20	7.2	12.3	0.85	Smith (1981)
HD 33328	λ Eri	10	6.0	17	2.1	Kambe *et al.* (1993)
HD 66811	ζ Pup	53	18	8.54	8.2	Reid & Howarth (1996)
HD 93521		19	8.1	2.91	7.1	Reid *et al.* (1997)
				1.77	8.5	
HD 149757	ζ Oph	16	7.5	3.339	2.6	Reid *et al.* (1993)
				2.435	6.4	
				1.859	2.8	
HD 217050	EW Lac	6.8	6.0	17.3	0.82	Stagg *et al.* (1988)
HD 218674	KY And	8.8	5.1	18.0	0.36	Stagg *et al.* (1988)

where, again, η_e is the effective polytropic index at the surface. Finally, for g-modes which are evanescent at the origin and at the surface, but which are propagative between two interior radii r_1 and r_2, the expression for the eigenfrequencies is

$$\sigma_{n,l} = \frac{\sqrt{l(l+1)}}{(2n+1)\pi/2} \int_{r_1}^{r_2} \frac{|N|}{r} dr. \tag{5.6}$$

For more complicated distributions of propagative and evanescent zones, such as ones incorporating the trapezoidal spike of *CoStar* model 151 (figure 4.7), the expressions for the eigenfrequencies become correspondingly more complex. The definite integral limits appearing in these three equations can be somewhat misleading; as Unno *et al.* (1989) point out, these limits formally depend on the frequencies themselves, and so must be treated with caution. Inspection of figure 4.7 shows that, for the *CoStar* models considered herein, low frequency g-modes will be propagative between the core boundary r_c and the stellar surface. Hence, the asymptotic expression for the frequencies of these modes will be, from equation (5.5),

$$\sigma_{n,l} = \frac{\sqrt{l(l+1)}}{(2n+\eta_e)\pi/2} \int_{r_c}^{R} \frac{|N|}{r} dr. \tag{5.7}$$

Whilst the compact semi-analytical forms of the p- and g-mode eigenfrequencies given by the asymptotic technique are very useful, this technique is not really applicable to the study of early-type stars. To appreciate this, table 5.1 summarizes some of the recent observations of pulsation in

early-type stars (for the 53 Per variable υ Ori and and five ζ Oph variables); the estimated mass and radius of the stars have been used to calculate the dimensionless frequency ω. All of the observed pulsations fall into the region $0.5 \lesssim \omega \lesssim 5$; this is obviously outside the remit of the asymptotic technique, which requires that $\omega^2 \ll 1$ or $\omega^2 \gg 1$. Accordingly, the asymptotic technique is not mentioned further in this chapter, although it is used again in §6.7 to gain qualitative insights into the effects of rotation on pulsation eigenfrequencies. The following section looks into alternative methods for solving the pulsation equations, more appropriate to the regions in frequency space described.

5.3 The Numerical Techniques

5.3.1 Introduction

The system of coupled, first-order ordinary differential equations which describe stellar pulsation (§2.6) form a two-point boundary value problem. In such problems, equations must be solved over some region subject to certain requirements at the boundary points, and, perhaps, at additional interior points. There exist two basic numerical techniques for obtaining solutions in such equation systems, those of *shooting* and *relaxation*.

These two methods are appropriate to both p- and g-modes with low radial order n, and have characteristics which complement one another; these characteristics are considered in the following two subsections, with particular emphasis on the relaxation technique, since it is that method which is used for actual numerical calculations in §5.4.

5.3.2 Shooting Techniques

Shooting techniques revolve around specifying the solution at one boundary in terms of one or more arbitrary parameters, subject to all of the boundary conditions applicable to that boundary. The full solution over the complete region are then developed via direct numerical integration of the differential equations. In general, this solution will not satisfy the other boundary condition; however, the discrepancy between the solution and the boundary condition is a function of the arbitrary parameters, and a complete solution, consistent with both boundary conditions, may be found via the application of a multi-dimensional root-finding algorithm to the discrepancy function (Press *et al.* 1992).

The advantages of shooting techniques are that, as the differential equations are directly integrated, the integration step-size can be controlled 'on the fly', and the accuracy of the solutions correspondingly monitored and controlled. For instance, if a region is reached where the solutions change rapidly with respect to integration variable, the step-size can be made smaller to ensure that

the solutions remain properly sampled. However, in the context of the forth-order pulsation equations, shooting has the drawback that the discrepancy function depends on three parameters, and it is thus cumbersome to find the roots; furthermore, shooting is, in general, numerically unstable for systems higher than second order.

Gautschy & Glatzel (1990*a*) have overcome these difficulties through the application of the Riccati method to the pulsation problem. In this method, the differential equations are transformed from a linear first-order boundary value problem to a numerically-stable, non-linear initial value problem. The initial value problem is then solved using a matrix shooting technique in which the pulsation frequency is the only arbitrary parameter; eigenfrequencies, and corresponding solutions to the pulsation equations, are found when one of the matrices, a function of the frequency, assumes a determinant of zero. This method works particularly well with highly non-adiabatic systems, which relaxation techniques have severe problems with, and has been applied with a considerable degree of success by the authors to a number of pulsation systems (*e.g.*, Gautschy & Glatzel 1990*b*; Gautschy & Glatzel 1991; Glatzel & Gautschy 1992).

For the purposes of this work, a full implementation of the Riccati shooting algorithm was considered too time-consuming and difficult, and, accordingly, the rest of this section concentrates on the relaxation technique which was used for actual numerical calculations.

5.3.3 Relaxation Techniques

Relaxation techniques revolve around the approximation that, to first order in Δx, the derivative of some function $y(x)$ may be written

$$\frac{dy}{dx} \approx \frac{y(x+\Delta x) - y(x-\Delta x)}{2\Delta x}. \tag{5.8}$$

By dividing the region of solution up into a finite grid mesh, and expressing all derivatives in this way, the two-point boundary value problem may be written in the form of a (high-dimensional) set of simultaneous algebraic equations for the dependent variables at each grid point. When written in matrix form, these equations may be solved using the standard method of Gaussian elimination (*e.g.*, Press *et al.* 1992).

For linear sets of equations, starting with arbitrary guesses for the dependent variables, this procedure gives the required solution in a single step. However, the pulsation equations are non-linear in the dimensionless frequency ω, and in such cases the relaxation procedure gives only a better approximation to the solution after a single step; accordingly, the solution is determined by starting with an initial guess and improving it iteratively, so that the result 'relaxes' to the true solution. For an initial guess suitably close to a solution, the iteration can be reasonably rapid (convergence to 1 part in 10^{-6} in ~ 6 steps), and relaxation techniques are generally quite robust; however, they are invariably accuracy-limited by the finite grid on which the equations are solved. The grid size is typically fixed over a sequence of iterations, and so accuracy cannot be maintained 'on the fly' as

it can for shooting techniques; however, this problem can be circumvented by choosing a suitably large grid size at the start of the relaxation. There do exist formulations of relaxation techniques which include adaptable grid meshes implicitly in the algorithm (*e.g.*, Press *et al.* 1992); however, such cases are not considered herein.

Henyey *et al.* (1964) presented an implementation, hereafter the Henyey method, of the relaxation technique, which has been used extensively in the calculation of stellar models (*e.g.*, Kippenhahn & Weigert 1990), and can also be used for solution of pulsation equations. Unno *et al.* (1989) give a very general and clear description of this implementation, in which a set of I first-order differential equations and K eigenvalues is solved on a grid of N points subject to $L = I + K$ boundary conditions, of which L_I are applied at the innermost grid point and the remaining $L - L_I$ at the outermost grid point.

Unno *et al.*'s (1989) description was used to write a completely general implementation of the Henyey method as a monolithic FORTRAN subroutine. This subroutine, hereafter HENITER, is called with arrays specifying the values of the differential equations, the boundary conditions, and the current trial solutions to the equations; it iterates the solutions once using the Henyey method, and returns their updated values. In the case of solution of the four pulsation equations, HENITER is called with the dimensions $I = 4$, $K = 1$ (for the single eigenvalue), $L = 5$ for the five boundary conditions including the normalization condition of §3.3, and $L - L_I = 3$ so that this normalization is specified at the outer boundary. The components of the HENITER calling arrays are documented in Appendix E; the values given are appropriate for solution with the Z-boundary outer boundary condition (§3.2). In cases where more physically realistic outer boundaries were required (see §5.6), these values were suitably modified.

One of the drawbacks of the Henyey method is that, for convergence to a particular solution out of all of the possible solutions to the pulsation equations, the initial guess must be suitably close to the desired solution. The task of choosing suitable initial guesses falls to the driving program in which the HENITER subroutine is embedded; this driving program is discussed in the following section, which also presents the results from solution of the pulsation equations for the two *CoStar* models.

5.4 The *CoStar* Pulsation Solutions

5.4.1 Introduction

As was indicated in the preceding section, the desired convergence of the Henyey method is strongly dependent on how close the initial trial solution is to the required solution. For each value of l, there exist an infinite number of different possible solutions to the pulsation equations, each with a different eigenvalue ω^2. To find all of the solutions in a given region of eigenvalue-space requires some method of finding approximately where each eigenvalue is, and then constructing

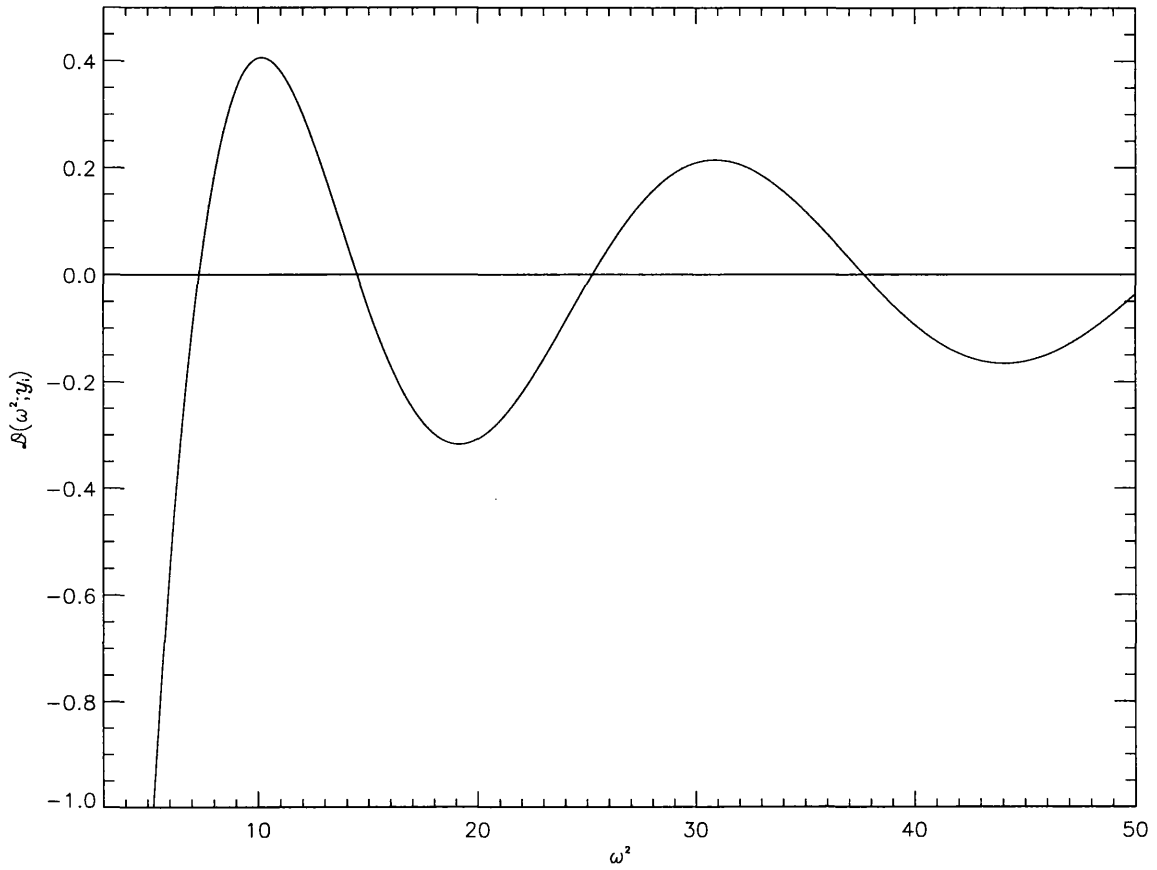

Figure 5.1: Castor's (1971) discriminant $\mathcal{D}(\omega^2; y_i)$, plotted as a function of ω^2 for *CoStar* model 6; l was taken to equal 2. The roots of this discriminant correspond to eigenvalues of the pulsation equations.

good trial solutions based on this eigenvalue, which may then be used to initiate a relaxation iteration.

Castor (1971) has presented such a method, albeit for the case of radial pulsation, which was used successfully by Osaki & Hansen (1973) for the corresponding non-radial problem. If one of the boundary conditions other than the normalization condition is neglected, then the pulsation equations can be solved with an arbitrary value of ω^2. No iteration is required in this case, since the system of equations is linear in the dependent variables, and can therefore be solved in a single HENITER step from a completely arbitrary trial solution. For arbitrary ω^2, the resulting solution will not, in general, satisfy the excluded boundary condition; however, the numerical value of this boundary condition may serve as a discriminant for the eigenvalues of the original system. This discriminant may be chosen so that it is zero if and only if ω^2 is one of the eigenvalues (Unno *et al.* 1989), and, accordingly, searching for initial trial values of the eigenvalues and eigenfunctions is reduced to a one-dimensional root-finding problem in ω^2-space.

The discriminant used herein is the same as that of Osaki & Hansen (1973), and comes from excluding the outer potential boundary condition (equation (3.18)); it is given by

$$\mathcal{D}(\omega^2; y_i) = (l+1)y_3 + y_4, \tag{5.9}$$

where the dependent variables y_i are evaluated at the outer boundary. Figure 5.1 illustrates this discriminant as a function of ω^2 for *CoStar* model 6, calculated with $l = 2$. The roots are well separated, with the left-most one corresponding to a fundamental ($n = 0$) pulsation mode, and the subsequent ones to $n = 1, 2, 3$ p-modes; accordingly, it would appear that the root-finding problem mentioned previously is quite trivial to implement, and that solution of the pulsation equations can be easily automated.

Unfortunately, this turns out not to be the case. For p-modes with large values of l and n, and for almost all g-modes, the discriminant $\mathcal{D}(\omega^2; y_i)$ assumes a highly pathological form. Figure 5.2 illustrates this point, plotting the same discriminant as figure 5.1, but over a range of ω^2-values corresponding to g-modes. It appears that almost every root of the discriminant has a singularity very close to it, such that the discriminant changes sign across the singularity. These singularities arise when y_1 accidentally takes a value of zero at the outer boundary; the application of the normalization condition ($y_1 = 1$) at this boundary then causes all other dependent variables to diverge to infinity. Whilst Unno *et al.* (1989) suggested that the singularities can be suppressed by dividing the above discriminant by the value of y_1 at the inner boundary, it was found that such a procedure did not appear to work.

The singularities bode ill for any root-finding algorithm, since such algorithms usually require that a root is bracketed before solution can commence. These brackets are set up on the criterion that the discriminant changes sign over the bracket interval; clearly, if the proximity of a singularity to a root is smaller than the bracket interval, the root will be completely overlooked by any automated algorithm. To overcome this problem, the bracketing intervals must be chosen to be smaller than the singularity/root separations; however, there is no *a priori* way of predicting these separations, and, furthermore, they are typically so small that an enormous amount of computer time is required to ensure that all roots are bracketed. Thus, whilst Castor's (1971) method works in theory, its implementation in a relatively automated computer program is not realistically possible.

Accordingly, an alternative method of finding good trial solutions for use by HENITER was developed. This method revolves around the fact that l need not be integral for solution of the radial parts of the full three-dimensional pulsation equations (equations (2.48)–(2.51)). The restriction on l actually arises from solution of the angular parts of the pulsation equations (see §2.4); therefore, whilst *physically realistic* solutions do require integral l, this restriction may temporarily be relaxed for the purposes of solving the radial equations.

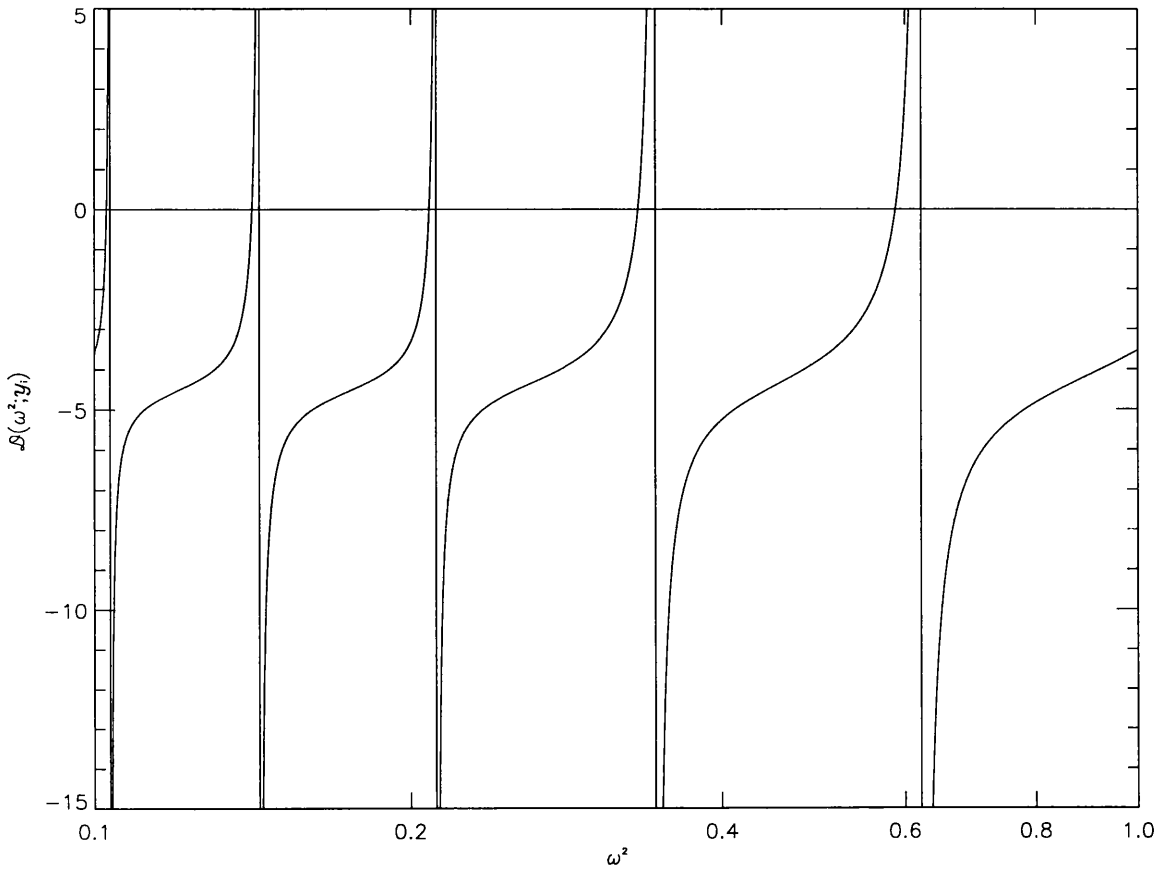

Figure 5.2: As for figure 5.1, except that the discriminant $\mathcal{D}(\omega^2; y_i)$ has been plotted over a frequency range corresponding to g-mode pulsation. The diagram shows that that roots of the discriminant (a rather pathological function) can occur quite close to singular points.

The relevance of this point is that solutions of the pulsation equations may be considered to be continuous functions of l; sets of solutions with $l = l'$ and $l = l' + \Delta l$ will approach one another as Δl is taken to zero, in both eigenvalues ω^2 and eigenfunctions y_i. Consequentially, for suitably small Δl, the sets of solutions at $l = l'$ can serve as initial guesses for use by HENITER to solve the pulsation equations at $l = l' + \Delta l$. A set of solutions at some starting value $l = l_s$ may be 'evolved' into all the corresponding sets of solutions at $l > l_s$ by repeatedly incrementing l by Δl and then solving the pulsation equations using the previous solutions as initial guesses.

This procedure was implemented in a computer program, hereinafter EVOLVE, which evolves a user-supplied set of eigenvalues from the starting point l_s to higher l, using a user-definable step-size Δl. Once all solutions up to a maximum value of l have been found, those with integral l are written out, since it is these which are of physical significance for the reasons mentioned. EVOLVE is very robust, in that it always converges to a valid solution close to that at the previous value of l; however, in cases when two solutions have eigenvalues and eigenfunctions which are very similar,

it may 'jump' from one solution to the other as l is stepped. This problem may be overcome by decreasing the step-size Δl.

The initial set of eigenvalues which are supplied to EVOLVE for development in l are best found using graphical implementations of Castor's (1971) method. Such implementations do not require the high resolution in ω^2 of corresponding computer implementations, since the human eye can usually pick out roots of the discriminant $\mathcal{D}(\omega^2; y_i)$ with sufficient accuracy from low-resolution plots. The following sections present the results from the application of EVOLVE to the *CoStar* models, with the initial set of eigenvalues found in this manner.

5.4.2 The *CoStar* Eigenfrequencies

Initial sets of eigenvalues where obtained at $l_s = 2$ for both of the *CoStar* models, consisting of the fundamental mode, and the first 20 p- and g-modes lying in frequency above and below the fundamental mode respectively. The fundamental, or f-mode, solution is the one which has no nodes in y_1; it essentially divides frequency space into the p- and g-mode regions respectively (although in complicated models this may not be the case). These initial sets of eigenvalues were then developed up to $l = 25$ using EVOLVE, with a step size Δl of 0.1 for the f- and p-modes, and 0.02 for the g-modes; the smaller step-size of the g-modes was chosen to ensure that the solution jumping discussed in the preceding section did not occur. The starting point l_s was set at 2 rather than 1 for the reason that the $l = 1$ f-mode has zero frequency and corresponds to an arbitrary displacement of the whole star (Unno *et al.* 1989). The grid-size N was taken to be 1000 throughout, a number large enough to ensure that all solutions were sampled properly, and that the numerical inaccuracy introduced by the finite differencing of the Henyey method was small. Since the *CoStar* models were specified over typically 300 non-uniform grid points, a cubic spline interpolation (Press *et al.* 1992) was used to increase the model resolution to 1000.

Figures 5.3 and 5.4 display the resulting eigenvalues ω^2, and their equivalent periods Π, as functions of l over the calculation range, for models 6 and 151 respectively. Although only integral values of l correspond to physically realistic solutions, l is plotted as a continuous function to allow the following of a given solution. These figures are broadly equivalent to the diagnostic diagram (figure 2.2) discussed is §2.5, due to the dependence of the horizontal wavenumber k_h on $\sqrt{l(l+1)} \approx l$. In the case of model 6, the p- and g-mode solutions are well separated, with the former increasing monotonically with l, and the latter asymptoting to some global average of the Brunt-Väisälä frequency. This relatively simple behaviour is typical of ZAMS models, or, indeed, any 'simple' stellar model such as a polytrope.

In contrast, model 151 shows somewhat more complex behavior; the eigenvalue curves for the p- and g-mode solutions are not well separated, and some of the low-order curves for the two mode types appear to intersect. Such an apparent intersection occurs between the fundamental mode and

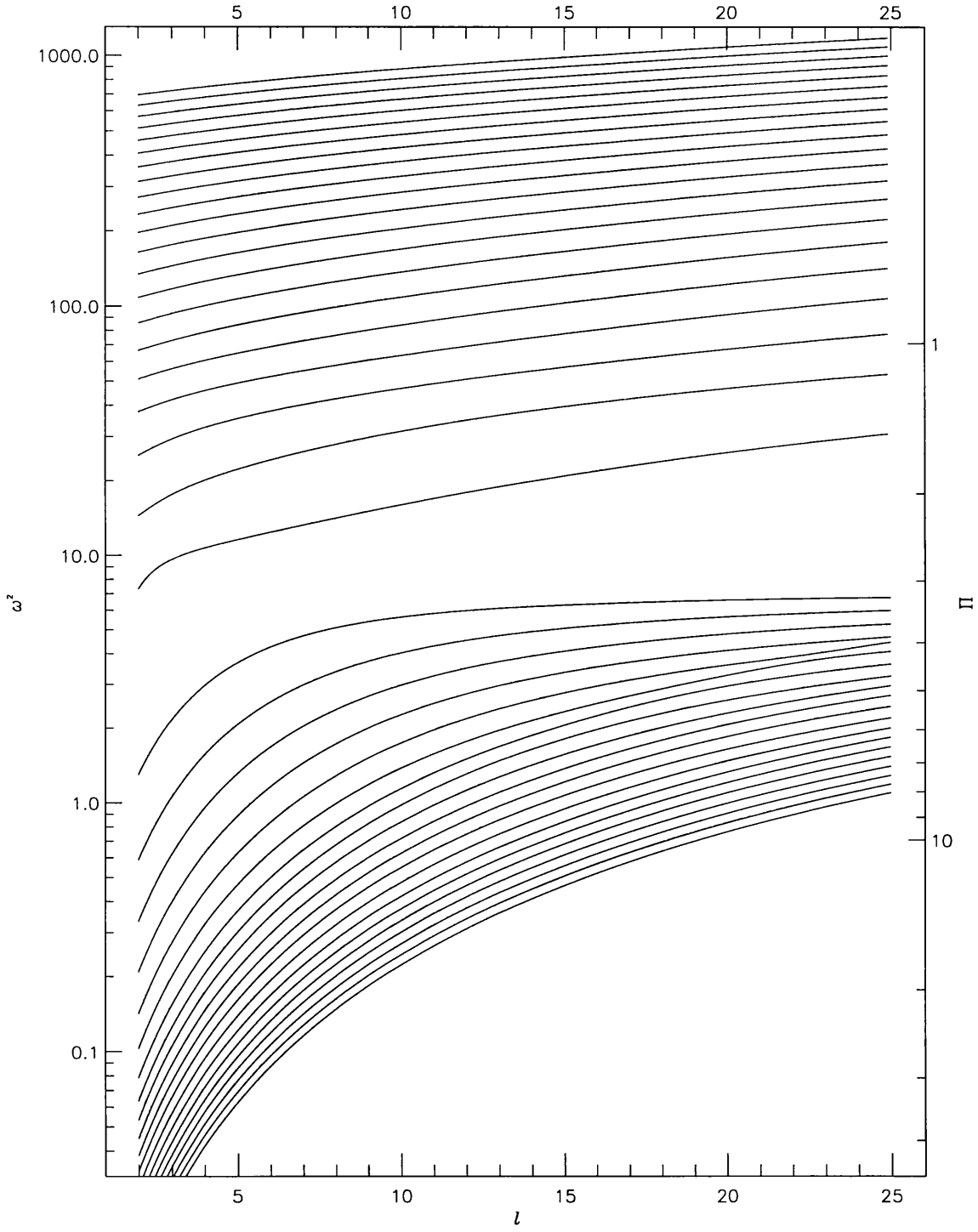

Figure 5.3: The pulsation eigenvalues ω^2 and periods Π (in hours) as a function of l for *CoStar* model 6. Each curve corresponds to the continuous evolution of a solution with respect to l; physically realistic solutions correspond to integral values of l.

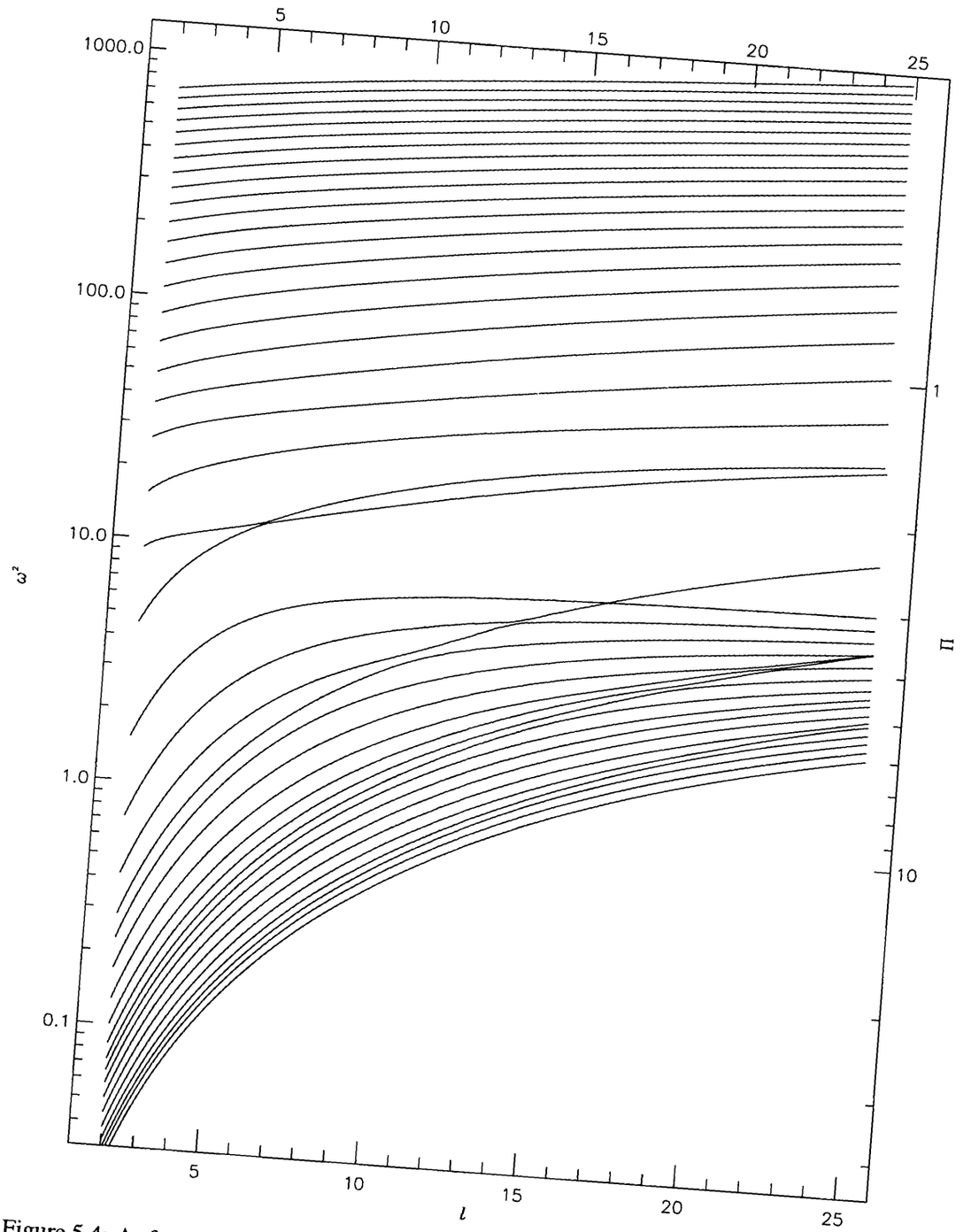

Figure 5.4: As for figure 5.3, except the solutions are plotted for *CoStar* model 151. Note the avoided crossings between solution curves at, for instance, $l \approx 6$.

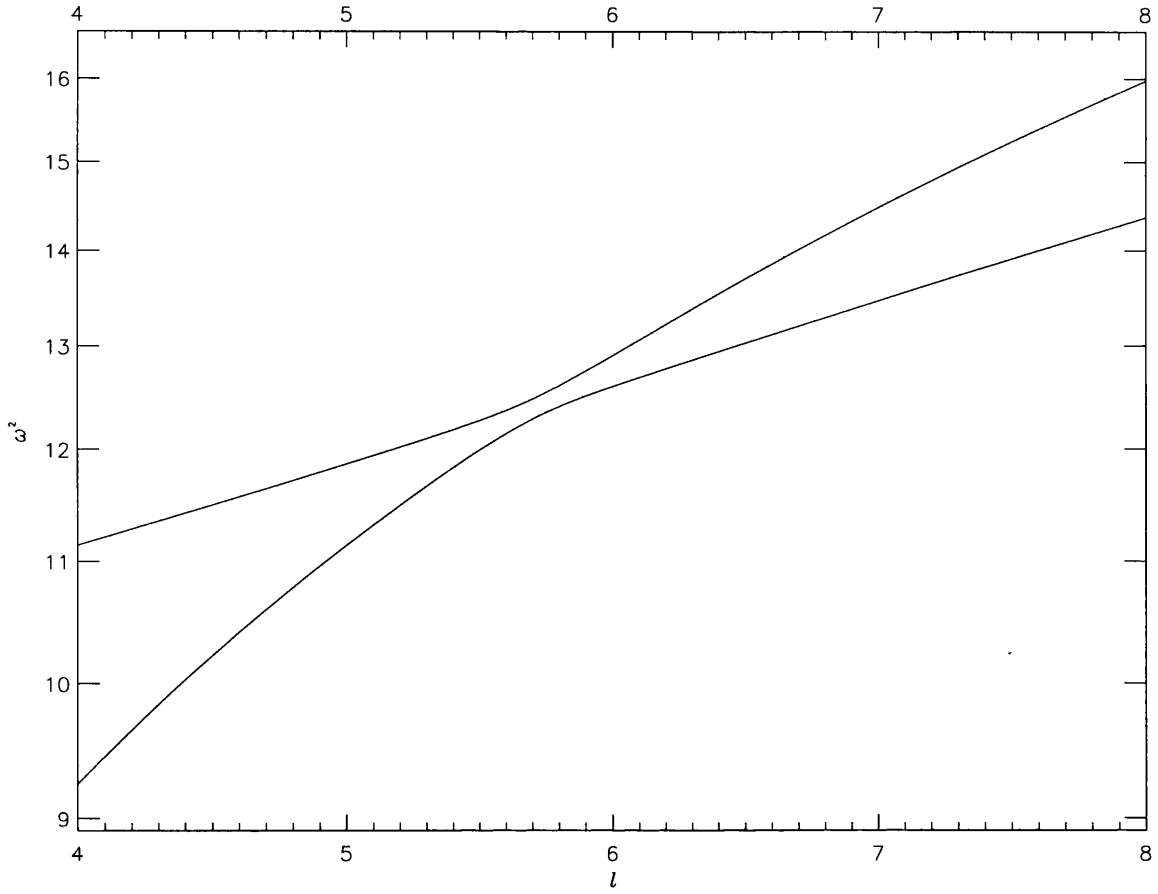

Figure 5.5: An avoided crossing between the f- and $n = 1$ g-modes of *CoStar* model 151 (taken from figure 5.4); the characteristics of the modes are exchanged over the crossing.

the $n = 1$ g-mode at $l \approx 6$; figure 5.5 illustrates the appropriate region of figure 5.4 in greater detail, and shows that the two curves do not actually intersect, but rather exhibit an 'avoided crossing', as do the solutions at all other apparent intersections. Aizenman *et al.* (1977) first introduced the concept of such avoided crossings in the context of stellar pulsation; they demonstrated that they arise from an eigenfrequency degeneracy between pulsation in two different regions of the star. The resulting resonant coupling between the two modes lifts the degeneracy to a degree inversely proportional to the strength of the coupling; weaker couplings corresponding to closer avoided crossings. Aizenman *et al.* (1977) also demonstrated that, over an avoided crossing, the characteristics of the two modes are exchanged, so that, in effect, the modes do cross one another even though there is no intersection.

In the case of the avoided crossings observed in model 151, the resonant coupling occurs between the envelope-confined f-mode and a g-mode trapped in the molecular-weight-gradient zone around the convective core (see §4.3.4). To demonstrate this, and discuss avoided crossings in more detail, the properties of the eigenfunctions of these modes must be investigated, as must the topic of modal classification; this is undertaken in the following section.

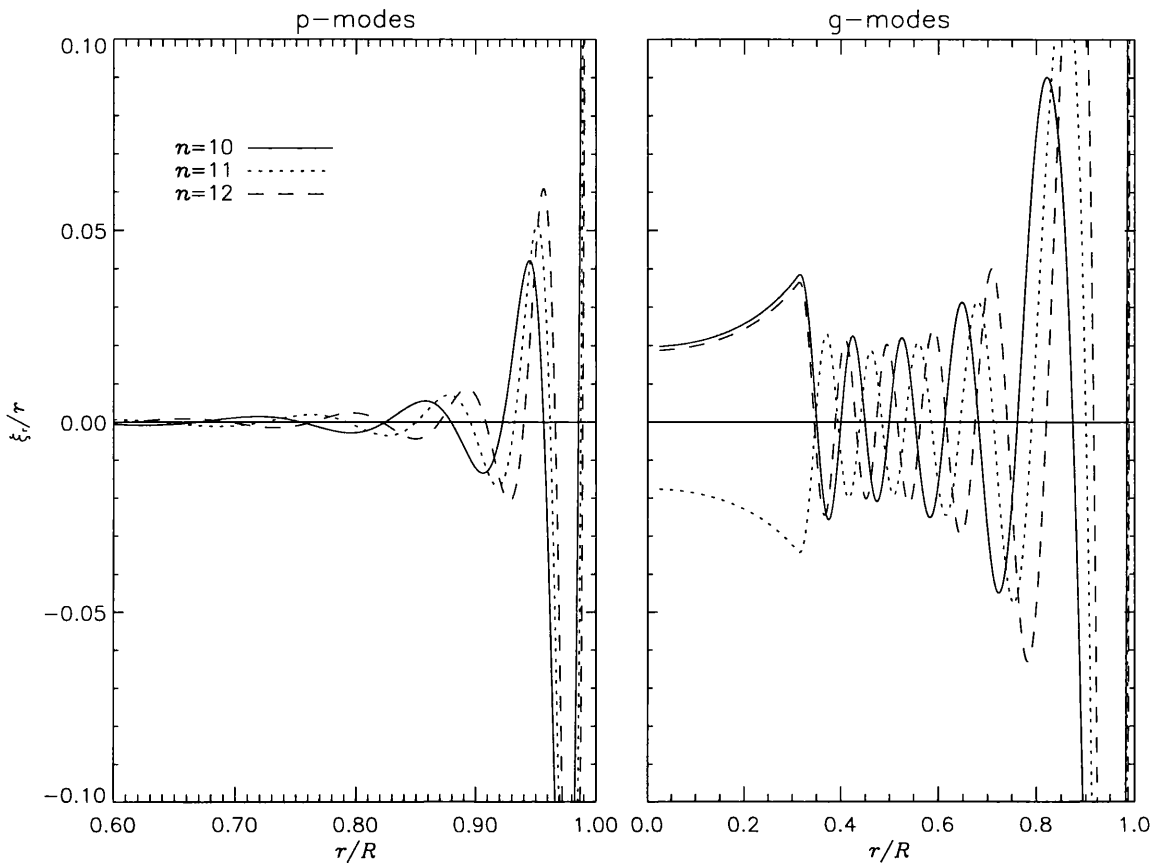

Figure 5.6: Radial eigenfunctions ξ_r/r plotted as a function of r/R for the $n = 10, 11, 12$ p- and g-modes of *CoStar* model 6. The ordinate range for the p-mode panel has been confined to the envelope, since the amplitude of these modes is small in the core.

5.4.3 The *CoStar* Eigenfunctions

Whilst the eigenfrequency of a given pulsation mode contains some information about the characteristics of that mode, it is the corresponding eigenfunction which holds the majority of this information; therefore, it is important to examine these eigenfunctions in greater detail. For each of the integral-l eigenfrequencies found in the preceding section, the corresponding eigenfunction was calculated; figure 5.6 illustrates a small subset of these eigenfunctions for *CoStar* model 6. The p-modes shown are propagative in the outer envelope, since they show an oscillatory character there, whilst the g-mode propagation is found deeper within the star, allowing the classification into p- and g-modes to be accomplished. However, this classification scheme is somewhat qualitative and arbitrary; a more quantitative scheme must be introduced to allow a mode to be uniquely classified.

Such a scheme has already been presented by Osaki (1975), who introduced the use of phase diagrams for the analysis of modal characteristics. In a phase diagram, the radial and horizontal displacements, ξ_r and ξ_h respectively, are plotted against one another in a progression from the core to the surface; Osaki (1975) demonstrated that the curve traced in such phase diagrams moves

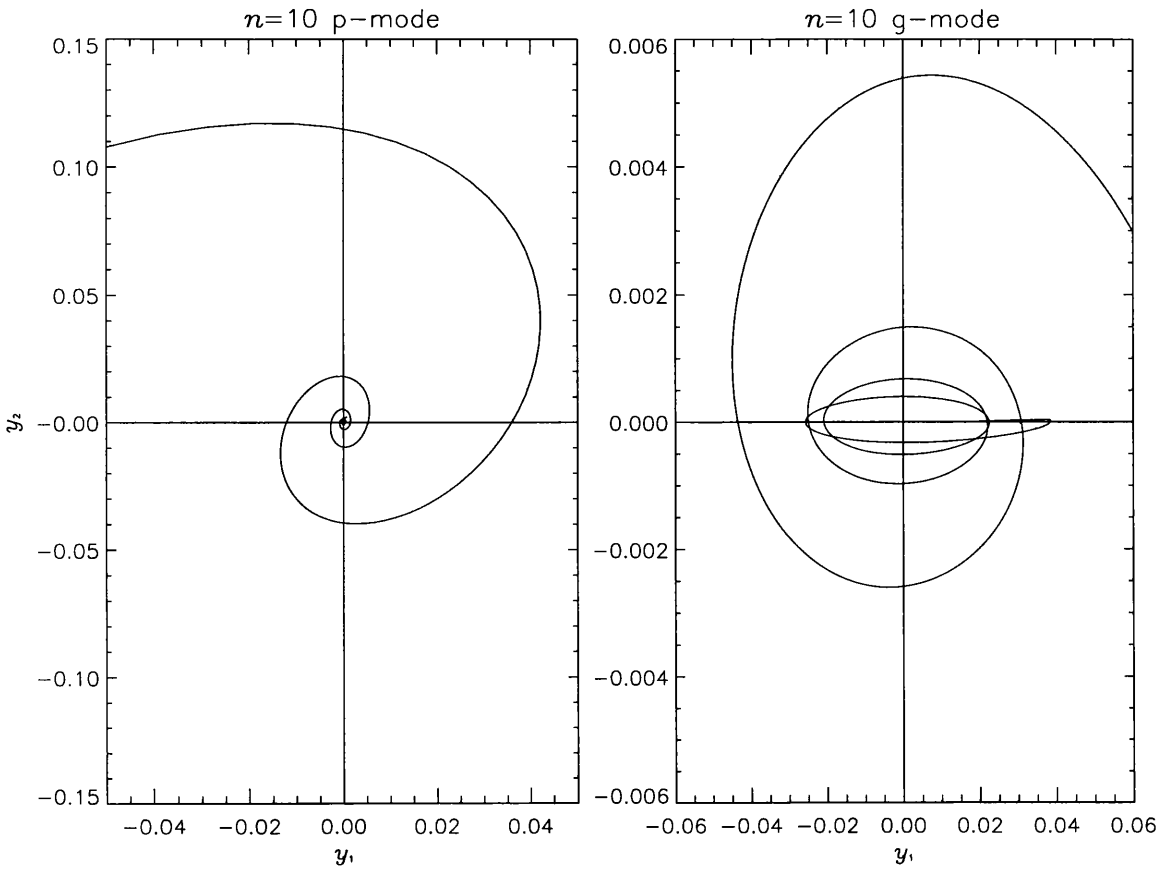

Figure 5.7: Phase diagrams for the $n = 10$ p- and g-modes of *CoStar* model 6. In each case, only the central regions of the phase diagrams are displayed.

clockwise in g-mode propagation zones, anticlockwise in p-mode propagation zones, and along hyperbolic trajectories in evanescent zones. By considering the curve trajectory at nodes of the radial displacement ($\xi_r = 0$), the number of p-mode and g-mode nodes, n_p and n_g respectively, may be counted. Whilst the total number of nodes $n \equiv n_p + n_g$ may not be a unique label for pulsation modes, since there may exist solutions with the same values of n but different eigenfrequencies, Osaki (1975) suggested that the quantity $\bar{n} \equiv n_p - n_g$ is monotonic with increasing eigenfrequency, and may be used as a unique mode label.

Based on this procedure, phase diagrams were constructed for all of the *CoStar* eigenfunctions, and then used to evaluate n_p, n_g and $\bar{n}$. Figure 5.7 illustrates the phase diagrams of the $n = 10$ eigenfunctions plotted in figure 5.6; in both cases, the central regions of the phase diagram have been shown, and the trajectories spiral outwards from core to surface. The classification of these two modes as $\bar{n} = 10$ and $\bar{n} = -10$ for the left- and right-hand panels respectively is quite straightforward, since the trajectories consistently move anticlockwise and clockwise respectively. Note that, in these phase diagrams, it is y_1 and y_2 which are plotted rather than ξ_r and ξ_h; however, since $y_1 \equiv \xi_r/r$ and $y_2 \equiv \xi_h/(c_1\omega^2 r)$, the nature of the phase diagrams will not be altered by this substi-

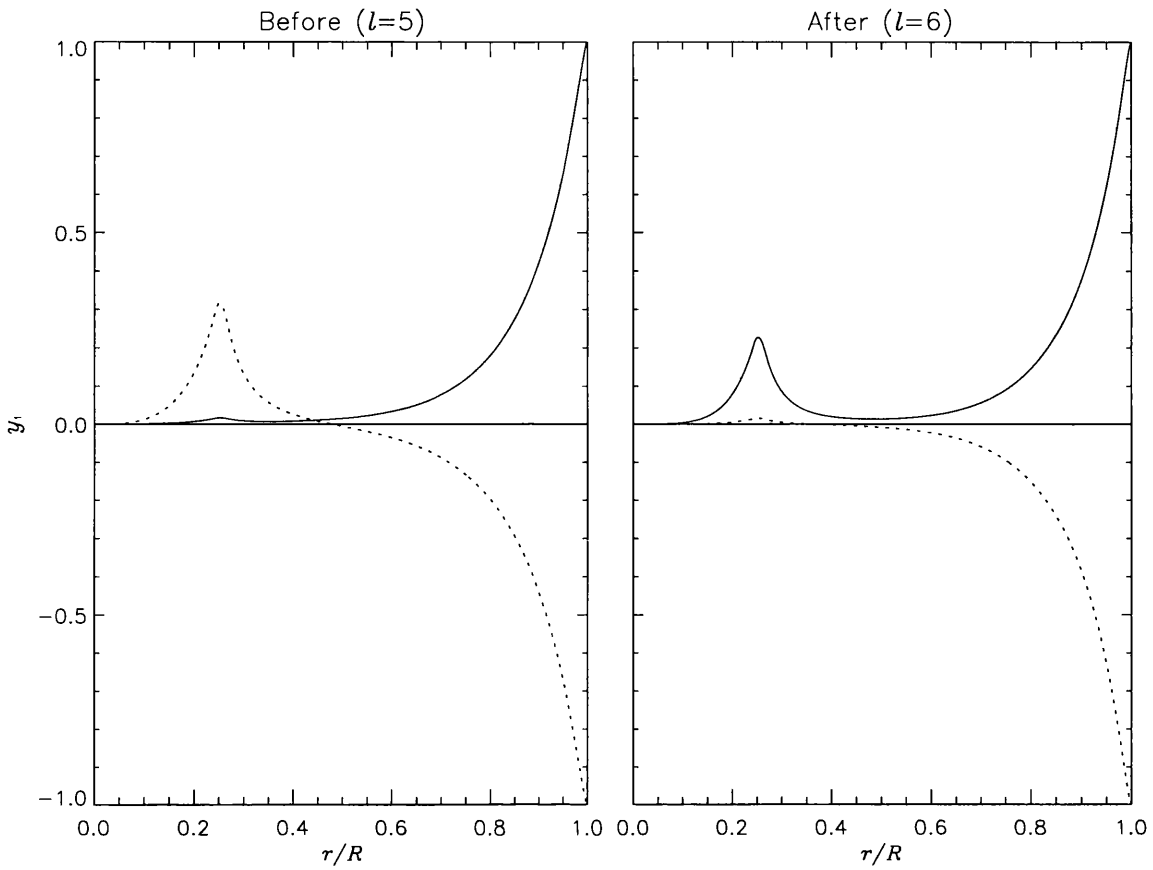

Figure 5.8: The eigenfunctions y_1 of the f-mode (solid) and $n = 1$ g-mode (dotted), plotted before (l=5) and after (l=6) the avoided crossing shown in figure 5.5; the outer normalization of $y_1 = -1$ has been used to calculate the g-mode solution. Note the exchange of modal characteristics over the crossing.

tution. For all of the modes, it was found that $\bar{n}$ served as a unique label of the eigenfrequency for a given l, supporting the findings of Osaki (1975).

To investigate the cause of the avoided crossings discussed in the previous section, it is useful to look at the eigenfunctions of the modes involved in the interaction. Again considering the avoided crossing illustrated in figure 5.5, figure 5.8 plots the eigenfunctions y_1 of the two modes involved, both before the crossing at $l = 5$, and after the crossing at $l = 6$. The g-mode has been calculated with the outer normalization $y_1 = -1$, as opposed to the usual $y_1 = 1$, to aid the readability of the figure.

Before the crossing, the g-mode (dotted) shows appreciable amplitude in both the envelope, and in a region associated with the molecular-weight-gradient zone around the core (see figure 4.7), whilst the f-mode (solid) is confined mainly to the outer envelope. After the crossing, these properties are exchanged, with the f-mode now having a significant amplitude in the molecular-weight-gradient zone (although the f-mode remains node-less and the g-mode still retains a single node).

Thus, over the avoided crossing, the properties of the two modes are exchanged, in this case because of a resonant coupling between the outer envelope and the molecular-weight-gradient zone. This highlights the fact that, whilst $\bar{n}$ is useful for uniquely labelling modes, it does not always provide a good indicator of the nature of a mode; in this case, the $\bar{n} = -1$ mode at $l \gtrsim 6$ behaves more like an f-mode than a g-mode, and, correspondingly, the $\bar{n} = 0$ mode behaves more like a g-mode than an f-mode. Shibahashi & Osaki (1976) have already discussed this problem, and present a supplementary scheme which classifies modes based more on their propagative character.

5.5 Quasi-adiabatic Stability Analysis

Whilst the entire spectrum of pulsation modes for a given stellar model is of interest from a theoretical standpoint, it is the globally unstable subset of these modes which is of import to the observer. Such unstable modes will have an amplitude which grows with time, and will thus be the ones which contribute to pulsation-originated stellar variability. Although the adiabatic analyses undertaken herein generally preclude an investigation of the stability of pulsation modes, since they neglect transfers between different forms of energy, it is possible in some cases to perform stability calculations using results from the adiabatic theory.

Osaki & Hansen (1973) presented such calculations, known as quasi-adiabatic stability analyses, which use only adiabatic eigenfrequencies and eigenfunctions to investigate the stability of pulsation modes. The analysis involves the calculation of the so-called work integral W, defined by

$$W = \oint \frac{dE_W}{dt} dt, \tag{5.10}$$

which measures the total change over one cycle of the pulsation energy,

$$E_W = \frac{\sigma^2}{2} \int_0^M |\boldsymbol{\xi}|^2 dM_r. \tag{5.11}$$

The work integral is related to the exponential growth rate $\tau_{\rm grow}$ of the pulsation by

$$\tau_{\rm grow} = \frac{W}{4E_W}, \tag{5.12}$$

so that modes with positive W are unstable, and grow in amplitude with time. Osaki & Hansen (1973) give the expression for the work integral as

$$W = W_1 + W_2 + W_3, \tag{5.13}$$

where

$$W_1 = \int_0^R \left(\frac{\delta T}{T}\right) \delta\epsilon 4\pi r^2 \rho dr, \tag{5.14}$$

$$W_2 = \int_0^R \left(\frac{\delta T}{T}\right) l(l+1) L_r \left(\frac{T'}{T}\right) \left(\frac{d\ln r}{d\ln T}\right) \frac{dr}{r} \tag{5.15}$$

and

$$W_3 = \int_0^R \left(\frac{\delta T}{T}\right)\left[\frac{dL_r}{dr}\frac{l(l+1)}{c_1\omega^2}y_2 - \frac{d(\delta L_r)}{dr}\right]dr. \tag{5.16}$$

The quantity W_1 represents the contribution to the work integral from thermonuclear energy sources and sinks, and is responsible for excitation due to the ϵ-mechanism, whilst W_2 and W_3 represent contributions from heat transfers in horizontal and radial directions respectively. Within the quasi-adiabatic stability analysis, all of the variables in these expressions are evaluated using the results from adiabatic calculations; in particular, the temperature perturbation is given from equation (3.44) by

$$\frac{\delta T}{T} = \nabla_{\rm ad} V(y_2 - y_1 - y_3), \tag{5.17}$$

and the perturbation to the nuclear energy generation rate will be given by

$$\frac{\delta \epsilon}{\epsilon} = (\epsilon_T + \nabla_{\rm ad}\epsilon_p)\left(\frac{\delta T}{T}\right), \tag{5.18}$$

where ϵ_T and ϵ_p were introduced in table 4.4. The luminosity perturbation δL_r is best evaluated using the form given by Osaki (1976),

$$\frac{\delta L_r}{L_r} = 4y_1 + \left(4 - \kappa_T - \nabla_{\rm ad}\kappa_p\right)\frac{\delta T}{T} + \frac{\nabla_{\rm ad} - \nabla}{\nabla}\frac{l(l+1)}{c_1\omega^2}y_2 - \frac{1}{\nabla_{\rm ad}}\left(1 + \frac{1}{V}\frac{d\ln\nabla_{\rm ad}}{d\ln r}\right)\frac{\delta T}{T} + \frac{\nabla_{\rm ad}}{\nabla}\left[(U - c_1\omega^2 - 4)y_1 + y_4\right], \tag{5.19}$$

where, again, κ_T and κ_p were introduced in tables 4.3 and 4.4. This expression is used to avoid the introduction of artifacts in δL_r caused by the differencing of two large but similar terms (Osaki 1976); it is only applicable to adiabatic pulsation, and thus is restricted to the quasi-adiabatic analysis. The second and third terms in this expression represent contributions to the work integral from the so-called κ- and δ-mechanisms respectively. The former of these generally operates in regions where

$$\frac{d}{dr}(\kappa_T + \nabla_{\rm ad}\kappa_p) > 0, \tag{5.20}$$

and can work effectively in exciting both p- and g-modes (although not f-modes due to their solenoidal nature); it is thought to be the excitation mechanism responsible for pulsation in both δ Cephei and β Cephei stars, and arises from the 'damming-up' of radiation by stellar material as the opacity rises with temperature. The δ-mechanism, on the other hand, only works for g-modes in regions which are dynamically stable, but have a super-adiabatic temperature gradient such that

$$\nabla - \nabla_{\rm ad} > 0. \tag{5.21}$$

The δ-mechanism was first considered by Cowling (1957), who examined oscillations in a stratified, super-adiabatic medium rendered dynamically stable by an external magnetic field; it was

demonstrated that radiative transfer between adjacent oscillating fluid parcels would lead to the effective excitation of pulsation. This variant of the δ-mechanism is generally unlikely to be relevant in early-type stars, due to the lack of globally-ordered magnetic fields (Barker 1986). However, Kato (1966) has considered super-adiabatic regions with a molecular-weight gradient ∇_μ satisfying

$$\delta\nabla_{\rm ad} + \nabla_\mu > \delta\nabla > \delta\nabla_{\rm ad}, \tag{5.22}$$

where δ was introduced in table 4.3. Such regions are obviously super-adiabatic, but will have $N^2 > 0$ from equation (4.28), and thus be dynamically stable. They generally occur in the semi-convective zones surrounding the cores of massive, evolved stars; Kato (1966) demonstrated that they will lead to the excitation of pulsation in a manner completely equivalent to Cowling's (1957) original formulation of the δ-mechanism. Whilst Kato's (1966) treatment of this δ-mechanism variant was strictly local, Shibahashi & Osaki (1976) have shown that it will operate on a global scale for massive stars, albeit not very effectively. With regards to the *CoStar* models, it was shown in §4.3.4 that model 151 has a mean molecular weight gradient around the core; however, the temperature gradient in this zone is sub-adiabatic, and so Kato's (1966) mechanism will not lead to excitation there.

It is important to note that the above expressions for the work integral neglect any perturbations to the convective flux; however, these perturbations are closely linked with pulsation-convection coupling theories (*e.g.*, Gabriel *et al.* 1975), which are generally too complicated to consider herein. In any case, the confinement of convection to the core in the *CoStar* models (where all pulsation is evanescent) should mean that the omission of the convective flux perturbation will not introduce any serious errors in the calculation of W.

Accordingly, expressions (5.14)–(5.16) were used to calculate the work integral for all pulsation modes found in the preceding sections. In cases where derivatives of certain functions were unavailable, numerical derivatives had to be resorted to; whilst these introduced a certain amount of numerical noise into the integrand, this noise was generally smoothed out in the resulting integration. The evaluation of the integral was terminated in the outer envelope at a point where ω_t, the transition frequency introduced in §3.6, exceeded the pulsation frequency ω, since above this point the pulsation becomes highly non-adiabatic, and no excitation or damping can occur (Unno *et al.* 1989). Figure 5.9 illustrates the result of these calculations for both *CoStar* models, plotting the value of the normalized work integral W/E_W against ω^2 for all of the modes considered.

Interestingly enough, this figure shows that all of the g-modes considered were found to be unstable for both models, as were a number of the p-modes with with $\omega^2 \lesssim 100$, whilst the f-modes are all found to be stable. The apparent gap at $\omega^2 \approx 10$ occurs due to the separation of the p- and g-modes in frequency space; either side of this gap, the values of W generally increase for all modes with $\omega^2 \lesssim 100$. Judging from the behaviour of W as a function of ω^2 for some of the p-modes in

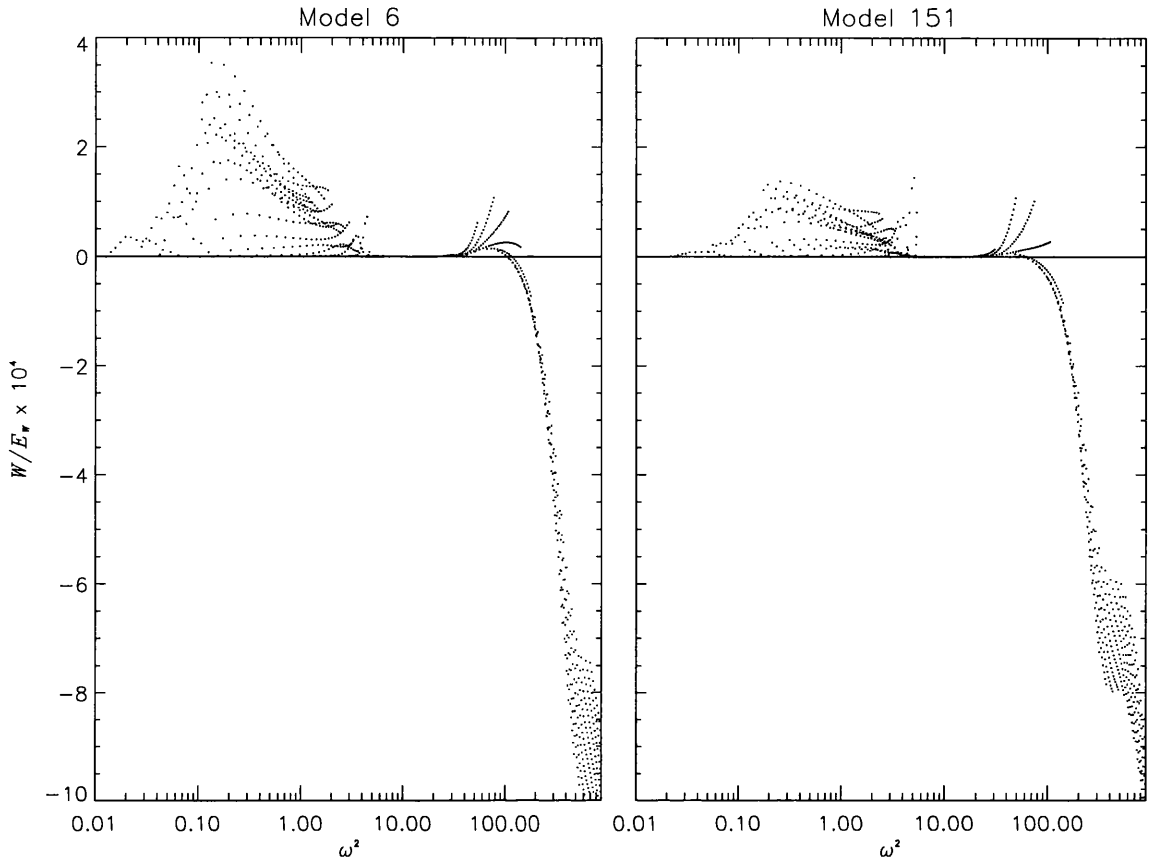

Figure 5.9: The values of the work integral W, normalized by E_W, plotted as a function of ω^2 for all of the modes considered in the *CoStar* models

figure 5.9, this upper limit on ω^2 is probably just a result of only considering modes with $l \leq 25$.

To investigate the cause of these instabilities in greater detail, it is useful to examine the differential work dW/dr, since this quantity is positive in excitation regions and negative in damping regions. Figure 5.10 shows this derivative as a function of $\log p$ for the most unstable p-mode ($n = 3$) and g-mode ($n = 20$) found for model 6 at $l = 10$; also shown are the contributions to the differential work from the second and third terms in equation (5.19), representing the κ- and δ-mechanisms respectively. It appears that, for both of the modes, the principal contribution to instability is from a pair of driving regions at $\log p \approx 5.5$ and $\log p \approx 7$; no driving is found at higher pressures, suggesting that the ϵ-mechanism, represented by equation (5.14), does not operate in these stars.

In the case of the p-mode, the differential work in the driving regions is dominated by contributions from the κ-mechanism, whilst the δ-mechanism is completely irrelevant. In contrast, the two driving regions which lead to the g-mode instability cannot be attributed to a single excitation mechanism; as well as the presence of the κ-mechanism, the δ-mechanism appears to make a positive contribution to the differential work in the inner region. Presumably, this is because part of this region occurs within the convection zone at $6.2 \lesssim \log p \lesssim 7.0$, where the temperature gradient is super-adiabatic. Whilst this region is not dynamically stable in the convective sense, it appears

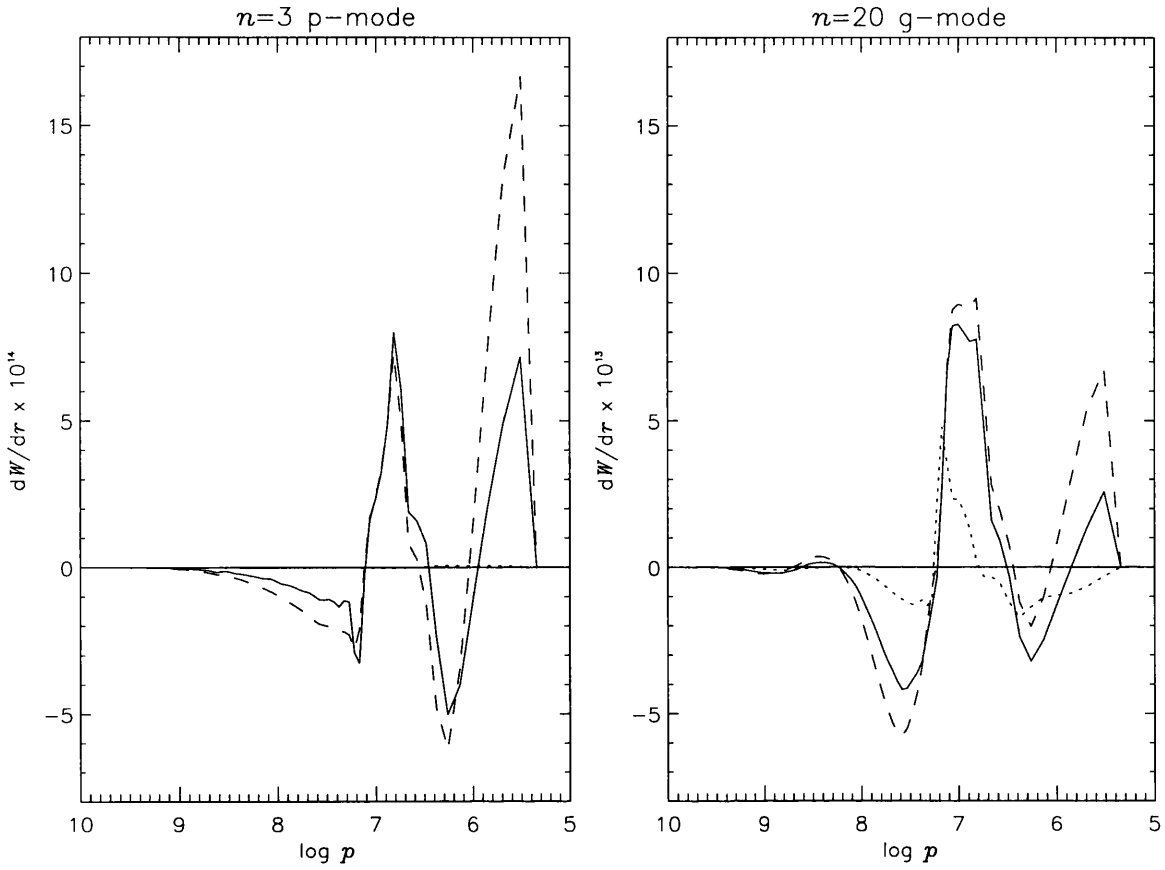

Figure 5.10: The differential work dW/dr (solid) plotted as a function of $\log p$ for the $n = 3$ p-mode and $n = 20$ g-mode of *CoStar* model 6; in both cases, l is taken to be 10. Also plotted are the contributions to the differential work from the κ- (dashed) and δ- (dotted) mechanisms. The derivatives have been normalized by E_W; they are positive in excitation zones, and negative in damping zones.

that the δ-mechanism can still operate within it to generate vibrational instability, presumably because the Lamb frequency is small enough there for pressure to serve as the restoring force (see figure 4.7). On the other hand, this apparent excitation by the δ-mechanism may be an artifact of excluding the perturbations to the convective flux. However, this is improbable, since it was found that, at most, only 0.15% of the total flux is transported by convection within this thin zone.

Instability due to the κ-mechanism has long been suspected as the cause of observed variability in β Cephei stars. Stellingwerf (1978) suggested that these stars are pulsationally unstable due to κ-mechanism driving arising in the He^+ ionization region, although it was later shown that this region lies exterior to the non-adiabatic transition point and therefore cannot contribute to stellar instability. However, Cox *et al.* (1992) have subsequently found that, when the opacity calculations of Rogers & Iglesias (1992) are included in stability analyses, these stars *can* be destabilized by a κ-mechanism. Iron-group transitions occurring above 100,000 K were found to introduce a

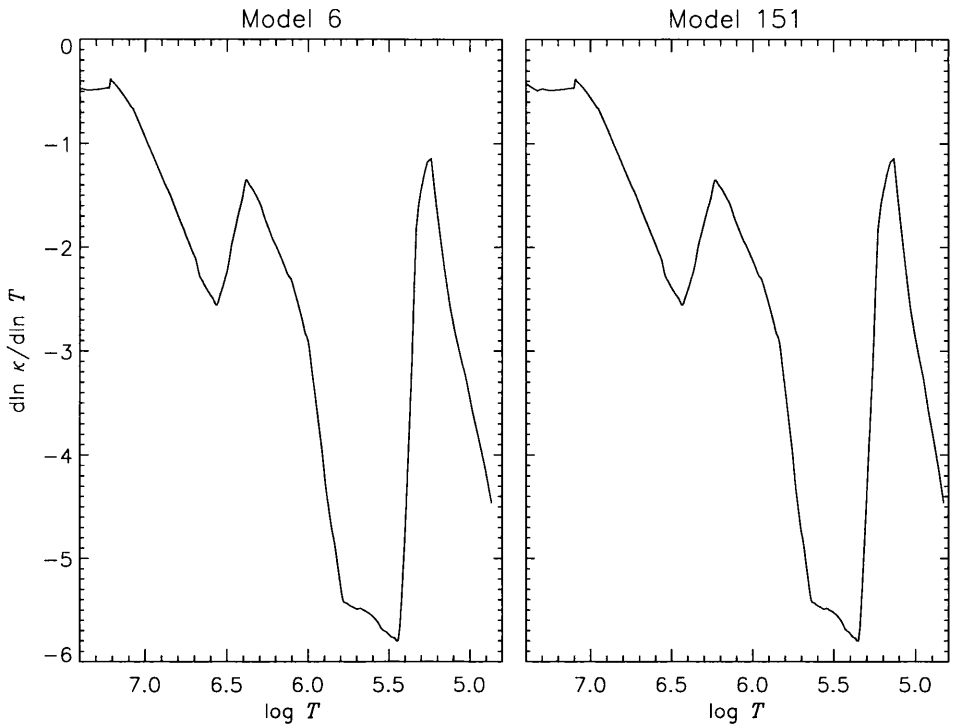

Figure 5.11: The opacity temperature derivative $d\ln\kappa/d\ln T$ plotted as a function of T throughout *CoStar* models 6 and 151. Note the prominent peak occurring at $\log T \approx 5$.

strong temperature-sensitivity to the opacity, which allows the effective excitation of pulsation in a number of the β Cepheid models studied.

It appears that the κ-mechanism-driven modes found in the *CoStar* models are unstable due to these same iron-group elements; figure 5.11 illustrates the opacity temperature derivatives for both of the models, showing quite clearly the iron-group peak at $\log T \approx 5$. Considering that the physical parameters of the *CoStar* models are quite close to those of HD 93521 (see §4.3), although the former are somewhat more metal-rich than the latter, it can therefore be tentatively suggested that the variability observed in this star and similar systems can be attributed to a κ mechanism driven by these iron-group elements. However, to formally confirm this, non-adiabatic calculations must be undertaken, and the perturbations to the convective flux should be treated properly.

5.6 Wave leakage

All of the calculations performed so far in this chapter have used, for the sake of simplicity, the Z-boundary formulation of the outer mechanical boundary condition. It is instructive to examine what the consequences are of using the more physically realistic Υ-boundary introduced in §3.4, which in some cases can permit wave leakage through the surface of the star. Accordingly, all of the $l = 2$ modes for model 6 were recalculated using the outer mechanical boundary condition formu-

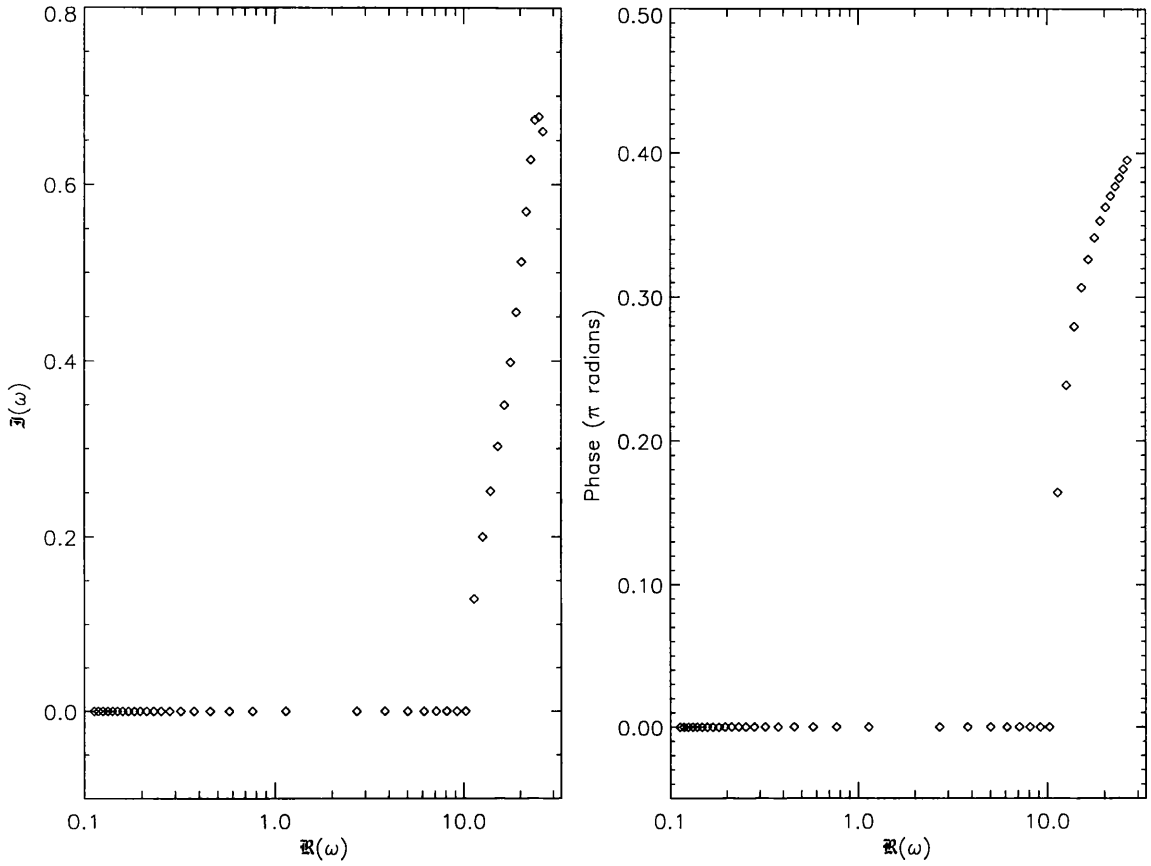

Figure 5.12: The eigenfrequencies ω plotted in the complex plane (left), and the complex phase of y_2 at the outer boundary, plotted as a function of $\Re(\omega)$ (right), for the $l = 2$ modes of *CoStar* model 6. The outer mechanical boundary condition of Unno *et al.* (1989) was used, so some modes show leakage ($\Im(\omega) \neq 0$).

lation of Unno *et al.* (1989). Modifications to HENITER to allow for the complex eigenfrequencies and eigenfunctions which this formulation entails were not required, since HENITER was originally written to operate with complex rather than real variables.

Figure 5.12 plots the resulting eigenfrequencies in the complex plane, along with the complex phase of y_2 at the outer boundary; in the diagram, $\Re$ and $\Im$ denote the real and imaginary parts respectively. For $\omega \lesssim 10$, the eigenfrequencies are purely real, and correspond to modes which are completely reflected from the outer boundary. All of the g-modes considered were found to behave in this manner, since the frequency of the highest order g-mode was found to fall above the lower cutoff frequency ω_{c_1} (see §3.4) for wave leakage.

Above $\omega \approx 10$, all of the eigenfrequencies are complex, corresponding to leakage through the outer boundary; the energy loss caused by this leakage will lead to the pulsation amplitude to decay as $\exp[-\Im(\sigma)t]$. The leakage rate increases monotonically until $\omega \approx 25$, where it reaches a peak and subsequently declines; the reason for this decline is not obvious. At this peak, the e-folding time of

the pulsation decay is only 12.4 hours, so the damping caused by wave leakage can be quite rapid.

The complex phase of y_2 at the outer boundary, shown in the right-hand panel of figure 5.12, is essentially the phase difference between y_1 and y_2 at this boundary, since $y_1 = 1$ there by the normalization adopted. In modes which exhibit a degree of leakage, this phase difference can approach $\pi/2$; since both the horizontal displacement $\boldsymbol{\xi}_h$ and the temperature perturbation δT at the surface depend on y_2 (§3.6), the phase difference will introduce an asymmetry in the lpv of these modes, as will be demonstrated in §7.5.9.

This discussion of wave leakage in the context of the *CoStar* models is somewhat academic; it should be recalled from §3.5 that a proper formulation of the outer mechanical boundary condition should incorporate a self-consistent treatment of the stellar wind. This has not been done here, due both to a lack of relevant data, and to a lack of any suitable theory, and therefore further investigations in this area are definitely required.

Chapter 6

Pulsation and Rotation

6.1 Introduction

Rotation is a phenomenon which is appears to be commonplace amongst O- and B-star populations. Howarth *et al.* (1997) have shown, in a comprehensive survey, that almost all such stars possess a line-width parameter $v_{\rm eq} \sin i$ in excess of 50 km s^{-1}, where, if rotation is the only significant line broadening mechanism operative in these systems, $v_{\rm eq}$ and i may be interpreted as the equatorial rotation velocity and polar inclination respectively. Figure 6.1 illustrates the probability density function of $v_{\rm eq} \sin i$ for the 373 stars in the survey, along with the inferred distribution of rotation velocities $v_{\rm eq}$, calculated assuming an isotropic alignment of polar axes; this distribution shows a pronounced peak at $v_{\rm eq} \sim 100$ km s^{-1}, but extends with non-negligible probability density up to velocities of ~ 400 km s^{-1}. The prevalence of significant rotation in early-type stars means that any thorough study of pulsation in such systems must include a proper treatment of the interaction between pulsation and rotation. Accordingly, this chapter examines the topic in some depth; the remainder of this section presents a broad overview, whilst subsequent sections discuss two of the principal techniques used to treat the pulsation–rotation interaction.

A significant degree of rotation modifies the pulsation characteristics of a star through two basic mechanisms. These mechanisms arise as a consequence of the fictitious centrifugal and coriolis forces, the two terms introduced into the equations of motion upon transformation from inertial to co-rotating frames of reference; together, these forces account for the non-inertial nature of the co-rotating frame by ensuring that angular momentum is conserved. To initiate an investigation of their effects on stellar pulsation, it is useful to consider the relationship between the time-derivatives of some vector $\mathbf{f}$ in an inertial frame, and its equivalent $\mathbf{f}_c$ in a frame rotating with angular velocity $\boldsymbol{\Omega}$, namely

$$\frac{d\mathbf{f}}{dt} = \frac{d\mathbf{f}_c}{dt} + \boldsymbol{\Omega} \times \mathbf{f}_c. \tag{6.1}$$

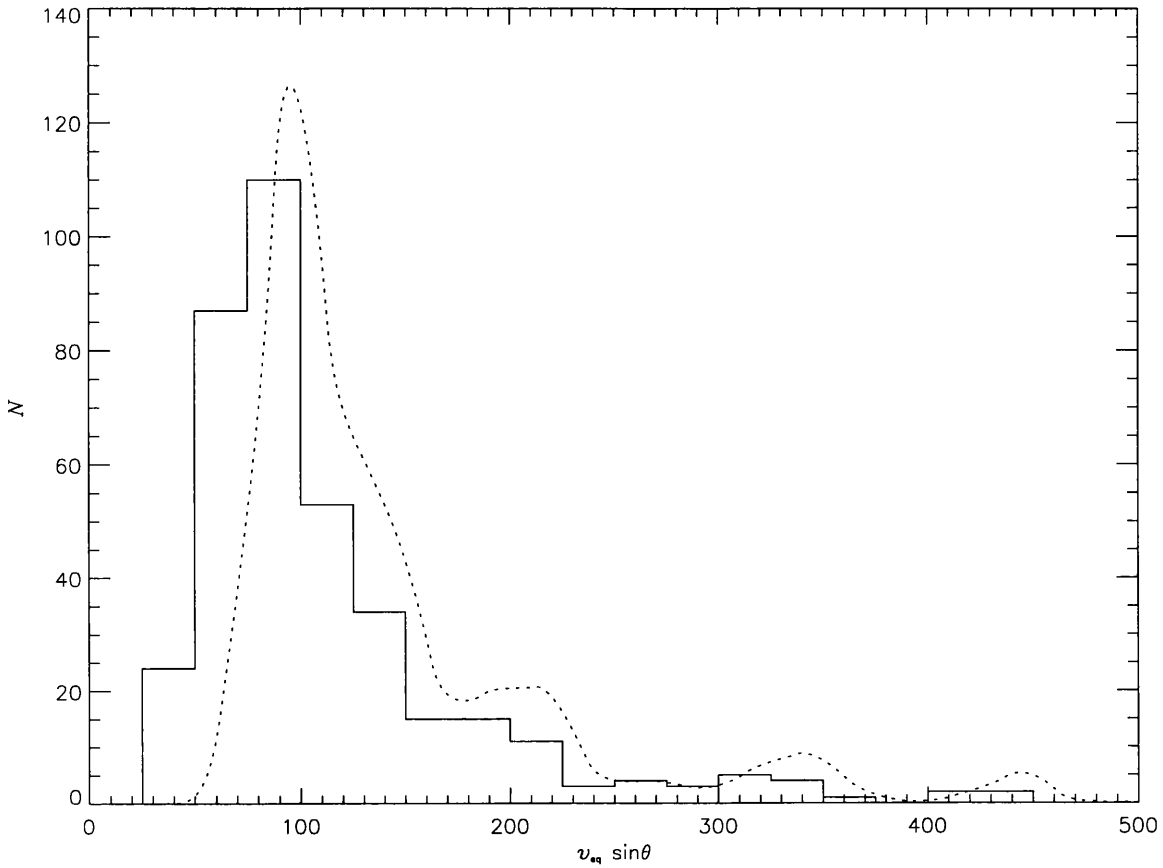

Figure 6.1: The distribution of rotational velocities for a sample of 373 OB stars. The solid histogram shows the probability density function of $v_{\rm eq} \sin i$, whilst the dashed curve shows the inferred distribution of equatorial velocities $v_{\rm eq}$ (from Howarth *et al.* 1997).

The relationship between the second time-derivatives then naturally follows as

$$\frac{d^2\mathbf{f}}{dt^2} = \frac{d^2\mathbf{f}_c}{dt^2} + 2\boldsymbol{\Omega} \times \frac{d\mathbf{f}_c}{dt} + \boldsymbol{\Omega} \times \left(\boldsymbol{\Omega} \times \mathbf{f}_c\right), \tag{6.2}$$

where the fact that $\boldsymbol{\Omega}$ is time-independent (in both frames of reference) has been exploited. Setting $\mathbf{f}$ equal to the position vector $\mathbf{r}$ of a fluid parcel, the accelerations in the two frames of reference are related by

$$\frac{d\mathbf{v}}{dt} = \frac{d\mathbf{v}_c}{dt} + 2\boldsymbol{\Omega} \times \mathbf{v}_c + \boldsymbol{\Omega} \times \left(\boldsymbol{\Omega} \times \mathbf{r}_c\right), \tag{6.3}$$

where $\mathbf{v}$ is the velocity vector of the fluid parcel in the appropriate frame of reference. From this expression, it can be seen that any equation of motion, when transformed from inertial to co-rotating frames, will undergo the addition of two supplementary fictitious forces, the coriolis and centrifugal forces represented by the second and third terms respectively of the right-hand side. Since $\mathbf{r}$ is radial in both frames of reference, the centrifugal force acts always directly towards the rotation axis; the coriolis force, on the other hand, has a direction dependent on the velocity in the co-rotating frame.

For systems rotating as solid bodies (*i.e.*, Ω is independent of position), it is usual to set the angular velocity Ω to be that of the star itself. In such cases, then, the equilibrium configuration of the star is solely affected by the centrifugal force, since the co-rotating velocity $\mathbf{v}_c$ appearing in the coriolis-force term will be zero (this is not strictly true when convection is considered, but a proper treatment of rotationally-modified convective mixing is highly non-trivial (*e.g.*, Sobouti 1975), and will not be considered herein). The centrifugal force serves to distort the equilibrium figure of the star into an oblate spheroid, and modify the internal structure (and evolution) of the star accordingly. These modifications represent the first mechanism by which the pulsation characteristics of a star are altered by rotation: the changes to the structure will introduce corresponding changes to the pulsation eigenfrequencies and eigenfunctions. However, since the centrifugal force modifies the pulsation only through changes to the underlying stellar structure, and does not directly alter the equations of pulsation themselves (at least, not for solid-body rotation), it does not lead to the introduction of new types of pulsation (Unno *et al.* 1989). The main problems with the treatment of the centrifugal force, then, lie in calculating the manner in which it will affect the equilibrium stellar structure. Much work has already been undertaken regarding its effects on spherical gaseous configurations (*e.g.*, Tassoul 1978), but attempts to integrate this work with proper stellar structure and evolution theories have proven, on the whole, rather unsuccessful; rotation remains one of the main stumbling blocks in that field.

However, for the purposes of pulsation studies, a number of techniques have proven useful in rendering the problem of the centrifugal force tractable; in particular, the so-called Chandrasekhar-Milne expansion (*e.g.*, Tassoul 1978) has allowed investigations of the pulsation–rotation interaction to include, to some degree, the centrifugal-force effects. This approach revolves around generating a one-to-one mapping between the equilibrium configurations of rotating and non-rotating stars, so that suitable rotationally-modified structure models may be constructed and integrated with pulsation studies. Lee (1993), and later Lee & Baraffe (1995), have presented such a treatment (initially for the study of global acoustic oscillations in Jupiter), and contributed significantly to current understanding of pulsation in rotating systems; Clement (1981; 1984; 1986; 1989) has also developed a complementary variational method for the integration of second-order centrifugal effects, which appears to produce similarly interesting results. In general, however, these treatments are too lengthy and complex to include herein; the remainder of this chapter, therefore, is exclusively concerned with the second pulsation–rotation interaction mechanism.

This second mechanism arises from the explicit modification of the pulsation equations by the fictitious forces discussed above. The rotationally-modified pulsation equations (to be compared with equations (2.15)–(2.17)) are given by

$$\rho' + \nabla \cdot (\boldsymbol{\xi}\rho) = 0, \tag{6.4}$$

$$-\sigma_c^2 \boldsymbol{\xi} + 2\mathrm{i}\sigma_c \boldsymbol{\Omega} \times \boldsymbol{\xi} - (\mathbf{r} \times \boldsymbol{\Omega}) \times \boldsymbol{\Omega}(\boldsymbol{\xi} \cdot \nabla \ln \Omega^2) = -\frac{1}{\rho}\nabla p' - \frac{\rho'}{\rho}\nabla\Phi - \nabla\Phi' \tag{6.5}$$

and

$$\nabla^2\Phi' = 4\pi G\rho' \tag{6.6}$$

(Lee & Saio 1986), where all vectors are with respect to the co-rotating frame of reference; σ_c is the pulsation frequency in this frame, and is related to the frequency σ in an inertial frame by

$$\sigma_c = \sigma + m\Omega, \tag{6.7}$$

where $\Omega \equiv |\boldsymbol{\Omega}|$. Since the phase velocity $v^{\rm phase}$ of a pulsation wave in the azimuthal direction is given by

$$v^{\rm phase} = -\frac{\sigma}{m}, \qquad v_c^{\rm phase} = -\frac{\sigma_c}{m}, \tag{6.8}$$

and the sign of $v^{\rm phase}$ determines whether the wave is prograde (+) or retrograde (−) with respect to the direction of rotation, it can be seen that the direction of travel of the wave in a given frame of reference depends not only on the sign m, but also on that of the appropriate frequency. Throughout the remainder of this chapter, exclusively negative values of m are considered, so that prograde and retrograde modes are associated with positive and negative frequencies respectively.

The second and third terms on the left-hand side of equation (6.5) are the rotation-induced terms due to the coriolis and centrifugal forces respectively; in the solid-body rotation systems considered herein, the centrifugal term vanishes (since Ω is constant); however, the coriolis term remains, and leads to significant, qualitative changes to the way the star pulsates. A number of approaches exist by which to treat the introduction of this term; two such techniques are discussed in the following sections, namely the perturbation-expansion method, first introduced by Ledoux (1951), and the (perhaps more elegant) matrix method, initially introduced by Berthomieu *et al.* (1978) and later extensively developed by Lee & Saio (1986; 1987*a*; 1987*b*; 1988; 1989; 1990). The matrix method is investigated in depth, with particular attention paid to to the similarity transformation technique introduced by Berthomieu *et al.* (1978) and Lee & Saio (1987*a*). This technique substantially simplifies the matrix method and reduces it to a form far less computationally expensive than its most general representation; as well as a review of the technique, a number of improvements and implementation considerations are discussed.

6.2 The Perturbation-Expansion Technique

The perturbation expansion technique (hereinafter PE) uses methods initially developed in the field of quantum mechanics to investigate the effects of small perturbations to the pulsation equations. It is quite general, in that it may be used not only to study rotational perturbations, but also the effects of magnetic fields (*e.g.*, Moss 1980) and external tidal forces (*e.g.*, Saio 1981) on stellar pulsation.

However, since this work is exclusively concerned with non-binary, non-magnetic systems, the discussion herein is restricted to the explicit rotational modification formulation.

The underlying goal of PE is to express the dependent pulsation variables as power series in $\Omega/\sigma_c^{(0)}$ (where $\sigma_c^{(0)}$ is the unperturbed, zero-rotation pulsation frequency), in which all but the first few terms are generally small enough to neglect. The calculation of the first-order terms is quite straightforward; higher-order terms become increasingly more difficult to calculate (*e.g.*, Saio 1981), and, accordingly, most treatments which use the PE technique (including this one) retain only first-order expressions. Note that PE is limited to cases where $\Omega/\sigma_c^{(0)}$ is less than unity, since the power-series expansions diverge otherwise; this is a consequence of the fact that, for $\Omega/\sigma_c^{(0)} \gtrsim 1$, the coriolis-force modifications to the pulsation eigenfunctions are quite significant, and beyond the scope of PE.

The first-order expression for the modified eigenfrequencies σ_c, in terms of their non-rotating equivalents $\sigma_c^{(0)}$, was found by Ledoux (1951) to be

$$\sigma_c = \sigma_c^{(0)} + m\Omega C_{n,l}, \tag{6.9}$$

where the Ledoux splitting factor $C_{n,l}$ is a constant for a mode of given harmonic degree l and radial order n which depends on an integral of the non-rotating eigenfunctions over the stellar volume. This expression indicates that the first-order effect of the coriolis force is to introduce an m-dependent splitting in the eigenfrequencies (which are degenerate in a non-rotating star), in much the same way that a magnetic field lifts the partial degeneracy of atomic energy levels via the Zeeman effect. The degeneracy splitting occurs because rotation (or, for that matter, a magnetic field) serves to define a 'preferred' axis for the star; it has already been observed in a number of magnetic A stars (Kurtz 1982), and is thought to be responsible for the long periods of some β Cepheid stars through beating between split modes (Ledoux 1951).

Aerts & Waelkens (1993) used a PE technique to find corresponding first-order expressions for the eigenfunctions, and subsequently, Schrijvers *et al.* (1997) presented these results in a compact form with a couple of errors in the former work corrected[1]. In the notation adopted herein, Schrijvers *et al.* (1997) find that the displacement perturbation $\boldsymbol{\xi}$ at the stellar surface is given, to first order, by

$$\frac{\boldsymbol{\xi}(\theta,\phi,t)}{R} = \Re\left\{\left[a_{\mathrm{sph},l}Y_l^m\mathbf{e}_r + k\nabla_h(a_{\mathrm{sph},l}Y_l^m) - \mathrm{i}\nabla_h\times\left(a_{\mathrm{tor},l-1}\frac{N_l^m}{N_{l-1}^m}Y_{l-1}^m\mathbf{e}_r - a_{\mathrm{tor},l+1}\frac{N_l^m}{N_{l+1}^m}Y_{l+1}^m\mathbf{e}_r\right)\right]\exp(\mathrm{i}\sigma_c t)\right\}, \tag{6.10}$$

[1]The azimuthal velocity fields have been omitted from expression [19] of Aerts & Waelkens (1993); see also Aerts & Waelkens (1995).

where $\mathbf{e}_r$ is the unit vector in the radial direction, and $a_{\mathrm{sph},l}$, $a_{\mathrm{tor},l+1}$ and $a_{\mathrm{tor},l-1}$ are the amplitudes of the spheroidal and two toroidal displacement components respectively; this expression differs slightly from that given by Schrijvers *et al.* (1997), since they adopt a different normalization for the spherical harmonics. The normalizing function N_l^m is given by

$$N_l^m = (-1)^{(m+|m|)/2} \sqrt{\frac{2l+1}{4\pi} \frac{(l-|m|)!}{(l+|m|)!}}, \tag{6.11}$$

whilst the term k is a rotationally-modified version of the quantity introduced in equation (3.42), such that

$$k = \frac{1}{\omega_c^2} + \frac{2m}{l(l+1)} \frac{\Omega}{\sigma_c} \left(1 + \frac{1}{\omega_c^2}\right), \tag{6.12}$$

where ω_c is the dimensionless pulsation frequency in the co-rotating frame. The amplitude terms introduced above are given by

$$a_{\mathrm{sph},l} = a^{(0)} + \frac{\Omega}{\sigma_c} a^{(1)}, \tag{6.13}$$

$$a_{\mathrm{tor},l+1} = \frac{\Omega}{\sigma_c} \frac{l-|m|+1}{l+1} \frac{2}{2l+1} \left(1 - \frac{l}{\omega_c^2}\right) a^{(0)} \tag{6.14}$$

and

$$a_{\mathrm{tor},l-1} = \frac{\Omega}{\sigma_c} \frac{l+|m|}{l} \frac{2}{2l+1} \left(1 + \frac{l+1}{\omega_c^2}\right) a^{(0)}, \tag{6.15}$$

where $a^{(0)}$ is the non-rotating displacement amplitude and $a^{(1)}$ is determined from the zeroth-order eigenfunctions. The latter two expressions differ from those given by Schrijvers *et al.* (1997), in that terms in $\Omega/\sigma_c^{(0)}$ have been replaced by Ω/σ_c, but it easy to demonstrate that, to first-order in $\Omega/\sigma_c^{(0)}$, these modifications make no difference. These modifications have been introduced to eliminate all references to the non-rotating frequency $\sigma_c^{(0)}$ from the first-order expressions.

The above expression for ξ_r indicates that, to first order, the action of rotation is to modify the relative amplitudes of the radial and horizontal displacement components, and, furthermore, to couple in two additional toroidal components $a_{\mathrm{tor},l+1}$ and $a_{\mathrm{tor},l-1}$. These toroidal components arise from the fact that the time-independent toroidal modes introduced in §2.8 acquire non-zero frequencies in a rotating system, and contaminate the existing spheroidal components. Whilst these first-order expressions are in themselves interesting, the remainder of this chapter focuses on the alternative matrix method discussed in the introduction; further mention of the first-order expressions is made only in a comparison between the matrix and PE methods in §6.10.

6.3 The Matrix Method

The matrix method is a very powerful technique for calculating the effects of the coriolis force on pulsation eigenfrequencies and eigenfunctions. In its most general form, it provides a complete

treatment of the coriolis force, without any of the power-series limitations of PE. In its more restricted form, which lends itself better to numerical calculations, it is formally applicable to only low-frequency modes ($\omega \lesssim 1$), but still may give useful results for higher-frequency modes. This section presents the matrix method in the general form, laying the foundations for the development of the restricted form in subsequent sections.

The matrix method essentially revolves around directly solving the pulsation equations without any significant approximations, but with a suitable manipulation of the equations to present them in a numerically tractable form. The real problems in treating the coriolis force lie in the fact that the rotationally-modified pulsation equations do not have solutions whose angular dependence is given by single spherical harmonics; this is evident even in the first order PE expression for the displacement ξ_r (equation (6.10)), which contains toroidal terms proportional to differing spherical harmonics. However, since the spherical harmonics form a complete orthonormal set over the surface of a sphere, they still may be used as the basis from which pulsation eigenfunctions may be constructed.

Zahn (1966) demonstrated that the coriolis force leads to pulsation eigenfunctions which contain only spherical harmonics of the same azimuthal order m; this is a direct consequence of the axial symmetry of the rotation perturbation itself. Furthermore, only harmonics of the same latitudinal parity π about the equator are coupled together. Adopting the Cowling approximation (which is not strictly necessary, but leads to significant mathematical simplification), it is therefore possible to write the pulsation eigenfunctions for a given value of m in their most general form as

$$\frac{\boldsymbol{\xi}}{r} = \mathbf{Y_1} \cdot \boldsymbol{\Phi} \mathbf{e}_r + \nabla_h \left(\mathbf{H} \cdot \boldsymbol{\Phi} \right) + \nabla_h \times \left(\mathbf{T} \cdot \boldsymbol{\Phi}^\dagger \mathbf{e}_r \right) \tag{6.16}$$

and

$$\frac{p'}{\rho g r} = \mathbf{Y_2} \cdot \boldsymbol{\Phi}. \tag{6.17}$$

The functions $\mathbf{Y_1}(r)$, $\mathbf{Y_2}(r)$, $\mathbf{H}(r)$ and $\mathbf{T}(r)$ are all vectors of infinite dimension, containing information concerning the radial dependence of the eigenfunctions, whilst the functions $\boldsymbol{\Phi}(\theta, \phi)$ and $\boldsymbol{\Phi}^\dagger(\theta, \phi)$, again vectors of infinite dimension, describe the angular dependence of the eigenfunctions, and have elements given by

$$(\boldsymbol{\Phi})_j = |l_j, m\rangle \tag{6.18}$$

and

$$(\boldsymbol{\Phi}^\dagger)_j = |n_j, m\rangle. \tag{6.19}$$

The symbols used in these expressions, in particular the Dirac bra-ket notation, have been adopted from the nomenclature of Lee & Saio (1990), so that

$$|l_j, m\rangle = Y_{l_j}^m(\theta, \phi) \tag{6.20}$$

and

$$|n_j, m\rangle = Y_{n_j}^m(\theta, \phi), \tag{6.21}$$

where

$$l_j = \begin{cases} |m| + 2(j-1) & \text{even-}\pi, \\ |m| + 2(j-1) + 1 & \text{odd-}\pi, \end{cases} \tag{6.22}$$

and

$$n_j = \begin{cases} |m| + 2(j-1) + 1 & \text{even-}\pi, \\ |m| + 2(j-1) & \text{odd-}\pi. \end{cases} \tag{6.23}$$

This nomenclature elegantly splits the even-π and odd-π modes, whilst allowing derivations to be performed without explicit reference to the parity (explicit reference *is* made when required). The term in equation (6.16) containing the vector $\mathbf{T}$ corresponds to the toroidal terms introduced by rotation.

When the expressions for ξ_r and p' are substituted into the rotationally-modified pulsation equations (6.4)–(6.5), the resulting equations for $\mathbf{Y_1}$, $\mathbf{Y_2}$, $\mathbf{H}$ and $\mathbf{T}$, after lengthy algebraic manipulations, can be shown to be given by

$$x\frac{d\mathbf{Y_1}}{dx} = (V_g - 3)\mathbf{Y_1} - V_g\mathbf{Y_2} + \mathbf{\Lambda H}, \tag{6.24}$$

$$x\frac{d\mathbf{Y_2}}{dx} = (c_1\omega_c^2 + A^\star)\mathbf{Y_1} + (1 - U - A^\star)\mathbf{Y_2} - 2c_1\omega_c\hat{\Omega}(m\mathbf{H} + \mathrm{i}\mathbf{CT}), \tag{6.25}$$

$$\mathbf{L_0 H} - \mathrm{i}\mathbf{M_-T} = \frac{\mathbf{Y_2}}{c_1\omega_c^2} + m\nu\mathbf{\Lambda}^{-1}\mathbf{Y_1} \tag{6.26}$$

and

$$-\mathbf{M_+ H} + \mathrm{i}\mathbf{L_1 T} = -\nu\mathbf{K Y_1} \tag{6.27}$$

(Unno *et al.* 1989), where the dimensionless rotation frequency $\hat{\Omega}$ is given by

$$\hat{\Omega}^2 \equiv \frac{\Omega^2 R^3}{GM}, \tag{6.28}$$

and the parameter ν, which quantifies the degree to which rotation modifies pulsation, is defined by

$$\nu \equiv 2\frac{\Omega}{\sigma_c} \equiv 2\frac{\hat{\Omega}}{\omega_c}. \tag{6.29}$$

Note that it is the rotationally modified frequency σ_c, and not the unperturbed frequency $\sigma_c^{(0)}$, which appears in the definition of ν. The infinite diagonal matrices $\mathbf{\Lambda}$, $\mathbf{L_0}$ and $\mathbf{L_1}$ have non-zero elements given by

$$(\mathbf{\Lambda})_{j,j} = \Lambda(l_j), \qquad (\mathbf{L_0})_{j,j} = 1 - \frac{m\nu}{\Lambda(l_j)}, \qquad (\mathbf{L_1})_{j,j} = 1 - \frac{m\nu}{\Lambda(n_j)}, \tag{6.30}$$

where $\Lambda(l) \equiv l(l+1)$, whilst the infinite bi-diagonal matrices $\mathbf{C}$ and $\mathbf{K}$ have non-zero elements

$$\left.\begin{aligned} (\mathbf{C})_{j,j} &= -(l_j+2)J^m_{l_j+1}, & (\mathbf{C})_{j+1,j} &= (l_j+1)J^m_{l_j+2} \\ (\mathbf{K})_{j,j} &= \frac{J^m_{l_j+1}}{l_j+1}, & (\mathbf{K})_{j,j+1} &= -\frac{J^m_{l_j+2}}{l_j+2} \end{aligned}\right\} \quad \text{even-}\pi, \tag{6.31}$$

and

$$\left.\begin{aligned} (\mathbf{C})_{j,j} &= (l_j+1)J^m_{l_j+2}, & (\mathbf{C})_{j,j+1} &= -(l_j+2)J^m_{l_j+1} \\ (\mathbf{K})_{j,j} &= -\frac{J^m_{l_j}}{l_j}, & (\mathbf{K})_{j+1,j} &= \frac{J^m_{l_j+1}}{l_j+1} \end{aligned}\right\} \quad \text{odd-}\pi. \tag{6.32}$$

The symbol J^m_l arises from recurrence relations between spherical harmonics (*e.g.*, Unno *et al.* 1989), and is defined by

$$J^m_l = \begin{cases} \sqrt{\frac{l^2-m^2}{(2l+1)(2l-1)}} & \text{if } l > |m|, \\ 0 & \text{otherwise.} \end{cases} \tag{6.33}$$

Following Lee & Saio (1990), the bi-diagonal matrices $\mathbf{M}_+$ and $\mathbf{M}_-$ are best represented by introducing $\mathbf{M_0}$ and $\mathbf{M_1}$, which have non-zero elements given by

$$(\mathbf{M_0})_{j,j} = \nu\frac{k_j}{k_j+1}J^m_{k_j+1}, \qquad (\mathbf{M_0})_{j,j+1} = \nu\frac{k_j+3}{k_j+2}J^m_{k_j+2}, \tag{6.34}$$

$$(\mathbf{M_1})_{j,j} = \nu\frac{k_j+2}{k_j+1}J^m_{k_j+1}, \qquad (\mathbf{M_1})_{j+1,j} = \nu\frac{k_j+1}{k_j+2}J^m_{k_j+2}, \tag{6.35}$$

where $k_j = |m| + 2(j-1)$. Then, $\mathbf{M}_+ = \mathbf{M_0}$ and $\mathbf{M}_- = \mathbf{M_1}$ for even-π modes, and $\mathbf{M}_+ = \mathbf{M_1}$ and $\mathbf{M}_- = \mathbf{M_0}$ for odd-π modes.

Solution of equations (6.24) and (6.25) may be accomplished using the relaxation technique discussed in Chapter 5, with the two algebraic relations (6.26) and (6.27) used to evaluate $\mathbf{H}$ and $\mathbf{T}$ at the start of each iteration. Since the infinite dimension of all vectors and matrices places them beyond the scope of numerical manipulation, for the purposes of solution they must be truncated at some (suitably large) dimension N. The boundary conditions which apply to the equations can be derived in a manner very similar to that used in Chapter 3; the fact that the boundary conditions are angle-independent (at least, under the approximation of no rotational deformation) means that the individual jth elements of $\mathbf{Y_1}$, $\mathbf{Y_2}$ $\mathbf{H}$ and $\mathbf{T}$ must each satisfy the original, non-rotating boundary

conditions with the appropriate values of l_j. This leads to $2N$ boundary conditions, corresponding to the $2N$ coupled equations represented by (6.4) and (6.5); the arbitrary normalization of ξ_r introduced in §3.3 constitutes one additional boundary condition, which must be specified not only at at given radius, but also at a given colatitude, because the angular dependence of ξ_r cannot be factored out as a single spherical harmonic.

Unfortunately, solution within the general formulation at suitably large matrix dimensions N presents an unreasonably large workload to even the fastest computers, since it involves simultaneous solution of $2N$ coupled differential equations. In an attempt to circumvent this problem, and those of numerical inaccuracy and instability, Berthomieu *et al.* (1978) introduced a very useful approach, the similarity transformation technique, which forms the core of the restricted form of the matrix method discussed in the following section.

6.4 The Similarity Transformation Technique

The similarity transformation technique, hereinafter ST, revolves around the application of a simple approximation to the general matrix equations presented in the preceding section, thus allowing the partial decoupling of the infinite set of differential equations discussed previously. Introduced by Eckart (1960) in the context of geophysics, this so-called 'traditional approximation' revolves around completely suppressing the horizontal component $-\Omega \sin\theta \mathbf{e}_\theta$ of the rotation angular velocity vector Ω. Physically, this approximation corresponds to neglecting the coriolis force associated with radial motion, and the radial component of the coriolis force associated with horizontal motion (Unno *et al.* 1989); it leads to acceptable results when applied to low-frequency modes (g-modes) in which the oscillation is dominated by horizontal motions. Berthomieu *et al.* (1978) arrived at the same approximation by considering a hierarchy of magnitudes occurring between different quantities in the rotationally-modified pulsation equations, and neglecting all terms of small magnitude.

Lee & Saio (1987*a*) have demonstrated that, within this traditional approximation, the pulsation equations (6.24)–(6.27) introduced in the preceding section may be rewritten as

$$x\frac{d\mathbf{Y_1}}{dx} = (V_g - 3)\mathbf{Y_1} - V_g\mathbf{Y_2} + \mathbf{\Lambda H}, \tag{6.36}$$

$$x\frac{d\mathbf{Y_2}}{dx} = (c_1\omega_c^2 + A^\star)\mathbf{Y_1} + (1 - U - A^\star)\mathbf{Y_2}, \tag{6.37}$$

$$\mathbf{L_0 H} - \mathrm{i}\mathbf{M_-T} = \frac{\mathbf{Y_2}}{c_1\omega_c^2} \tag{6.38}$$

and

$$-\mathbf{M_+ H} + \mathrm{i}\mathbf{L_1 T} = 0. \tag{6.39}$$

Eliminating the term i$\mathbf{T}$ between the last two algebraic equations leads to an expression for $\mathbf{\Lambda H}$,

$$\mathbf{\Lambda H} = \mathbf{\Lambda}\left(\mathbf{L_0} - \mathbf{M_-}\mathbf{L_1}^{-1}\mathbf{M_+}\right)^{-1}\frac{\mathbf{Y_2}}{c_1\omega_c^2}, \tag{6.40}$$

which may be substituted into equation (6.36) to give the pulsation equations in their final form as

$$x\frac{d\mathbf{Y_1}}{dx} = (V_g - 3)\mathbf{Y_1} + \left(\frac{\mathbf{W}}{c_1\omega_c^2} - V_g\right)\mathbf{Y_2} \tag{6.41}$$

and

$$x\frac{d\mathbf{Y_2}}{dx} = (c_1\omega_c^2 + A^\star)\mathbf{Y_1} + (1 - U - A^\star)\mathbf{Y_2}, \tag{6.42}$$

where the symmetric matrix $\mathbf{W}$ is given by

$$\mathbf{W} = \mathbf{\Lambda}\left(\mathbf{L_0} - \mathbf{M_-}\mathbf{L_1}^{-1}\mathbf{M_+}\right)^{-1}. \tag{6.43}$$

These two vector differential equations encapsulate an infinite set of coupled pairs of scalar differential equations, in which the coupling between equation pairs is completely described by the matrix $\mathbf{W}$; for this reason, $\mathbf{W}$ is hereinafter termed the coupling matrix. Lee & Saio (1987*a*) gave expressions, but not derivations, for the elements of the coupling matrix (or rather, its inverse) in the case of even-π modes; Appendix C derives corresponding expressions for odd-π modes (which turn out to be the same).

The underlying importance of the fact that the rotational coupling between equation pairs is expressed by a single matrix is that the whole system of rotationally-modified pulsation equations may be brought into diagonal form via a similarity transformation (hence the name of this section). In general, a matrix $\mathbf{X}$ may be written in the form

$$\mathbf{X} = \mathbf{YZY}^{-1}, \tag{6.44}$$

where the matrix $\mathbf{Z}$ is diagonal and has elements given by the eigenvalues λ of $\mathbf{X}$; the eigenvectors x of $\mathbf{X}$ form the corresponding columns of $\mathbf{Y}$. These eigenvalues and eigenvectors are, of course, given by solution of the classical matrix eigenvalue problem (*e.g.*, Arfken 1970),

$$\mathbf{Xx} = \lambda\mathbf{x}; \tag{6.45}$$

if $\mathbf{X}$ is hermitian, its eigenvalues are real, and its eigenvectors are mutually orthogonal (Arfken 1970), leading to a purely real $\mathbf{Z}$ and a unitary $\mathbf{Y}$. Real symmetric matrices, being a subset of hermitian matrices, are also subject to these requirements; in particular, the symmetric coupling matrix $\mathbf{W}$ has real eigenvalues and an orthogonal (real unitary) transformation matrix $\mathbf{Y}$.

The significance of this discussion is that $\mathbf{W}$ may always be written in the form

$$\mathbf{W} = \mathbf{BD\tilde{B}}, \tag{6.46}$$

where $\mathbf{D}$ is diagonal and $\mathbf{B}$ orthogonal (the tilde denotes the matrix transpose, so that for orthogonal $\mathbf{B}$, $\tilde{\mathbf{B}} \equiv \mathbf{B}^{-1}$). If this expression is used to replace $\mathbf{W}$ in equations (6.41)–(6.42), subsequent multiplication through by $\tilde{\mathbf{B}}$ leads to

$$x\frac{d\mathbf{Z_1}}{dx} = (V_g - 3)\mathbf{Z_1} + \left(\frac{\mathbf{D}}{c_1\omega_c^2} - V_g\right)\mathbf{Z_2} \tag{6.47}$$

and

$$x\frac{d\mathbf{Z_2}}{dx} = (c_1\omega_c^2 + A^\star)\mathbf{Z_1} + (1 - U - A^\star)\mathbf{Z_2}, \tag{6.48}$$

where, again following the nomenclature of Lee & Saio (1990),

$$\mathbf{Z_1} = \tilde{\mathbf{B}}\mathbf{Y_1} \tag{6.49}$$

and

$$\mathbf{Z_2} = \tilde{\mathbf{B}}\mathbf{Y_2}. \tag{6.50}$$

The diagonal form of the transformed coupling matrix $\mathbf{D}$ appearing in equation (6.47) means that the differential equation pairs discussed previously are now completely decoupled from one another. This can be seen by considering the jth elements of equations (6.47)–(6.48),

$$x\frac{d(\mathbf{Z_1})_j}{dx} = (V_g - 3)(\mathbf{Z_1})_j + \left(\frac{\lambda_{l_j,m}}{c_1\omega_c^2} - V_g\right)(\mathbf{Z_2})_j \tag{6.51}$$

and

$$x\frac{d(\mathbf{Z_2})_j}{dx} = (c_1\omega_c^2 + A^\star)(\mathbf{Z_1})_j + (1 - U - A^\star)(\mathbf{Z_2})_j, \tag{6.52}$$

where

$$\lambda_{l_j,m} \equiv (\mathbf{D})_{j,j} \tag{6.53}$$

is the symbol for the eigenvalues of $\mathbf{W}$ introduced by Lee & Saio (1990); these elements, for each value of j, are completely self-contained differential-equation pairs and have thus been decoupled. Furthermore, they are essentially identical to the non-rotating pulsation equations (2.48)–(2.49), with the replacement of the $\Lambda(l) = l(l+1)$ term by $\lambda_{l_j,m}$. Accordingly, they may be solved using the procedures given in Chapter 5 for non-rotating stars.

By analogy to equations (6.49) and (6.50), the transformed horizontal and toroidal displacement vector functions are given by

$$\mathbf{Z_3} = \tilde{\mathbf{B}}\mathbf{H} \tag{6.54}$$

and

$$\mathbf{Z_4} = \mathrm{i}\tilde{\mathbf{B}}^{\dagger}\mathbf{T}, \tag{6.55}$$

where $\mathbf{B}^{\dagger}$ is the eigenvector matrix of the coupling matrix $\mathbf{W}^{\dagger}$ associated with the same value of m *but the opposite parity* to that of $\mathbf{W}$ (*i.e.*, $\mathbf{W}^{\dagger}$ is odd-π if $\mathbf{W}$ is even-π, and *vice-versa*); this demonstrates that the toroidal displacement fields have a parity opposite to that of the spheroidal fields. Both $\mathbf{H}$ and $\mathbf{T}$ can be eliminated from these equations by writing them in terms of $\mathbf{Y_2}$, which in turn may be expressed in terms of $\mathbf{Z_2}$ using equation (6.50), so that

$$\mathbf{Z_3} = \tilde{\mathbf{B}}\mathbf{\Lambda}^{-1}\mathbf{W}\mathbf{B}\frac{\mathbf{Z_2}}{c_1\omega_c^2} \tag{6.56}$$

and

$$\mathbf{Z_4} = \mathrm{i}\tilde{\mathbf{B}}^{\dagger}\mathbf{L_1}^{-1}\mathbf{M}_{+}\mathbf{\Lambda}^{-1}\mathbf{W}\mathbf{B}\frac{\mathbf{Z_2}}{c_1\omega_c^2}. \tag{6.57}$$

These two equations may be used to reconstruct $\mathbf{Z_3}$ and $\mathbf{Z_4}$ from the solutions found for $\mathbf{Z_1}$ and $\mathbf{Z_2}$.

Expressions for the displacement vector $\boldsymbol{\xi}$ and the pressure perturbation p', for a given value of m, can be found by substituting equations (6.49)–(6.50) and (6.54)–(6.55) into equations (6.16) and (6.17) respectively, to give

$$\frac{\boldsymbol{\xi}}{r} = \mathbf{Z_1}\cdot\mathbf{\Psi}\mathbf{e}_r + \nabla_h\left(\mathbf{Z_3}\cdot\mathbf{\Psi}\right) + \nabla_h\times\left(-\mathrm{i}\mathbf{Z_4}\cdot\mathbf{\Psi}^{\dagger}\mathbf{e}_r\right) \tag{6.58}$$

and

$$\frac{p'}{\rho g r} = \mathbf{Z_2}\cdot\mathbf{\Psi}. \tag{6.59}$$

Here, the identity

$$\mathbf{B}\mathbf{Z_1}\cdot\mathbf{\Phi} \equiv \mathbf{Z_1}\cdot\tilde{\mathbf{B}}\mathbf{\Phi}, \tag{6.60}$$

and similar expressions, have been used to define a new angular basis $\mathbf{\Psi}$, given by

$$\mathbf{\Psi} = \tilde{\mathbf{B}}\mathbf{\Phi} \tag{6.61}$$

and

$$\mathbf{\Psi}^{\dagger} = \tilde{\mathbf{B}}^{\dagger}\mathbf{\Phi}^{\dagger}. \tag{6.62}$$

The orthogonal nature of the matrix $\mathbf{B}$ means that the transformation to this new basis constitutes a (multi-dimensional) rotation in 'basis space'. This rotation preserves the orthonormal nature of the angular basis, so that

$$\langle\lambda_{l_k,m}|\lambda_{l_j,m}\rangle = \langle l_k, m|l_j, m\rangle = \delta_{l_k,l_j}. \tag{6.63}$$

Here, as before, the bra-ket notation used by Lee & Saio (1990) has been adopted, so that

$$|\lambda_{l_j,m}\rangle \equiv (\mathbf{\Psi})_j = \sum_{k=0}^{\infty}(\tilde{\mathbf{B}})_{j,k}(\mathbf{\Phi})_k = \sum_{k=0}^{\infty}(\mathbf{B})_{k,j}|l_k, m\rangle \tag{6.64}$$

and

$$|\lambda_{n_j,m}\rangle \equiv (\mathbf{\Psi}^\dagger)_j = \sum_{k=0}^{\infty}(\tilde{\mathbf{B}}^\dagger)_{j,k}(\mathbf{\Phi}^\dagger)_k = \sum_{k=0}^{\infty}(\mathbf{B}^\dagger)_{k,j}|n_k, m\rangle \tag{6.65}$$

The significance of these new basis states $|\lambda_{l_j,m}\rangle$ is that they represent the set of angular normal modes for a rotating star, in analogy to the spherical harmonics in the non-rotating case. This is demonstrated in the following section.

6.5 The Rotational Basis States

Since the equation pairs represented by (6.47) and (6.48) are decoupled and independent, the amplitudes of all but the jth solution pair may be set identically to zero, so that for $k \neq j$, $(\mathbf{Z_1})_k = (\mathbf{Z_2})_k = 0$. This corresponds to considering the excitation of a single pulsation mode of the given m and l_j, and it is therefore apparent that the solutions of the decoupled equations form the normal mode set of rotating stars. From an inspection of equations (6.58) and (6.59), it can now be seen that the angular dependence of the radial displacement ξ_r and pressure perturbation p, for a given normal mode, will be described by a single angular function $|\lambda_{l_j,m}\rangle$.

However, this turns out not to be the case for the horizontal and toroidal displacements, since the transformed horizontal and toroidal vector functions $\mathbf{Z_3}$ and $\mathbf{Z_4}$ are rotated with respect to $\mathbf{Z_2}$ via equations (6.56) and (6.57) respectively. Even in the case described above, where all but one element of $\mathbf{Z_2}$ is set to zero, these functions are given by

$$\mathbf{Z_3} = \mathbf{h_j}\frac{(\mathbf{Z_2})_j}{c_1\omega_c^2}, \qquad \mathbf{Z_4} = \mathbf{t_j}\frac{(\mathbf{Z_2})_j}{c_1\omega_c^2}, \tag{6.66}$$

where the two vectors $\mathbf{h_j}$ and $\mathbf{t_j}$, given by

$$(\mathbf{h_j})_i = (\tilde{\mathbf{B}}\mathbf{\Lambda}^{-1}\mathbf{W}\mathbf{B})_{i,j} \tag{6.67}$$

and

$$(\mathbf{t_j})_i = (\tilde{\mathbf{B}}^\dagger\mathbf{L_1}^{-1}\mathbf{M_+}\mathbf{\Lambda}^{-1}\mathbf{W}\mathbf{B})_{i,j}, \tag{6.68}$$

do not share the same sparse form as $\mathbf{Z_2}$. Consequently, the angular dependence of the horizontal and toroidal displacements cannot be described by a single $|\lambda_{l_j,m}\rangle$ function, but instead depend on sums of these functions through the scalar products appearing in equation (6.58).

Whilst the behaviour of the vector functions $\mathbf{Z_1}$, $\mathbf{Z_2}$, $\mathbf{Z_3}$ and $\mathbf{Z_4}$ throughout the stellar interior is of interest in the consideration of pulsation driving mechanisms and similar issues, it is the manner in which rotation modifies pulsation *at the stellar surface* which is of primary importance from an observational standpoint. Accordingly, the following subsections use the boundary conditions developed in Chapter 3 to find expressions for the displacement and pressure perturbations at the stellar surface, and use this context to highlight $|\lambda_{l_j,m}\rangle$ as an angular basis function for pulsation in rotating stars; two new basis functions $|\eta_{l_j,m}\rangle$ and $|\tau_{l_j,m}\rangle$ are also introduced, to handle the complications in the angular dependence of the horizontal and toroidal displacements discussed above.

6.5.1 The $|\lambda_{l_j,m}\rangle$ Angular Basis Functions

Following Lee & Saio (1990), at the surface of the star the Z-boundary (see §3.2) may be used to find an expression for $(\mathbf{Z_2})_j$ in terms of $(\mathbf{Z_1})_j$; although the Δ-boundary or the Υ-boundary are probably more accurate in the case of systems with low surface values of V, the following discussion is somewhat simplified if the Z-boundary is used, and it is relatively straightforward to generalize the results presented to more realistic boundary conditions. With the Z-boundary then, the dependent variables at the stellar surface are related by

$$(\mathbf{Z_1})_j - (\mathbf{Z_2})_j = 0. \tag{6.69}$$

This expression may be used to eliminate all terms in $(\mathbf{Z_2})_j$ from expressions for the displacement and pressure perturbations at the surface of the star, so that, for a pulsation mode associated with m and l_j, these quantities are given by

$$\frac{\boldsymbol{\xi}(\theta,\phi,t)}{R} = A\Re\left\{\left[|\lambda_{l_j,m}\rangle \mathbf{e}_r + \frac{1}{\omega_c^2}\left(\nabla_h \sum_{k=1}^{\infty}(\mathbf{h_j})_k|\lambda_{l_k,m}\rangle + \nabla_h \times \sum_{k=1}^{\infty}(-\mathbf{it_j})_k|\lambda_{n_k,m}\rangle \mathbf{e}_r\right)\right]\exp(\mathrm{i}\sigma_c t)\right\} \tag{6.70}$$

and

$$\frac{p'(\theta,\phi,t)}{\rho g R} = A\Re\left[|\lambda_{l_j,m}\rangle \exp(\mathrm{i}\sigma_c t)\right], \tag{6.71}$$

where A is the (arbitrary) value of $(\mathbf{Z_1})_j$ at this boundary. These two expressions demonstrate that, at least for radial displacements and pressure perturbations, the functions $|\lambda_{l_j,m}\rangle$ actually represent the normal mode set of angular functions for a rotating star (within the traditional and Cowling approximations). This is, indeed, why ST is so useful, since it not only decouples the rotationally-modified pulsation equations to permit numerical tractability, but also, and perhaps more importantly, allows the calculation of the angular dependence of pulsation variables at the surface of the star, vital for the understanding and modelling of stellar variability.

As demonstrated in the previous subsection, the horizontal and toroidal displacement functions are not proportional to individual $|\lambda_{l_j,m}\rangle$ functions, although they can be expressed as summations of $|\lambda_{l_k,m}\rangle$ over $k \geq 1$; however, these summations are computationally expensive (of order N^2 operations) and mathematically inelegant, and accordingly, the following subsection introduces new horizontal and toroidal angular basis functions, the use of which solves both of these problems.

For the sake of completeness, the remainder of this subsection is concerned with a discussion of the mechanical boundary condition applicable at the stellar origin. This is easily shown to be given by

$$c_1 \omega^2 (\mathbf{Y_1})_j - \tilde{l}_j (\mathbf{Z_2})_j = 0. \tag{6.72}$$

The constant $\tilde{l}_j$ is the rotationally-modified equivalent of l, in much the same way that $\lambda_{l_j,m}$ corresponds to $\Lambda(l)$ in a rotating star; it is given by

$$\tilde{l}_j = \frac{-5 \pm \sqrt{1 + 4\lambda_{l_j,m}}}{2}. \tag{6.73}$$

Since $x(\mathbf{Z_1})_j \equiv \xi_r$ varies as $x^{\tilde{l}_j - 1}$ near the core (§3.2), physically realistic solutions only exist for $\tilde{l}_j \geq 1$; thus, $\lambda_{l_j,m}$ must exceed 2. However, as will be demonstrated in §6.6, there exist regions in ν-space where $\lambda_{l_j,m} < 2$ (indeed, for some values of ν, $\lambda_{l_j,m}$ is negative). This difficulty arises due to a breakdown of the traditional approximation in the core regions, where the assumptions made in the formulation of the approximation become invalid, highlighting one of the main limitations in ST. Even in such cases, however, the results still retain some degree of validity for the purposes of calculating eigenfrequencies and the surface morphology of pulsation modes (Lee & Saio 1989).

6.5.2 The $|\eta_{l_j,m}\rangle$ and $|\tau_{l_j,m}\rangle$ Angular Basis Functions

Since the angular basis function $|\lambda_{l_k,m}\rangle$ in equation (6.70) is itself constructed from summations of spherical harmonics, the calculation of the horizontal and toroidal functions involves two *nested* summations, which is both mathematically unnecessary and computationally expensive. Therefore, it is useful to introduce two new angular basis functions, defined by

$$|\eta_{l_j,m}\rangle \equiv \sum_{k=1}^{\infty} (\mathbf{h_j})_k |\lambda_{l_k,m}\rangle = (\tilde{\mathbf{Q}}\mathbf{\Phi})_j \tag{6.74}$$

and

$$|\tau_{l_j,m}\rangle \equiv \sum_{k=1}^{\infty} (\mathbf{t_j})_k |\lambda_{n_k,m}\rangle = (\tilde{\mathbf{R}}\mathbf{\Phi}^\dagger)_j, \tag{6.75}$$

which complement $|\lambda_{l_j,m}\rangle$. The two matrices $\mathbf{Q}$ and $\mathbf{R}$ are the horizontal and toroidal equivalents of the transformation matrix $\mathbf{B}$; expressions for them may be found by using equations (6.67)

and (6.68) to eliminate $\mathbf{h_j}$ and $\mathbf{t_j}$ from the above identities, giving

$$\tilde{\mathbf{Q}}\mathbf{\Phi} = \tilde{\mathbf{B}}\mathbf{W}\mathbf{\Lambda}^{-1}\mathbf{B}\mathbf{\Psi} \tag{6.76}$$

and

$$\tilde{\mathbf{R}}\mathbf{\Phi}^{\dagger} = \tilde{\mathbf{B}}\mathbf{W}\mathbf{\Lambda}^{-1}\tilde{\mathbf{M}}_{+}^{\dagger}\mathbf{L_1}^{-1}\mathbf{B}^{\dagger}\mathbf{\Psi}^{\dagger}. \tag{6.77}$$

Using equations (6.61) and (6.62) to write $\mathbf{\Psi}$ and $\mathbf{\Psi}^{\dagger}$ in terms of $\mathbf{\Phi}$ and $\mathbf{\Phi}^{\dagger}$ respectively, these expressions become

$$\tilde{\mathbf{Q}} = \mathbf{D}\tilde{\mathbf{B}}\mathbf{\Lambda}^{-1} \tag{6.78}$$

and

$$\tilde{\mathbf{R}} = \mathbf{D}\tilde{\mathbf{B}}\mathbf{\Lambda}^{-1}\tilde{\mathbf{M}}_{+}\mathbf{L_1}^{-1}, \tag{6.79}$$

where equation (6.46) has been used to eliminate $\mathbf{W}$. A significant point about the second of these expressions is that it does not involve any terms in $\mathbf{B}^{\dagger}$. Thus, calculation of the toroidal basis functions $|\tau_{l_j,m}\rangle$ for a given m and parity may be accomplished without reference to any matrices belonging to the opposite parity, much simplifying the treatment. After somewhat lengthy but straightforward algebra, the elements of the transformation matrix $\mathbf{Q}$ are found to be

$$(\mathbf{Q})_{j,k} = \frac{\lambda_{l_j,m}}{\Lambda(l_k)}(\mathbf{B})_{k,j}, \tag{6.80}$$

whilst those of $\mathbf{R}$ are found to be

$$(\mathbf{R})_{j,k} = \frac{\nu\lambda_{l_j,m}}{1 - m\nu/\Lambda(n_k)}\left[\frac{J^m_{n_k}}{n_k^2}(\mathbf{B})_{k,j} + \frac{J^m_{n_k+1}}{(n_k+1)^2}(\mathbf{B})_{k+1,j}\right] \tag{6.81}$$

for even-π modes, and

$$(\mathbf{R})_{j,k} = \frac{\nu\lambda_{l_j,m}}{1 - m\nu/\Lambda(n_k)}\left[\frac{J^m_{n_k+1}}{(n_k+1)^2}(\mathbf{B})_{k,j} + \frac{J^m_{n_k}}{n_k^2}(\mathbf{B})_{k-1,j}\right] \tag{6.82}$$

for odd-π modes. With the new horizontal and toroidal basis functions so defined, the displacement at the stellar surface may now be written

$$\frac{\boldsymbol{\xi}(\theta,\phi,t)}{R} = A\Re\left\{|\lambda_{l_j,m}\rangle\mathbf{e}_r + \frac{1}{\omega_c^2}\left[\nabla_h|\eta_{l_j,m}\rangle - \mathrm{i}\nabla_h \times |\tau_{l_j,m}\rangle\mathbf{e}_r\right]\exp(\mathrm{i}\sigma_c t)\right\}, \tag{6.83}$$

which is a somewhat more elegant form than that given in equation (6.70), from both a theoretical and computational standpoint, since it obviates the need to perform two nested summations in constructing the horizontal and toroidal terms.

With the theoretical framework of ST laid down, it is pertinent to investigate the mathematical properties of the matrices and basis functions appearing throughout the treatment. This is undertaken in the following sections; in particular, §6.8 continues the discussion of the rotationally-modified angular basis states presented here.

6.6 Implementing the Similarity Transformation

As has been previously mentioned, the coupling between the equation pairs (6.41) and (6.42) is wholly encapsulated by the matrix $\mathbf{W}$. Within the theory, this matrix is of infinite dimension, as are all of the other matrices appearing in the treatment. For computational purposes, however, this infinite dimension must be truncated at some finite value N, so that any calculations can be performed in a reasonable amount of time. This dimension must be carefully chosen to be large enough so that the effects of truncation do not (significantly) distort results, whilst being small enough to retain computational efficiency. A standard, although heuristic, approach to achieving this goal is to calculate the necessary results with some given matrix dimension, and then repeat the exercise with double the dimension; if there is little significant change between the two calculations, then it is reasonable to assume that truncation at the dimension used is not introducing any serious inaccuracies. A discussion of the truncation effects which do remain is undertaken in §6.9. In the meantime, the values of N used in the following section are usually taken to be large (~ 100) when accuracy is required, and small (~ 3) when qualitative results are all that are needed.

Since expressions for the elements of the inverse matrix $\mathbf{W}^{-1}$ are available in closed form (Appendix C), it is more efficient to perform calculations with this inverse, hereinafter $\aleph$, than with the coupling matrix itself, thus obviating the need for any (possibly time-consuming and inaccurate) matrix inversions. This procedure does not introduce any unwanted complications to the theory, since

$$\mathbf{W}^{-1} \equiv \aleph = \mathbf{B}\mathbf{D}^{-1}\tilde{\mathbf{B}} \tag{6.84}$$

(compare with equation (6.46)), so that $\aleph$ shares the same set of eigenvectors as $\mathbf{W}$, and has eigenvalues reciprocal to those of $\mathbf{W}$; indeed, by performing all calculations using $\aleph$, not even a single matrix need be inverted throughout (here, it is noted that a matrix inversion has an operation count of order N^3 (Press *et al.* 1992), and thus is quite computationally expensive).

As is demonstrated in Appendix C, $\aleph$ is symmetric and tridiagonal. These properties are ones which lend themselves very well to numerical manipulation and efficient diagonalization; much work has already been performed on tridiagonal matrices due to their relatively common occurrence in the treatment of coupled oscillator problems. Parlett (1980) has given a comprehensive treatment of symmetric eigenvalue problems, and discusses many of the useful properties which symmetric tridiagonal matrices possess. One of the most salient features of these matrices is that, barring trivial diagonal cases, they are the easiest of all matrix morphologies to diagonalize. The method of choice to perform this diagonalization is the iterative QL algorithm, so-named due to the mathematical symbols traditionally used in its implementation. This algorithm is not especially useful for a general matrix type, but turns out to be highly efficient (of order N per iteration) for tridiagonal matrices — in all but the most ill-behaved cases, the convergence rate is generally cubic.

Furthermore, the algorithm is guaranteed to converge for matrices whose off-diagonal elements are all non-zero, the so-called un-reduced matrices (Parlett 1980). There are a number of ways in which the *QL* algorithm may be implemented; the method used herein is the *Numerical Recipes* (Press *et al.* 1992) implementation of the implicit-shift *QL* algorithm discussed by Parlett (1980), which can find all eigenvalues and (orthonormal) eigenvectors of a symmetric tridiagonal matrix with a total operation count of order N^3.

The implementation presented by Press *et al.* (1992) returns an array of N eigenvalues $\lambda^{-1}_{l_j,m}$, accompanied by the corresponding eigenvector matrix $\mathbf{B}$. However, there is no way of telling which eigenvalues in the array are associated with which values of j ($1 \leq j \leq N$). Accordingly, a procedure must be derived by which to perform this identification. The derivation begins by noting that the eigenvalues of $\aleph$ are distinct; to see this, consider the N-dimensional parametric matrix $\mathbf{X}(\lambda) = (\aleph - \lambda\mathbf{I})$, where $\mathbf{I}$ is the identity matrix of dimension N and λ is a scalar variable. The rank $\mathcal{R}$ of $\mathbf{X}(\lambda)$ is, by definition, at least $(N-1)$, since the first $(N-1)$ columns of $\mathbf{X}(\lambda)$ form a set of N-dimensional linearly-independent vectors. This rank is subject to the restriction that

$$\mathcal{R} + \mathcal{N} = N \tag{6.85}$$

(Parlett 1980), where the nullity $\mathcal{N}$ is the multiplicity of vectors $\mathbf{x}$, excluding the null vector $\mathbf{0}$, which satisfy the requirement

$$\mathbf{X}(\lambda)\mathbf{x} = \mathbf{0}; \tag{6.86}$$

these vectors are said to span the null space of $\mathbf{X}(\lambda)$. The restriction (6.85), and the fact that $\mathcal{R} \geq N-1$, means that $\mathcal{N}$ can only assume the values zero or one; since equation (6.86) is the eigenequation associated with $\aleph$, it can therefore be seen that, when λ is an eigenvalue of $\aleph$, there can be at most one eigenvector $\mathbf{x}$ which satisfies this equation. Thus, the eigenvalues of $\aleph$ must be distinct. However, as Parlett (1980) stresses, they may be very close together for certain matrices, and it is found that, for certain values of m and ν, $\aleph$ is one such case.

Continuing with the discussion, it can be observed that, in the non-rotating case ($\nu = 0$), $\aleph$ is already diagonal, and has eigenvalues given by

$$(\aleph)_{j,j} = 1/\Lambda(l_j). \tag{6.87}$$

This can be seen either from inspection of the expressions given Appendix C, or just from consideration of the correspondence between $\lambda_{l_j,m}$ and $\Lambda(l_j)$. Accordingly, in the non-rotating case, the eigenvalues of $\aleph$ have a well defined positive-to-negative ordering of $j = 1, 2, 3, \ldots, N-1, N$. As ν is moved monotonically away from zero (in either the positive or negative direction), the fact that the eigenvalues are distinct means that no two eigenvalue curves may intersect, at any value of ν. Thus, the only mechanism by which this zero-rotation positive-to-negative ordering may be altered is when there is a singularity in the behaviour of an eigenvalue with respect to ν.

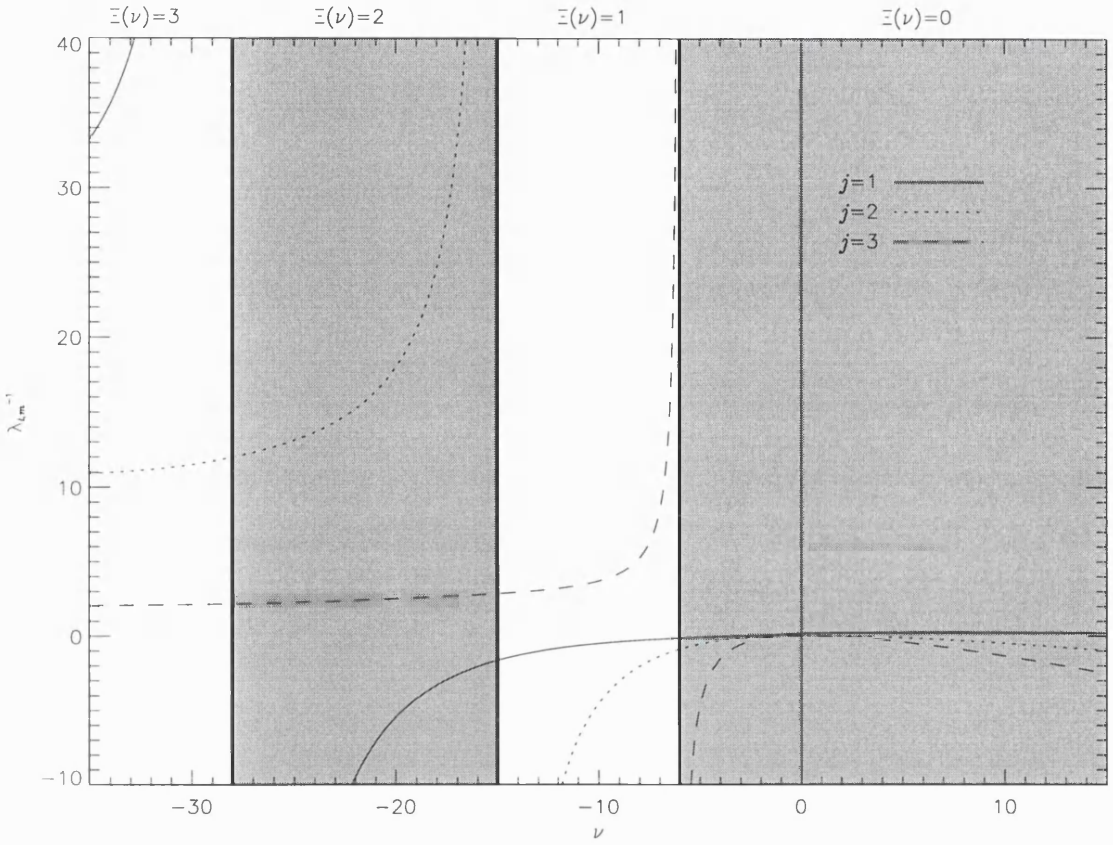

Figure 6.2: The eigenvalues $\lambda^{-1}_{l_j,m}$ of the $m = -2$, even-π coupling matrix of dimension 3, plotted as a function of ν. The $j = 1, \ldots, 3$ eigenvalues are shown, and zones of differing $\Xi(\nu)$ (see text) are marked with alternate shading. The $\lambda^{-1}_{l_j,m} = 0$ axis has been omitted for clarity.

These singularities can arise when $m\nu = \Lambda(n_j)$ for some value of j ($1 \leq j \leq N$), since one of the two denominators of the function $F(l_j)$ (Appendix C) passes through zero. In such cases, the elements $(\aleph)_{j,j}$, $(\aleph)_{j,j\pm1}$, $(\aleph)_{j\pm1,j}$ and $(\aleph)_{j\pm1,j\pm1}$ exhibit poles for even (+) and odd (−) parity matrices. These poles cause the most negative eigenvalues to tend to $-\infty$ as ν approaches the singular points $\nu_-^{l_j}$ (different for each l_j and m) from $|\nu| < |\nu_-^{l_j}|$. For $|\nu| > |\nu_-^{l_j}|$, the same eigenvalue becomes the most positive, and it can be observed that the passage of ν through the singular point $\nu_-^{l_j}$ has permuted the positive-to-negative ordering of the eigenvalues cyclically once. Note that the other eigenvalues are generally unaffected by these singularities in the elements of $\aleph$. For even-π matrices there exist N singular points $\nu_-^{l_j}$ for all ν, whilst for odd-π matrices there exist $N + 1$ such points.

It is now apparent that the identification of which QL-eigenvalue corresponds to which value of j is quite straightforward. Let $\Xi(\nu')$ represent the number of singular points $\nu_-^{l_j}$ falling between

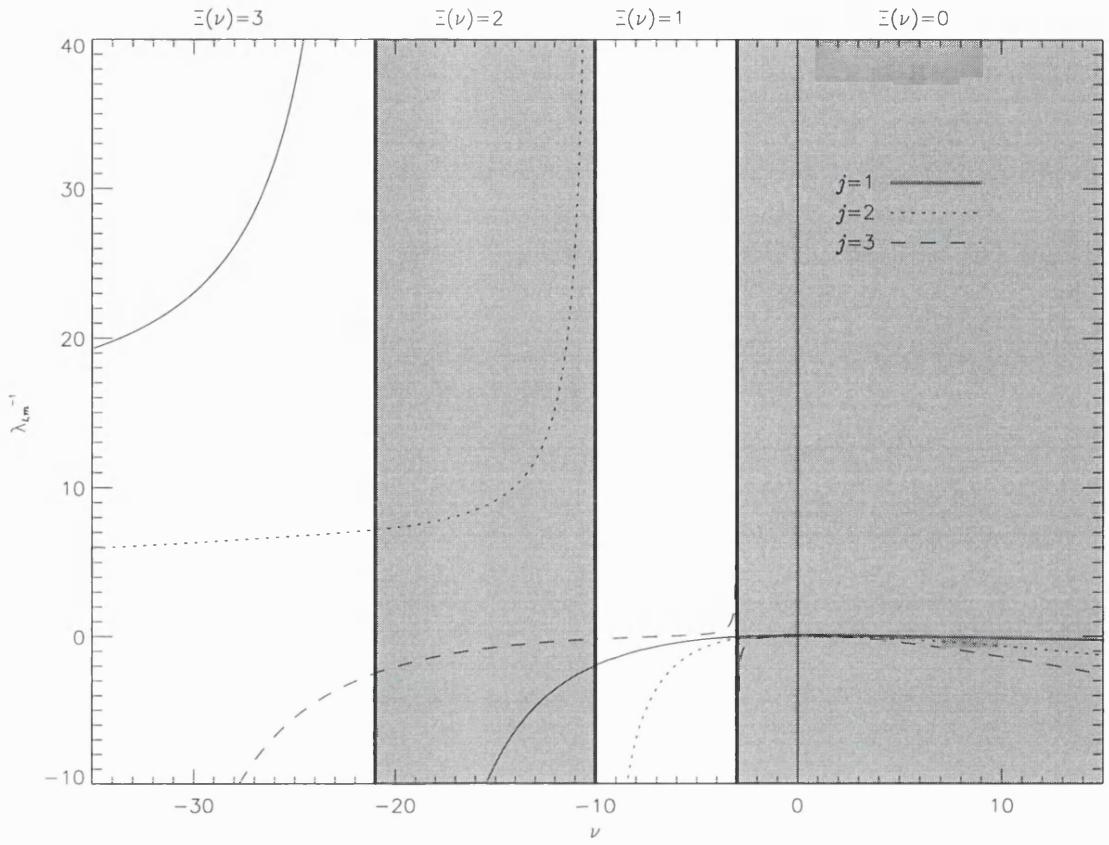

Figure 6.2 (cont): As before, except that the corresponding odd-π eigenvalues are plotted.

$\nu = \nu'$ and $\nu = 0$; then the positive-to-negative ordering of the QL-eigenvalues at $\nu = \nu'$ is given by the sequence $j = 1, 2, 3, \ldots, N-1, N$ permuted $\Xi(\nu')$ times *to the right* (so that $j = 1, 2, 3, \ldots, N-1, N \rightarrow j = N, 1, 2, \ldots, N-2, N-1$, and so on). Given a full set of eigenvalues for known m and ν, calculating $\Xi(\nu)$ is trivial, and correct values of j may be assigned to each of the QL-eigenvalues (and their corresponding eigenvectors). This procedure is illustrated by figure 6.2, which plots the eigenvalues of the $m = -2$ matrix $\aleph$ (both parities) as a function of ν for a dimension of 3; zones of differing $\Xi(\nu)$ are labelled and alternately shaded, and thick vertical lines mark the singular points $\nu_-^{l_j}$. It is apparent that adjacent zones have eigenvalue orderings which differ by a single cyclic permutation, and so the procedure used to label the QL-eigenvalues is demonstrated to work. Since the points $\nu_-^{l_j}$ occur at $m\nu = \Lambda(n_j)$, these singularities only arise for positive $m\nu$, and hence the figure primarily displays the negative region of the ν axis.

6.7 Rotationally-modified Wave Propagation

As was mentioned in §6.4, the pulsation equations within the traditional approximation are identical to those for non-rotating stars, save that the term in $\Lambda(l)$ is replaced by the eigenvalue $\lambda_{l_j,m}$.

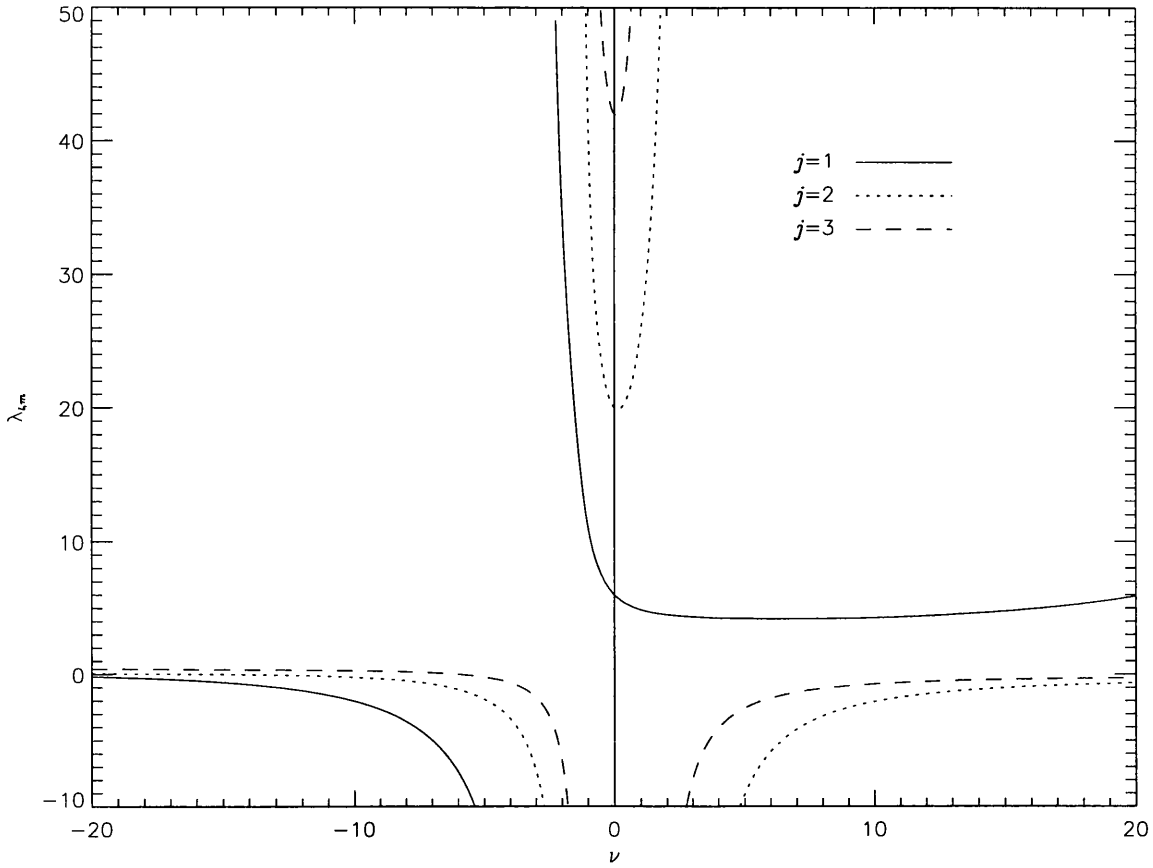

Figure 6.3: The eigenvalues $\lambda_{l_j,m}$ of the $m = -2$, even-π coupling matrix of dimension 3, plotted as a function of ν. Again, the $\lambda_{l_j,m} = 0$ axis has been omitted for clarity.

Thus, it is possible to look into the qualitative effects of rotation on pulsation, in particular on the pulsation eigenfrequencies, by examining in what way $\lambda_{l_j,m}$ differs from $\Lambda(l)$ for various values of the parameter ν. Figure 6.3 shows a plot of $\lambda_{l_j,m}$ as a function of ν for the $m = -2$, $N = 3$ coupling matrix; note that in this figure, the eigenvalues of $\mathbf{W}$ rather than those of $\aleph$ are shown, and so this figure is essentially the reciprocal of figure 6.2.

Inspection of the eigenvalues over the negative cut of the ν axis shows that, beginning at $\nu = 0$, they all initially diverge to infinity as ν becomes more negative, and consequently change sign at some value of ν, hereafter denoted $\nu^-_{l_j}$ (different for each value of l_j and m); these points correspond to the $\lambda^{-1}_{l_j,m} = 0$ axis-crossings in figure 6.2. Unlike the $\nu^{l_j}_-$ singularities of the $\aleph$ matrix discussed previously, however, there do not exist analytical expressions for $\nu^-_{l_j}$, although they can be represented by the equation $\det(\aleph) = 0$. After the eigenvalue sign changes, all eigenvalues steadily increase with progressively more negative ν, and eventually cross the $\lambda_{l_j,m} = 0$ axis at $\nu = \nu^{l_j}_-$ to become positive again (this can be seen for the $j = 2$ and $j = 3$ modes, but occurs outside the figure for the $j = 1$ mode). In contrast, the eigenvalues show the same divergent behaviour at the $\nu^+_{l_j}$ points along the positive cut of the ν-axis (for the same reasons as before), but subsequently

never again cross the $\lambda_{l_j,m} = 0$ axis to become positive again; this is because, as discussed in the preceding section, the matrix singularities which give $\lambda^{-1}_{l_j,m} \to \infty$ only occur for $m\nu > 0$.

With the general behaviour of the eigenvalues as a function of ν so discussed, the following subsections look into how these changing eigenvalues modify the pulsation eigenfrequencies, and lead to the introduction of new types of pulsation which do not appear in non-rotating stars. The asymptotic technique presented in §5.2 is used throughout to obtain expressions for the eigenfrequencies; whilst for some modes these expressions may be somewhat in error, the simple forms obtained in this manner are useful for qualitative studies of the effects of rotation on pulsation.

6.7.1 Propagative Modes

With the replacement of the $\Lambda(l)$ term in the pulsation equations by $\lambda_{l_j,m}$, the co-rotating eigenfrequencies for a mode of radial order n will be given, for suitably large n, by the asymptotic expression

$$\sigma_c = \frac{\sqrt{\lambda_{l_j,m}}}{(2n + \eta_e)\pi/2} \int_{r_c}^{R} \frac{|N|}{r} dr \tag{6.88}$$

(Berthomieu *et al.* 1978; Lee & Saio 1989), which should be compared with equation (5.7). This expression was used to calculate eigenfrequencies as a function of ν for all modes with $l = 3$ and arbitrary (but fixed) values of n, η_e and the integral, chosen so that at $\nu = 0$, $\sigma_c = 1$; although in a rotating star, l is no longer a 'good' eigenvalue, it is still possible to label a mode with the value of l to which it corresponds to in the zero-rotation limit (Lee & Saio 1990). Modes of the same l but differing m were considered to allow investigation of the rotational m-dependent splitting discussed in §6.2. Figure 6.4 illustrates the eigenfrequencies calculated in this manner, plotted as a function of Ω as opposed to ν, since the former is the more physically significant parameter; the scaling of Ω is arbitrary, but chosen to be the same as that of σ_c. Contours of constant ν are plotted as dotted lines, spaced at intervals of 0.1, and are labelled with their appropriate values at the top of the figure. This figure demonstrates that, for suitably small Ω ($\lesssim 0.03$), the rotational modifications to the pulsation frequency are proportional to m, in agreement with the PE expression found in §6.2. For larger values of Ω, however, the modifications depart from this linear behaviour, such that as $\Omega \to \infty$, $\sigma_c \to \infty$. This departure appears to be most severe for the modes with small $|m|$; those with $m = \pm l$ remain more or less linear over the region plotted.

The sign changes in $\lambda_{l_j,m}$ discussed previously mean that real eigenfrequencies only exist for $|\nu| < |\nu^{\pm}_{l_j}|$. Accordingly, one consequence of rotation is the existence of a low-frequency cutoff for g-modes, such that all prograde propagative modes must satisfy

$$|\sigma_c| > 2\Omega/|\nu^{\pm}_{l_j}|, \tag{6.89}$$

for all n. Although equation (6.88) suggests that, as $n \to \infty$, the pulsation frequency will tend to zero, this does not in fact occur, because $\lambda_{l_j,m}$ becomes correspondingly large as $\nu \to \nu^{+}_{l_j}$. Fig-

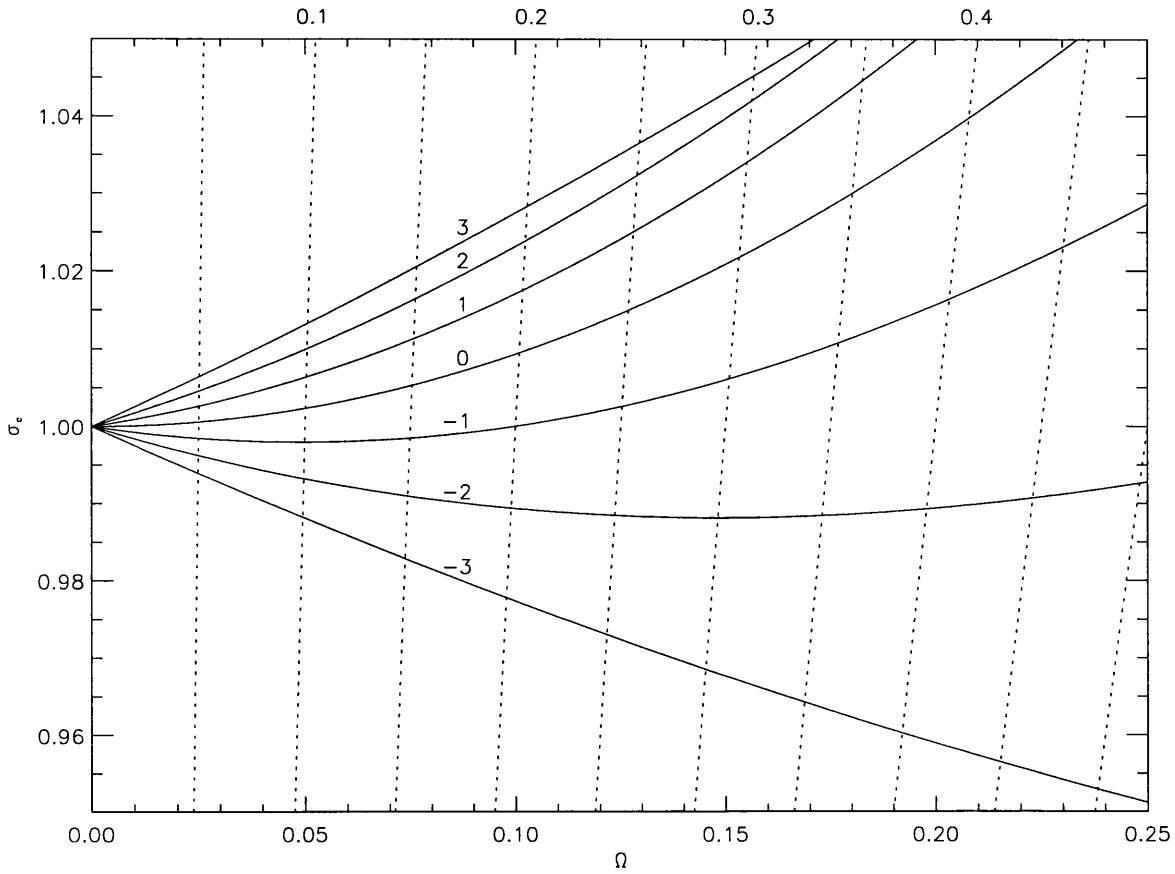

Figure 6.4: The eigenfrequencies σ_c plotted as a function of rotation rate Ω for $l = 3$ and $m = 3, 2, \ldots, -2, -3$ modes, and labelled with the appropriate values of m. The dotted lines mark contours of constant ν and are labelled at the top. Note the linear splitting proportional to m at small Ω.

ure 6.5 illustrates this cutoff frequency for prograde $m = -2$, $l = 2, 4$ modes; σ_c is plotted as a function of Ω, with $n = 2, 6$ for each value of l. The two cutoff asymptotes represented by $\nu = \nu_2^+$ and $\nu = \nu_4^+$ are marked as dotted and dashed lines respectively, and an effective polytropic index $\eta_e = 3.0$ was adopted; as before, the scaling of the frequencies is arbitrary. It is evident that, whilst modes of the same l have eigenfrequencies which never intersect, modes with differing l can undergo an 'accidental' eigenfrequency degeneracy; however, Lee & Saio (1989) have demonstrated that this degeneracy is actually an artifact of the traditional approximation, and when the full set of coupled equations are solved, the eigenfrequencies exhibit an avoided crossing (see §5.4.2). The Ω–σ_c diagram for retrograde modes ($\nu < 0$ for $m < 0$) is essentially similar to that for prograde modes (although the $\nu = \nu_{l_j}^-$ asymptotes fall in different places to the $\nu_{l_j}^+$ ones), and so does not require discussion here.

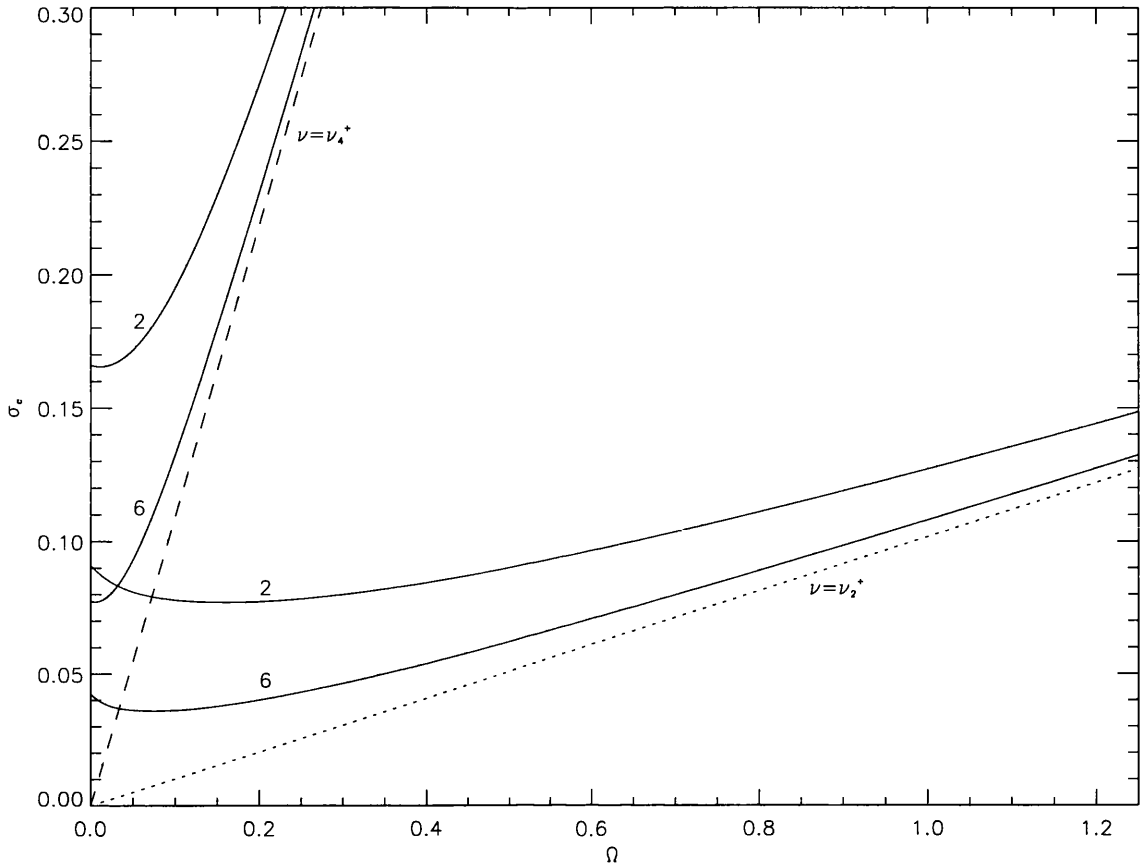

Figure 6.5: The eigenfrequencies σ_c of $m = -2$, $l = 2, 4$ prograde propagative modes as a function of rotation angular frequency Ω; for each value of l, the $n = 2, 6$ modes are plotted. The dotted and dashed lines represent the asymptotes $\nu = \nu_2^+$ and $\nu = \nu_4^+$ respectively, corresponding to the low-frequency cutoff boundaries for $l = 2$ and $l = 4$.

6.7.2 Convective Modes

Whilst no propagative pulsation modes in the normal sense can exist below the cutoff frequency, as explained above, the coriolis force due to rotation can serve to stabilize convection in regions where $N^2 < 0$. This dynamical stability supplies the necessary restoring force for pulsation modes to exist in regions which would be convectively unstable (and thus evanescent towards pulsation) in a non-rotating star; these modes are termed convective or inertial (Lee & Saio 1987*a*; Lee *et al.* 1992*b*) (strictly, inertial modes are ones in convectively-neutral media, but convective modes can be considered the generalization of inertial modes to cases where N^2 is non-zero). Whilst a proper treatment of convective (in)stability in rotating stars (*e.g.*, Sobouti 1975), or, indeed, rotation-convection coupling (*e.g.*, Gabriel *et al.* 1975; Gonczi & Osaki 1980; Stellingwerf 1982*a*; Stellingwerf 1982*b*; Stellingwerf 1984*a*; Stellingwerf 1984*b*; Stellingwerf 1984*c*), is beyond the scope of this work, it is still possible to apply a basic treatment to the subject to obtain insights on

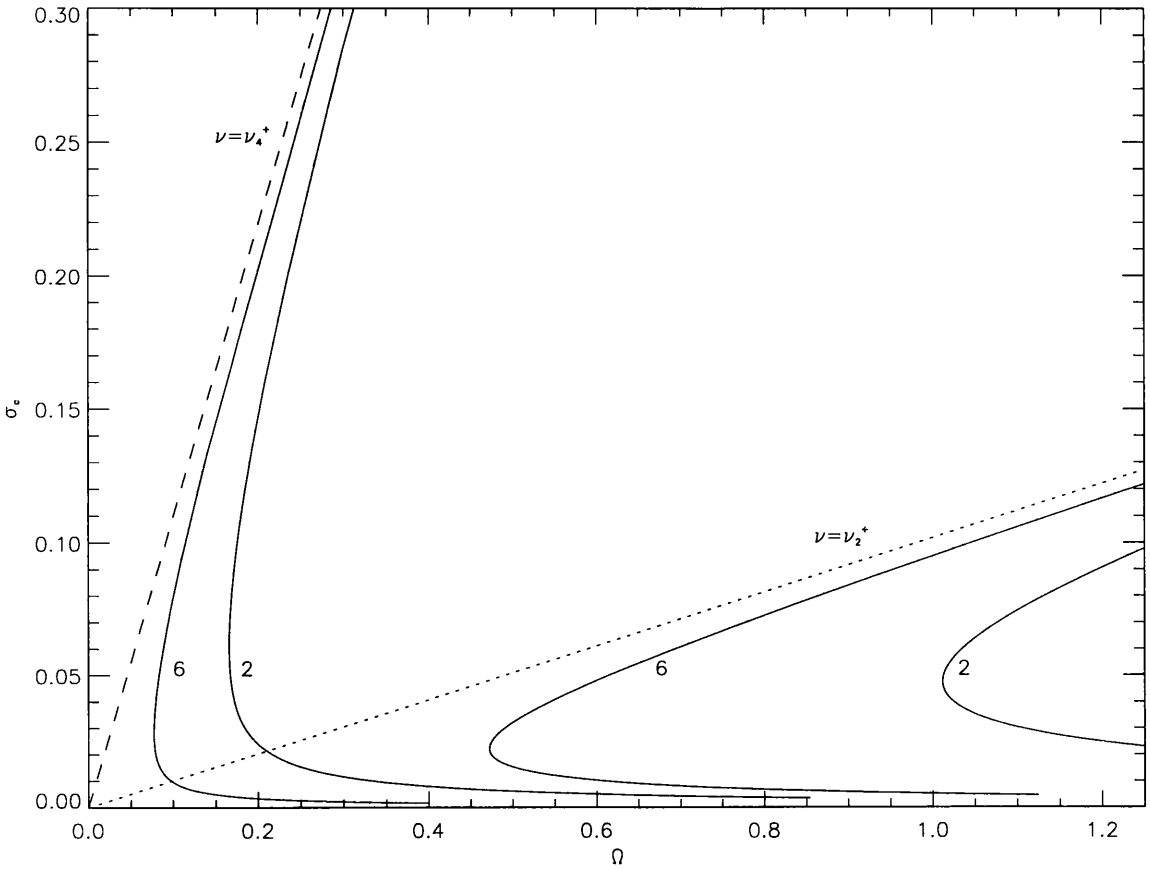

Figure 6.6: As for Fig 6.5, except the eigenfrequencies σ_c of prograde *convective* modes are now plotted against rotation angular velocity Ω.

how it arises. Appendix D presents the equations of motion for a fluid parcel in a rotating, stratified medium at the most basic level, and demonstrates that for $\Omega^2 > -N^2$ oscillatory solutions exist in which the fluid parcel moves in planar elliptical orbits perpendicular to the rotation axis.

For a somewhat more quantitative investigation of these convective modes, the approach used in the preceding subsection may be used to calculate eigenfrequencies below the low-frequency cutoff associated with prograde propagative modes. Lee & Saio (1987*a*) demonstrated that, for convective modes, equation (6.88) is rewritten in the form

$$\sigma_c = \frac{1}{(2n+\varsigma)\pi/2} \int_0^{r_c} \frac{\sqrt{\lambda_{l_j,m} N^2}}{r} dr, \tag{6.90}$$

where ς is an arbitrary constant to be found from the full matrix treatment. This expression leads to real eigenfrequencies if $|\nu| > |\nu_{l_j}^{\pm}|$ (since $\lambda_{l_j,m}$ is then negative) and $N^2 < 0$; as was pointed out in §6.5.1, though, it is not strictly valid, since the core boundary condition presented in §3.2 breaks down for $\lambda_{l_j,m} < 2$. However, Lee & Saio (1987*a*) managed to reproduce results found without the traditional approximation using this expression, with a suitable choice of ς, and thus demonstrated

that, whilst it is not correct in the mathematical sense, the above expression for the eigenfrequencies of convective modes may still give useful results. In analogy to figure 6.5, figure 6.6 illustrates the behaviour of prograde convective-mode eigenfrequencies calculated in this manner, plotted as a function of Ω. The same l and m have been used, so that the asymptotic lines are again represented by $\nu = \nu_2^+$ and $\nu = \nu_4^+$, and ς has been set equal to the previously-used value of η_e. It is evident that, as $\nu \to \infty$, the eigenfrequencies of all prograde convective modes approach zero asymptotically, so rotation not only stabilizes convection and leads to convective modes, but also, when rapid enough, completely 'freezes' any form of radial motion whatsoever in convective zones.

Osaki (1974) has suggested that overstable pulsation in rotationally-stabilized semi-convective zones may be responsible for the variability observed in rotating early-type stars. This proposed overstability arises as a subset of the δ-mechanism introduced in §5.5; the dynamical stability introduced to super-adiabatic zones by rotation will again lead to vibrational instability through radiative transfer between adjacent fluid parcels. Whilst this overstable pulsation will primarily be confined to the core boundary, it may be possible for these convective modes to couple with envelope modes of the same frequency, leading to an observable pulsation amplitude at the stellar surface. Lee & Saio (1986; 1987*b*) have performed a comprehensive mathematical treatment based on Osaki's (1974) mechanism, and found that it does indeed work. The coupling between convective modes and propagative envelope modes occurs when the propagative-mode eigenfrequencies (figure 6.5) undergo an avoided crossing with the convective-mode eigenfrequencies (figure 6.6); this intersection will obviously occur only between modes of differing l.

The importance of Osaki's (1974) mechanism is not to be underestimated. Since Kato's (1966) mechanism requires a molecular weight gradient to dynamically stabilize a super-adiabatic zone, it can only function in evolved stellar systems; Osaki's (1974) mechanism is not subject to this restriction, and only needs (sufficient) rotation to operate. Furthermore, since it depends on the rotational properties of the star at the core boundary, it may be used to infer information from surface observations concerning the internal rotation structure of the star (Lee 1988).

6.7.3 Quasi-toroidal Modes

Unlike normal propagative modes, the behaviour of the eigenfrequencies for retrograde convective modes is not quite the same as that for prograde modes. This is because, in the latter (prograde) case, $\lambda_{l_j,m}$ for any given mode approaches zero asymptotically once it has become negative, and never becomes positive again; in the former (retrograde) case, on the other hand, $\lambda_{l_j,m}$ actually passes through zero at the points $\nu = \nu_-^{l_j}$ discussed in §6.6 after becoming negative, and hence becomes positive again at suitably large ν (see figure 6.3). At these $\nu = \nu_-^{l_j}$ points, $\lambda_{l_j,m}$ is zero, as are the corresponding eigenfrequencies, and for $|\nu| > |\nu_-^{l_j}|$, the positive sign of $\lambda_{l_j,m}$ means that, whilst convective modes can no longer propagate, there will exist a new type of mode in the non-convective region of the rotating star. These new types are usually termed quasi-toroidal or Rossby

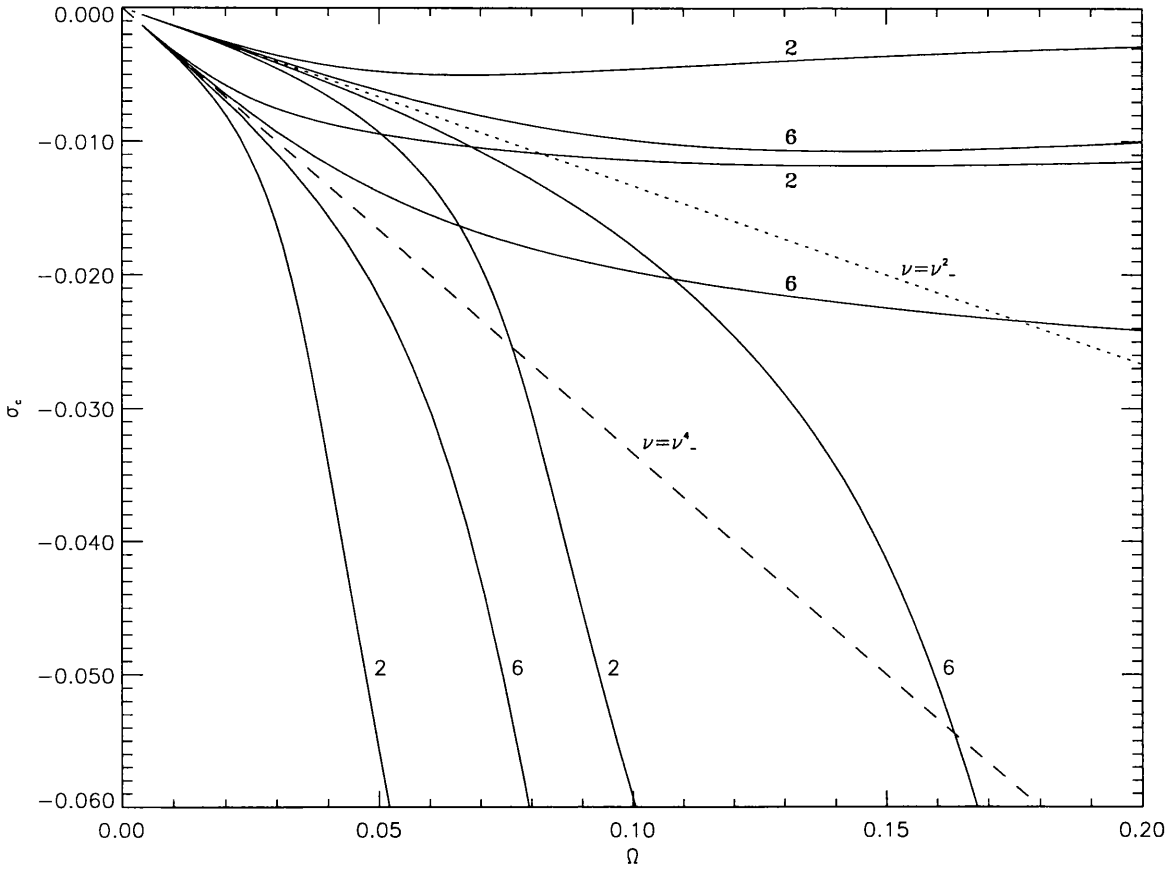

Figure 6.7: The eigenfrequencies σ_c of $m = -2$, $l = 2, 4$ retrograde convective (normal labels) and quasi-toroidal (boldface labels) modes as a function of rotation angular frequency Ω; for each value of l, the $n = 1, 2$ modes are plotted. The dotted and dashed lines represent the asymptotes $\nu = \nu_-^2$ and $\nu = \nu_-^4$ respectively, corresponding to the low-frequency quasi-toroidal modes for $l = 2$ and $l = 4$.

modes, since they are related to the Rossby waves found in the Earth's atmosphere (Eckart 1960). Figure 6.7 shows the eigenfrequencies of *retrograde* convective modes and quasi-toroidal modes, plotted as a function of Ω, for the mode parameters and matrix dimension adopted in figures 6.5 and 6.6; the asymptotic lines ν_-^2 (dotted) and ν_-^4 (dashed) represent the slow-rotation limits of the quasi-toroidal modes. Analytical expressions for the quasi-toroidal eigenfrequencies in these limits can be found by recalling that the singular points $\nu_-^{l_j}$ where $\lambda_{l_j,m} \to 0$ (and thus $\sigma_c \to 0$) are given by

$$m\nu_-^{l_j} = n_j(n_j + 1), \tag{6.91}$$

which may be solved for the eigenfrequency using $\nu \equiv 2\Omega/\sigma_c$ to give

$$\sigma_c = \frac{2m\Omega}{n_j(n_j + 1)}. \tag{6.92}$$

This linear dependence on Ω corresponds to the straight-line portion of the eigenfrequency curves, seen in the upper-left hand corner of figure 6.7. For large enough Ω, the quasi-toroidal eigenfrequencies depart from this linear behaviour, and generally decrease monotonically to zero as rotation completely stabilises the stellar material. Note that this slow-rotation expression is independent of n, so that the eigenfrequency of a quasi-toroidal mode is completely specified by l, m and Ω.

The corresponding displacement vector $\boldsymbol{\xi}$ for the low-frequency quasi-toroidal modes can be found at the stellar surface by considering equation (6.83) for small $\lambda_{l_j,m}$ and ω_c. The $1/\omega_c^2$ term preceding the horizontal and toroidal terms of equation (6.83) indicates that these terms will completely dominate the radial displacement ξ_r, and that for any reasonable choice of normalization A, $\xi_r = 0$. Furthermore, the horizontal basis function $|\eta_{l_j,m}\rangle$ is proportional to $\lambda_{l_j,m}$ (see equation (6.80)) and thus will be effectively zero, leaving just the toroidal basis function $|\tau_{l_j,m}\rangle$ to contribute to $\boldsymbol{\xi}$. Equations (6.81) and (6.82) show that the elements of the toroidal matrix $\mathbf{R}$ are proportional to $\lambda_{l_j,m}/[m\nu - \Lambda(n_k)]$, so that for $m\nu \to n_j(n_j+1)$ and $\lambda_{l_j,m} \to 0$,

$$(\mathbf{R})_{j,k} \to A'\delta_{j,k}, \tag{6.93}$$

where A' is some number and $\delta_{j,k}$ the usual Kronecker-delta. Hence, the toroidal basis function for these low-frequency modes will be proportional to a single spherical harmonic,

$$|\tau_{l_j,m}\rangle = A'|n_j, m\rangle, \tag{6.94}$$

and the displacement perturbation $\boldsymbol{\xi}$ at the stellar surface will have the form

$$\frac{\boldsymbol{\xi}(\theta,\phi}{R} = A''\left(0, -\frac{1}{\sin\theta}\frac{\partial}{\partial\phi}, \frac{\partial}{\partial\theta}\right) Y_{n_j}^m, \tag{6.95}$$

where A'' is a constant which sets the amplitude of the mode. This expression, and equation (6.92) for the eigenfrequencies, are in agreement with the first-order expressions found by Papaloizou & Pringle (1978) in their extensive treatment of quasi-toroidal modes in rotating white dwarf stars. It is evident that these quasi-toroidal modes are essentially time-dependent equivalents of the time-independent toroidal modes (steady eddies) found in non-rotating stars (see §2.8), hence the choice of nomenclature.

A physical explanation of the origin of quasi-toroidal modes is not quite as simple as that for convective modes. Essentially, they arise from the conservation of vorticity $\nabla \times \mathbf{v}$ in an inertial frame; this conservation requirement serves as the restoring force which leads to retrograde oscillatory eddies in a manner described well by Saio (1982). The question of whether quasi-toroidal modes can actually be excited in various types of stars has been raised by a number of authors (Papaloizou & Pringle 1978; Saio 1982; Berthomieu & Provost 1983; Strohmayer & Lee 1996). Saio (1982) found that the envelope opacity bump suggested by Stellingwerf (1978) as the mechanism for (spheroidal) pulsation in massive stars did not excite quasi-toroidal modes in 20 $M_\odot$ or

7 $M_\odot$ models, although Smith (1985) has reported observations of lpv in Spica (α Vir) consistent with an $l = 5, m = -4$ quasi-toroidal mode. However, the excitation in Spica probably occurs due to the binary nature of the system, and the debate concerning quasi-toroidal mode excitation in isolated systems continues.

With this brief discussion of the new wave types introduced by rotation completed, the following section returns to the rotationally-modified angular basis states $|\lambda_{l_j,m}\rangle$, $|\eta_{l_j,m}\rangle$ and $|\tau_{l_j,m}\rangle$ introduced in §6.5

6.8 Calculating the new Basis States

Once the matrix $\aleph$ has been diagonalized using the method presented in §6.6, the resulting eigenvector matrix $\mathbf{B}$ may be used to calculate the new basis states $|\lambda_{l_j,m}\rangle$, $|\eta_{l_j,m}\rangle$ and $|\tau_{l_j,m}\rangle$ through equations (6.64), (6.74) and (6.75). All of these calculations involve weighted summations over spherical harmonics of a given azimuthal order m and harmonic degree l_j with $1 \leq j \leq N$; the proportionality of the spherical harmonics to associated Legendre polynomials means that a suitable algorithm must be found by which to calculate the latter for the given values of l and m.

Press *et al.* (1992) present a useful discussion of the many ways in which associated Legendre polynomials may be calculated, stressing the pitfalls in some of the more obvious implementations. Their procedure of choice revolves around the *stable* recurrence relation for $P_l^m(z)$, namely

$$(l-m)P_l^m = z(2l-1)P_{l-1}^m - (l+m-1)P_{l-2}^m, \tag{6.96}$$

which is applicable for all $m > 0$. The recurrence is started using the identities

$$P_m^m = (-1)^m(2m-1)!!(1-z^2)^{m/2} \tag{6.97}$$

and

$$P_{m+1}^m = z(2m+1)P_m^m, \tag{6.98}$$

where the double factorial $n!!$ indicates the product of all odd, positive integers less than or equal to n. These expressions demonstrate that, serendipitously, the sequence of polynomials generated in this manner coincide with the set needed for the calculation of the basis functions. Note that polynomials with $m < 0$ are not required with the definition of the spherical harmonics used herein (see equation (2.29)).

Once the appropriate associated Legendre polynomials have been calculated for a given $z \equiv \cos\theta$, they may be used in equations (6.64), (6.74) and (6.75) to evaluate the basis functions at that colatitude θ. Figures 6.8, 6.9 and 6.10 show $|\lambda_{l_j,m}\rangle$ $|\eta_{l_j,m}\rangle$ and $|\tau_{l_j,m}\rangle$ respectively as functions of $\cos\theta$ and ν for all of the $l_j = 8$, $1 \leq -m \leq l$ pulsation modes, calculated using a matrix dimension

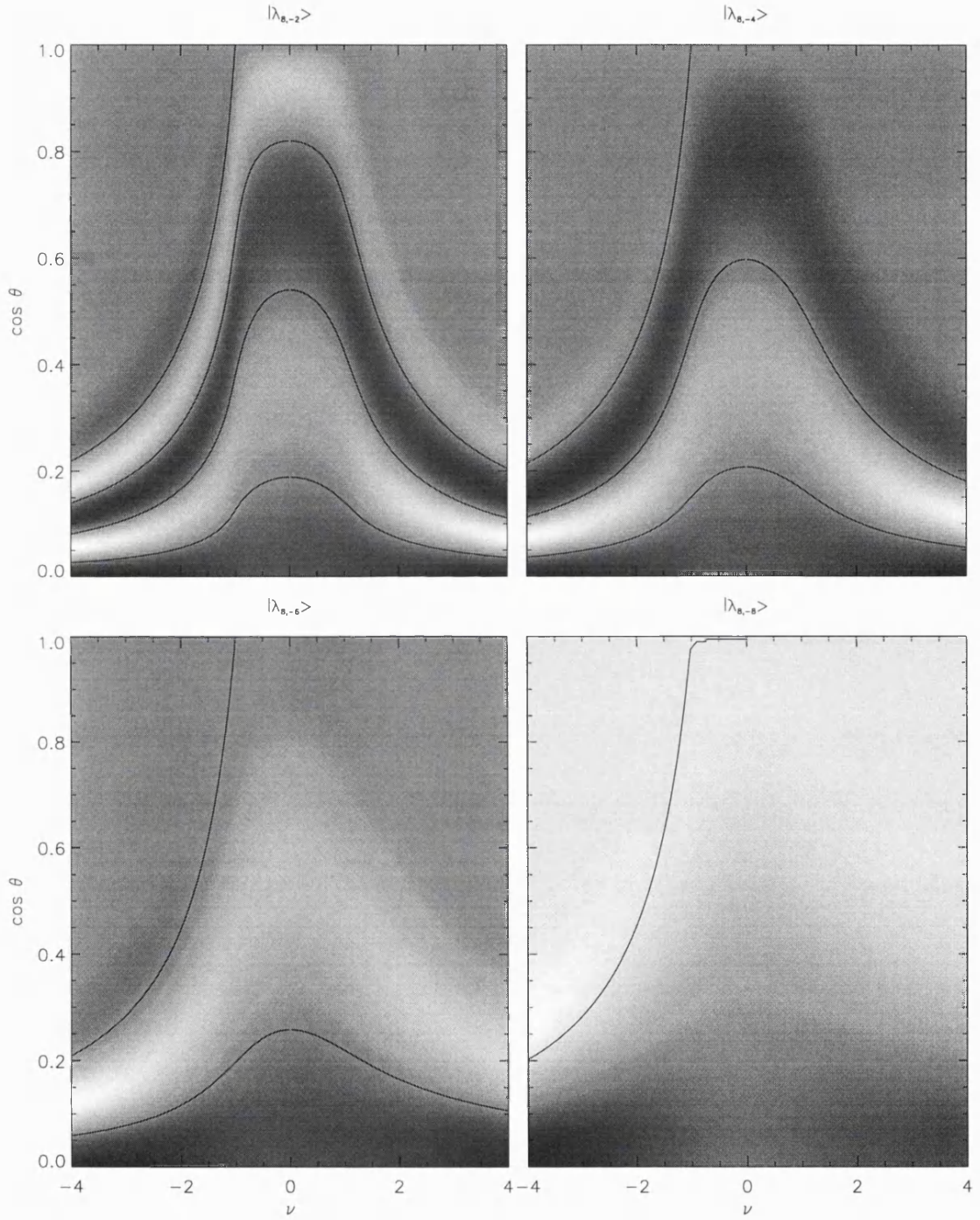

Figure 6.8: The radial basis states $|\lambda_{l_j,m}\rangle$ plotted as a function of $\cos\theta$ and $\nu \equiv 2\Omega/\sigma_c$ for the $l_j = 8$, $-m = 2, 4, 6, 8$ (even-π) modes. The normalization of the grey-scales in each panel is arbitrary, and contours mark the $|\lambda_{l_j,m}\rangle = 0$ nodes.

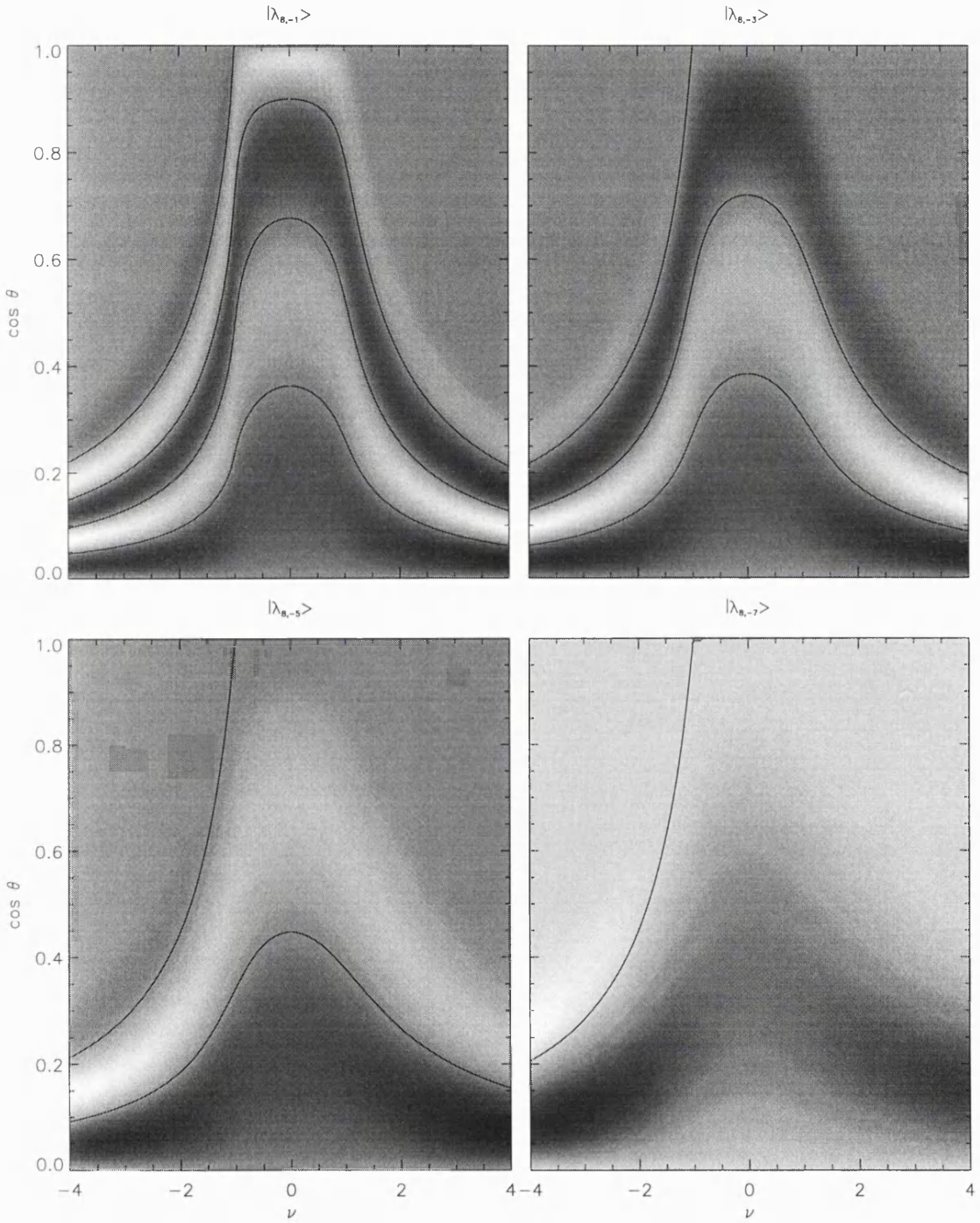

Figure 6.8 (cont): As before, except the $-m = 1, 3, 5, 7$ (odd-π) modes are plotted.

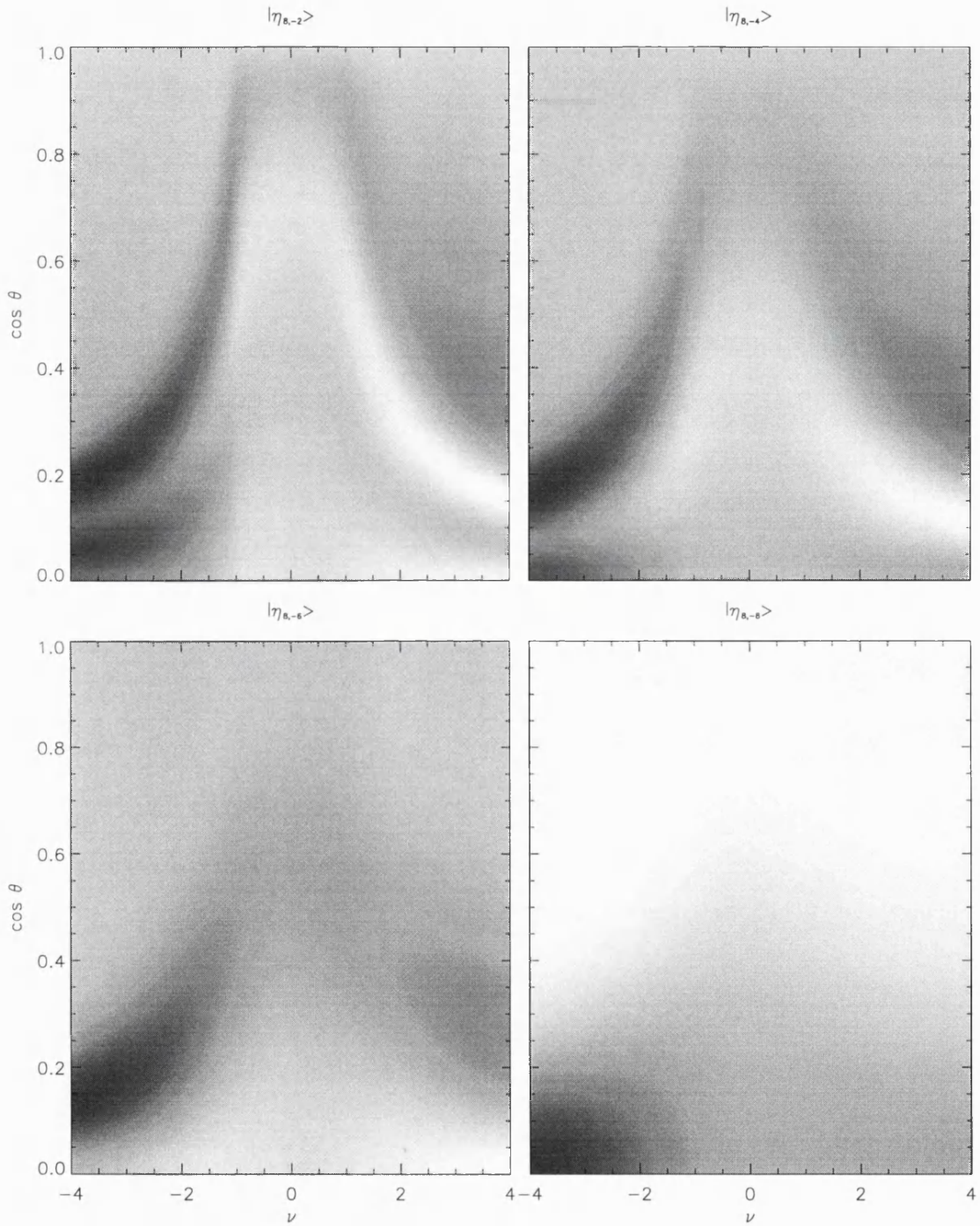

Figure 6.9: The horizontal basis states $|\eta_{l_j,m}\rangle$ plotted as a function of $\cos\theta$ and $\nu \equiv 2\Omega/\sigma_c$ for the $l_j = 8$, $-m = 2, 4, 6, 8$ (even-π) modes. The normalization of the grey-scales in each panel is arbitrary.

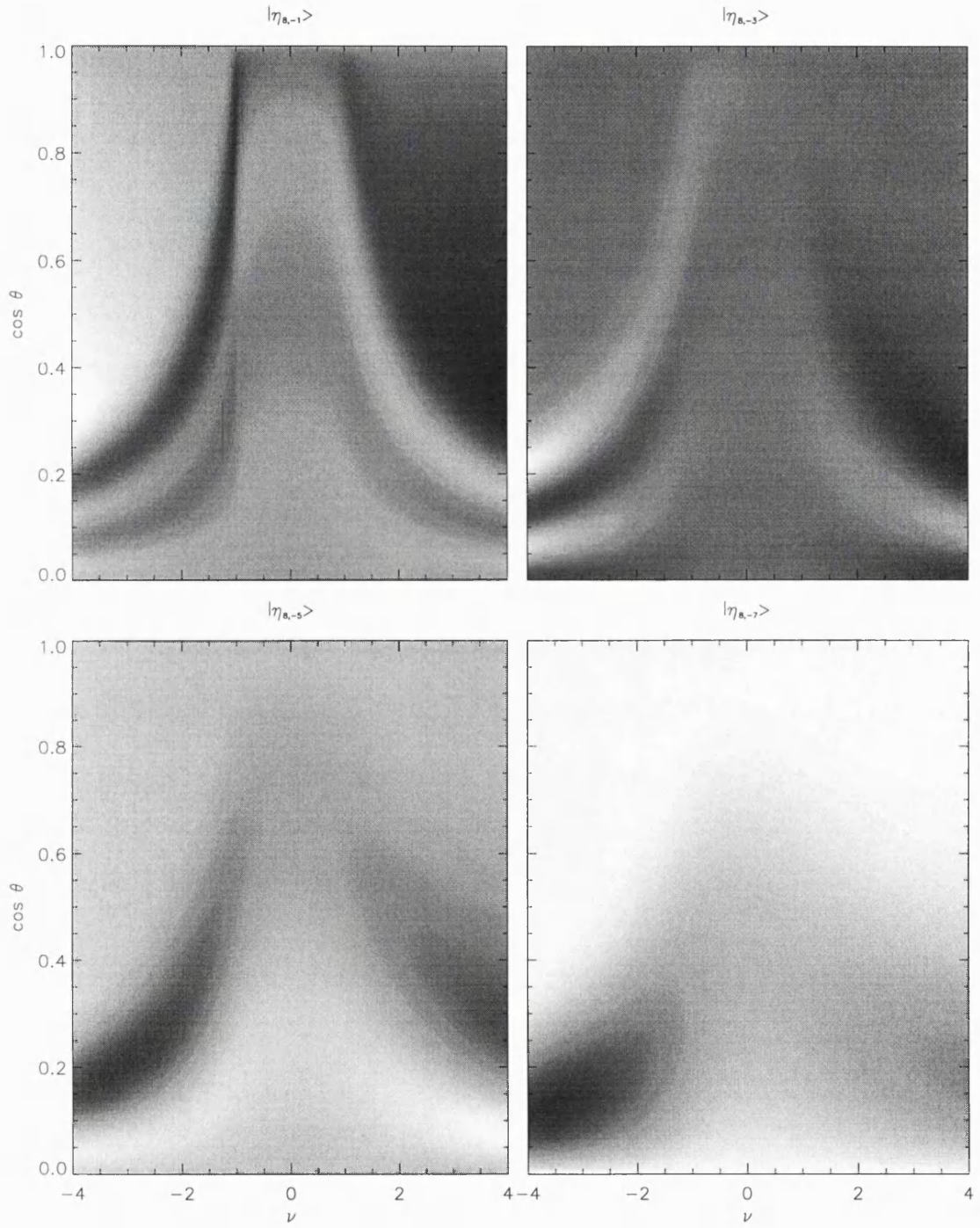

Figure 6.9 (cont): As before, except the $-m = 1, 3, 5, 7$ (odd-π) modes are plotted.

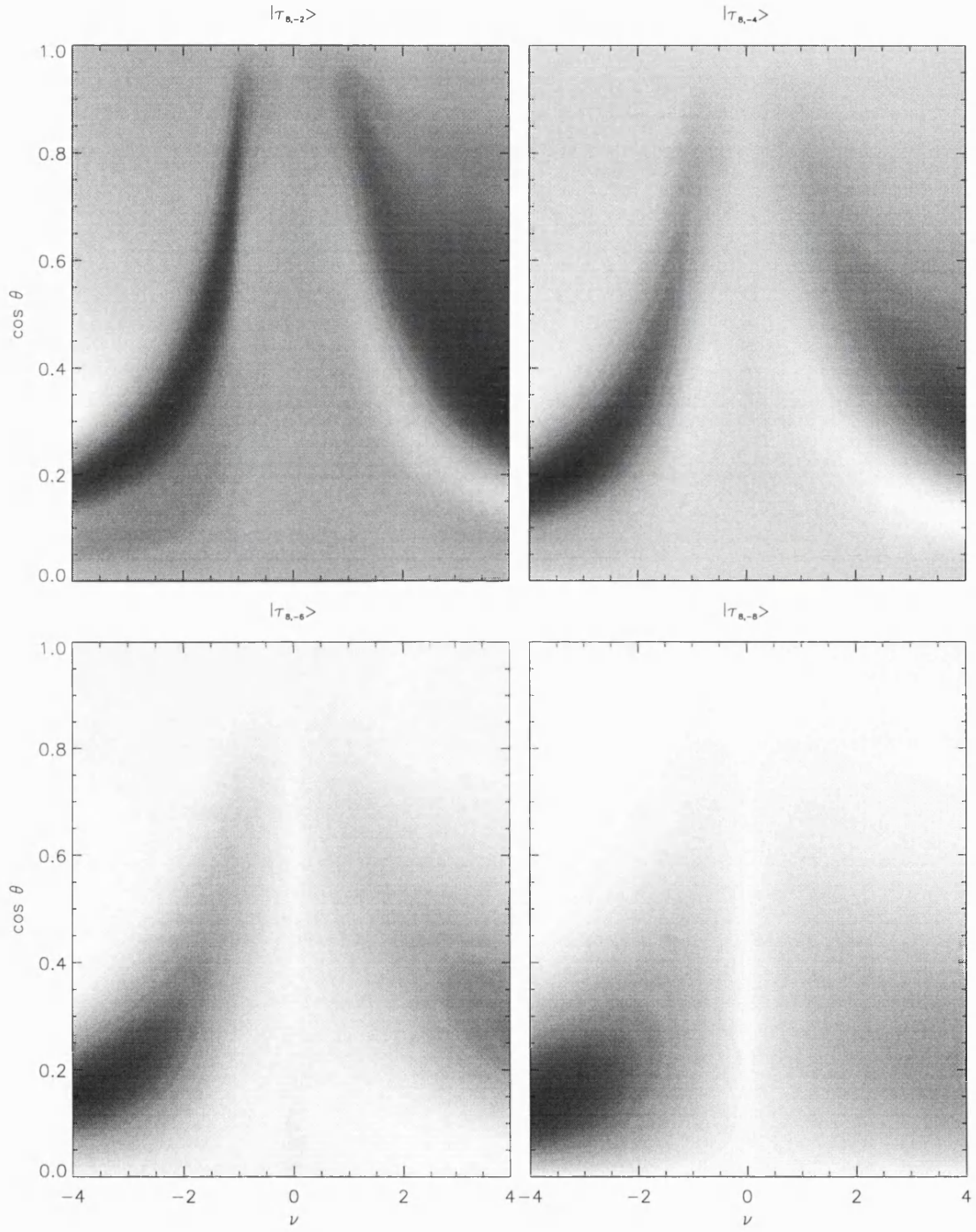

Figure 6.10: The toroidal basis states $|\tau_{l_j,m}\rangle$ plotted as a function of $\cos\theta$ and $\nu \equiv 2\Omega/\sigma_c$ for the $l_j = 8$, $-m = 2, 4, 6, 8$ (even-π) modes. The normalization of the grey-scales in each panel is arbitrary.

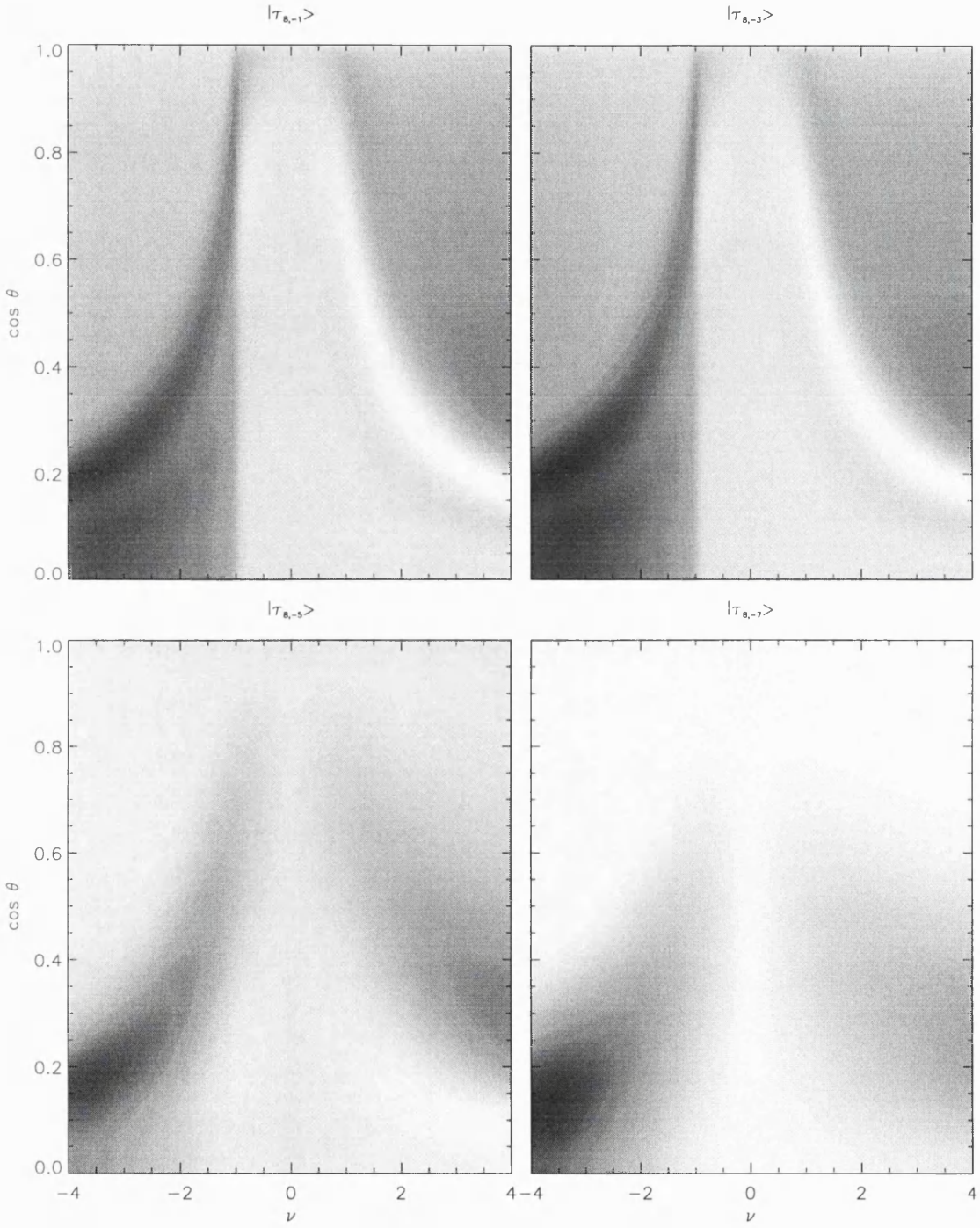

Figure 6.10 (cont): As before, except the $-m = 1, 3, 5, 7$ (odd-π) modes are plotted.

N of 100 to preserve numerical accuracy (this value was chosen in accordance with the procedure discussed in §6.6). The grey-scale normalization in each panel has been chosen arbitrarily to extend from the maximum (white) to the minimum (black) values of the basis states, and contours have been used to mark the latitudinal nodes ($|\lambda_{l_j,m}\rangle = 0$) in figure 6.8.

Inspection of these figures shows immediately that the most important qualitative effect of rotation on the angular basis states is to confine the majority of pulsation activity towards the stellar equator ($\cos\theta = 0$). This confinement is observed for all of the angular basis states of all of the modes; it appears to be most severe for the modes of lowest $|m|$, and those which are retrograde ($\nu < 0$). The onset of this confinement does not occur typically until $|\nu| \gtrsim 1$, at which point the confinement manifests itself quite rapidly with increasing $|\nu|$; from this observation, it is reasonable to suggest that first-order PE techniques, which predict nothing about this equatorial confinement, should be used for modes with $\Omega/\sigma_c > 0.5$ only with extreme caution. In any case, PE techniques of *any* order should never be used for modes with Ω/σ_c greater than unity, since the power-series expansions around which they are based diverge in that region.

An examination of the $|\lambda_{l_j,m}\rangle = 0$ contours in figure 6.8 shows that, for retrograde modes, the rotation serves to introduce an extra latitudinal node between pole and equator for the radial basis states; this can be seen as a contour which occurs solely on the left-hand side of the panels. This extra node, mentioned by Lee & Saio (1990), means that a mode of given harmonic degree l will appear, to all intents and purposes, to have an effective harmonic degree of $l+2$ at the stellar surface. Since modes of large $(l - |m|)$ typically lead to only low-amplitude line-profile variability due to cancellation effects at near equator-on viewing angles, this extra node will suppress variability from retrograde modes, and make them more difficult to observe in systems with large values of $|\nu|$.

Another mechanism by which rotation may serve to suppress observable variability arises simply from the fact that, for appreciable values of $|\nu|$, only a small area of the stellar surface will have a significant pulsation velocity. Although the maximum and minimum amplitudes of the basis functions in such situations are much larger than in the corresponding non-rotating cases, it must be remembered that the basis functions are all scaled by some arbitrary amplitude A (equation (6.83)). Since this amplitude is usually chosen to achieve a given maximum velocity on the stellar surface (typically the local sound speed), it counteracts the increase in the maximum magnitude of the basis functions with increasing $|\nu|$, and the variability associated with a given mode *will* decrease for physically realistic models as $|\nu|$ is increased. Note that the increase in the magnitude of the basis functions discussed here arises from their normalization; since they form an orthonormal set over the stellar surface (equation (6.63)), they must increase in maximum magnitude if the area over which they differ significantly from zero decreases.

Latitudinal nodes are not marked on figures 6.9 and 6.10, since $\boldsymbol{\xi}$ at the stellar surface is not directly proportional to the horizontal and toroidal basis functions (in contrast the radial basis func-

tion), but instead depends on their various vector derivatives through equation (6.83). It does, however, appear that their behaviour with respect to ν is somewhat more complicated than for the radial basis functions; the asymmetry between retrograde and prograde modes is much more pronounced in the former than in the latter, and and an appreciable amount of structure is seen in these horizontal and toroidal basis states for large values of $|\nu|$.

It is difficult to explain this structure in terms of *simple* underlying physics; some comment can be made, however, on the forms of the horizontal and toroidal basis functions for $\nu = 0$. In such zero-rotation cases, the horizontal transformation matrix $\mathbf{Q}$, given by equation (6.80), is equal to the identity matrix $\mathbf{I}$, and so the horizontal basis functions $|\eta_{l_j,m}\rangle$ are identical to the spherical harmonics $|l_j, m\rangle$ (as, of course, are the radial basis functions). In contrast, the toroidal transformation matrix $\mathbf{R}$ (equations (6.81) and (6.82)), is equal to the null matrix $\mathbf{0}$ through the factor ν appearing in these equations, and so the toroidal basis functions $|\tau_{l_j,m}\rangle$ are identically equal to zero for all values of θ. This feature stands out well as a ridge in the lower panels of figure 6.10; it is, of course, to be expected, since the toroidal terms arise as a result of rotation, and are absent in non-rotating stars.

It is worth mentioning that an interesting problem was encountered in the construction of these figures. Initially, it was found that some of the panels exhibited discontinuities with respect to ν consistent with sign changes in the basis states. These discontinuities arise because, whilst the eigenvectors of $\aleph$ are constrained to have unit magnitude, their sign is not specified, and they can be chosen to point in one of two opposing directions in the N-dimensional space which they span. Since the *QL* algorithm used to obtain these eigenvectors contains no information of their functional dependence on ν, it may introduce sign changes in the eigenvectors as ν is varied infinitesimally, leading to the observed discontinuities in the basis states (but not their absolute values) as ν is varied. To eliminate this problem, the 'smoothness' function

$$\mathcal{S}_{\pm} \equiv \left| \, |\ldots\rangle_{\nu+\delta\nu} \pm |\ldots\rangle_{\nu} \, \right| \tag{6.99}$$

is introduced between two 'adjacent' basis functions $|\ldots\rangle$ separated in ν by the infinitesimal $\delta\nu$. Then, the relative sign of the adjacent functions is flipped if $\mathcal{S}_- > \mathcal{S}_+$, and left unaltered otherwise. This procedure was used to ensure that no sign discontinuities appeared in figures 6.8, 6.9 and 6.10, and that the basis functions were smooth with respect to both $\cos\theta$ *and* ν.

With this discussion of the angular basis functions concluded, the following section looks into the effects on results of truncating the coupling matrix $\aleph$ at some finite dimension N. This investigation highlights some of the limitations of the traditional approximation, and also underlines the inadequacy of first-order PE techniques in modelling the gross qualitative modifications which the angular basis states undergo when rotation is introduced.

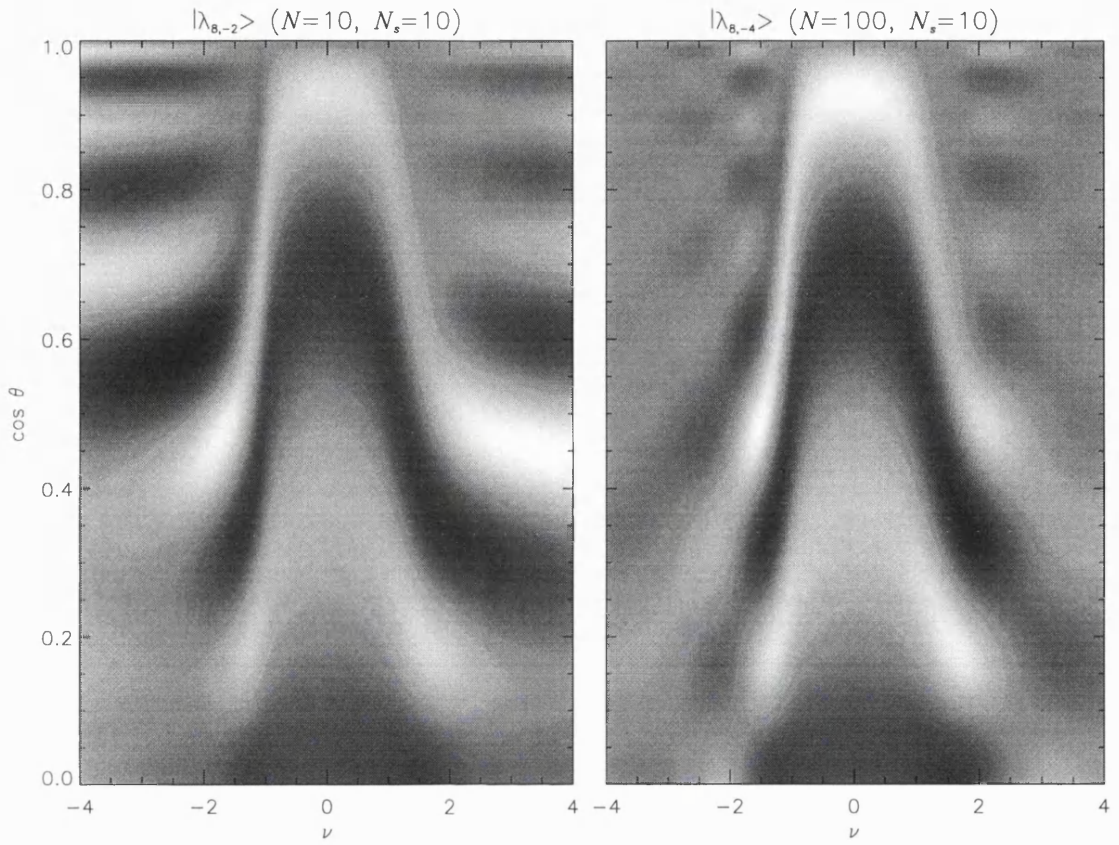

Figure 6.11: The radial basis state $|\lambda_{l_j,m}\rangle$ plotted as a function of $\cos\theta$ and $\nu \equiv 2\Omega/\sigma_c$ for the $m = -2$, $l_j = 8$ mode (compare figure 6.8). The left-hand panel shows the result of truncating the matrix dimension at 10. The right-hand panel shows the result of using a matrix dimension of 100, but only using the first 10 elements of the resulting eigenvector to calculate $|\lambda_{l_j,m}\rangle$

6.9 Truncation & The Traditional Approximation

As was mentioned in §6.6, the coupling matrix $\aleph$ must be truncated at some suitably large dimension N to render the ST technique computationally tractable. Whilst it is obvious that such a truncation will invariably introduce quantitative changes, however small, in the results of the theory, what is less obvious is that definite qualitative changes will also arise with truncation, in a number of areas. This section is primarily concerned with these qualitative changes, since they have the most impact on the interpretation of the theory. The use of the traditional approximation is also discussed towards the end of the section, with particular attention paid to some of the problems and artifacts which its use entails.

One rather catastrophic effect of severe truncation is the introduction of spurious oscillatory

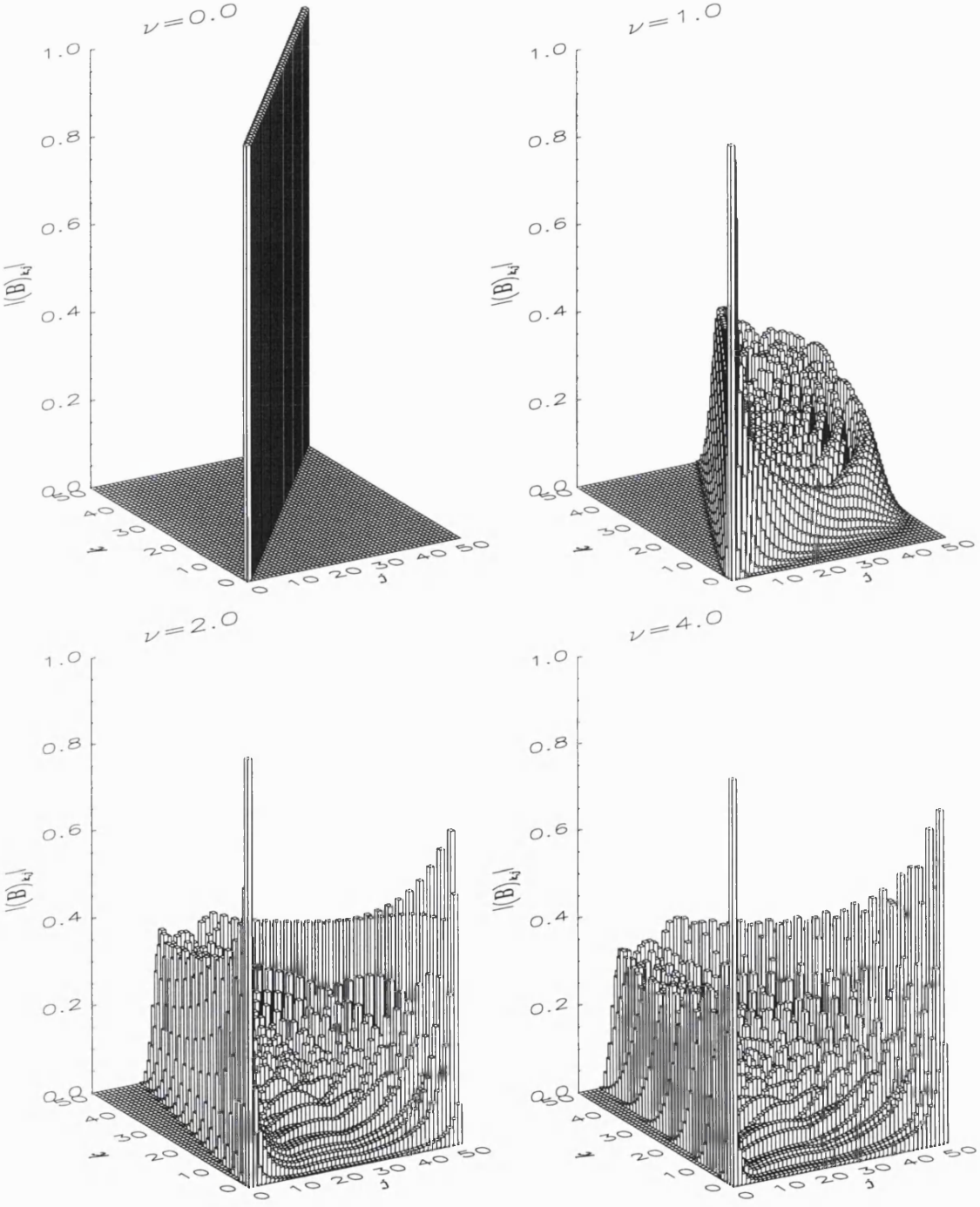

Figure 6.12: The modulus of the elements of the eigenvector matrix $|(\mathbf{B})_{kj}|$, plotted as a function of indices k and j for $m = -2$, for four differing values of ν. Each panel shows the contribution to the $|\lambda_{l_j,m}\rangle$ basis function from the $|l_k, m\rangle$ spherical harmonic for the given value of ν. The matrix dimension was taken to be 50.

features in the basis functions discussed in the previous section. Figure 6.11 illustrates the $l_j = 8$, $m = -2$ radial basis function $|\lambda_{l_j,m}\rangle$ as a function of $\cos\theta$ and ν, calculated with two differing forms of truncation. The left-hand panel was calculated using a matrix dimension N of 10, and clearly shows these oscillatory features as alternate dark and light banding down its left- and right-hand sides (compare this with the corresponding panel in figure 6.8). The features arise through two basic mechanisms; the first of these is simply a result of the fact that the truncation alters the matrix eigenvectors $\mathbf{B}$ with respect to their true infinite-dimension values. The second and perhaps more important mechanism is related to the Gibbs'-phenomenon ringing observed in the truncated Fourier series expansion of periodic functions (*e.g.*, Arfken 1970). The fact that only ten spherical harmonics are used in the construction of the left-hand panel means that there are insufficient high-degree harmonics to reproduce the steep gradients of the basis function with respect to $\cos\theta$ seen in figure 6.8; the smoothness of the function is lost when insufficient terms are used in its calculation. This point is emphasized by the right-hand panel of Fig 6.11, which was calculated with a matrix dimension of 100 but a 'summation' dimension N_s, the number of terms used in the summation of equation (6.64), of only 10. For this matrix dimension, the eigenvectors $\mathbf{B}$ will be a reasonably close approximation to their true infinite-dimension values, so the first mechanism discussed above is suppressed. However, the *summation* truncation (*i.e.*, $N_s < N$) still leads to ringing features through the second mechanism, so it can be concluded that as many terms in the equation (6.64) as are available must be used to preserve the smoothness of the basis functions.

To highlight further the importance of maintaining high-order terms in the summation of equation (6.64) (and, indeed, of equations (6.74) and (6.75)), figure 6.12 shows the magnitude of the elements of the eigenvector matrix $|(\mathbf{B})_{k,j}|$ plotted as a function of indices k and j, for $\nu = 0$, 1, 2 and 4. A matrix dimension of 50 was used in this plot; it was found that the previously-used dimension of 100 produced an unreadable figure. The plots essentially show the contribution to the $|\lambda_{l_j,m}\rangle$ basis function from the $|l_k, m\rangle$ spherical harmonic. In the non-rotating ($\nu = 0$) case, the eigenvector matrix is, of course, just the identity matrix $\mathbf{I}$, explaining the distinctive form of the top-left panel. The other panels demonstrate that, for ν suitably different from zero, the basis functions are mainly comprised of high-order spherical harmonics (this is particularly striking in the $\nu = 4$ panel), as indicated in the preceding paragraph. Indeed, for low-j modes (excluding the $j = 1$ case), the contribution to the $|\lambda_{l_j,m}\rangle$ basis function from its corresponding non-rotating spherical harmonic $|l_j, m\rangle$ is almost negligible, underlining the fact that rotation introduces quite severe modifications to the rotational basis functions. It is for this reason that first-order PE techniques, which model the radial basis functions with only a few spherical harmonics, are to be treated with extreme caution for $\Omega/\sigma_c \gtrsim 0.5$.

The problems described herein of eigenvector inaccuracy and summation truncation are not just restricted to the ST technique, but are also found in the full matrix formulation presented in §6.3. One problem which does appear to be particular to ST, however, is the dependence of the

singular points $\nu_-^{l_j}$ and $\nu_{l_j}^{\pm}$ (see §6.7) on the matrix dimension N. This dependence arises as a consequence of the Cauchy Interlace Theorem (Parlett 1980), which requires that the eigenvalues of the N-dimensional $\aleph$ matrix interlace those of the $(N+1)$-dimensional matrix. Combining this theorem with the fact that the eigenvalues of the matrices are never degenerate (§6.6) means that, as N is incremented, each and every singular point must move away from the $\nu = 0$ origin by some finite amount. Lee & Saio (1989) demonstrated this in their figure 6, which essentially shows that as $N \to \infty$, all singular points $\nu_{l_j}^{\pm}$ (where $\lambda_{l_j,m} \to \infty$) associated with a finite l_j will be such that $|\nu_{l_j}^{\pm}| \to \infty$ too.

Recalling from §6.7 that these singular points are associated with the low-frequency cutoff of propagative waves, it appears that their behaviour will entail this cutoff tending to zero as $N \to \infty$. This phenomenon is most likely an artifact resulting from the introduction of the traditional approximation, since non-zero cutoffs *do* exist in rotating bodies. It is rather paradoxical that as the matrix dimension is increased and its eigenvectors approach more accurate values, the traditional approximation produces this increasingly erroneous qualitative artifact.

Since the convective modes introduced in §6.7.2 exist below the low-frequency cutoff, it would appear that they will be completely suppressed as $N \to \infty$ within the traditional approximation. However, this turns out not to be the case; Lee & Saio (1989) demonstrated that, whilst the finite-l_j modes will have zero cutoff frequencies in this infinite limit, those with l_j such that $j = N, N-1, N-2, \ldots \to \infty$ *will* retain finite cutoff frequencies in the limit. Furthermore, it turns out that these modes are dominated below their respective cutoff frequencies by low-l_j spherical harmonics, even though they are *labelled* by large (limiting at infinity) values of l_j. Thus, even though their labels are unrealistic, the actual physical characteristics of these convective modes are perfectly well behaved, and realistic convective modes remain even when the traditional approximation artifact discussed above is present.

To illustrate this point further, the similar case of the quasi-toroidal modes discussed in §6.7.3, which arise when ν is near the $\nu_-^{l_j}$ ($\lambda_{l_j,m}^{-1} \to \infty$) singular points, can be considered. These singular points occur when

$$m\nu = n_j(n_j + 1), \tag{6.100}$$

and it is the l_{N-j} eigenvalue which exhibits the singularity. To appreciate this, observe that for the $j = 1$ singular point, it is $\lambda_{l_N,m}^{-1}$ which diverges, for the $j = 2$ singular point, it is $\lambda_{l_{N-1},m}^{-1}$ which diverges, and so on. Therefore, it is the $j = N, N-1, N-2, \ldots$ singularities which generate the quasi-toroidal modes whose frequencies (from equation (6.92)) are given by

$$\sigma_c = \frac{2m\Omega}{n_j(n_j+1)} \tag{6.101}$$

for $j = 1, 2, 3, \ldots$, and whose eigenfunctions are related to the single spherical harmonic $|n_j, m\rangle$

(see §6.7.3). As $N \to \infty$, these frequencies will remain finite (and in this case unchanged) as discussed above, even though they arise from modes with $j = N, N-1, N-2, \ldots \to \infty$, demonstrating that whilst the mode labels are unrealistic, the actual physical characteristics of the modes are well behaved.

Having discussed the intricacies of ST in some detail over the preceding sections, the final section of this chapter is concerned with a comparison between the PE and ST techniques, with a investigation of whether they produce the same results in comparable regions of parameter space, and a discussion of their relative merits.

6.10 A Comparison between PE and ST

To investigate whether the results produced by the PE and ST techniques agree with one another over comparable domains, expressions must be found to first order in $\Omega/\sigma_c^{(0)}$ for the non-zero elements of the coupling matrix $\aleph$. As was pointed out in §6.2, first order in $\Omega/\sigma_c^{(0)}$ is essentially equivalent to first order in Ω/σ_c or, indeed, ν. Accordingly, the elements of $\aleph$ in the first-order limit are found to be given by

$$(\aleph)_{j,j} = \left[1 - \frac{m\nu}{\Lambda(l_j)}\right] \Big/ \Lambda(l_j), \tag{6.102}$$

such that $\aleph$ is diagonal. The eigenvalues $\lambda_{l_j,m}$, which are just the reciprocals of these elements, are given by

$$\lambda_{l_j,m} = \Lambda(l_j) + m\nu, \tag{6.103}$$

and the eigenvector matrix $\mathbf{B}$ is simply the unit matrix $\mathbf{I}$. The asymptotic technique used in §6.7 then gives the eigenfrequencies as

$$\sigma_c = \sigma_c^{(0)} \sqrt{1 + \frac{m\nu}{\Lambda(l_j)}}, \tag{6.104}$$

where the usual structure integral has been expressed in terms of $\sigma_c^{(0)}$. Expanding this equation to first order in ν, and subsequently multiplying through by σ_c, gives a quadratic equation for σ_c,

$$\sigma_c^2 - \sigma_c^{(0)}\sigma_c - \frac{\sigma_c^{(0)} m\Omega}{\Lambda(l_j)} = 0, \tag{6.105}$$

where the substitution $\nu \equiv 2\Omega/\sigma_c$ has been made. Solving this equation for σ_c and then expanding the solution to first order in $\Omega/\sigma_c^{(0)}$ leads to the final expression for the rotationally-modified eigenfrequencies,

$$\sigma_c = \sigma_c^{(0)} + \frac{m\Omega}{\Lambda(l_j)}, \tag{6.106}$$

where only the positive solution has been retained. The corresponding PE expression for the eigenfrequencies, equation (6.9), is given by

$$\sigma_c = \sigma_c^{(0)} + m\Omega C_{n,l};$$

for suitably low-frequency modes, to which ST is applicable, the Ledoux splitting constant $C_{n,l}$ is equal to $1/\Lambda(l)$ (Schrijvers *et al.* 1997), and so the ST and PE results for the eigenfrequencies are seen to be in agreement.

To investigate whether the eigenfunctions of PE and ST likewise agree, the basis states $|\lambda_{l_j,m}\rangle$, $|\eta_{l_j,m}\rangle$ and $|\tau_{l_j,m}\rangle$ are written to first-order in ν as

$$|\lambda_{l_j,m}\rangle = Y^m_{l_j}, \tag{6.107}$$

$$|\eta_{l_j,m}\rangle = \left[1 + \frac{m\nu}{\Lambda(l_j)}\right] Y^m_{l_j} \tag{6.108}$$

and

$$|\tau_{l_j,m}\rangle = \nu \left[\frac{l_j+1}{l_j} J^m_{l_j} Y^m_{l_j-1} + \frac{l_j}{l_j+1} J^m_{l_j+1} Y^m_{l_j+1}\right]. \tag{6.109}$$

A cursory comparison of these expressions with those given in §6.2 for the radial, horizontal and toroidal displacement functions shows that they agree with respect to their spherical-harmonic content. To examine whether the *coefficients* of the spherical harmonics match properly, a number of manipulations of the PE expressions must be undertaken. Firstly, it should be remembered that the results of ST are only strictly applicable to low-frequency modes ($\omega_c^2 \ll 1$); therefore, terms of order unity may be discarded from equations (6.12), (6.14) and (6.15), to give

$$k = \frac{1}{\omega_c^2}\left[1 + \frac{m\nu}{l(l+1)}\right], \tag{6.110}$$

$$a_{\mathrm{tor},l+1} = -\frac{\nu}{\omega_c^2}\frac{l(l-|m|+1)}{(l+1)(2l+1)} a^{(0)} \tag{6.111}$$

and

$$a_{\mathrm{tor},l-1} = \frac{\nu}{\omega_c^2}\frac{(l+1)(l+|m|)}{l(2l+1)} a^{(0)}, \tag{6.112}$$

where j-subscripts have been omitted since PE recognises no difference between even- and odd-π modes, and $2\Omega/\sigma_c$ has been substituted for ν. Now, as Schrijvers *et al.* (1997) point out, it is possible to replace $a^{(0)}$ by $a_{\mathrm{sph},l}$ in the latter two of these equations without affecting the results to first order. With this replacement, and a subsequent factoring out of $a_{\mathrm{sph},l}$, the displacement given by PE (equation (6.10)) may be written in the familiar ST-style form

$$\frac{\boldsymbol{\xi}(\theta,\phi,t)}{R} = a_{\mathrm{sph},l}\Re\left\{\left[|\lambda_{l,m}\rangle \mathbf{e}_r + \frac{1}{\omega_c^2}\left(\nabla_h|\eta_{l,m}\rangle - \mathrm{i}\nabla_h \times |\tau_{l,m}\rangle \mathbf{e}_r\right)\right]\exp(\mathrm{i}\sigma_c t)\right\}, \tag{6.113}$$

where, after some algebra, the PE basis functions introduced here are found to be

$$|\lambda_{l,m}\rangle = Y_l^m, \tag{6.114}$$

$$|\eta_{l,m}\rangle = \left[1 + \frac{m}{\nu} l(l+1)\right] Y_l^m \tag{6.115}$$

and

$$|\tau_{l,m}\rangle = \nu \left[\frac{l+1}{l} J_l^m Y_{l-1}^m + \frac{l}{l+1} J_{l+1}^m Y_{l+1}^m\right] \tag{6.116}$$

A comparison between these expressions and equations (6.107)–(6.109) shows that they are identical. With the PE displacement (6.113) in canonical ST form (compare with equation (6.83)), and recognising that the normalization amplitudes A and $a_{\mathrm{sph},l}$ may be set equal, it is thus demonstrated that the pulsation eigenfunctions of PE and ST are, as were the eigenfrequencies, in full agreement.

This discussion highlights the fact that PE and ST can only be shown to be in full agreement when they are compared in the same region of parameter space. In turn, this suggests that it is inadvisable to use the results of the two techniques outside the domains for which they were intended. Schrijvers *et al.* (1997) adopted a heuristic $\Omega/\sigma_c < 0.5$ upper limit on the systems to which they applied PE; this seems to be a reasonable procedure, since second-order effects will be quite significant above this limit. As has been previously demonstrated, ST is applicable to all values of Ω/σ_c, provided that the pulsation frequency is suitably low. This limitation may be expressed in terms of the dimensionless frequency by $\omega_c < 1$, since this requirement selects only low-frequency g-modes. An upper limit on Ω for both PE and ST must be set below which the coriolis force effects dominate those of the centrifugal force, since the latter is neglected in both treatments. This limit is best expressed in terms of the dimensionless rotation angular frequency $\hat{\Omega}$ (equation (6.28)); in all cases, $\hat{\Omega}$ must be less than $\sqrt{8/27}$, since this represents the critical rate at which significant rotationally-induced mass loss will begin to occur from the stellar surface. A prudent upper limit on $\hat{\Omega}$ is 3/4 of this value — below this limit, the equilibrium figure of the star is almost spherical, although the internal structure of the star may be significantly altered from its non-rotating equivalent through changes to the stellar evolution (§6.1).

Figure 6.13 illustrates the regions in the $\hat{\Omega}$–$\log \omega_c^2$ plane over which PE and ST are applicable. The PE region, delimited by the $\hat{\Omega} = 0.75\sqrt{8/27}$ and $\hat{\Omega}/\omega_c = 0.5$ dashed lines, is marked with ($\diagdown$) hatching, whilst the ST region, delimited by the $\hat{\Omega} = 0.75\sqrt{8/27}$ and $\omega_c = 1$ dashed lines, is marked with ($\diagup$) hatching. The cross-hatched area shows the region over which both PE and ST are applicable; this is the region over which the above comparison between the two techniques was made.

This figure would appear to suggest that PE is applicable over a wider ranger of frequency space than ST. However, this interpretation is rather misleading, since the $\omega_c < 1$ region is far more densely packed with pulsation modes than the corresponding $\omega_c > 1$ region (see figure 5.3).

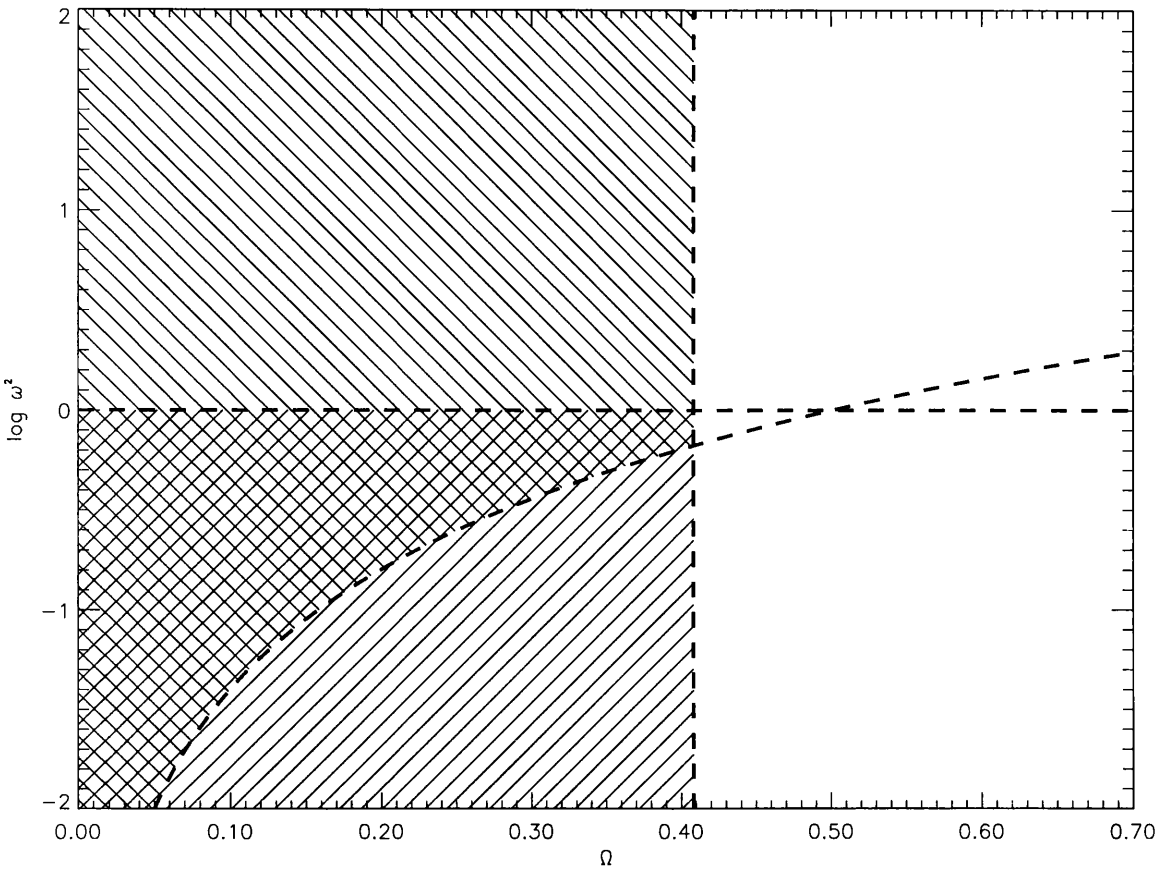

Figure 6.13: The domains of applicability for PE (\) and ST (/) in the $\hat{\Omega} - \log \omega_c^2$ plane. The dashed lines represent the limits of these regions, discussed in the text. The cross-hatched area shows the region over which both PE and ST are applicable.

Furthermore, the rotational modifications to the angular eigenfunctions are treated much more comprehensively by ST than by PE, since these modifications only become significant at large values of ν ($\omega_c \ll 1$). It is for this reason that the line-profile variability models presented in the following chapter use ST in favour of PE.

Chapter 7

Spectroscopic Modelling

7.1 Introduction

Whilst the theoretical treatments developed in the preceding chapters are of interest in themselves, from a purely academic standpoint, their most important purpose is to provide the foundations for constructing models of the *observables* of pulsating stars. Only by comparing the results of these models with real observations can any scientific progress be made, and any possibility exist of using pulsation as a means to probe stellar interiors. Accordingly, this chapter is primarily concerned with such modelling, from a discussion of implementation issues to a consideration of the diagnostic potential of, and the underlying mechanisms behind, pulsation-originated line-profile variability.

Although studies of pulsation in nearby systems have been accomplished partly through direct and indirect imaging (such as interferometry), observational data concerning variability in early-type stars are restricted to disk-integrated light. Accordingly, any model of pulsation in these stars must revolve around some form of combined spectral synthesis and disk-integration procedure, from which theoretical predictions of both line-profile and photometric variability may be derived. Osaki (1971) presented the first such spectroscopic model in an attempt to explain the lpv of β Cephei stars; subsequently, the focus of spectroscopic modelling has been on 53 Per and ζ Oph pulsators, beginning with the treatment of Smith (1977), and continuing with contributions from a number of other authors (*e.g.*, Vogt & Penrod 1983; Pesnell 1985; Kambe & Osaki 1988; Gies 1991; Aerts & Waelkens 1993; Schrijvers *et al.* 1997). For the purposes of this work, a pair of complementary computer models were written, based on the theories developed in the preceding chapters; these models, hereinafter BRUCE and KYLIE, calculate time-resolved disk-integrated spectra for a rotating star undergoing non-radial pulsation. The former, BRUCE, models the photosphere of the star using a grid of surface elements, and subjects this grid to temperature, velocity and geometric perturbations over a sequence of time points, consistent with the model star undergoing multi-modal non-radial pulsation. The results from BRUCE are written out as files containing pertinent

information on all of the observationally-visible grid points; these files are subsequently read by KYLIE, which constructs observer-directed synthetic spectra for each of the grid points, and disk-integrates these spectra to generate time-resolved 'observed' spectra for the entire model star.

The following two sections describe the implementation details of both BRUCE and KYLIE, with some emphasis given to the spectral synthesis approach adopted in the latter, whilst section §7.4 presents a comparison between the BRUCE/KYLIE combination and other models. Subsequent sections then use the results of these codes to discuss the origins of line-profile variability and the diagnostic potential of lpv.

7.2 BRUCE

7.2.1 Introduction

The general procedure used within BRUCE to construct pulsationally-perturbed stellar photospheres is relatively straightforward. Initially, an equilibrium surface grid for the photosphere is constructed, taking into account any effects of rotation on both the figure of the star, and on the surface temperature distribution. The grid is then perturbed with an arbitrary number of pulsation modes (defined by the user), each characterized by its own set of parameters, over a progressive sequence of time points; at each time point, the relevant parameters describing the stellar photosphere are written to output files for subsequent use by KYLIE. All parameters for a given model are supplied to BRUCE in the form of a simple ASCII text file, containing specifications of both the equilibrium stellar parameters, and the pulsation modes excited in the model star; the syntax for this file is documented in Appendix F, which also presents the syntax used in corresponding KYLIE command files.

The following subsections discuss some of the more important aspects of BRUCE in greater detail, with particular focus on the construction of the surface grid and its subsequent perturbation.

7.2.2 The Surface Grid

The surface grid on which the pulsation perturbations are overlaid may be implemented in a number of ways. Some authors (*e.g.*, Pesnell 1985; Aerts & Waelkens 1993) adopt a semi-analytical approach, whereby the co-ordinate system of the model star is taken with the azimuthal axis directed towards the observer. With such a configuration, the disk integration procedure is trivial, since the disk is defined as all points with a colatitude θ less than $\pi/2$. However, this approach suffers from a number of drawbacks. Firstly, the azimuthal axis with respect to which the pulsation modes are defined does not necessarily coincide with the observer-directed axis. Accordingly, spherical harmonics, defined with respect to the observer's azimuthal axis, must be rotated around

the surface of the star to place them on the stellar axis. This rotation is best accomplished using the results of group theory; a spherical harmonic $\tilde{Y}_l^m$ rotated by an angle ι around the y-axis (with the convention that positive ι rotates the positive z-axis into the positive x-axis) may be written in terms of unrotated spherical harmonics as

$$\tilde{Y}_l^m(\theta,\phi) = \sum_{m'=-l}^{l} (\mathbf{D}^{(l)})_{m',m}(0,\iota,0) Y_l^{m'}, \tag{7.1}$$

where $\mathbf{D}^{(l)}$ is the irreducible representation of the full rotation group of dimension $(2l+1)$. Expressions for the components of $\mathbf{D}^{(l)}$ are given by Tinkham (1964), who assumes the Condon-Shortley phase convention discussed in §2.4.

The other problem with the semi-analytical grid formulation is that it is decidedly non-trivial to implement for stars with non-spherical geometry, such as those with an appreciable degree of centrifugal distortion; unlike the axis issue, this problem is not easily resolved using analytical expressions. Accordingly, BRUCE does not use this formulation, but rather implements the grid as a two-dimensional mesh wrapped around the entire surface of the star, with the appropriate stellar radius and photospheric physical quantities assigned to each grid point; the co-ordinate system of the model star is chosen so that the azimuthal axis coincided with the stellar rotation axis. Although this approach, which is also adopted by Gies (1996), leads to a certain amount of redundancy (*e.g.*, calculations made for non-visible grid points), it is far more flexible than semi-analytical approaches, and also more representative of the star itself as a physical entity, as opposed to a two-dimensional disk.

The equilibrium grid, describing the photospheric surface before any perturbations have been applied, is uniquely specified within BRUCE by the polar temperature T_p, the polar gravity g_p, the polar radius R_p, and the azimuthal rotation velocity at the equator, v_eq. The surface of the star is then found from equipotentials of the effective gravitational potential Φ_eff, given in the Roche model (Collins & Harrington 1966) by

$$\Phi_\mathrm{eff} = -\frac{GM}{R_\theta} - \frac{1}{2}\Omega^2 \sin^2\theta, \tag{7.2}$$

where the subscript on R_θ indicates that, for a non-zero rotation rate Ω, the stellar radius is a function of colatitude θ due to centrifugal distortion. The effective potential at the pole,

$$\Phi_\mathrm{eff} = -\frac{GM}{R_p} = -g_\mathrm{p} R_\mathrm{p}, \tag{7.3}$$

sets the potential across the whole stellar surface, so that the surface of the star is defined by the cubic equation in R_θ,

$$-g_\mathrm{p} R_\mathrm{p} = -\frac{g_\mathrm{p} R_\mathrm{p}^2}{R_\theta} - \frac{1}{2}\Omega^2 \sin^2\theta. \tag{7.4}$$

To find the angular velocity Ω from the specified equatorial rotation velocity $v_{\rm eq}$, the identity $\Omega \equiv v_{\rm eq}/R_{\rm eq}$ is substituted into this equation to give the equatorial radius $R_{\rm eq}$ as

$$R_{\rm eq} = \frac{GM}{\frac{GM}{R_{\rm p}} - \frac{v_{\rm eq}^2}{2}}, \tag{7.5}$$

from which Ω may be calculated. Equation (7.4) is solved by BRUCE using a Newton-Raphson algorithm, which finds the radius R_θ of each grid point to a fractional tolerance of 10^{-6}.

The size of the surface grid is governed by $N_{\rm eq}$, the number of points lying around the equator. At colatitude θ, there are approximately $N_{\rm eq} \sin\theta$ points arrayed in a ring coplanar with the equator, such that, neglecting the effects of centrifugal distortion, each grid point encompasses an approximately equal area of the stellar surface. Furthermore, there are $N_{\rm eq}/4$ such rings from pole to equator, so that there are $N_{\rm eq}$ points in a great circle of constant ϕ, and approximately $N_{\rm eq}^2/\pi$ points on the whole grid, although storage requirements for the grid are only of order $N_{\rm eq}/4$ due to the rotational and reflectional symmetry of the star. This overall geometry ensures that the grid used within BRUCE is relatively uniform (although, in the limit of large $N_{\rm eq}$, uniformity is not strictly required). Throughout the remainder of this chapter, $N_{\rm eq}$ is taken to be 400, leading to a grid containing 51030 points, of which (approximately) half are visible at any one time; it was found that results did not vary significantly if $N_{\rm eq}$ was increased, indicating that the grid is sufficiently fine.

Once the radius at each grid point has been evaluated using the method described, the effective gravitational potential $\Phi_{\rm eff}$ defines the local (scalar) gravity

$$g_\theta = |\nabla\Phi_{\rm eff}|, \tag{7.6}$$

and the local surface normal

$$\hat{\mathbf{n}}_\theta = \nabla\Phi_{\rm eff}/g_\theta, \tag{7.7}$$

with the usual convention that the normal points outwards from the surface. The temperature of each grid point is found from the local gravity using a gravity darkening law of the form

$$T_\theta = T_{\rm p}\left(\frac{g_\theta}{g_{\rm p}}\right)^\beta, \tag{7.8}$$

where the coefficient β is assigned a value of 0.25 throughout this chapter, consistent with the radiative photospheres found in early-type stars (von Zeipel 1924). The dependence of line profiles on both T_θ and g_θ means that some species will primarily be formed in polar regions, and others in equatorial regions; this has important implications for the relative strengths of line-profile variability in different species if the pulsation is confined to equatorial regions (Walker 1991; Reid *et al.* 1993; Howarth & Reid 1993), and is considered in greater detail in §7.5.8.

The surface area element associated with each grid point is given by the modulus of the vector $d\mathbf{A}$,

$$d\mathbf{A} = \left(\frac{d\mathbf{R}}{d\theta} \times \frac{d\mathbf{R}}{d\phi} \right) d\theta \, d\phi, \tag{7.9}$$

where $\mathbf{R}$ is the position vector of the grid point. Noting that $\mathbf{R}$ is a function of θ, the derivatives appearing in this expression are given by

$$\frac{d\mathbf{R}}{d\theta} = R_\theta \mathbf{e}_\theta + \frac{dR_\theta}{d\theta}\mathbf{e}_r, \qquad \frac{d\mathbf{R}}{d\phi} = R_\theta \sin\theta \mathbf{e}_\phi, \tag{7.10}$$

so that equation (7.9) may be written in the form

$$d\mathbf{A} = R_\theta^2 \sin\theta \, d\theta \, d\phi \left(\mathbf{e}_r - \frac{1}{R_\theta}\frac{dR_\theta}{d\theta} \right); \tag{7.11}$$

by definition, this vector is parallel to $\hat{\mathbf{n}}$.

Once a grid consistent with the required stellar parameters has been established within BRUCE, every point is subject to a perturbation due to one or more user-definable pulsation modes. The syntax for defining a pulsation mode within a BRUCE command file is given in Appendix F; each mode is specified by harmonic degree l, azimuthal order m, velocity amplitude V_0 and period $\Pi = 2\pi/\sigma$, plus a number of other parameters which will be discussed shortly. The pulsation perturbations are considered in turn in the following subsections.

7.2.3 Velocity Perturbations

The total velocity $\mathbf{v}_t$ of each grid point, with respect to the stellar origin, is calculated by adding the pulsation velocity $\mathbf{v}$ to the underlying equilibrium rotation velocity $\boldsymbol{\Omega} \times \mathbf{R}$ of the star. The displacement perturbations used to calculate $\mathbf{v}$ are taken from equation (6.83), so that the effects of the coriolis force on pulsation discussed in Chapter 6 are fully incorporated through the use of the ST technique; the matrix dimension N used for all calculations is user-definable, and taken to be 100 throughout this chapter.

The amplitude of horizontal displacement perturbations is dependent on the dimensionless pulsation frequency ω_c (see equation (6.83)); since this quantity depends on the stellar radius through equation (2.56), there exists some ambiguity in how it should be calculated in the case where the radius has a colatitude dependence. This ambiguity arises because the rotationally-modified pulsation theory developed in Chapter 6 does not explicitly incorporate the deformation of the equilibrium stellar structure by centrifugal forces. Within BRUCE, the polar radius R_p is used in calculating ω_c; this choice is justified by noting that it is the dependence of the dimensionless frequency on the dynamical time-scale τ_dyn (equation (2.1)) which leads to the radius term in equation (2.56). Since almost all of the stellar mass lies within the polar radius R_p, it is this radius which is probably the most appropriate in calculating both τ_dyn and ω_c.

When the velocity fields are calculated, they are scaled by some velocity amplitude V_0. This amplitude is more a mathematical quantity than an observational quantity, in that it does not actually represent the maximum pulsation velocity on the surface of the star; rather, it is a measure of the RMS radial velocity averaged over the stellar surface. Whilst this RMS velocity is a measure of the kinetic energy in the photosphere, a more physically realistic parameterization of the pulsation amplitude is to specify the maximum velocity amplitude $V_{\max}$ at the surface. Accordingly, BRUCE allows the pulsation amplitude to be set through the specification of either the mathematical V_0, or the more physically realistic $V_{\max}$, from which the appropriate value of V_0 is calculated.

The non-spherical nature of the surface grid leads to non-radial surface normals. This raises the question as to whether so-called 'radial' velocity fields should be directed along the local radial vector or the local surface normal vector. From a physical standpoint, the local surface normal would seem to be the more natural choice, since it defines the direction of the effective gravitational field, and hence the direction of atmospheric stratification. To answer this question properly, the full treatment of Lee & Baraffe (1995), or an equivalent, must be applied to the problem; as an interim solution, BRUCE is able to apply the 'radial' velocity fields along either the local surface normal vector (with the 'horizontal' velocity fields in correspondingly perpendicular directions) or the local radial vector; the latter is the default.

To allow consideration of the mechanisms behind different line-profile variability phenomena, BRUCE is designed to allow, as an option, the use of single spherical harmonics instead of the full rotational basis sets $|\lambda_{l_j,m}\rangle$, $|\eta_{l_j,m}\rangle$and $|\tau_{l_j,m}\rangle$ defined in Chapter 6. Furthermore, horizontal velocity fields may be suppressed to allow the study of the effects of radial velocity fields alone.

7.2.4 Temperature Perturbations

The equilibrium temperature structure of the surface grid, discussed in §7.2.2, is perturbed using a modified version of the adiabatic expression for δT given in equation (3.48). Since non-adiabatic pulsation may lead to amplitude and phase deviations from this expression (Lee & Saio 1990), the temperature perturbations are calculated within BRUCE using the equation

$$\frac{\delta T(\theta,\phi)}{T} = \Delta_T \nabla_{\rm ad} \left[\frac{\lambda_{l_j,m}}{\omega_c^2} - 4 - \omega_c^2 \right] \frac{\xi_r(\theta,\phi)}{r} \exp(\mathrm{i}\psi). \tag{7.12}$$

Here, Δ_T and ψ quantify the non-adiabatic deviation of the temperature perturbation amplitude and phase from adiabacity; in the purely adiabatic case, they take the values 1 and 0 respectively. Note that the term $l(l+1)$ appearing in equation (3.48) has been replaced by the rotationally-modified eigenvalue $\lambda_{l_j,m}$, in accordance with similar replacements in the pulsation equations discussed in §6.4.

7.2.5 Geometric Perturbations

Buta & Smith (1979) have considered the geometrical effects of pulsation on the apparent brightness of a surface element. These geometrical effects are essentially twofold: the first is a variation in the area associated with the surface element, leading to a change in the next radiation flux through the element, whilst the second is a variation in the surface normal of the element, which, when combined with the projection of the element and a suitable limb-darkening law, will lead to changes in the observed brightness.

These changes can be considered together by evaluating the perturbation to the surface area element vector $d\mathbf{A}$ given by equation (7.9). This perturbation $\delta d\mathbf{A}$ will be

$$\delta d\mathbf{A} = \left(\frac{d\delta\mathbf{R}}{d\theta} \times \frac{d\delta\mathbf{R}}{d\phi} \right) d\theta\, d\phi, \tag{7.13}$$

where, in this case, the derivatives are given by

$$\frac{d\delta\mathbf{R}}{d\theta} = \xi_r \mathbf{e}_\theta + \frac{d\xi_r}{d\theta}\mathbf{e}_r, \qquad \frac{d\delta\mathbf{R}}{d\phi} = \xi_r \sin\theta \mathbf{e}_\phi + \frac{d\xi_r}{d\phi}\mathbf{e}_r. \tag{7.14}$$

The projection of $\delta d\mathbf{A}$ onto the line of sight then gives the perturbations to the projected surface normal and surface area.

It is interesting to observe that a star may (theoretically) exhibit lpv due to surface velocity fields but show *no* ostensible photometric variability, owing to cancellations between the temperature, surface-area and surface-normal perturbations. To investigate this possibility, the intensity perturbation δI from a surface element may be expressed in the approximate form

$$\frac{\delta I}{I} = (\chi_1 + \chi_2)\frac{\delta R}{R} + \chi_3 \frac{\delta T}{T}, \tag{7.15}$$

where χ_1, χ_2 and χ_3 are constants representing the weights of the surface area, surface normal and temperature perturbations respectively. For radial pulsation, χ_1 is 2 and χ_2 is 0; in the non-radial case, their values depend on the pulsation mode under consideration, but χ_1 will be close to 2. In the case of a blackbody at temperature T, χ_3 will be given by

$$\chi_3 = \frac{hc}{\lambda kT}\frac{\exp(hc/\lambda kT)}{\exp(hc/\lambda kT) - 1}, \tag{7.16}$$

where the symbols have their usual meanings. In the case of adiabatic pulsation, equation (7.12) may be used to write equation (7.15) as

$$\frac{\delta I}{I} = \left[\chi_1 + \chi_2 + \chi_3 \nabla_{\mathrm{ad}} \left(\frac{\lambda_{l_j,m}}{\omega_c^2} - 4 - \omega_c^2 \right) \right] \frac{\delta R}{R} \tag{7.17}$$

Setting $\delta I = 0$ as an appropriate condition for a lack of photometric variability, and assuming that $\delta R \neq 0$, leads to a quadratic equation in ω_c^2, with roots $\omega_{c,0}^2$ given by

$$\omega_{c,0}^2 = \frac{\tilde{\nabla} \pm \sqrt{\tilde{\nabla}^2 + 4\lambda_{l_j,m}}}{2}, \tag{7.18}$$

where

$$\tilde{\nabla} = \frac{\chi_1 + \chi_2}{\chi_3 \nabla_{\rm ad}} - 4. \tag{7.19}$$

Thus, for stars pulsating near the 'critical' frequency $\omega_{c,0}$, it is possible that there will be little or no photometric (continuum) variability. It should be emphasized that equation (7.15) is an approximation, in that χ_1 and χ_2 are not completely constant over the stellar surface or over a pulsation cycle, and χ_3 is wavelength dependent through equation (7.16), so that complete cancellation may not occur. This issue is considered in greater detail in §7.5.7.

7.2.6 The Output Files

Once the surface grid has been perturbed in the manner described, all of the parameters relevant to spectral synthesis are written to output files, known as 'dump' files, for every visible point on the stellar surface; the criterion of positive projected surface normal is used to decide which grid points are visible. The information in the dump files consists of the temperature T, gravity g, projected velocity $\mathbf{v}_t \cdot \hat{\mathbf{n}}_o$, projected surface area $d\mathbf{A} \cdot \hat{\mathbf{n}}_o$ and projected surface normal $\hat{\mathbf{n}} \cdot \hat{\mathbf{n}}_o$ for each grid point, where $\hat{\mathbf{n}}_o$ is a unit vector directed towards the observer. This information is sufficient to construct synthetic spectra for all visible grid points, which may be subsequently added together in a disk integration procedure. The spectral synthesis and disk integration is performed by KYLIE, which is considered in the next section.

7.3 KYLIE

7.3.1 Introduction

The dump files generated by BRUCE are subsequently read by KYLIE, the disk-integration code, which is controlled by a command file whose syntax is described in Appendix F. This file specifies which dump files to read, and also for which wavelength regions disk-integrated spectra are to be calculated; these regions are comprised of a discrete number of wavelength points, which may be defined in a number of ways by the user. For each wavelength point, the emergent intensity for a given grid point is calculated using a spectral synthesis routine; this intensity is then weighted by the projected surface area of the grid point, and combined with the weighted intensity of all other grid points in a given dump file to yield a disk-integrated spectrum. This spectrum is written out as a `.sdf` Starlink Data Format file, a subset of the general NDF file format (Lawden 1996).

The spectral synthesis routine forms the core of KYLIE, in that it contains the majority of the relevant physics, and therefore requires particular attention. Accordingly, the issue of spectral synthesis is discussed in the following subsection.

7.3.2 Spectral Synthesis

Historically, a number of approaches have been used in NRP models to construct synthetic spectra. The most simplistic of these approaches assumes that the emergent spectrum is composed of Gaussians with fixed equivalent widths and line depths; these Gaussians are Doppler-shifted in accordance with the projected velocity $\mathbf{v}_t \cdot \hat{\mathbf{n}}_o$ at each grid point, and then added together through a disk integration. It is surprising that this approach has been adopted by so many authors (*e.g.*, Baade 1984; Pesnell 1985; Kambe & Osaki 1988; Lee & Saio 1990; Aerts & Waelkens 1993; Schrijvers *et al.* 1997), since it treats only the contributions to line-profile variability from velocity perturbations; the temperature dependence of line profiles is not considered, and so temperature perturbations are completely disregarded. Lee *et al.* (1992*a*) have refined this approach by using Gaussians with variable equivalent widths, taken from a temperature-resolved grid calculated using LTE model atmospheres of Kurucz (1979). Telting & Schrijvers (1997) have adopted a similar technique, although they use a single constant to parameterize the temperature dependence of the Gaussian equivalent widths, as opposed to a full grid. Unfortunately, the refinement of Lee *et al.* (1992*a*) still suffers from the drawback that Gaussian profiles are, in many cases, poor approximations to true line profiles; this is one of the biggest problems with their use.

An altogether more physically realistic approach was taken by Vogt & Penrod (1983), who used synthetic flux spectra based on LTE model atmosphere calculations; they incorporated temperature and gravity dependencies in their model by performing a linear interpolation between two temperature/gravity points. Synthetic flux spectra calculated in a similar way have also been used by Gies (1991) and Kennelly *et al.* (1991), although the latter did not account for the temperature and gravity sensitivity of their spectra. These approaches represent a significant advance on the use of Gaussians, in that the synthetic flux spectra represent much better approximations to true line profiles than Gaussians. However, it still contains some short-falls, in that the flux spectra are being used as angle-dependent intensity spectra by the addition of some limb-darkening law. This limb-darkening law is usually taken to have the form

$$I_\lambda(\mu) = I_\lambda(0)[1 - u(1 - \mu)] \tag{7.20}$$

(*e.g.*, Kennelly *et al.* 1991), where $I_\lambda(\mu)$ is the intensity at angle parameter $\mu = \hat{\mathbf{n}} \cdot \hat{\mathbf{n}}_o$ and wavelength λ, and the limb-darkening coefficient u is a constant; the flux spectra used are taken to represent the normally-emergent intensity $I_\lambda(0)$. The drawback with this formulation is that u is assumed to be independent of wavelength. For continuum regions of a spectrum, this is a reasonable assumption, but it breaks down quite significantly across line profiles; in some cases, u can actually assume negative values in line centres (see §7.5.6). Even approaches which use limb-darkening approaches more sophisticated than that of equation (7.20) suffer from this drawback.

Accordingly, perhaps the best approach to the spectral synthesis problem is to use angle-

dependent *intensity* spectra from model atmosphere calculations, as opposed to the corresponding flux spectra. Smith (1977) and Kambe *et al.* (1990) have adopted such an approach, although they did not account for the temperature and gravity dependency of their intensity spectra; in contrast, KYLIE implicitly accounts for these dependencies by synthesising spectra from the comprehensive grids calculated by Smith & Howarth (1994). These grids were calculated using a non-LTE model atmosphere code, and consist of sets of intensity spectra defined over temperature, gravity and angle parameter, with the inclusion of all spectral lines due to hydrogen and helium transitions. The routine used within KYLIE to access the grids consists of a single functional call, which returns the spectral intensity given the rest wavelength λ_0, the temperature T, the gravity g, and the angle parameter μ. The rest wavelength is related to the observed wavelength λ through the usual Doppler-shift formula, so that

$$\lambda_0 = \frac{\lambda}{1 - (\mathbf{v}_t \cdot \hat{\mathbf{n}}_o)/c}, \tag{7.21}$$

where c is the speed of light *in vacuo*.

The resolution of the grids is typically 1,000 K in temperature, 0.1 dex in gravity, and 0.05 in angle parameter; tri-linear interpolation in these variables, plus linear interpolation in wavelength, is used to calculate spectra at intermediate points. A number of grids of differing helium abundance and microturbulence are available; solar helium abundance and zero microturbulence are used herein.

To allow a comparison between the full intensity spectra used in KYLIE and other spectral synthesis approaches, two variants of KYLIE, hereafter FKYLIE and GKYLIE, were written. The former of these uses a grid of flux spectra calculated with the same non-LTE model atmosphere code, and applies the limb-darkening law (7.20) to 'convert' the flux spectra to intensity spectra. The second variant, GKYLIE, uses Gaussian profiles for the purposes of spectral synthesis, which are again limb-darkened in the usual manner. The temperature and gravity dependence of the Gaussians is accounted for by interpolating the FWHM and depth of each line in a temperature-gravity grid; this grid was computed by measuring the FWHM and depth of lines appearing in the the flux spectra grid used by FKYLIE.

The following section presents a comparison between the BRUCE/KYLIE combination and other models described in the literature, whilst the results produced by KYLIE and the two variants are compared in §7.5.6, which brings to light the importance of using intensity rather than flux spectra for the purposes of disk integration.

7.4 Comparison with other models

Beginning with Osaki's (1971) seminal treatment, a variety of models have been put forward by authors for the synthesis of lpv, each with a different (and not always progressive) degree of sophis-

tication. To allow a comparison between BRUCE/KYLIE and these models, table 7.1 lists the salient features of each model; the table is divided into three sections, corresponding to the approaches used for the equilibrium stellar grid, the pulsation perturbations, and the spectral synthesis. The last of these sections classifies models depending on whether they use Gaussian, flux or intensity profiles, and whether they account for the temperature dependence of profiles ('variable') or not ('constant'); Osaki's (1971) model is not included in this table, since it actually synthesizes spectra using limb-darkened Dirac δ-functions. The table should not be considered to be exhaustive, but does permit broad, qualitative comparisons between the models of different authors.

7.5 Results

7.5.1 Introduction

With a basic description of both BRUCE and KYLIE given in the preceding three sections, this section presents some preliminary results from their use. With so many free parameters available to describe even single-mode pulsation, the extent and depth of the results presented is limited by both the time and the space available; however, some interesting issues concerning the origins of lpv are raised.

Unless otherwise stated, the basic stellar parameters of all models were chosen to correspond approximately to those of ζ Oph, and are documented in table 7.2. This table specifies both the free parameters, which uniquely determine the star being modelled, and the derived parameters, which are calculated from the free parameters using the appropriate relations. The following subsection illustrates basic line-profile variability in this model star for a number of mode excitations, and introduces some of the techniques used for analysis in subsequent subsections.

7.5.2 Basic Line-Profile Variability

To demonstrate line-profile variability at its most basic level, models were calculated for $l = 4$ single-mode pulsation, for all values of m excluding $m = 0$ (the zonal mode was excluded because it does not lead to lpv in the form of travelling features). A co-rotating period of 2 hours was chosen, and 24 consecutive spectra, covering one period in the observer's frame of reference, were calculated for each mode. These spectra extend from 6663Å to 6693Å at a resolution of 0.15Å, covering the He I line at 6678Å. For all modes, the velocity amplitude was chosen so that the maximum pulsation velocity $V_{\max}$ was 20 km s^{-1}, corresponding approximately to the local sound speed.

Figure 7.1 illustrates the results from these calculations. For each mode considered, the difference between the individual rectified spectrum and the time-averaged mean rectified spectrum is plotted as a function of time in grey-scale format. Below each grey-scale, the mean rectified spectrum is plotted; the normalization of the grey-scales is arbitrary, but is chosen such that white

Table 7.1: A comparison between the features of various NRP lpv models. The key is as follows: RD–rotational deformation; GD—gravity darkening; Vel.—velocity-field perturbations; Tem.—temperature perturbations; Geo.—geometric perturbations; SH—spherical-harmonic modes; PE—PE-modified modes; ST—ST-modified modes; CG—constant Gaussian profiles; VG—variable Gaussian profiles; CF—constant flux profiles; VF—variable flux profiles; CI—constant intensity profiles; VI—variable intensity profiles

Model	Equilibrium Grid		Pulsation Perturbations						Spectral Synthesis					
	RD	GD	Vel.	Tem.	Geo.	SH	PE	ST	CG	VG	CF	VF	CI	VI.
Smith (1977)			•			•							•	
Buta & Smith (1979)			•	•	•	•						•		
Vogt & Penrod (1983)			•			•						•		
Baade (1984)			•			•			•					
Lee & Saio (1990)			•					•	•					
Kambe *et al.* (1990)			•			•							•	
Gies (1991)	•	•	•	•	•	•						•		
Kennelly *et al.* (1991)			•			•					•			
Lee *et al.* (1992*a*)			•	•				•		•				
Aerts & Waelkens (1993)			•			•	•		•					
Schrijvers *et al.* (1997)			•			•	•		•					
Telting & Schrijvers (1997)			•	•		•	•			•				
BRUCE/KYLIE	•	•	•	•	•	•		•		•		•		•

Table 7.2: The free and derived parameters of the ζ Oph-type star used for variability modelling.

Free		Derived	
g_p	4.00 dex	g_{eq}	3.73 dex
T_p	38000 K	T_{eq}	32500 K
R_p	9.0 $R_\odot$	R_{eq}	10.3 $R_\odot$
v_{eq}	400 km s^{-1}	Ω	5.57 $\times$ 10$^{-5}s^{-1}$
i	60°	M	29.6 $M_\odot$

and black correspond to the maximum increases and decreases respectively relative to the mean intensity.

It is apparent that all modes exhibit the travelling emission and absorption features characteristic of lpv observed in rapidly-rotating stars (*e.g.*, ζ Oph, HD 93521). These features evolve from blue to red for the $m < 0$ modes, and from red to blue for $m > 0$ modes; this is because the former are prograde in the observational frame of reference, whilst the latter are retrograde (although, in some cases, modes which are prograde in the observational frame may lead to red-to-blue variations). At any given pulsation phase, all modes appear to show two emission/absorption features; this suggests that a correlation between the number of features and the value of m, as suggested by Gies & Kullavanijaya (1988) and others (*e.g.*, Kambe *et al.* 1990; Reid *et al.* 1993), is probably invalid. Rather, it seems that m governs the acceleration of features across the line-profiles; modes with the largest m appear to show a constant acceleration, leading to the characteristic 'barbers-pole' appearance of the grey-scales, whilst those with smaller m have somewhat more 'kinked' accelerations. Indeed, the $m = 1$ mode has completely lost the barbers-pole appearance, and instead exhibits the checkerboard pattern which is more typical of low-m tesseral modes.

One important point to note is that equivalent (*i.e.*, same $|m|$) prograde and retrograde modes are not simply mirror images of one another. This is because the horizontal velocity fields are dependent on the sign of m; furthermore, as was demonstrated in §6, prograde and retrograde modes are affected by rotation to different degrees, although, in this case, this is unlikely to be the cause of the disparity, since ν is only 0.13 for all modes.

7.5.3 The Mechanisms behind Line-Profile Variations

In any type of star undergoing non-radial pulsation, the resulting lpv are caused by the three basic mechanisms considered in §7.2, namely, velocity fields, temperature perturbations and geometric perturbations. This section looks into the relative contributions of these mechanisms to lpv, and

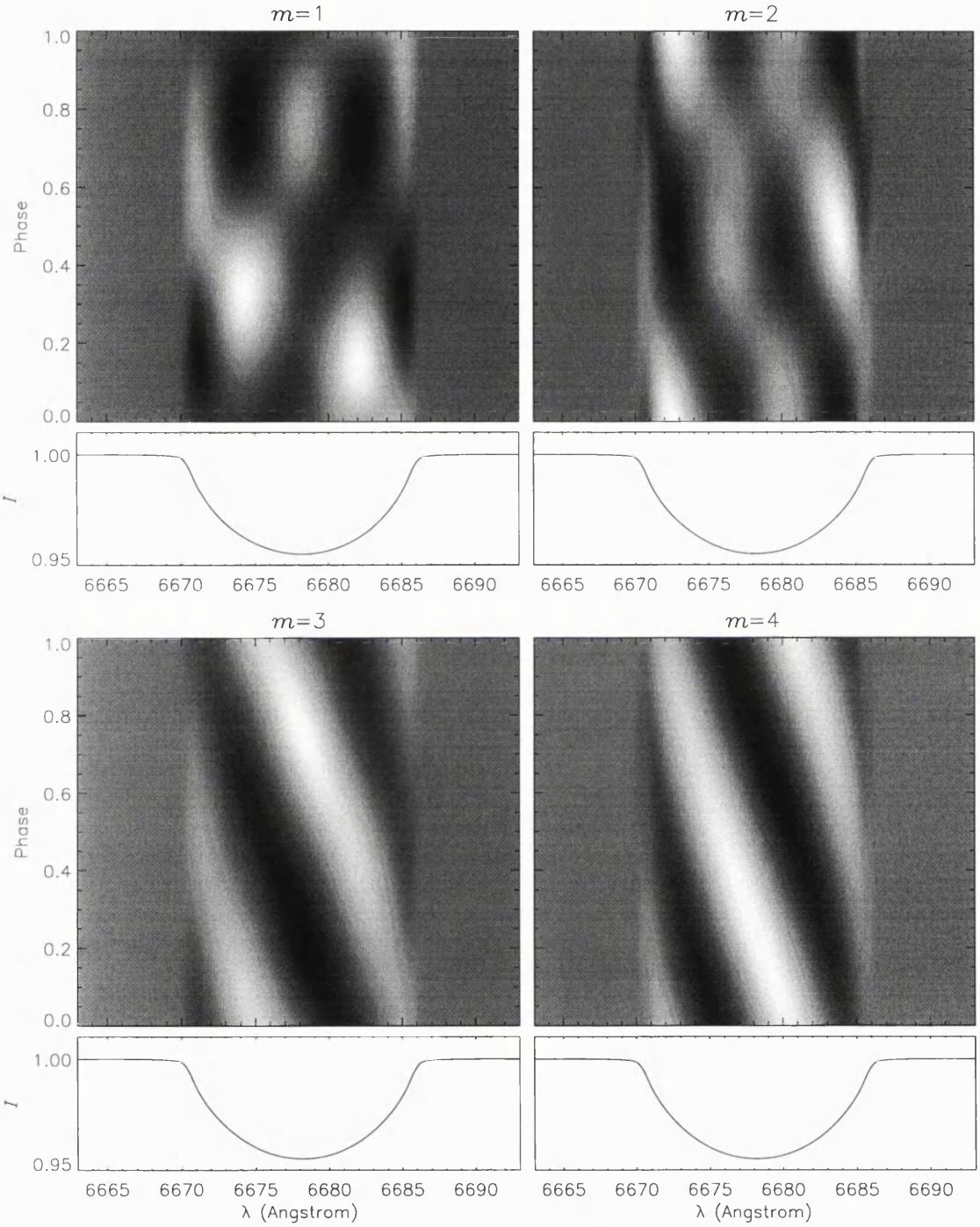

Figure 7.1: Line-profile variations for $l = 4$, $m = 1, 2, 3, 4$ (retrograde) modes in the He I 6678Å line. The lpv are plotted in grey-scale format as deviations from the mean spectrum, which is shown below each grey-scale. In each case, one full pulsation cycle is plotted. The grey-scale normalization is arbitrary in each panel.

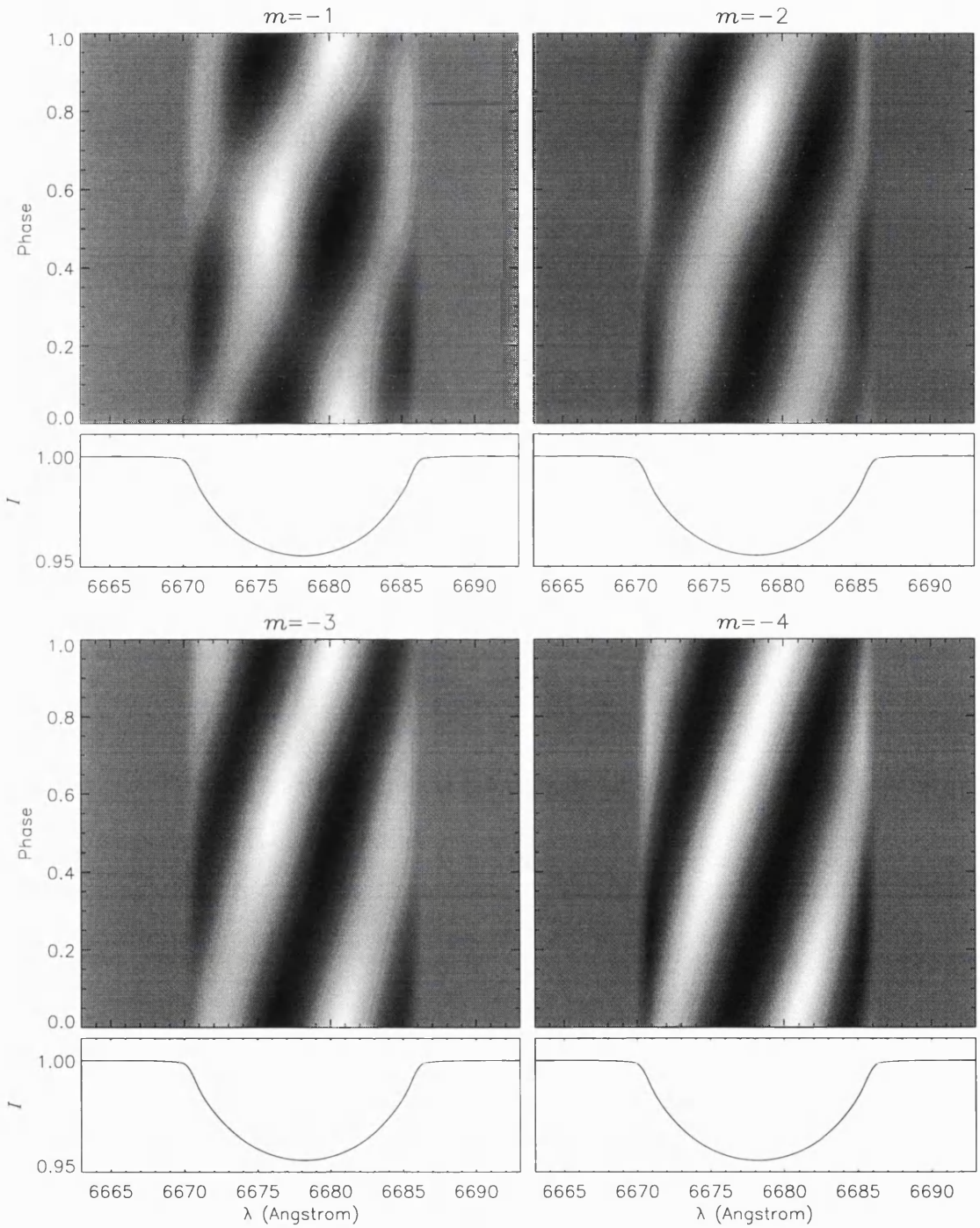

Figure 7.1 (cont): As before, except the $l = 4$, $m = -1$,-2, -3, -4 (prograde) modes are shown

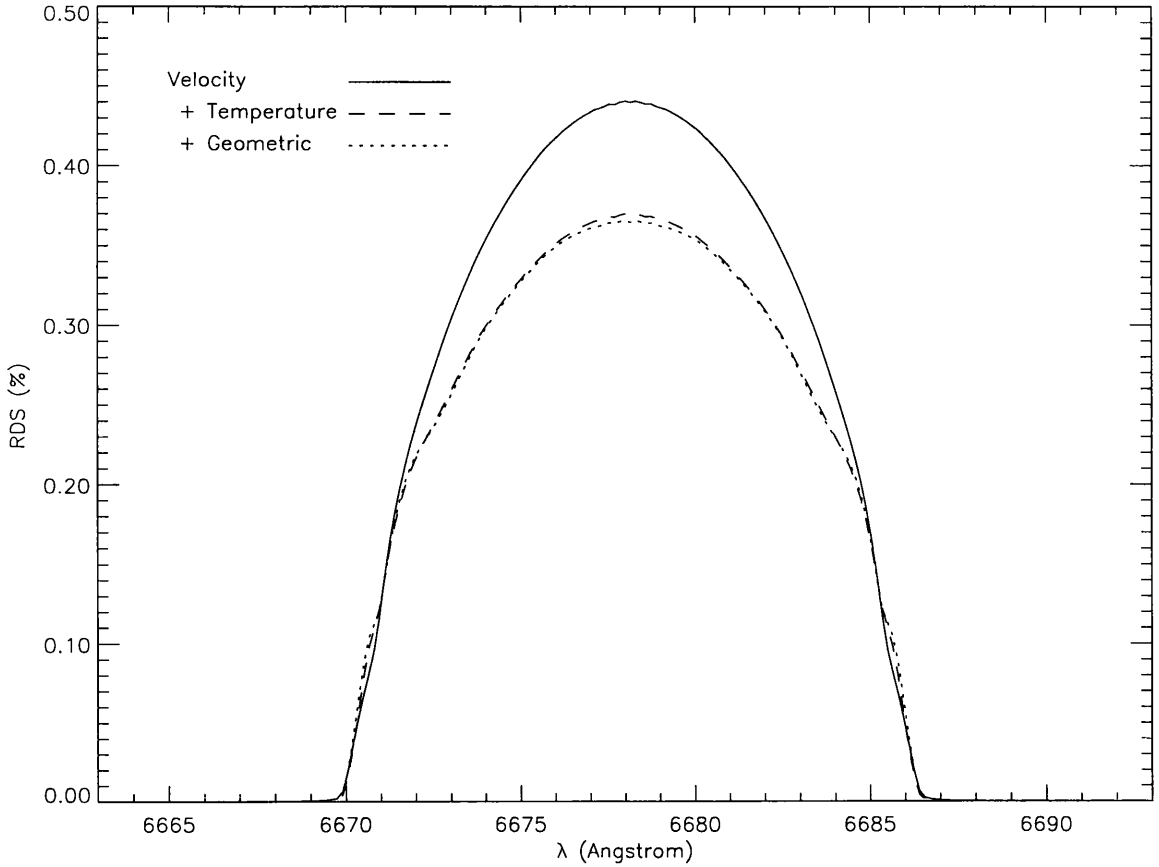

Figure 7.2: The RDS (as a percentage of the continuum) for an $l = 8$, $m = -8$ sectoral pulsation mode in the He I 6678Å line; the pulsation modelled include (cumulatively) velocity fields, temperature perturbations and geometric perturbations.

examines how they actually serve to generate variability.

To investigate the relative importance of these three mechanisms, three time-series of 24 spectra were calculated for a star pulsating in an $l = 8$, $m = -8$ sectoral mode; the maximum velocity amplitude, co-rotating period and spectral range were the same as in the preceding section. The first of these time-series was calculated with the suppression of both temperature and geometric perturbations (so that velocity fields were the only variability mechanism), whilst the second and third were calculated with the *cumulative* inclusion of temperature and geometric perturbations respectively. Each time-series was then used to calculate the RMS deviation from the mean spectrum, averaged over one pulsation cycle, at each wavelength; the resulting RMS deviation spectra, hereinafter RDS, are plotted in figure 7.2. These RDS are similar to the TVS discussed by Fullerton *et al.* (1996), with suitable modifications to account for the arbitrary signal-to-noise of artificial spectra.

It is apparent from this figure that the main sources of line-profile variability, for this set of parameters, are velocity fields and temperature perturbations. Whilst the geometric perturbations (which arise from $\delta R/R \approx 0.3\%$ radius variations) lead to a (theoretically) noticeable change in the

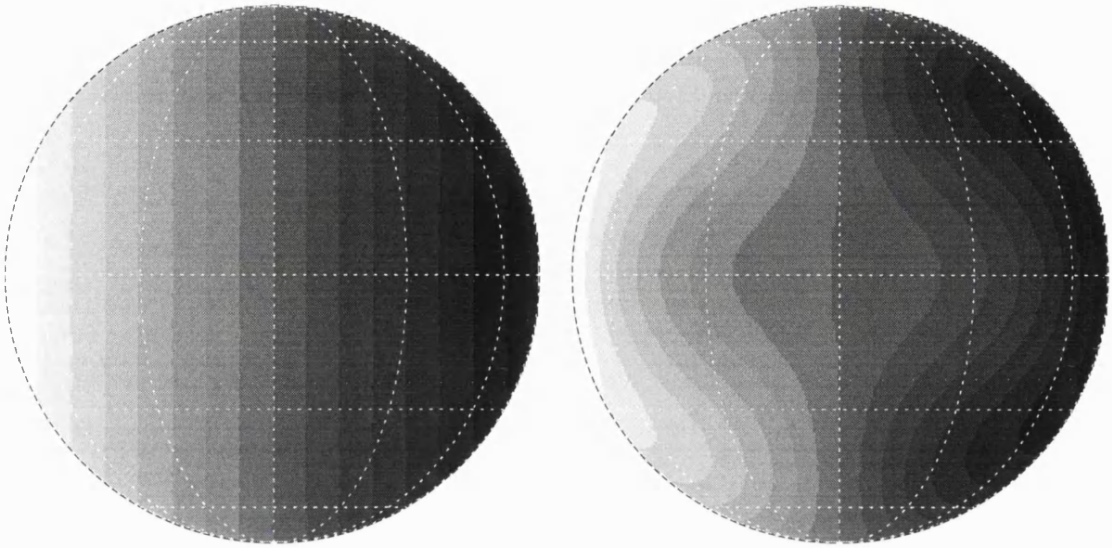

Figure 7.3: The projected velocity plotted on the stellar disk for an equilibrium model rotating at $v_{eq} = 50$ km s^{-1} (left), and the same model with an $l = 4$, $m = -2$ pulsation mode added in (right); the maximum velocity amplitude of the pulsation mode is 20 km s^{-1}.

RDS, this change has no distinguishing signature and probably falls below the current threshold of observational detectability (although this is not the case for continuum variability — see §7.5.7). Thus, it can be assumed that a thorough understanding of line-profile variability can be obtained by examining the precise way in which velocity fields and temperature perturbations generate lpv.

Line-profile variability due to temperature perturbations arises from two sources, namely, changes to the continuum intensity and changes to line-profile equivalent widths. If a surface element undergoes a temperature enhancement (and therefore a continuum enhancement), the increased contribution of that element to the disk-integrated spectrum will lead to (relative) absorption feature at the corresponding points in line profiles. However, the strength of this feature will depend on the temperature-sensitivity of a given line-profile's equivalent width; if the temperature enhancement decreases this equivalent width, the strength of the absorption feature will be reduced, and, in some cases, become negative, leading to a (relative) emission feature.

A proper understanding of how the pulsation velocity fields lead to line-profile variability is somewhat more difficult to come by. Vogt & Penrod (1983), in their figure 16, give a rather sim-

plistic view of this issue, suggesting that lpv features caused by pulsation velocity fields arise from individual points on the stellar surface. This view is somewhat misleading, since it is actually whole regions of the surface which generate the features. To demonstrate this, figure 7.3 shows the projected velocity across the stellar disk for an equilibrium-model star, viewed equator-on with an equatorial rotation velocity $v_{\rm eq}$ of 50 km s^{-1}, and the projected velocity for the same model star with the addition of an $l = 4$, $m = -2$, $V_{\rm max} = 20$ km s^{-1} pulsation mode. The rotation velocity was taken to be small (when compared with other values in this chapter) to ensure that the pulsation velocity fields were not swamped, and only 16 grey levels were used in the figure to aid the visualization of separate constant-velocity areas.

The significance of this figure is that regions of constant velocity (same shade) will contribute to the same wavelength in any disk-integrated line-profiles. In the case of the equilibrium model, these regions are strips of constant disk-parameter $y \equiv \sin\theta \sin\phi$ parallel to the rotation axis; the total disk area of each strip dictates the relative degree of absorption in the disk-integrated line-profiles at the corresponding velocity of the strip (with the addition of suitable limb darkening). When pulsation velocity fields are added in, the boundaries these strips are distorted, and, in some cases, fragmented, leading to a change in their total area. It is this change in constant-velocity area which is responsible for the velocity-field generated lpv. This can be seen by considering that an increase in iso-velocity area at a given velocity is equivalent to a constant-equivalent width temperature enhancement at the same velocity; both lead to an increase in the relative weight of spectrum at that velocity, generating a corresponding absorption feature. In this sense, the pulsation velocity fields generate line-profile variability by perturbing the iso-velocity areas of the equilibrium star.

To place this description on a more mathematical footing, consider the projected velocity along the equator of a star pulsating in a sectoral mode. If the star is equator-on, this projected velocity will be given by

$$[\mathbf{v}_t \cdot \hat{\mathbf{n}}_o](\phi) = v_{\rm eq} \sin\phi + V_{\rm max} \cos m\phi. \tag{7.22}$$

Figure 7.4 shows $\mathbf{v}_t \cdot \hat{\mathbf{n}}_o$ as a function of disk-parameter y for an $m = -4$ mode, calculated with $v_{\rm eq} = 100$ km s^{-1} and $V_{\rm max} = 20$ km s^{-1}. Also shown in this figure is the underlying projected rotation velocity of the non-pulsating star; this is, of course, a straight line. It can be seen that when the gradient of $\mathbf{v}_t \cdot \hat{\mathbf{n}}_o$ with respect to y is shallower (closer to horizontal) than the corresponding gradient of the underlying projected rotation velocity, adjacent points on the equator will be relatively closer in velocity space for the pulsating star than for the non-pulsating star. Accordingly, there will be relatively more of the equator covering a given region of velocity space, and an absorption feature will occur at the appropriate velocity in line profiles. In mathematical terms, pseudo-absorption features will occur in line-profiles at velocities where the relation

$$\frac{d}{dy}\left|\frac{d(\mathbf{v}_t \cdot \hat{\mathbf{n}}_o)}{dy}\right| = 0 \tag{7.23}$$

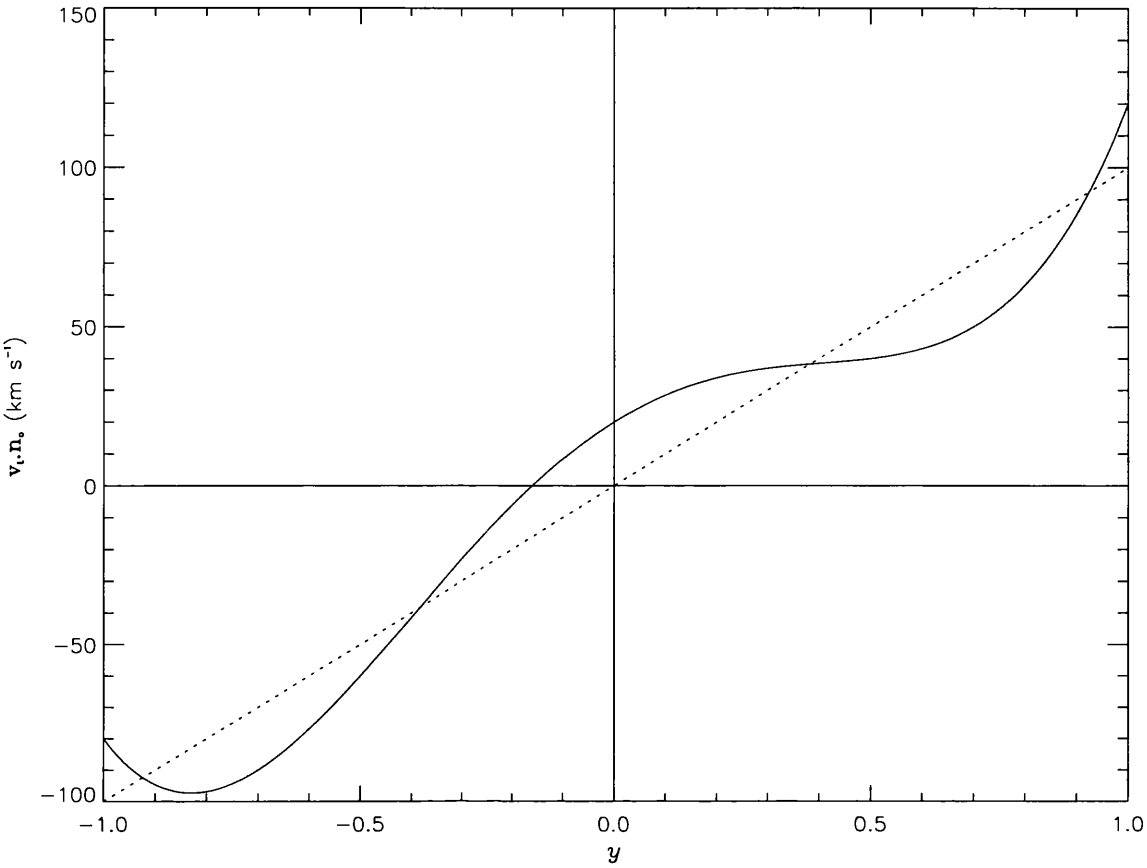

Figure 7.4: The total projected velocity plotted as a function of $y \equiv \sin\phi$ along the equator of a rotating star pulsating in an $l = 4$, $m = -4$ sectoral mode (solid); the underlying projected rotation velocity is also shown (dotted).

is satisfied. In the case of figure 7.4, this will occur at $y \approx -0.8$ and $y \approx 0.4$, corresponding to velocities of approximately -97 km s^{-1} and 38 km s^{-1} respectively.

Of course, this treatment deals only with the restrictive case of an equator-on sectoral mode, and furthermore considers only contributions from equatorial points to the disk-integrated spectrum. However, it does incorporate the most important points concerning lpv formation, and may be easily extended to cover the most general case. In particular, the above equation is generalized to

$$\nabla_d |\nabla_d (\mathbf{v}_t \cdot \hat{\mathbf{n}}_o)| = 0, \tag{7.24}$$

where y and z are the two parameters which uniquely specify a point on the disk, and ∇_d is given by

$$\nabla_d = \mathbf{e}_y \frac{d}{dy} + \mathbf{e}_z \frac{d}{dz}; \tag{7.25}$$

here, $\mathbf{e}_y$ and $\mathbf{e}_z$ are the unit vectors on the stellar disk.

7.5.4 The Detectability of Line-Profile Variations

Analyses of lpv in early-type stars over the past 15 years or so, beginning with that of Smith (1977), seem to suggest that these lpv predominantly arise from sectoral ($l = |m|$) pulsation (*e.g.*, Smith 1981; Vogt & Penrod 1983; Gies & Kullavanijaya 1988; Kambe *et al.* 1990; Reid *et al.* 1993; Howarth & Reid 1993; Hahula 1993). The question therefore arises as to whether this apparent bias is due to some underlying m-dependent excitation mechanism operating in these systems, or merely due to observational selection effects. The latter hypothesis has been put forward by a number of authors (*e.g.*, Smith 1978; Gies & Kullavanijaya 1988; Reid *et al.* 1993) as an *a priori* reason for considering all pulsation-originated lpv to be caused by sectoral modes alone; however, it appears that this hypothesis has never been tested with any degree of rigour.

Accordingly, this subsection looks into the comparative observational detectability of lpv due to a variety of non-radial pulsation modes. Time-series of 12 spectra were calculated for modes with $l = 10$ and $-m = 1 \ldots 10$, covering one observational period; only prograde modes were considered, since retrograde modes will lead to similar results, and the $m = 0$ zonal mode was not included for the reasons given in §7.5.2. For each value of m, the polar inclination i was varied from from 5° to 85° in steps of 10°; in all cases, the equatorial rotation velocity was maintained at 400 km s^{-1}. As before, $V_{\max}$ was taken to be 20 km s^{-1}, and the co-rotating period set at 2 hours. The spectral region considered extended from 4671Å to 4728Å in increments of 0.15Å, chosen to include the He II line at 4686Å and the He I line at 4713Å; this choice allows a consideration of the visibility difference between lines of differing species.

To obtain estimates of the observational detectability of lpv for each of these time-series, RDS (see previous section) were calculated for all values of m and i. Each RDS was then integrated in wavelength over the ranges 4686 ± 15Å and 4713 ± 15Å (which should ensure that any variability beyond the rotational line-width is included) to yield variability factors $\mathcal{V}$ for the 4686Å and 4713Å lines respectively. These variability factors represent the 'summed' RMS deviation from the mean spectrum, and should be a good indication of how easy lpv are to detect observationally.

Figure 7.5 plots the values of $\mathcal{V}$ calculated in this way, as a function of m and i for all of the modes considered. Both lines seem to exhibit a distinct ridge in $\mathcal{V}$ at an inclination of $i \approx 35°$, and, furthermore, the He I 4713Å line shows a pronounced peak in $\mathcal{V}$ at $i = 85°$ for the $m = -10$ sectoral mode. This same peak is somewhat smaller in the He II 4686Å line, probably because He II lines will be preferentially formed at the hotter poles (recalling that the model star is gravity darkened), whilst variability is confined primarily to equatorial regions in sectoral modes; this gravity-darkening selection effect is considered in greater detail in §7.5.8.

The non-negligible values of $\mathcal{V}$ for modes other than sectoral suggests that observational selection effects are unlikely to single out sectoral modes for preferential detection. Thus, it appears that the *a priori* reasons for considering observed lpv to be due to sectoral modes alone are invalid.

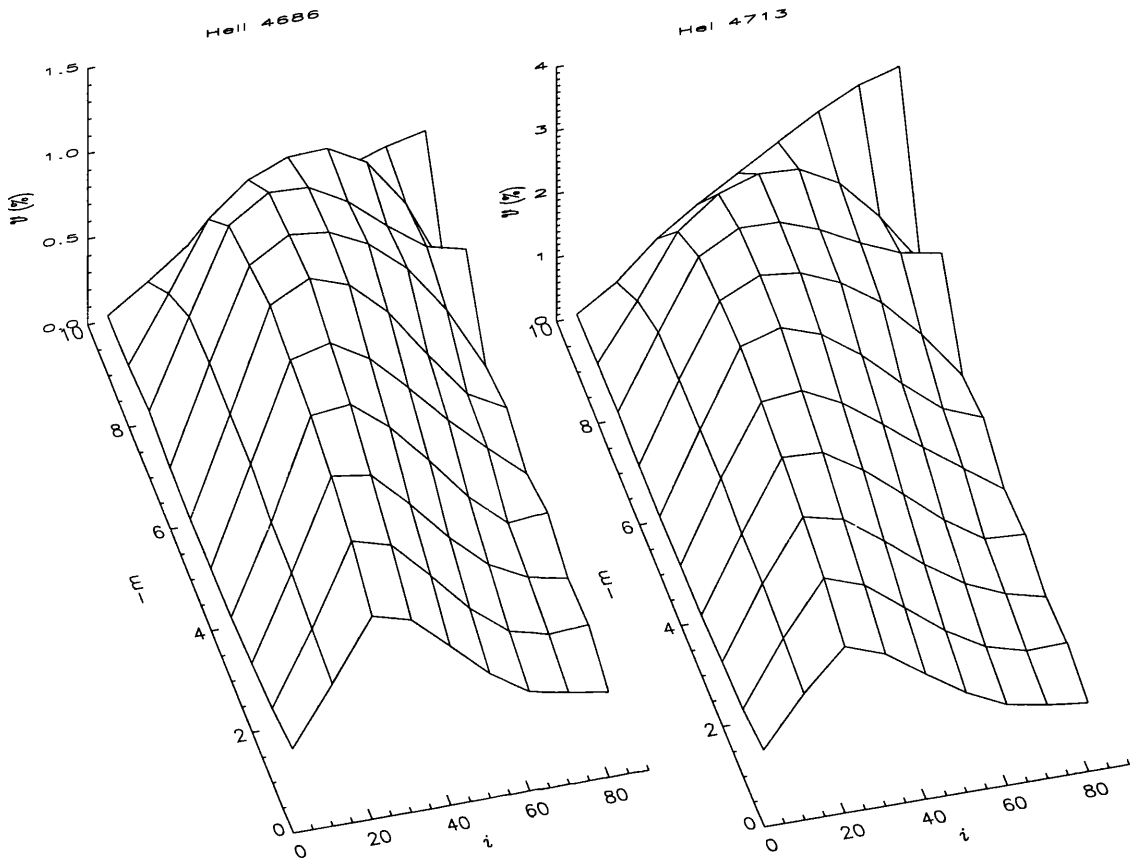

Figure 7.5: The variability factor $\mathcal{V}$ (as a percentage of the continuum) plotted as a function of azimuthal order m and inclination i for $l = 10$ models, in the He II 4686Å and He I 4713Å lines.

Accordingly, it is preferable that a re-analysis of existing observational data should be undertaken without the prior assumption of sectoral-mode pulsation. Once this is accomplished, the true underlying distribution of mode excitations may be calculated. If this distribution shows a marked bias towards some modes, important information concerning the excitation mechanisms prevalent in early-type stars may be inferred; in particular, if the distribution is highly m-dependent, it may be deduced that the excitation mechanism is intimately entwined with the rotation of these stars, since excitation mechanisms in non-rotating stars are independent of m.

7.5.5 The Diagnostic Potential of RDS

Currently, two principal approaches are used in the field to obtain pulsation parameters from observations of lpv. The first of these, introduced by Gies & Kullavanijaya (1988) and subsequently extended by Telting & Schrijvers (1997), relies on taking the Fourier transform along each wavelength bin of spectral time-series, and inferring values of l and m from the resulting Fourier phase

information; the Fourier amplitude information, which is broadly equivalent to the RDS introduced in §7.5.3, is not used in the analysis. The second approach, the so-called moments method, was introduced by Balona (1986), and calculates pulsation parameters based on the time-dependences of the spectral moments. Both of these approaches can yield useful information concerning the nature of underlying pulsation, but appear to share the common drawback that they do not compare lpv data from differing spectral lines.

Such a comparison is useful because each spectral line is formed in varying amounts at differing points on the stellar surface (due to gravity darkening); furthermore, each line possesses its own unique profile and temperature dependence. Accordingly, a comparison of the degree and form of variability between different lines can yield important information concerning underlying pulsation parameters. To demonstrate this, a number of models were calculated with $l = 4$ and $-m = 1, \ldots, 4$; in each model, $V_{\max}$ was set at 20 km s^{-1}, and the pulsation period *in the observational frame* was taken to be 2 hours (since it is this which is directly observed). The differing values of m will lead to different co-rotating periods, and thus different relative magnitudes of temperature and geometric perturbations. For each model, RDS were calculated using the method described in §7.5.3 for the He I lines at 4713Å and 6678Å, and for the He II lines at 4542Å and 4686Å; figure 7.6 illustrates these RDS for each value of m.

It can be seen from this figure that, for a given value of m, the RDS differ quite significantly from line profile to line profile. Furthermore, a change in m affects the RDS of each line profile in a different way; this occurs due to a combination of the change in the relative magnitude of temperature and geometric perturbations, and the different temperature sensitivities and profiles of each line.

The significance of these points is that the modelling of observed lpv using a single spectral line is to be treated with extreme caution. A set of proposed pulsation parameters may reproduce the observed variability in one line profile well, but lead to results dramatically different from observations in other profiles, due to the complex interplay between the two basic mechanisms (see §7.5.3) which generate line-profile variability. Thus, the simultaneous modelling (*i.e.*, with the same basic pulsation parameters) of many different lines is to be strongly recommended. Indeed, the significant differences between lpv from line profile to line profile should be viewed as highly serendipitous, since it means that it is unlikely that observed lpv can be reproduced with more than one set of pulsation parameters (which might occur if variability in only one profile is considered)

One important point about this discussion is that multi-line lpv modelling depends quite critically on the spectral synthesis approach adopted in the modelling. Accordingly, the following section investigates by how much the RDS depend on the different spectral synthesis approaches.

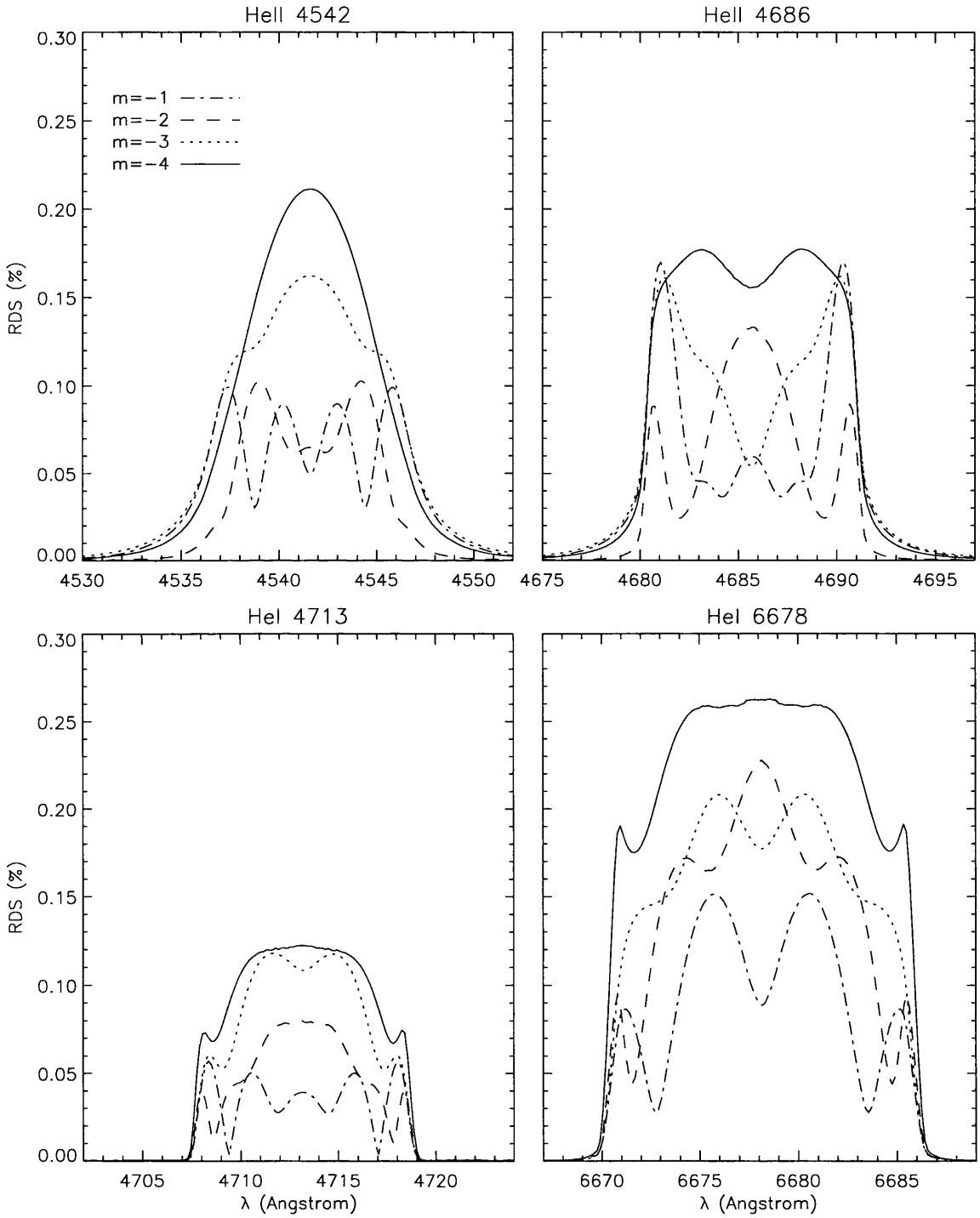

Figure 7.6: The RDS for $l = 4$, $-m = 1, \ldots, 4$ modes across the He I lines at 4713Å and 6678Å, and across the He II lines at 4542Å and 4686Å. In all cases, the pulsation period in the observational frame was set at 2 hours.

Table 7.3: The lines used by GKYLIE for spectral synthesis

Wavelength (Å)	Transition	Wavelength (Å)	Transition
4009.27	He I $1s2p\,^1P$–$1s7d\,^1D$	4685.68	He II 3s–4p
4101.74	Hδ 2s–6p	4713.14	He I $1s2p\,^3P$–$1s4s\,^3S$
4120.81	He I $1s2p\,^3P$–$1s5s\,^3S$	4861.33	Hβ 2s–4p
4143.76	He I $1s2p\,^1P$–$1s6d\,^1D$	5015.68	He I $1s2s\,^1S$–$1s3p\,^1P$
4168.99	He I $1s2p\,^1P$–$1s4s\,^1S$	5047.74	He I $1s2p\,^1P$–$1s4s\,^1S$
4199.83	He II 4s–11p	5411.52	He II 4s–7p
4340.47	Hγ 2s–5p	5875.63	He I $1s2p\,^3P$–$1s3d\,^3D$
4437.55	He I $1s2p\,^1D$–$1s5s\,^1S$	6678.14	He I $1s2p\,^1P$–$1s3d\,^1D$
4541.59	He II 4s–9p		

7.5.6 Spectral Synthesis Approaches

Historically, there exist a variety of approaches to spectral synthesis when modelling lpv, as is evident from §7.3.2. It is pertinent, therefore, to question whether these differing approaches lead to similar results, or whether some approaches are misleading due to an over-simplification of the underlying physics. This question is precisely the reason why the two KYLIE variants presented in §7.3.2, FKYLIE and GKYLIE, were developed; this section undertakes a comparison between these variants and the 'complete' version of KYLIE which uses the synthetic intensity spectra grids.

For the usual model star, perturbations due to an $l = 8$, $m = -8$ prograde sectoral mode were applied to the model using BRUCE, over a 24-point time-series covering the observational period of the pulsation. The period in the co-rotating frame was set at 2 hours, and $V_{\max}$ was chosen, as before, to be 20 km s^{-1}. The resulting perturbed model was passed to each of KYLIE, FKYLIE and GKYLIE for spectral synthesis and subsequent disk-integration; in the latter two codes, a limb parameter u of 0.3 was selected (see equation (7.20)), which provides a reasonable match to the observed continuum limb-darkening in the synthetic intensity spectra used by KYLIE. The lines modelled by GKYLIE are listed in table 7.3; this list has been chosen to exclude any blended lines, which are difficult to decompose into individual Gaussian fits. Spectra were calculated covering fragments of the 4000–7000Å wavelength range, chosen to include a number of hydrogen and helium lines. For each spectral time-series, RDS were calculated using the procedure described in §7.5.4. Figure 7.7 plots these RDS over the wavelength ranges considered, for the three spectral synthesis codes used; in comparing the results of GKYLIE with those of KYLIE and FKYLIE, it should be noted that comparisons are only valid for lines defined in table 7.3.

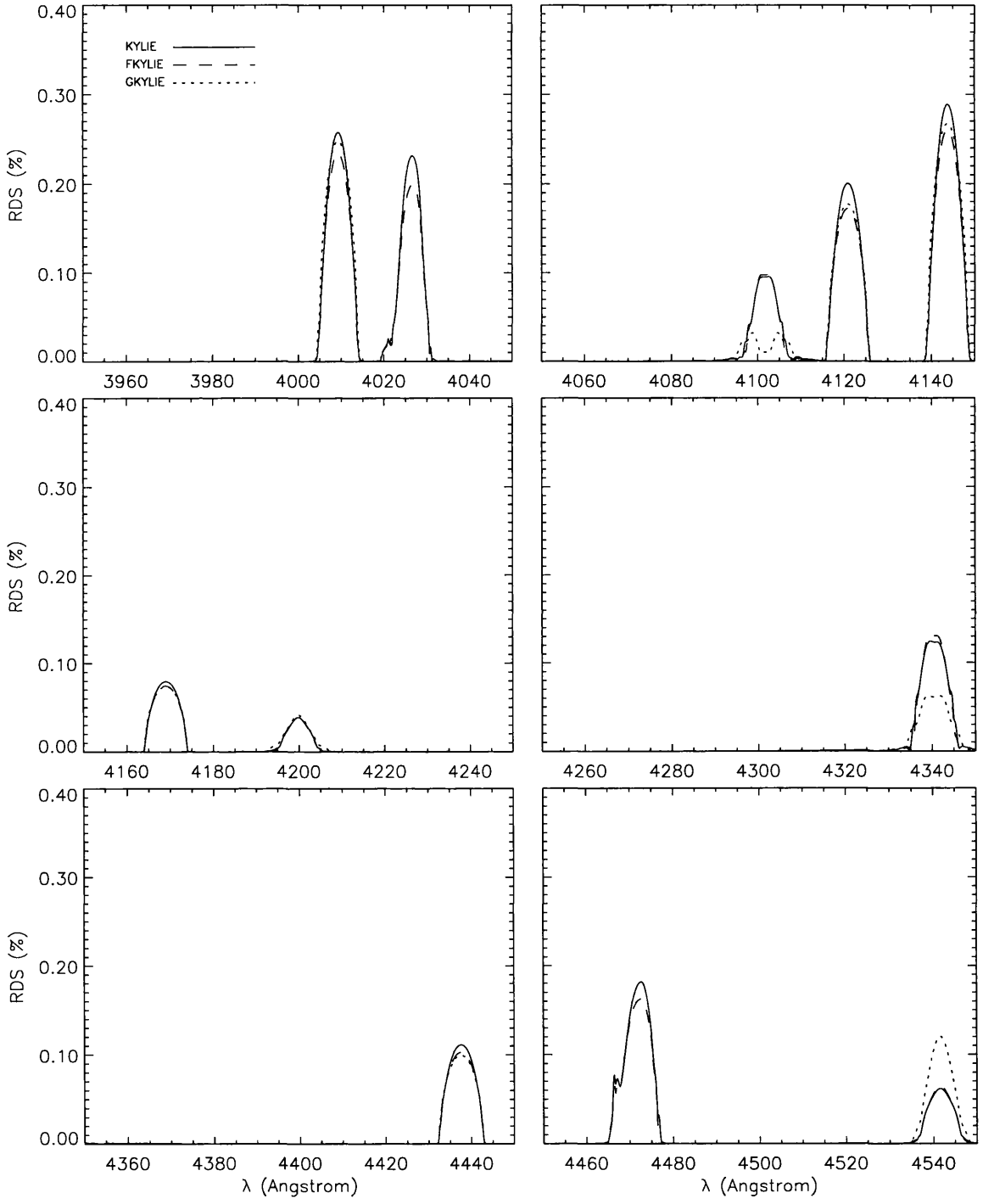

Figure 7.7: The RDS (as a percentage of the continuum) over various wavelength ranges for an $l = 8$, $m = -8$ pulsation mode, calculated using KYLIE, FKYLIE and GKYLIE.

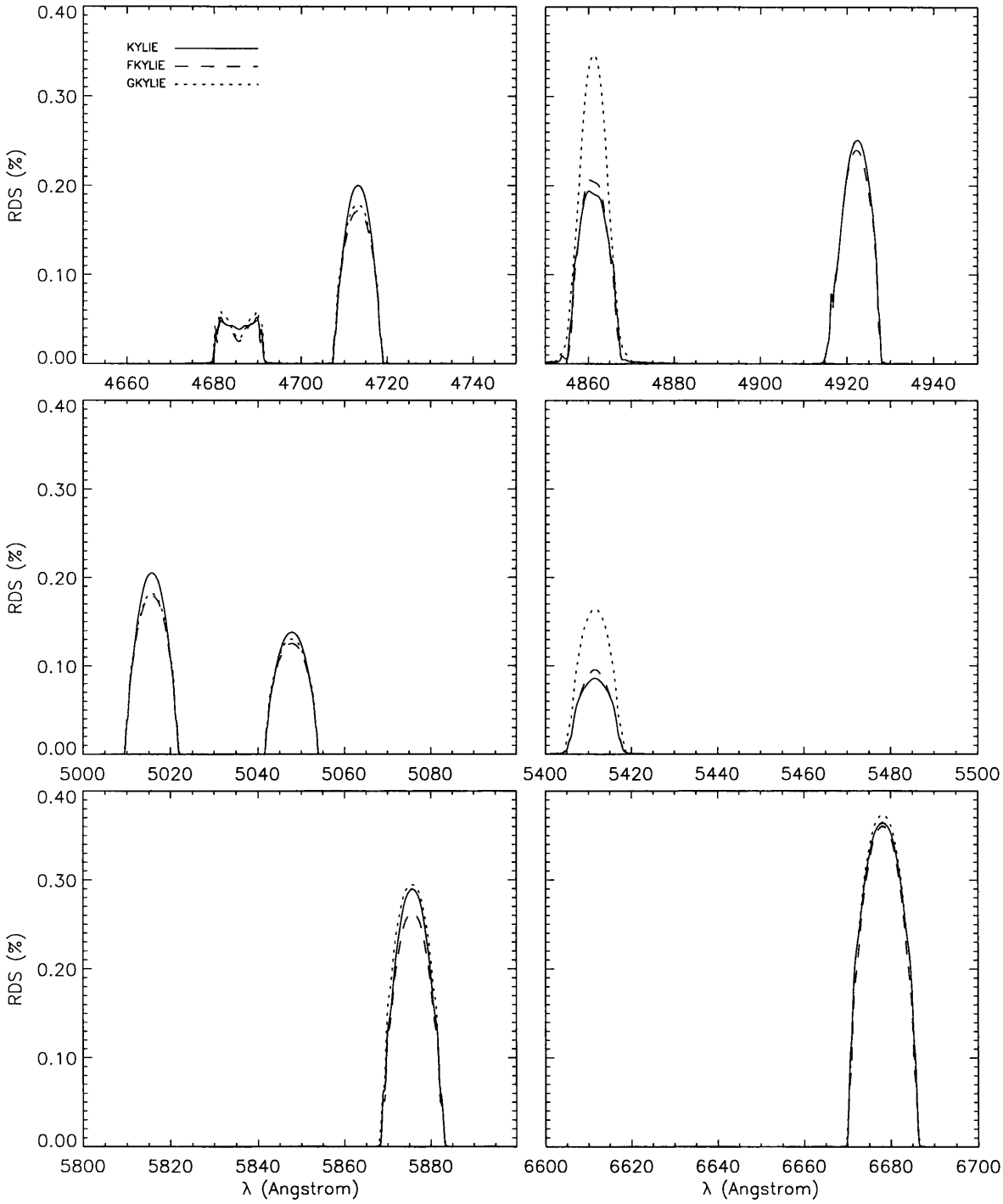

Figure 7.7 (cont): As before.

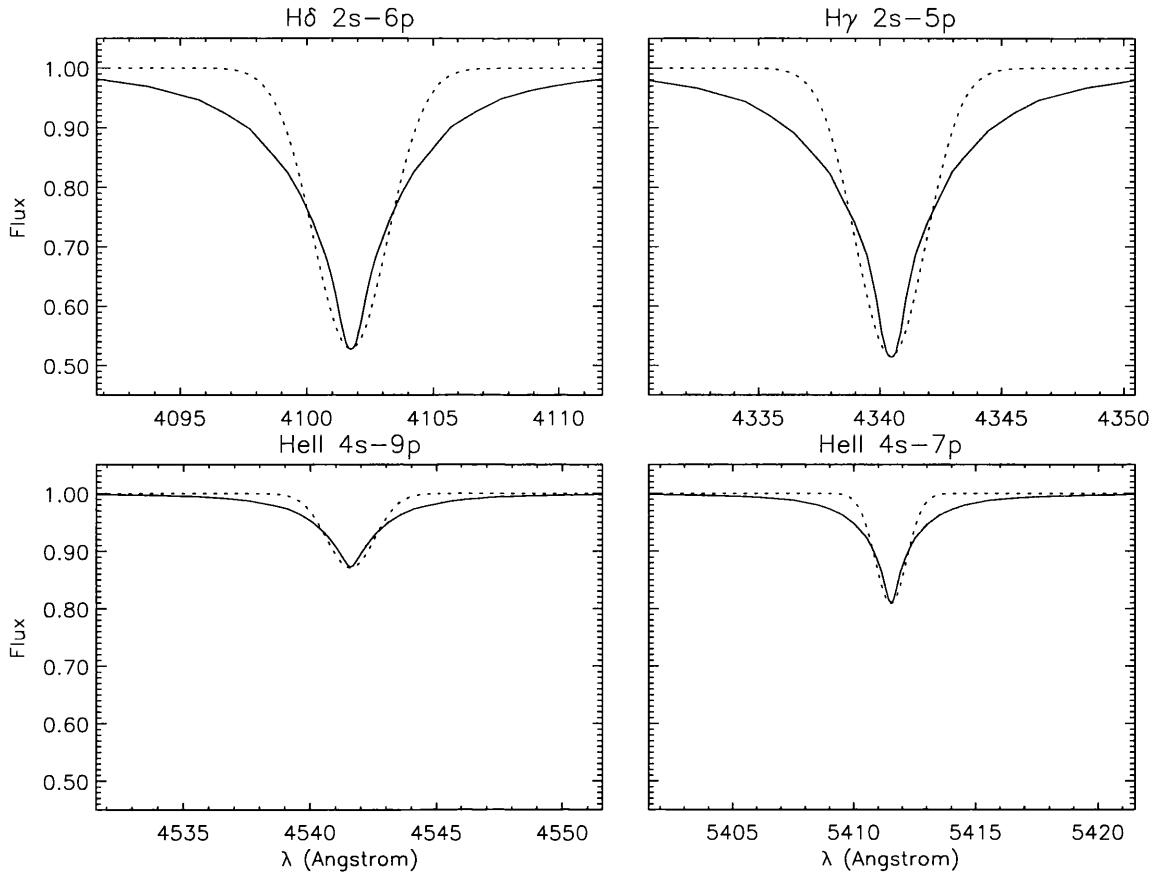

Figure 7.8: The Gaussian profiles (dotted) used by FKYLIE for the purposes of spectral synthesis; these are fits to flux spectra (solid), with the same depth and FWHM.

This figure demonstrates that agreement between the results of GKYLIE and KYLIE depends on which line is being considered; in some cases GKYLIE reproduces the results of KYLIE quite accurately, in others it over- or under-estimates the degree of variability. Particularly significant discrepancies occur for the lines at 4102Å, 4340Å, 4542Å, 4861Å and 5412Å. Since the Gaussian profiles used by GKYLIE are based on the flux spectra grids of FKYLIE, and the latter is not significantly discrepant with respect to KYLIE, the reason for the discrepancies must be determined by plotting the Gaussian fits to the flux spectra for these lines. Figure 7.8 shows these fits for four of the discrepant lines (two He II and two H), using the typical values of $T = 35000$K and $g = 3.8$ dex.

It is evident that, whilst the FWHM and depth of all Gaussians are in agreement with the flux spectra (as, indeed, they should be), the Gaussians seriously overestimate the profile wings; since these lines arise from H and He II transitions, they are subject to significant broadening due to a linear Stark effect, leading to the extensive wings which the Gaussians fail to reproduce. The corresponding broadening mechanism in He I lines is a quadratic Stark effect, due to the extra electron, which is much less effective than the linear Stark effect; accordingly, the Gaussian fits to these lines are much more satisfactory, as is the agreement between GKYLIE and KYLIE. It would therefore

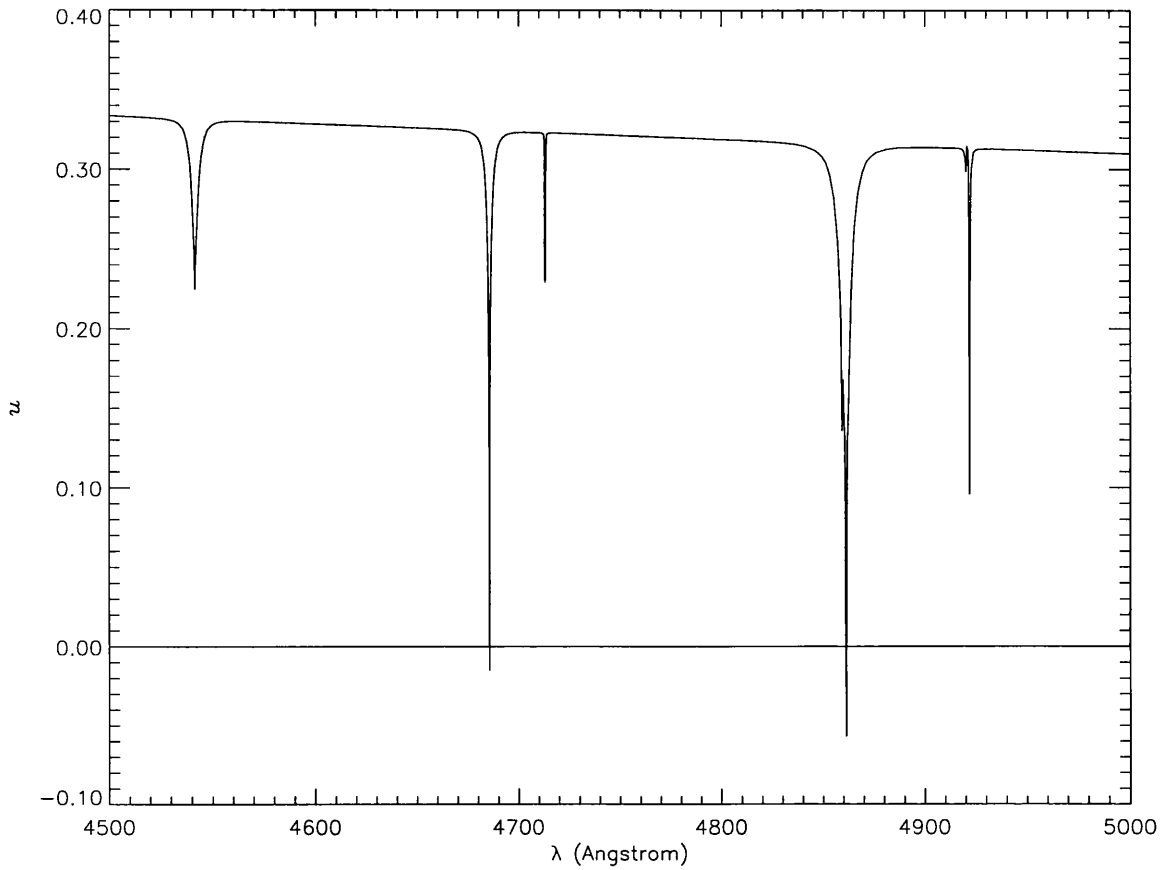

Figure 7.9: The limb-darkening coefficient u plotted as a function of wavelength for a model atmosphere at $T = 35000$K and $g = 3.8$dex.

appear that the use of Gaussian profiles in modelling lpv depends critically on how well the intrinsic line profiles are represented by Gaussians, reminiscent of the popular adage 'garbage in, garbage out'.

The results of FKYLIE are in reasonably good agreement with those of KYLIE. Any discrepancies between the two can be put down to the limb-darkening law used; whilst this law in the form of equation (7.20) is good at reproducing continuum limb darkening, it can be significantly in error in line profiles. To demonstrate this, figure 7.9 plots the limb-darkening parameter u as a function of wavelength for the previously-used values of $T = 35000$K and $g = 3.8$ dex. It is apparent that u changes quite appreciably from its continuum value across line profiles; indeed, in the case of Hβ, it actually becomes negative at the line centre, indicating that this line goes into emission at the limb. Accounting for this behaviour using a modified wavelength-dependent limb-darkening law is counter-productive, since the data requirements will probably exceed those of the full intensity spectra used by KYLIE.

To conclude, then, the use of Gaussian profiles in lpv modelling, even if temperature and gravity dependencies are incorporated, works well only for lines whose intrinsic profiles are well repro-

duced by Gaussians; in other cases, it may lead to significant under- or over-estimates of the degree of variability predicted. The use of flux profiles, calculated from model atmospheres, is to be preferred, although the inadequacy of limb-darkening laws may lead to some errors. The method of choice, however, is to use full angle-dependent intensity spectra (as KYLIE does), so that no inappropriate approximations are made in the spectral-synthesis part of the lpv modelling.

7.5.7 Continuum Variability

Spectroscopy does not represent the only approach by which pulsation-originated variability may be studied; photometry can also lead to useful information, and, indeed, was the method by which such variability was first detected. The advantages of photometric studies are that they can typically be conducted on much smaller telescopes than corresponding spectroscopic studies, and have generally better signal-to-noise performances (due to the integration of light over a range of wavelengths). However, there exists a drawback to photometry; as was demonstrated in §7.2.5, it is possible for a star to exhibit line-profile variability, but ostensibly no photometric variability.

To investigate whether this possibility can actually occur, and, more generally, to examine typical values for the amplitude of photometric variability, four sets of models were calculated for an $l = 2, m = -2$ pulsation mode, with a co-rotating period ranging from 1 to 30 hours in 100 equally-spaced steps. The first three of these sets included only the effects of temperature, surface area and surface normal perturbations respectively (velocity perturbations were also included, but these will have a negligible effect on continuum variability); the fourth set included the combined effects of all three of these perturbations. In all cases, $V_{\rm max}$ was set at 20 km s^{-1}.

For each value of the period in each set, the time-dependence of the continuum intensity at 5100Å (chosen to be well-separated from spectral lines) was decomposed into a complex Fourier series representation. Figure 7.10 plots the resulting sinusoidal semi-amplitudes and phases at the pulsation frequency as a function of period, for the four model sets; the semi-amplitudes are expressed in magnitudes. The first and higher overtones of the pulsation frequency were found to have negligible amplitudes, and so are not plotted.

It is evident from inspection of this figure that the photometric zero, anticipated when the variability due to all three perturbations cancels, does indeed occur, at a co-rotating period of approximately 23 hours; this corresponds to an observational period of 9.3 hours. If this model star pulsates at, or near, this period, therefore, it will exhibit lpv but no ostensible photometric variability. Hence, a certain degree of caution must be exercised when using photometry to analyze, and indeed discover, variability due to non-radial pulsation. Multi-band photometry should be used overcome this problem, since the temperature perturbation coefficient χ_3 (equation (7.15)) and the limb-darkening coefficient u (equation (7.20)) are wavelength-dependent; if complete cancellation occurs at one wavelength, it will not, in general, occur at another wavelength.

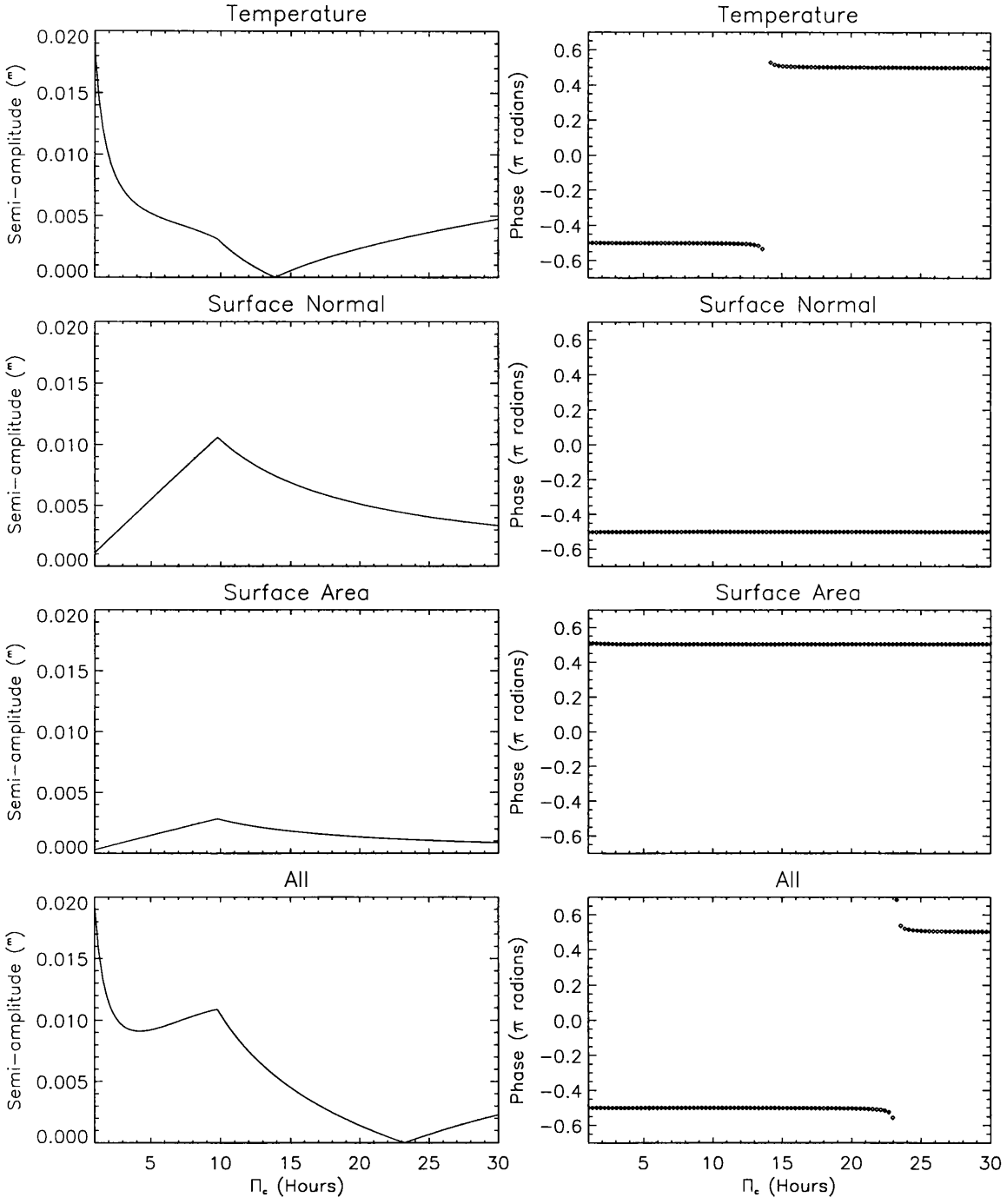

Figure 7.10: The sinusoidal semi-amplitudes (left) and phases (right) for the intensity variations of the 5100Å continuum point, calculated for models containing temperature perturbations, surface normal perturbations, surface area perturbations, and the combined effects of all three perturbations.

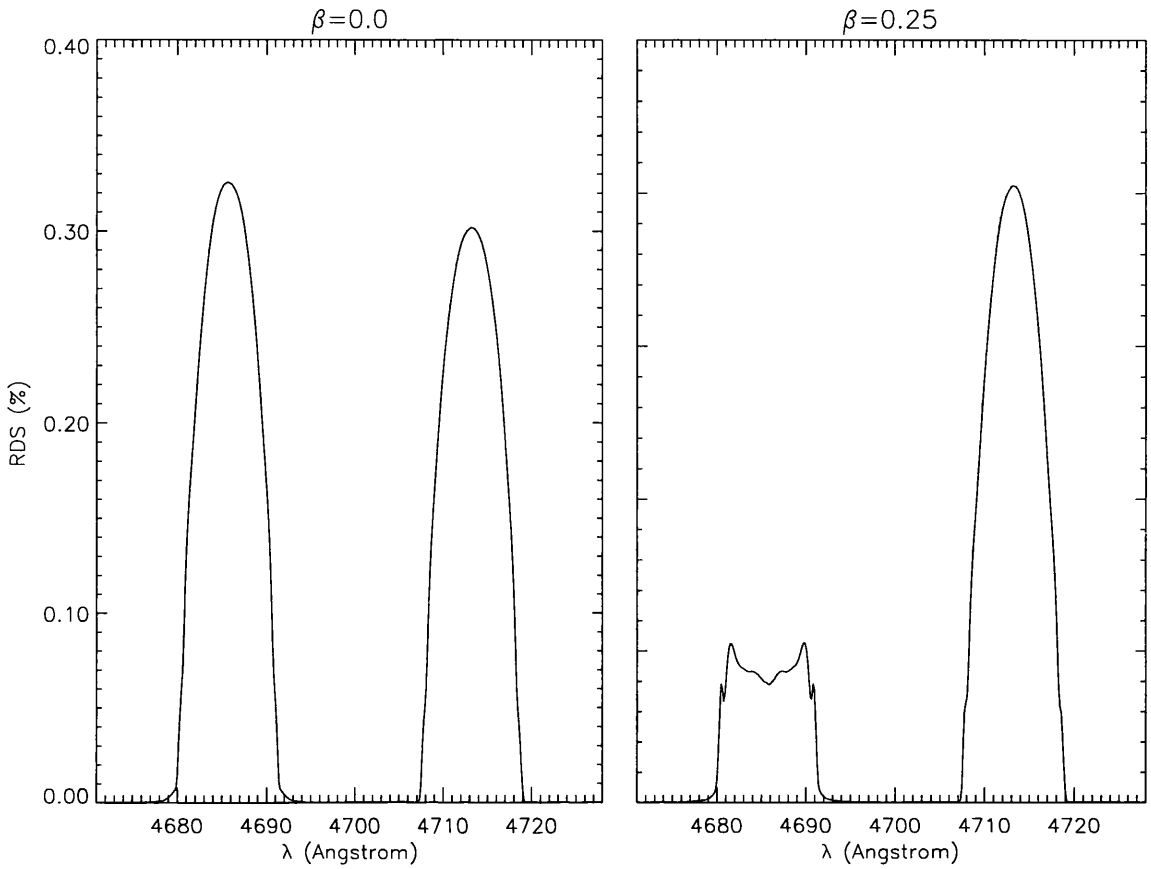

Figure 7.11: The RDS (as a percentage of the continuum) for an $l = 8$, $m = -8$ sectoral pulsation mode, calculated with a gravity-darkening parameter β of 0.0 (left) and 0.25 (right), corresponding to models without and with gravity darkening respectively.

In cases where the three perturbations discussed do not completely cancel one another, the model star does exhibit some degree of photometric variability. However, this variability is typically small when compared with the degree of variability exhibited by classical (δ) Cepheid pulsators; over the range of periods shown in figure 7.10, it attains a maximum amplitude of only approximately 0.02 magnitudes. Whilst this maximum amplitude depends on the pulsation velocity amplitude, the value of 20 km s^{-1} adopted herein is quite close to the local sound speed on the stellar surface, and therefore can be considered to be a reasonable upper limit. Thus, even when photometric cancellation does not occur, stars undergoing non-radial pulsation will exhibit photometric variability which is typically small.

One point concerning figure 7.10 which merits a mention is the discontinuity in the sinusoidal amplitude gradient which occurs at a period of approximately 10 hours. This discontinuity arises due to the velocity amplitude normalization adopted, since at this period the maximum pulsation velocity changes from being dominated by radial fields to being dominated by horizontal fields; it therefore has no physical importance.

7.5.8 Pulsation and Gravity Darkening

Observations of lpv in rapidly-rotating early-type stars show that line-profile variability often appears to be weakest in lines of species of highest ionization (Walker 1991; Reid *et al.* 1993). Walker (1991) has suggested that, since these lines will be preferentially formed towards the (hotter) poles in a gravity-darkened star, this phenomenon arises from modes in which the pulsation activity is confined towards the equator, namely sectoral modes and modes with small $(l - |m|)$. This argument has been used as an *a priori* reason for modelling lpv with sectoral modes when the variability/ionization correlation is observed.

To investigate this hypothesis, two sets of 24 spectral time-series were calculated for an $l = 8$, $m = -8$ sectoral mode, pulsating with a co-rotating period of 2 hours and a maximum velocity amplitude of 20 km s^{-1}. The first set was calculated in the normal manner, whilst the second set was calculated using a gravity-darkening parameter β of 0 (see equation (7.8)); this choice will completely suppress any gravity darkening, so that the entire stellar surface has an equilibrium temperature of 38000 K. For each set, RDS were calculated for the 4686Å He II line and the 4713Å He I line; figure 7.11 illustrates the RDS for both lines.

It is apparent that the inclusion of gravity darkening leads to a significant reduction of the variability observed in the 4686Å He II line, in agreement with a similar result found by Gies (1996) (there is also a small increase in the variability of the He I 4713Å line due to an overall cooling of the model star). It is quite possible that this reduction would render variability in this line unobservable, and it would thus appear that the mechanism proposed by Walker (1991) for the observed variability/ionization correlation does indeed work. However, it should be remembered that this mechanism will work for any mode with a suitable degree of equatorial confinement, and not just sectoral modes. As was demonstrated in §6, one of the effects of rapid rotation is to confine pulsation activity towards equatorial regions for *all* modes. Therefore, it is important not to take observations of variability/ionization correlations as irrefutable evidence of pulsation in sectoral or low $(l - |m|)$ modes.

7.5.9 Wave Leakage

In both §3.5 and §5.6, the possibility of wave leakage through the stellar surface was considered in some detail, and it was pointed out that one consequences of wave leakage is that y_2 will undergo a phase shift (see figure 5.12) with respect to y_1. This phase shift will mean that both horizontal velocity and temperature perturbations will no longer be in phase with the radial velocity perturbations. As a consequence, the line-profile variability of a star with wave leakage through the outer boundary will show a wavelength asymmetry.

To demonstrate this, models were calculated for all of the $l = 2$ f- and p-modes modes of *CoStar*

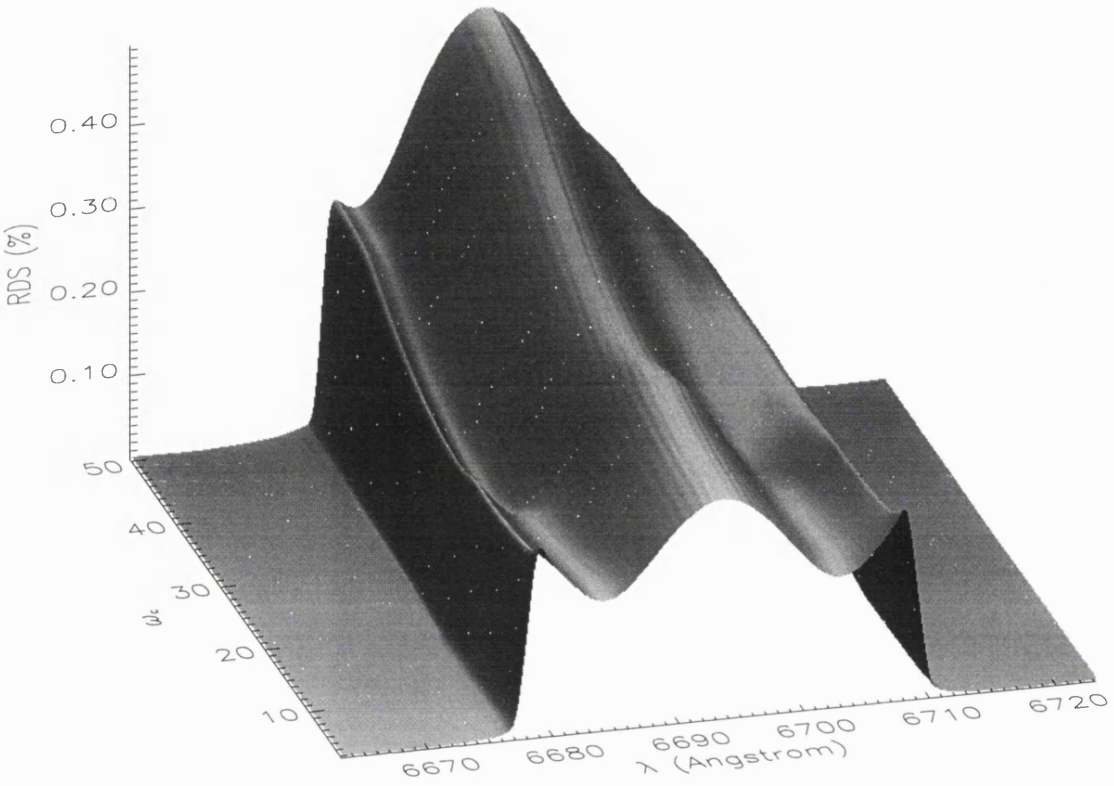

Figure 7.12: The RDS (as a percentage of the continuum) plotted as a function of co-rotating dimensionless frequency ω_c for an $l = 2$, $m = -2$ sectoral mode. For $\omega_c \gtrsim 10$, wave leakage occurs through the stellar surface, leading to the definite asymmetry in the RDS.

model 6, based on the eigenfrequencies found in §5.6. The y_1–y_2 phase displacements were incorporated in the horizontal velocity and temperature perturbations; $V_{\max}$ and m were assigned the values 20 km s^{-1} and -2 respectively. For each mode, time-series of 24 spectra were calculated for the He I 6678Å line, and the corresponding RDS evaluated. Figure 7.12 plots these RDS as a function of co-rotating dimensionless frequency ω_c; at points between the discrete eigenfrequencies of modes, the RDS has been interpolated using cubic splines to generate a continuous function of frequency.

It is evident from this figure that, for modes with $\omega_c \gtrsim 10$, the RDS become progressively more asymmetric, with the peak variability shifting towards the blue wing of the line profile. This shift will be caused primarily by the phase-displaced temperature perturbations, since the horizontal velocity fields for these modes become negligible as ω_c is increased. If observations of a pulsating star show such an asymmetry, and non-adiabatic temperature perturbations can be ruled out (since these will also cause an asymmetry), then it can be deduced that the star has a certain degree of

wave leakage through the surface and presumably into the wind.

The importance of this point is that the detection of lpv asymmetry in this manner would provide the first evidence of a causal link between photospheric and wind variability. This link, usually known as the 'photospheric connection', has long been mooted (see Fullerton *et al.* (1996) for a review of the topic), but has never been placed on a sound physical grounding, nor has a means of detecting its existence been developed; a search for lpv asymmetry could provide these means. Interestingly enough, observations of the O supergiant ζ Pup by Reid & Howarth (1996) show lpv asymmetry in a number of lines, but the variability is biased towards the red (rather than blue) wings of line-profiles. However, it should be noted that g-mode pulsation will generally show a red-wing asymmetry bias when leakage occurs; since the period of the lpv in ζ Pup is consistent with g-mode pulsation, and the wind of this star exhibits variability consistent with co-rotating streaming from the surface, it would appear that the asymmetry observations of Reid & Howarth (1996) represent the first evidence of a photospheric connection at work. ζ Pup is a very likely candidate for wave leakage in any case, due to its extended envelope and well-developed wind.

On a final note, however, the results presented herein should be treated with some degree of caution, since the phenomenon of wave leakage is still poorly understood. One point which should be raised is that equation (3.48), used to calculate the temperature perturbations within BRUCE, is based on the boundary-condition formulation of Dziembowski (1971), rather than that of Unno *et al.* (1989), and, accordingly, the results may well possess significant quantitative errors (the qualitative conclusions should still stand, however). Evidently, this topic requires further investigation, since there would be a certain aesthetic appeal to being able to group photospheric and wind variability together as a result of the same basic pulsation mechanism; even if this is not possible, a thorough study should be able to pin down the reason for periodic wind variability.

Chapter 8

Summary

8.1 Review

Over the preceding six chapters, the theory of non-radial pulsation in early-type stars has been developed, from the derivation of the basic pulsation equations in Chapter 2, right through to their application in the spectroscopic modelling undertaken in Chapter 7. This chapter presents a general review and summary of some of the points raised throughout the thesis; it is a somewhat shorter summary than would be found in a more observationally-based work, due to the absence of any specific, individual result, but it aims to highlight some of the more important conclusions from each chapter, and look towards future work that may be undertaken

In Chapter 2, the equations of adiabatic NRP were derived from the basic equations of hydrodynamics. One important assumption made in this derivation was that all perturbations to the star were small, so that the equations were linear in all dependent variables. This linearization can be found in almost every theoretical treatment of non-radial pulsation, since it leads to a system of equations which is both mathematically and numerically tractable. Unfortunately, it may be an over-simplification; to appreciate this, consider that unstable pulsation modes will not grow in amplitude indefinitely, but eventually be stabilized at some definite amplitude by the action of non-linear dissipative effects. Thus, it is evident that stable pulsation observed in any star will be occurring at amplitudes were non-linear effects are significant, and that any comprehensive treatment should incorporate these effects in some way. Furthermore, phenomena such as the mode-switching observed in 53 Per (Smith 1978) and other stars are impossible to explain without reference to non-linear models. Whilst non-linear radial pulsation has been considered by some authors (Fadeyev & Lynas-Gray 1996), progress in the study of non-linear NRP remains very slow (see Gautschy & Saio (1995) for a review of recent developments). Nevertheless, it remains one area of stellar pulsation which definitely requires investigation in the future, not only for the reasons mentioned, but also for an understanding of the chaos which is apparently inherent in some

systems undergoing NRP (Dappen & Perdang 1985; Perdang 1991).

Another important approximation made in Chapter 2 was that of adiabacity, whereby heat transfers between adjacent oscillating fluid parcels are neglected. This approximation was made primarily to keep the derivation of the pulsation equations, and their subsequent solution, at a relatively simple level. Whilst it is generally a good approximation for p-modes and low-order g-modes in early-type stars (see, for instance, the discussion in §3.6), cases where it is seriously in error, such as extreme helium stars, should use the well-developed non-adiabatic theory instead.

Chapter 3 presented the boundary conditions which must be applied to the pulsation equations before solution can be achieved. The boundary-condition formulations of both Dziembowski (1971) and Unno *et al.* (1989) were derived and discussed, with particular emphasis on the latter, since it admits cases where the leakage of progressive waves through the stellar surface may occur. This leakage, whilst mentioned by Unno *et al.* (1989), still remains one area of pulsation in early-type stars which merits considerably more investigation. It is possible that it plays a significant role in the wind variability and episodic mass loss which are observed in many early-type stars; if this is the case, all types of variability in these stars could be unified under the mantle of a single underlying mechanism. Whilst an investigation of some issues regarding trans-photospheric wave leakage was undertaken in Chapter 3, the discussion was somewhat speculative due to a paucity of any comprehensive, self-consistent models of the phenomenon. Cranmer (1996) and other authors have made some progress from the 'wind side' of the problem, so perhaps now is the time when a commensurate effort can be made from the 'pulsation side', to produce a unified model.

With the basic equations and boundary conditions discussed in Chapters 2 and 3 respectively, Chapter 4 presented stellar structure models suitable for investigation with these equations. The emphasis of this chapter was primarily on implementation, with a derivation of the dimensionless variables of Dziembowski (1971) for polytropic stars, and an in-depth discussion of the use of *CoStar* models in pulsation studies. The latter represent the state-of-the-art in stellar structure and evolution calculations, and therefore their use in pulsation models is to be recommended, as they incorporate the latest advances in their field.

However, as was demonstrated in the chapter, they require a significant amount of numerical manipulation before they can be considered useable, and it is for this reason that better collaboration between the stellar structure and stellar pulsation fields is imperative, perhaps in the form of structure models specifically calculated for the purposes of pulsation modelling. This has been accomplished to some extent by authors such as Gautschy & Glatzel (1990*b*), who generate their own 'home-brew' structure models, but such an approach may lead to the use of models which are not as up-to-date as would be preferred.

Chapter 5 combined the results of the preceding three chapters with a code, EVOLVE, to generate solutions of the pulsation equations for the *CoStar* models. The asymptotic solution technique

of Tassoul (1980) was reviewed, but it was stressed that its applicability to early-type stars is somewhat limited by the low radial order n of most modes observed in these stars. Two complementary numerical solution approaches were also presented, the shooting and relaxation techniques, and the latter of these was used for actual solution of the pulsation equations in the case of the *CoStar* models. Whilst this technique, based on the algorithm of Henyey *et al.* (1964), is quite powerful, it was found that a great amount of time and effort was required to ensure that convergence towards desired solutions was achieved. In retrospect, the Riccati shooting method introduced by Gautschy & Glatzel (1990*a*) appears to be a preferable approach, judging from the sheer quantity and quality of results produced by these authors, and, if Chapter 5 were to be repeated, this approach would definitely be implemented.

Once solution of the pulsation equations was achieved in §5.4, the avoided crossings exhibited by *CoStar* model 151 were discussed, with a demonstration of the exchange of modal properties over such a crossing. The vibrational stability of both models was investigated in §5.5 using the quasi-adiabatic treatment introduced by Osaki & Hansen (1973), with a discussion of the various excitation mechanisms which arise from terms appearing the work integral. It was found that, in both *CoStar* models, many p-modes and all g-modes exhibited some degree of instability; in the case of the former, this excitation was shown to be due to a κ-mechanism caused by iron-group transitions above 100,100 K, whilst the latter were found to be excited by a combination of this κ-mechanism and a δ-mechanism operating in the thin convective shell at $6.2 \lesssim \log p \lesssim 7.0$. These results are very interesting, since they suggest that the κ-mechanism thought to be responsible for pulsation in β Cepheids (Cox *et al.* 1992) will also operate in early-type main-sequence stars. However, they should be treated with some caution, since perturbations to the convective flux were neglected, and the treatment was quasi-adiabatic; accordingly, this investigation should be followed up by a full non-adiabatic one.

The closing section of Chapter 5 looked again into the issue of trans-photospheric wave leakage. It was demonstrated that all $l = 2$ modes of *CoStar* model 6 above $\omega \approx 11$ will not be reflected at the outer boundary, and therefore leak through the stellar photosphere; such leakage was found to be quite significant, with an e-folding time for pulsation decay due to the energy loss as low as 12.4 hours. All leaking modes exhibited a phase displacement between the radial and pressure perturbations at the stellar surface, in some cases as large as 0.4π radians. Again, it is stressed that these results are derived at a very basic level, and that a proper treatment of leakage should be high on the agenda of future work.

The apparent incidence of significant rotation in early-type stars means that its effects on pulsation should be included in any comprehensive treatment. A consideration of such effects was accomplished in Chapter 6; the size of this chapter is commensurate with the considerable richness which rotation introduces into pulsation theory. It was demonstrated that, whilst the centrifugal

force will only modify the pulsation equations through corresponding modifications to the equilibrium stellar structure, the coriolis force leads to modifications of the pulsation equations themselves, generating new types of wave propagation. It is for this reason that effects of the coriolis force were examined in detail, with a discussion of the two principal techniques currently used to account for these effects. The first of these, the PE technique, was discussed briefly, with an examination of its inherent limitations, whilst the second, the ST technique, was derived in its entirety from the completely general matrix method introduced by Berthomieu *et al.* (1978) and Lee & Saio (1986).

The ST technique was covered in detail, with a presentation of its derivation and a subsequent discussion of how rotation modifies pulsation through the introduction of convective and quasi-toroidal pulsation modes. Particular emphasis was placed on the implementation of ST, since it represents a major component of the work undertaken herein. The effect of rotation to compress pulsation activity towards the equator for both retrograde and prograde modes was demonstrated, and the limitations of ST were discussed. The chapter closed with a comparison between ST and PE, with the conclusion that, whilst both represent useful approaches, the former is better suited to the modelling of lpv in rotating stars.

Based on all of the developments in the preceding chapters, Chapter 7 presented two codes, BRUCE and KYLIE, which together calculate time-resolved, disk-integrated non-LTE spectra for a rotating, gravity-darkened star undergoing multi-mode non-radial adiabatic pulsation; the development of these codes represents a major part of the work for the thesis. The codes were compared with other approaches used for lpv modelling in §7.4; whilst they probably represent the most sophisticated models currently available, there is still room for much improvement. In particular, a full implementation of the theory of Lee & Baraffe (1995), which incorporates the effects of the coriolis *and* centrifugal forces on pulsation, would represent a great advance in the field of lpv modelling, since the ST technique used in BRUCE to model the surface pulsation fields is strictly applicable only to low-frequency modes.

BRUCE and KYLIE were used in §7.5 to investigate some aspects of line-profile variability. It was demonstrated in §7.5.3 that velocity and temperature perturbations are the only significant mechanisms in lpv formation; these mechanisms were therefore discussed in some detail, with particular attention to the former. In §7.5.4, the visibility of lpv due to different NRP modes at different inclinations was investigated; it was found that the *a priori* assumption by some authors that the majority of lpv are due to sectoral-mode pulsation is probably unjustified. Since the statistical occurrence of different pulsation modes contains important information concerning the excitation mechanism responsible for NRP in early-type stars, it is therefore imperative that old data be re-examined in the light of this dubious assumption.

The importance of wavelength-resolved lpv amplitude information, in addition to the phase information currently used by many authors, was highlighted in §7.5.5; a comparison of the amplitude

of variability between different spectral lines can lead to additional information concerning the surface morphology of pulsation modes. However, such a comparison is dependent on the lpv model spectral synthesis approach used; it was demonstrated in §7.5.6 that model results have a significant dependence on this approach, and that the use of temperature- and gravity-sensitive Gaussian synthetic profiles is insufficient. Whilst temperature- and gravity-sensitive synthetic flux profiles produced results in general agreement with corresponding intensity profiles, some discrepancies were observed due to the wavelength-dependence of the limb-darkening law adopted; the use of fully-angle dependent intensity spectra in lpv modelling was therefore advocated.

One interesting issue raised in §7.5.7 was that continuum (photometric) variability arising from temperature and geometric perturbations may vanish at certain pulsation periods due to a cancellation effect. This will have an impact on attempts to both discover and analyse NRP; in such cases, multi-band photometry must be used to resolve the problem. In any case, photometric variability is typically small for early-type stars undergoing NRP, and so the parallel observation of line-profile variability is to be recommended.

The incidence of rapid rotation in a number of early-type stars means that gravity darkening will be significant in many of these systems. Walker (1991) has suggested that this gravity darkening, when combined with equatorially-confined pulsation activity, can explain the apparent correlation between the ionization state and degree of line-profile variability observed in many stars; this hypothesis was supported in §7.5.8, which demonstrated that variability in the (pole-formed) He II 4686Å line-profile is significantly reduced for an equatorially-confined sectoral mode when the effects of gravity darkening are introduced. However, it was stressed that this ionization/variability correlation should not be used as an *a priori* reason for the exclusive consideration of sectoral modes, since, as was demonstrated in Chapter 6, rotation can confine the pulsation activity of *all* types of modes to equatorial regions.

Chapter 7 was concluded in §7.5.9 with a return to the topic of trans-photospheric wave leakage. Using the phase displacements found in §5.6 for *CoStar* model 6, lpv were calculated as a function of pulsation period for a leaking $l = 2$ sectoral mode. It was found that wave leakage introduces a blue-wing biased asymmetry in lpv for p-modes, representing the first ever observational diagnostic for wave propagation through the stellar photosphere and into the wind. Furthermore, it was pointed out that lpv asymmetry appearing in the observations of ζ Pup by Reid & Howarth (1996) could be attributed to such leakage, providing evidence for the long-mooted 'photospheric connection' between photospheric and wind variability.

8.2 Future Directions

With the work undertaken so reviewed, it is now pertinent to look towards the future direction of research into NRP of early-type stars. Whilst the theoretical foundations of such research are gen-

erally well-developed, there is a conspicuous paucity both of models which implement the theories, and of observations suitable for confrontation with the theories. The former problem has (one hopes!) been addressed to some extent by this thesis, although there remains considerable scope for progress; the latter problem, unfortunately, has no realistic solution in sight.

The real difficulty lies in the small number of pulsation modes detected in early-types stars. The application of the technique of asteroseismology to the Sun (*i.e.*, helioseismology) has only really proven successful due to the large number of different pulsation modes detected, and also due to the fact that pulsation perturbations on the solar disk may be directly observed. Whilst indirect disk imaging of pulsation in nearby stars may be accomplished using techniques such as interferometry, the low incidence of early-type stars in the galaxy means that they are typically observed at distances too large for such approaches. Furthermore, observations of such stars have detected to date at most only four distinct modes (*e.g.*, Reid *et al.* 1997), far too few for the application of asteroseismology. With the cancellation of the proposed STARS satellite (Fridlund *et al.* 1994), whose remit was the photometric analysis of variable stars, a resolution of these problems does not appear to be imminent.

However, there are still many opportunities for progress in the field. Whilst lpv modelling has met with some degree of success in the past, particularly with the 53 Per class of pulsators, there remain many cases where observations cannot be accurately reproduced by current models; for example, the so-called 'k-problem' discussed by Smith (1986) still awaits solution. The theoretical focus of this thesis, and simple considerations of time and space, have meant that it was not possible for a comprehensive confrontation between the models presented and recent observations; such a confrontation should be high on the list of future work, as BRUCE/KYLIE might be able to resolve some of the current modelling problems.

Accordingly, any interested parties are invited to contact the author (either by conventional mail or via email at [1]) regarding obtaining the FORTRAN source code for BRUCE. It is hoped that, by making BRUCE freely available, the confrontation between theory and observations can occur as quickly as possible. Unfortunately, the corresponding source code for KYLIE cannot be made similarly available, since the grids of intensity spectra which it uses are not formatted for distribution; it is anticipated that authors will write their own disk-integration codes for use with BRUCE.

In summary, then, the study of non-radial pulsation in early-type stars is still in its dawn, awaiting comprehensive confrontation between *recent* theories and observations. The focus on implementation in this thesis has hopefully moved the field one step closer to this goal, and the author looks to the future development of early-type star pulsation with great interest.

[1] rhdt@star.ucl.ac.uk

Bibliography

Abramowitz, M. & Stegun, I., 1964, *Handbook of Mathematical Functions*, volume 55 of *Applied Mathematics Series* (National Bureau of Standards, USA)

Aerts, C. & Waelkens, C., 1993, *A&A*, **273**, 135

Aerts, C. & Waelkens, C., 1995, *A&A*, **293**, 978

Aizenman, M. L., Smeyers, P. & Weigert, A., 1977, *A&A*, **58**, 41

Arfken, G., 1970, *Mathematical Methods for Physicists* (Academic Press, London)

Baade, D., 1984, *A&A*, **135**, 101

Baker, N. & Kippenhahn, R., 1965, *ApJ*, **148**, 868

Balona, L. A., 1986, *MNRAS*, **219**, 111

Barker, P., 1986, *PASP*, **98**, 44

Berthomieu, G., Gonczi, G., Graff, P., Provost, J. & Rocca, A., 1978, *A&A*, **70**, 597

Berthomieu, G. & Provost, J., 1983, *A&A*, **122**, 199

Boas, M. L., 1983, *Mathematical Methods in the Physical Sciences* (John Wiley & Sons, Singapore)

Boury, A., Scuflaire, R., Noels, A. & Gabriel, M., 1980, *A&A*, **85**, 20

Brassard, P., Fontaine, G., Wesemael, F., Kawaler, S. D. & Tassoul, M., 1989, *ApJ*, **367**, 601

Buta, R. J. & Smith, M. A., 1979, *ApJ*, **232**, 213

Castor, J. I., 1971, *ApJ*, **166**, 109

Castor, J. I., Abbott, D. C. & Klein, R. I., 1975, *ApJ*, **195**, 157

Chandrasekhar, S., 1967, *An Introduction to the Study of Stellar Structure* (Dover, New York)

Clement, M. J., 1981, *ApJ*, **249**, 746

Clement, M. J., 1984, *ApJ*, **276**, 724

Clement, M. J., 1986, *ApJ*, **301**, 185

Clement, M. J., 1989, *ApJ*, **339**, 1022

Collins, G. W. & Harrington, J. P., 1966, *ApJ*, **146**, 152

Coulson, C. A. & Jeffrey, A., 1977, *Waves* (Longman, New York), 2nd edition

Cowling, T. G., 1941, *MNRAS*, **101**, 367

Cowling, T. G., 1957, *Magnetohydrodynamics* (Interscience Tract, New York)

Cox, A. N., Morgan, S. M., Rogers, F. J. & Iglesias, C. A., 1992, *ApJ*, **393**, 272

Cox, J. P., 1980, *Theory of Stellar Pulsation* (Princeton University Press, Princeton)

Cranmer, S., 1996, *CCP7 Newsletter*, Technical Report XX, Daresbury Laborotory

Dappen, W. & Perdang, J., 1985, *A&A*, **151**, 174

Duvall, T. L., Harvey, J. W., Libbrecht, K. G., Popp, B. D. & Pomerantz, M. A., 1988, *ApJ*, **324**, 1158

Dziembowski, W., 1971, *Act Ast*, **21**, 289

Eckart, C., 1960, *Hydrodynamics of Oceans and Atmospheres* (Pergamon Press, London)

Edmonds, P., Cram, L., Demarque, P., Guenther, D. B. & Pinsonneault, M. H., 1992, *ApJ*, **394**, 313

Fadeyev, Y. A. & Lynas-Gray, A. E., 1996, *MNRAS*, **280**, 427

Frazier, E. N., 1968, *Z Ast*, **68**, 345

Fridlund, M., Appourchaux, T., Pace, O. & Volonte, S., 1994, *ESA Journal*, **18**, 247

Fullerton, A. W., Gies, D. R. & Bolton, C. T., 1996, *ApJSS*, **103**, 475

Gabriel, M. & Noels, A., 1976, *A&A*, **46**, 313

Gabriel, M., Scuflaire, R., Noels, A. & Boury, A., 1975, *A&A*, **40**, 33

Gautschy, A. & Glatzel, W., 1990*a*, *MNRAS*, **245**, 154

Gautschy, A. & Glatzel, W., 1990*b*, *MNRAS*, **245**, 597

Gautschy, A. & Glatzel, W., 1991, *MNRAS*, **253**, 509

Gautschy, A. & Saio, H., 1995, *Ann. Rev. Astron. Astrophys.*, **33**, 75

Gies, D. R., 1991, in D. Baade (ed.), *Rapid variability of OB-Stars: Nature and Diagnostic Value* (ESO, Munich), p. 229

Gies, D. R., 1996, in K. G. Strassmeier & J. L. Linsky (eds.), *Stellar Surface Structure* (IAU, Netherlands), p. 121

Gies, D. R. & Kullavanijaya, A., 1988, *ApJ*, **326**, 813

Glatzel, W., 1994, *MNRAS*, **271**, 66

Glatzel, W. & Gautschy, A., 1992, *MNRAS*, **256**, 209

Gonczi, G. & Osaki, Y., 1980, *A&A*, **84**, 304

Guenther, D. B., 1994, *ApJ*, **422**, 400

Hahula, M. E., 1993, *BAAS*, **183**, 2302

Henyey, L. G., Forbes, J. E. & Gould, N. L., 1964, *ApJ*, **139**, 306

Howarth, I. D. & Reid, A. H. N., 1993, *A&A*, **279**, 148

Howarth, I. D., Siebert, K. W., Hussain, A. J. & Prinja, R. K., 1997, *MNRAS*, **284**, 265

Kambe, E., Ando, H. & Hirata, R., 1990, *PASJ*, **42**, 687

Kambe, E., Ando, H., Hirata, R., Walker, G. A. H., Kennelly, E. J. & Matthews, J. M., 1993, *PASP*, **105**, 1222

Kambe, E. & Osaki, Y., 1988, *PASJ*, **40**, 313

Kato, S., 1966, *PASJ*, **18**, 18

Kennelly, E. J., Walker, G. A. H. & Hubeny, I., 1991, *PASP*, **103**, 1250

Kippenhahn, R. & Weigert, A., 1990, *Stellar Etructure and Evolution* (Springer-Verlag, Berlin)

Kovacs, G., 1990, in *Confrontation between Stellar Pulsation and Evolution*, p. 141

Kurtz, D., 1982, *MNRAS*, **200**, 807

Kurucz, R. L., 1979, *ApJSS*, **40**, 1

Lane, J. H., 1870, *Amer. J. Sci.*, **50**, 57

Lawden, M. D., 1996, *Starlink User Note 1.15*, Rutherford Appleton Laborotory, Oxford

Ledoux, P., 1951, *ApJ*, **114**, 373

Ledoux, P. & Walraven, T., 1958, in S. Flügge (ed.), *Handbuch der Physik* (Springer-Verlag, Berlin), volume 51, p. 353

Lee, U., 1988, *MNRAS*, **232**, 711

Lee, U., 1993, *ApJ*, **405**, 359

Lee, U. & Baraffe, I., 1995, *A&A*, **301**, 419

Lee, U. & Saio, H., 1986, *MNRAS*, **221**, 365

Lee, U. & Saio, H., 1987*a*, *MNRAS*, **224**, 513

Lee, U. & Saio, H., 1987*b*, *MNRAS*, **225**, 643

Lee, U. & Saio, H., 1989, *MNRAS*, **237**, 875

Lee, U. & Saio, H., 1990, *ApJ*, **349**, 570

Lee, U., Saio, H. & Jeffery, C. S., 1992*a*, *MNRAS*, **254**, 185

Lee, U., Strohmayer, T. E. & Van Horn, H. M., 1992*b*, *ApJ*, **397**, 674

Leighton, R. B., Noyes, R. W. & Simon, G. W., 1962, *ApJ*, **135**, 474

Managan, R. A., 1986, *ApJ*, **309**, 598

Massa, D., 1995, *ApJ*, **438**, 376

Morgan, W. W., Keenan, P. C. & Kellman, E., 1943, *An Atlas of Stellar Spectra with an outline of Spectral Classification.* (University of Chicago Press, Chicago)

Moss, D., 1980, *A&A*, **85**, 135

Osaki, Y., 1971, *PASJ*, **23**, 485

Osaki, Y., 1974, *ApJ*, **189**, 469

Osaki, Y., 1975, *PASJ*, **27**, 237

Osaki, Y., 1976, *PASJ*, **28**, 105

Osaki, Y. & Hansen, C. J., 1973, *ApJ*, **185**, 277

Owocki, S. P. & Rybicki, G. B., 1986, *ApJ*, **309**, 127

Papaloizou, J. & Pringle, J. E., 1978, *MNRAS*, **182**, 423

Parlett, B. N., 1980, *The Symmetric Eigenvalue Problem* (Prentice-Hall, Englewood Cliffs)

Pauldrach, A., Puls, J. & Kudritzki, R. P., 1986, *A&A*, **164**, 86

Perdang, J., 1991, in D. Baade (ed.), *Rapid variability of OB-Stars: Nature and Diagnostic Value* (ESO, Munich), p. 349

Pesnell, W. D., 1985, *ApJ*, **292**, 238

Press, W., Teukolsky, S., Vetterling, W. & Flannery, B., 1992, *Numerical Recipies in Fortran* (Cambridge University Press, Cambridge)

Reid, A. H. N., Bolton, C. T., Crowe, R. A., Fieldus, M. S., Fullerton, A. W., Gies, D. R., Howarth, I. D., McDavid, D., Prinja, R. K. & Smith, K. C., 1993, *ApJ*, **417**, 320

Reid, A. H. N. & Howarth, I. D., 1996, *A&A*, **311**, 616

Reid, A. H. N., Townsend, R. H. D. & Howarth, I. D., 1997, *In preparation*

Ritter, A., 1878, *Wiedemann Annalen*, 135

Rogers, F. J. & Iglesias, C. A., 1992, *ApJ*, **401**, 361

Rosenbluth, M. N. & Bahcall, J. N., 1973, *ApJ*, **184**, 9

Saio, H., 1980, *ApJ*, **240**, 685

Saio, H., 1981, *ApJ*, **244**, 299

Saio, H., 1982, *ApJ*, **256**, 717

Saio, H. & Cox, J. P., 1980, *ApJ*, **236**, 549

Saio, H., Cox, J. P. & Hansen, C. J., 1980, *A&A*, **85**, 263

Schaerer, D., 1991, Diploma thesis, ETH Zürich

Schaerer, D., 1995, *Complete Stellar Models: Spectral and Interior Evolution of Massive Stars*, Ph.D. thesis, University of Geneva

Schaller, G., Schaerer, D., Meynet, G. & Maeder, A., 1992, *A&ASS*, **96**, 269

Schmutz, W., Leitherer, C., Hubeny, I., Vogel, M., Hamann, W.-R. & Wessolowski, U., 1991, *ApJ*, **372**, 664

Schrijvers, C., Telting, J. H., Aerts, C., Ruymaekers, E. & Henrichs, H. F., 1997, *A&ASS*, **121**, 343

Schwarzchild, M., 1965, *Structure and Evolution of the Stars* (Dover, New York)

Scuflaire, R., 1974, *A&A*, **36**, 107

Shibahashi, H. & Osaki, Y., 1976, *PASJ*, **28**, 199

Smith, K. C. & Howarth, I. D., 1994, *A&A*, **290**, 868

Smith, M. A., 1977, *ApJ*, **215**, 574

Smith, M. A., 1978, *ApJ*, **223**, 221

Smith, M. A., 1981, *ApJ*, **248**, 214

Smith, M. A., 1985, *ApJ*, **297**, 224

Smith, M. A., 1986, in Y. Osaki (ed.), *Hydrodynamics and Magnetohydrodynamic Problems in the Sun and Stars* (University of Toyko Press, Tokyo), p. 145

Smith, M. A., Fitch, W. S., Africano, J. L., Goodrich, B. D., Halbedel, W., Palmer, L. H. & Henry, G. W., 1984, *ApJ*, **282**, 226

Smith, M. A. & Karp, A. H., 1976, in A. N. Cox & R. G. Deupree (eds.), *Solar and Stellar Pulsation* (Los Alamos Publications, Los Alamos), p. 289

Sobolev, V. V., 1960, *Moving Envelopes of Stars* (Havard University Press, Cambridge), trans. S. Gaposchkin

Sobouti, Y., 1975, *A&A*, **70**, 665

Stagg, C. R., Bozic, H., Fullerton, A. W., Gao, W. S., Guo, Z. H., Harmanec, P., Horn, J., Huang, L., Iliev, L. H., Koubsky, P., Kovachev, B. Z., Pavlovski, K., Percy, J. R., Schmidt, F., Stefl, S., Tomov, N. A. & Ziznovsky, J., 1988, *MNRAS*, **234**, 1021

Stellingwerf, R. F., 1978, *AJ*, **83**, 1184

Stellingwerf, R. F., 1980, in *Nonradial and nonlinear stellar pulsation; Proceedings of the Workshop, Tucson, Arizona'* (Springer-Verlag, Berlin), p. 50

Stellingwerf, R. F., 1982*a*, *ApJ*, **262**, 330

Stellingwerf, R. F., 1982*b*, *ApJ*, **262**, 339

Stellingwerf, R. F., 1984*a*, *ApJ*, **277**, 322

Stellingwerf, R. F., 1984*b*, *ApJ*, **277**, 327

Stellingwerf, R. F., 1984*c*, *ApJ*, **284**, 712

Strohmayer, T. E. & Lee, U., 1996, *ApJ*, **467**, 773

Tassoul, J.-L., 1978, *Theory of Rotating Stars* (Princeton University Press, Princeton)

Tassoul, M., 1980, *ApJSS*, **43**, 469

Telting, J. H. & Schrijvers, C., 1997, *A&A*, **317**, 723

Thomson, W., 1863, *Phil. Trans. Roy. Soc. London*, **153**, 612

Thomson, W., 1887, *Phil. Mag.*, **22**, 287

Tinkham, M., 1964, *Group Theory and Quantum Mechanics* (McGraw-Hill)

Unno, W., Osaki, Y., Ando, H., Shibahashi, H. & Saio, H., 1989, *Nonradial Oscillations of Stars* (University of Tokyo Press, Tokyo), 2nd edition

Vogt, S. S. & Penrod, G. D., 1983, *ApJ*, **275**, 661

von Zeipel, H., 1924, *MNRAS*, **84**, 665

Walker, G. A. H., 1991, in D. Baade (ed.), *Rapid variability of OB-Stars: Nature and Diagnostic Value* (ESO, Munich), p. 27

Walker, G. A. H., Yang, S. & Fahlman, G. G., 1979, *ApJ*, **233**, 199

Zahn, J.-P., 1966, *Ann Ast*, **29**, 313

Appendix A

The Brunt-Väisälä Frequency

The Brunt-Väisälä frequency N arises in the study of non-radial pulsation (§2.5) in connection with the existence of gravity modes, whereby the principal restoring force is the local buoyancy discrepancy of a displaced fluid parcel. An understanding of the significance of the Brunt-Väisälä frequency is best obtained by actually deriving the expression for N.

Accordingly, consider an infinitesimal fluid parcel, defined to contain a fixed mass of matter dm, in a star under hydrostatic equilibrium. The net radial force on this parcel due to pressure and gravitational forces is given by

$$F = \left(-\frac{1}{\rho}\frac{dp}{dr} - g \right) dm, \tag{A.1}$$

with the convention that F is positive when the force acts away from the origin. Assuming that the parcel is initially at rest, this force will evaluate to zero. Now suppose that the parcel is subject to a small radial displacement ξ_r from its equilibrium position; the change in F resulting from this displacement will be given, to first order, by

$$\delta F = \left[\frac{\delta\rho}{\rho^2}\frac{dp}{dr} - \frac{1}{\rho}\delta\left(\frac{dp}{dr}\right) - \delta g \right] dm, \tag{A.2}$$

where the Lagrangian formalism of §2.3 has been used, since it is a fixed-mass (rather than fixed-position) perturbation which is appropriate in this case. The density perturbation $\delta\rho$ may be written in terms of ξ_r by noting that the fluid parcel remains in pressure equilibrium with the surrounding material at all times, and therefore the Eulerian (fixed-position) perturbation to the pressure is zero, giving

$$\delta p = p' + \boldsymbol{\xi} \cdot \nabla p = \xi_r \frac{dp}{dr}. \tag{A.3}$$

If it is assumed that this Lagrangian pressure change corresponds to an adiabatic expansion process (no heat transferred), then $\delta\rho$ is given by equation (2.18),

$$\frac{\delta\rho}{\rho} = \frac{1}{\Gamma_1}\frac{\delta p}{p},$$

which, when combined with the expression for δp, gives

$$\delta\rho = \frac{\rho}{\Gamma_1 p}\frac{dp}{dr}\xi_r. \tag{A.4}$$

The perturbation to the pressure gradient is found in a similar manner to be

$$\delta\left(\frac{dp}{dr}\right) = \left(\frac{dp}{dr}\right)' + \xi_r \cdot \nabla\left(\frac{dp}{dr}\right) = \xi_r\frac{d^2p}{dr^2}, \tag{A.5}$$

as is the perturbation to the gravitation field strength,

$$\delta g = g' + \boldsymbol{\xi} \cdot \nabla g = \xi_r\frac{dg}{dr} \tag{A.6}$$

The equation of hydrostatic equilibrium may be used to give the gravitational field gradient as

$$\frac{dg}{dr} = \frac{d}{dr}\left(-\frac{1}{\rho}\frac{dp}{dr}\right), \tag{A.7}$$

so that

$$\delta g = \frac{1}{\rho}\left(\frac{1}{\rho}\frac{d\rho}{dr}\frac{dp}{dr} - \frac{d^2p}{dr^2}\right)\xi_r. \tag{A.8}$$

Substitution of equations (A.4), (A.5) and (A.8) into the expression (A.2) for δF leads to

$$\delta F = \left[\frac{1}{\Gamma_1 p\rho}\left(\frac{dp}{dr}\right)^2\xi_r - \frac{1}{\rho^2}\frac{d\rho}{dr}\right]dm; \tag{A.9}$$

the equation of hydrostatic equilibrium may be used one final time to simplify this to

$$\delta F = -g\left(\frac{1}{\Gamma_1}\frac{d\ln p}{dr} - \frac{d\ln\rho}{dr}\right)\xi_r dm. \tag{A.10}$$

Since the net force on the parcel is zero in the equilibrium position ($\xi_r = 0$), this expression represents the restoring force on the parcel when it is displaced by ξ_r. The corresponding equation of motion is

$$-N^2\xi_r dm = \frac{d^2\xi_r}{dr^2}dm, \tag{A.11}$$

where, of course, N is the Brunt-Väisälä frequency,

$$N^2 = g\left(\frac{1}{\Gamma_1}\frac{d\ln p}{dr} - \frac{d\ln\rho}{dr}\right). \tag{A.12}$$

Assuming a time-dependence of the form $\exp(\mathrm{i}\sigma t)$ leads to the solution

$$\xi_r(t) = \xi_{r,0}\exp(\pm\mathrm{i}Nt), \tag{A.13}$$

where $\xi_{r,0}$ is some arbitrary amplitude. It can therefore be seen that, when a fluid parcel is displaced from its equilibrium position in a star under hydrostatic equilibrium, it will undergo free oscillations at the Brunt-Väisälä frequency due to a buoyancy discrepancy with the surrounding material; this kind of oscillation is entirely analogous to a cork bobbing in a pond. Note that, if N^2 is negative, the equation of motion represents exponentially increasing/decreasing displacement, corresponding to convective instability. Thus, stable oscillation can only occur in zones with $N^2 > 0$, unless rotation is present (see Chapter 6 and Appendix D).

Appendix B

The Associated Legendre Polynomials

The associated Legendre polynomials $P_l^m(z)$ are defined as the solutions of the associated Legendre equation,

$$(1-z^2)\frac{d^2P_l^m}{dz^2} - 2z\frac{dP_l^m}{dz} + \left[l(l+1) - \frac{m^2}{1-z^2}\right]P_l^m = 0, \tag{B.1}$$

where l and m are constants, with the restriction that m is an integer. Solution usually proceeds with the substitution

$$P_l^m = (1-z^2)^{m/2}\frac{d^m\mathcal{P}}{dz^m}, \tag{B.2}$$

where $\mathcal{P}(z)$ is some arbitrary function; it would appear that such a substitution requires that m be positive, but it will demonstrated that this is not the case. The resulting equation for $\mathcal{P}(z)$ is given by

$$(1-z^2)\frac{d^2\mathcal{P}}{dz^2} - 2z\frac{d\mathcal{P}}{dz} + l(l+1)\mathcal{P} = 0, \tag{B.3}$$

which can be recognized as Legendre's equation. It may be solved using Frobenius' method (*e.g.*, Arfken 1970), to give two power series solutions $P(z)$ and $Q(z)$, known as Legendre functions of the first and second kinds respectively (Boas 1983). The function $Q(z)$ is discarded since it diverges at $z = \pm 1$; furthermore, $P(z)$ diverges at $z = 1$ unless l is a non-negative integer, in which case $P(z)$ is a polynomial of degree l in z. With the normalisation $P(1) = 1$, this physically-acceptable solution is known as the *Legendre polynomial* $P_l(z)$ of degree l.

Expressions for the Legendre polynomials P_l may be found using various recurrence relations (*e.g.*, Arfken 1970); however, the most compact formulation is the Rodrigues' formula expression,

$$P_l(z) = \frac{1}{2^l l!}\frac{d^l}{dz^l}(z^2-1)^l. \tag{B.4}$$

This may be substituted into equation (B.2) to give the expression for the associated Legendre polynomials $P_l^m(z)$ as

$$P_l^m(z) = \frac{(1-x^2)^{m/2}}{2^l l!} \frac{d^{l+m}}{dz^{l+m}}(z^2-1)^l. \tag{B.5}$$

It can now be seen that it is meaningful to discuss the associated Legendre polynomials with negative degree m; in fact, the polynomials are well defined over $m \leq l \leq m$. With this definition, the functions $P_l^{\mu}(z)$ and $P_l^{-\mu}(z)$, where $0 \leq \mu \leq l$, are proportional (*e.g.*, Arfken 1970; Boas 1983), so that

$$P_l^{-\mu}(z) = (-1)^{\mu} \frac{(l-\mu)!}{(l+\mu)!} P_l^{\mu}(z). \tag{B.6}$$

Appendix C

The Elements of ℵ

In order to use the similarity transform technique introduced in §6.4, it is first necessary to diagonalize the matrix $\mathbf{W}$. Whilst expressions for the elements of this matrix are not available in closed form, they can be found for the inverse coupling matrix $\aleph$. Lee & Saio (1987*a*) presented (but did not derive) such expressions for the inverse matrix pertinent to even-π modes; here, the corresponding expressions are derived for odd-π modes.

The reason why these expressions actually exist (and the elements need not be calculated by successive numerical matrix multiplications) is that all of the matrices in the expression (6.43) for $\mathbf{W}$ are very sparse, being either diagonal, upper bi-diagonal or lower bi-diagonal. Accordingly, it is useful to introduce a few identities for the products of such matrices, prior to the actual derivation.

If $\mathbf{D}$, $\mathbf{X}^b$ and $\mathbf{X}_b$ denote diagonal, upper bi-diagonal and lower bi-diagonal matrices, and $\mathbf{X}$ denotes a general matrix, then products between these matrices have (non-zero) elements given by

$$(\mathbf{D}^{-1})_{j,j} = (\mathbf{D})_{j,j}^{-1}, \qquad (\mathbf{XD})_{i,j} = (\mathbf{X})_{i,j}(\mathbf{D})_{j,j}, \qquad (\mathbf{DX})_{i,j} = (\mathbf{D})_{i,i}(\mathbf{X})_{i,j} \tag{C.1}$$

and

$$(\mathbf{X}^b\mathbf{X}_b)_{j,j} = (\mathbf{X}^b)_{j,j}(\mathbf{X}_b)_{j,j} + (\mathbf{X}^b)_{j,j+1}(\mathbf{X}_b)_{j+1,j}, \tag{C.2}$$

$$(\mathbf{X}^b\mathbf{X}_b)_{j+1,j} = (\mathbf{X}^b)_{j+1,j+1}(\mathbf{X}_b)_{j+1,j}, \tag{C.3}$$

$$(\mathbf{X}^b\mathbf{X}_b)_{j,j+1} = (\mathbf{X}^b)_{j,j+1}(\mathbf{X}_b)_{j+1,j+1}. \tag{C.4}$$

From equation (6.43), the matrix $\aleph$ is then formed for odd-π modes by

$$\aleph = (\mathbf{L_0} - \mathbf{M_0}{\mathbf{L_1}}^{-1}\mathbf{M_1})\mathbf{\Lambda}^{-1}, \tag{C.5}$$

so the derivation may begin by noting that the only non-zero elements of the product ${\mathbf{L_1}}^{-1}\mathbf{M_1}$ (which is an $\mathbf{X}_b$-type matrix) are given by

$$({\mathbf{L_1}}^{-1}\mathbf{M_1})_{j,j} = (\mathbf{L_1})_{j,j}^{-1}(\mathbf{M_1})_{j,j} \tag{C.6}$$

and

$$(\mathbf{L_1}^{-1}\mathbf{M_1})_{j+1,j} = (\mathbf{L_1})^{-1}_{j+1,j+1}(\mathbf{M_1})_{j+1,j}. \tag{C.7}$$

Since $\mathbf{M_0}$ is a $\mathbf{X}^b$-type matrix, the tri-diagonal matrix $\mathbf{Y} \equiv \mathbf{M_0}\mathbf{L_1}^{-1}\mathbf{M_1}$ is formed using the identity given for a $\mathbf{X}^b$–$\mathbf{X}_b$ product, so that $\mathbf{Y}$ has the non-zero elements

$$(\mathbf{Y})_{j,j} = (\mathbf{M_0})_{j,j}(\mathbf{L_1})^{-1}_{j,j}(\mathbf{M_1})_{j,j} + (\mathbf{M_0})_{j,j+1}(\mathbf{L_1})^{-1}_{j+1,j+1}(\mathbf{M_1})_{j+1,j}, \tag{C.8}$$

$$(\mathbf{Y})_{j+1,j} = (\mathbf{M_0})_{j+1,j+1}(\mathbf{L_1})^{-1}_{j+1,j+1}(\mathbf{M_1})_{j+1,j} \tag{C.9}$$

and

$$(\mathbf{Y})_{j,j+1} = (\mathbf{M_0})_{j,j+1}(\mathbf{L_1})^{-1}_{j+1,j+1}(\mathbf{M_1})_{j+1,j+1}. \tag{C.10}$$

Using the expressions given in §6.3 for the elements of $\mathbf{M_0}$, $\mathbf{M_1}$ and $\mathbf{L_1}$, the elements of $\mathbf{Y}$ thus evaluate to

$$(\mathbf{Y})_{j,j} = \nu^2 \left\{ \frac{k_j(k_j+2)(J^m_{k_j+1})^2}{(k_j+1)^2[1-m\nu/\Lambda(n_j)]} + \frac{(k_j+1)(k_j+3)(J^m_{k_j+2})^2}{(k_j+2)^2[1-m\nu/\Lambda(n_j+2)]} \right\}, \tag{C.11}$$

$$(\mathbf{Y})_{j+1,j} = \nu^2 \frac{\Lambda(k_j+1)J^m_{k_j+2}J^m_{k_j+3}}{\Lambda(k_j+2)[1-m\nu/\Lambda(n_j+2)]} \tag{C.12}$$

and

$$(\mathbf{Y})_{j,j+1} = \nu^2 \frac{\Lambda(k_j+3)J^m_{k_j+2}J^m_{k_j+3}}{\Lambda(k_j+2)[1-m\nu/\Lambda(n_j+2)]}. \tag{C.13}$$

These may be further simplified by eliminating k_j and n_j in terms of l_j, giving

$$(\mathbf{Y})_{j,j} = \nu^2 \left\{ \frac{(l_j-1)^2(J^m_{l_j})^2}{l_j^2[1-m\nu/\Lambda(l_j-1)]} + \frac{l_j(l_j+2)(J^m_{l_j+1})^2}{(l_j+1)^2[1-m\nu/\Lambda(l_j+1)]} \right\}, \tag{C.14}$$

$$(\mathbf{Y})_{j+1,j} = \nu^2 \frac{\Lambda(l_j)J^m_{l_j+1}J^m_{l_j+2}}{\Lambda(l_j+1)-m\nu} \tag{C.15}$$

and

$$(\mathbf{Y})_{j,j+1} = \nu^2 \frac{\Lambda(l_j+2)J^m_{l_j+1}l_j+2}{\Lambda(l_j+1)-m\nu}. \tag{C.16}$$

The final step in the derivation is performed by observing that $\aleph$ is the product between the tri-diagonal matrix $(\mathbf{L_0}-\mathbf{Y})$ and the diagonal matrix $\mathbf{\Lambda}^{-1}$, and hence is also tri-diagonal, with non-zero elements given by

$$(\aleph)_{j,j} = [(\mathbf{L_0})_{j,j} - (\mathbf{Y})_{j,j}](\mathbf{\Lambda})^{-1}_{j,j}, \tag{C.17}$$

$$(\aleph)_{j+1,j} = -(\mathbf{X})_{j+1,j}(\mathbf{\Lambda})^{-1}_{j,j} \tag{C.18}$$

and

$$(\aleph)_{j,j+1} = -(\mathbf{X})_{j,j+1}(\Lambda)^{-1}_{j+1,j+1}. \tag{C.19}$$

Using the expressions derived above for the elements of $\mathbf{Y}$, and those for Λ and $\mathbf{L}_0$ given in §6.3, the final expressions for the non-zero elements of the (symmetric) tri-diagonal inverse coupling matrix $\aleph$ are

$$(\aleph)_{j,j} = \left[1 - m\nu/\Lambda(l_j) - \nu F(l_j)\right] / \Lambda(l_j) \tag{C.20}$$

and

$$(\aleph)_{j+1,j} = (\aleph)_{j,j+1} = \nu^2 J^m_{l_j+1} J^m_{l_j+2} / \left[\Lambda(l_j+1) - m\nu\right] , \tag{C.21}$$

where the function $F(l_j)$ is given by

$$F(l_j) = \frac{(l_j^2 - 1)(J^m_{l_j})^2}{l_j^2[1 - m\nu/\Lambda(l_j - 1)]} + \frac{l_j(l_j+2)(J^m_{l_j+1})^2}{(l_j+1)^2[1 - m\nu/\Lambda(l_j+1)]} \tag{C.22}$$

The expressions found for the elements of $\aleph$ are, interestingly enough, the same as those found by Lee & Saio (1987*a*) for even-π modes (remembering that the derivation presented herein applies specifically to odd-π modes). Note that $(\aleph)_{1,1}$ always diverges for $m = 0$, even-π modes, due to the division by $\Lambda(l_j)$ in equation (C.20) when $l_j = 0$. This is not a problem with the underlying theory *per se*, but more an implementation problem; in such cases, $\mathbf{W}$ must be used instead of $\aleph$ for calculations.

Appendix D

Convective Modes

To obtain insights into how rotation may act to stabilize convection, and lead to the convective modes discussed in §6.7.2, it is useful to reproduce the equation of motion in a stratified medium, presented in Appendix A, with the inclusion of a velocity-dependent term representing the coriolis force. If it is assumed that the stellar material is stratified in the Cartesian x-direction, and that this material has associated with it a constant angular velocity Ω around the z-axis, then the equation of motion for a fluid parcel, in the co-rotating frame of reference, is found to be given by

$$\frac{d^2\boldsymbol{\xi}}{dt^2} + 2(\Omega \mathbf{e}_z) \times \frac{d\boldsymbol{\xi}}{dt} + N^2 \boldsymbol{\xi} \cdot \mathbf{e}_x = \mathbf{0}, \tag{D.1}$$

where $\mathbf{e}_x$ and $\mathbf{e}_z$ are the unit vectors in the x- and z-directions respectively. Assuming a time-dependence for all variables of the form $\exp(\mathrm{i}\sigma_c t)$, the equation of motion may be reduced to the two-dimensional vector equation

$$-\sigma_c^2 \begin{pmatrix} \xi_x \\ \xi_y \end{pmatrix} + 2\mathrm{i}\sigma_c \begin{pmatrix} -\Omega\xi_y \\ \Omega\xi_x \end{pmatrix} + N^2 \begin{pmatrix} \xi_x \\ 0 \end{pmatrix} = \mathbf{0}, \tag{D.2}$$

where the z component has been omitted since no forces exist in the z-direction. This equation may further be rewritten in the matrix form

$$\begin{pmatrix} N^2 - \sigma_c^2 & -2\mathrm{i}\sigma_c\Omega \\ 2\mathrm{i}\sigma_c\Omega & -\sigma_c^2 \end{pmatrix} \begin{pmatrix} \xi_x \\ \xi_y \end{pmatrix} = \mathbf{0}, \tag{D.3}$$

which can be recognized as an eigenvalue problem in σ_c^2. The resulting eigenfrequencies are given by

$$\sigma_c^2 = N^2 + 4\Omega^2 \tag{D.4}$$

and

$$\sigma_c^2 = 0. \tag{D.5}$$

The second of these solutions represents an arbitrary (but time-independent) displacement in the y-direction, and is not of interest here. However, the first solution represents oscillatory motion for $(N^2 + 4\Omega^2) > 0$, in which the fluid parcel moves in elliptical orbits lying in the xy-plane, with semi-major axes in the x- and y-directions. For non-zero Ω, it can be seen that, even in regions of negative N^2 (which are convectively unstable in non-rotating stars), there can exist oscillatory motion; thus, the action of rotation is to stabilize the stellar material against convection.

Physically, this can be understood by noting that the coriolis force will always act perpendicular to the fluid parcel velocity, resulting in circular motion if $N^2 = 0$ (akin to a charged particle in a magnetic field) and elliptical motion otherwise. In the convectively-neutral ($N^2 = 0$) scenario, the energy of the fluid parcel is exclusively kinetic, and such oscillation modes are correspondingly known as inertial; in other cases, the fluid parcel does possess some degree of potential energy due to the convective restoring forces, but these modes are, in some cases, still termed inertial if the majority of the parcel's energy is kinetic.

Appendix E

The HENITER Calling Arrays

The Henyey subroutine HENITER, discussed in §5.3.3, is called with a number of arrays which specify the values of the differential equations, the boundary conditions and the current trial solutions; these arrays are used to perform one iteration of the Henyey method for solving two-point boundary-value problems, and then update the solutions accordingly.

Following the nomenclature of Unno *et al.* (1989) in their comprehensive description of the Henyey method, the array which specifies the right-hand sides of the adiabatic, non-radial pulsation equations is given by

$$\bar{\mathbf{f}}_{\mathbf{n}} = x_n^{-1} \left\{ \begin{array}{c} (V_g^n - 3)\bar{y}_1^n + \left[\frac{l(l+1)}{c_1^n \bar{\lambda}} - V_g^n\right] \bar{y}_2^n + V_g^n \bar{y}_3^n \\ (c_1^n \bar{\lambda} - A^{\star n})\bar{y}_1^n + (A^{\star n} - U^n + 1)\bar{y}_2^n - A^{\star n}\bar{y}_3^n \\ (1 - U^n)\bar{y}_3^n + \bar{y}_4^n \\ U^n A^{\star n}\bar{y}_1^n + U^n V_g^n \bar{y}_2^n + [l(l+1) - U^n V_g^n]\bar{y}_3^n - U^n \bar{y}_4^n \end{array} \right\}, \tag{E.1}$$

where an n superscript denotes the appropriate value at the nth grid point, except in the case of x_n, which is the fractional radius x of that grid point; the quantity $\bar{\lambda}$ is the trial value of the eigenvalue, which equals ω^2 in the case of the pulsation equations. The derivatives of this array with respect to the trial solutions $\bar{y}_i^n$ (where $i = 1, \ldots, 4$) and the trial eigenvalue $\bar{\lambda}$ are given by

$$\mathbf{F}^{\mathbf{n}} = x_n^{-1} \left\{ \begin{array}{cccc} V_g^n - 3 & \frac{l(l+1)}{c_1^n \bar{\lambda}} - V_g^n & V_g^n & 0 \\ c_1^n \bar{\lambda} - A^{\star n} & A^{\star n} - U^n + 1 & -A^{\star n} & 0 \\ 0 & 0 & 1 - U^n & 1 \\ U^n A^{\star n} & U^n V_g^n & l(l+1) - U^n V_g^n & -U^n \end{array} \right\} \tag{E.2}$$

and

$$\mathbf{L}^{\mathbf{n}} = x_n^{-1} \left\{ \begin{array}{cccc} -\frac{l(l+1)}{c_1^n \bar{\lambda}^2}\bar{y}_2^n & c_1^n y_1^n & 0 & 0 \end{array} \right\} \tag{E.3}$$

respectively. The corresponding boundary conditions at the inner- and outer-most grid points are specified by $\bar{g}_l^1$ and $\bar{g}_{l'}^N$ respectively (Unno *et al.* 1989), where $l = 1,2$ and $l' = 1,2,3$; these quantities may be combined into a single array given by

$$\bar{\mathbf{g}}^{\mathbf{n}} = \left\{ \begin{array}{c} \frac{c_1^1 \bar{\lambda} \bar{y}_1^1}{l} - \bar{y}_2^1 \\ l\bar{y}_3^1 - \bar{y}_4^1 \\ \bar{y}_1^N - 1 \\ \bar{y}_1^N - \bar{y}_2^N + \bar{y}_3^N \\ (l+1)\bar{y}_3^N + \bar{y}_4^N \end{array} \right\}, \tag{E.4}$$

so that $(\bar{\mathbf{g}}^{\mathbf{n}})_l \equiv \bar{g}_l^1$ for $l = 1,2$ and $(\bar{\mathbf{g}}^{\mathbf{n}})_{l'+2} \equiv \bar{g}_{l'}^N$ for $l' = 1,2,3$. The boundary conditions represented by this array are those of the Z-boundary (§3.2), where the normalization $y_1^N = 1$ has been applied at the outer boundary after equation (3.27). As with the array $\bar{\mathbf{f}}^{\mathbf{n}}$, the derivatives of this array with respect to the trial solutions and trial eigenvalue are given by

$$\mathbf{G}^{\mathbf{n}} = \left\{ \begin{array}{cccc} \frac{c_1^1 \bar{\lambda}}{l} & -1 & 0 & 0 \\ 0 & 0 & l & -1 \\ 1 & 0 & 0 & 0 \\ 1 & -1 & 1 & 0 \\ 0 & 0 & l+1 & 1 \end{array} \right\} \tag{E.5}$$

and

$$\Lambda^{\mathbf{n}} = \left\{ \begin{array}{ccccc} \frac{c_1^1 \bar{y}_1^1}{l} & 0 & 0 & 0 & 0 \end{array} \right\} \tag{E.6}$$

respectively, where, with $i = 1, \ldots, 4$, $l = 1,2$, $l' = 1,2,3$ and $k = 1$, the variables introduced by Unno *et al.* (1989) have the values $(\mathbf{G}^{\mathbf{n}})_{l,j} \equiv G_{lj}^1$, $(\Lambda^{\mathbf{n}})_{l,k} \equiv \Lambda_{lk}^1$, $(\mathbf{G}^{\mathbf{n}})_{l'+2,j} \equiv G_{l'j}^N$, $(\Lambda^{\mathbf{n}})_{l'+2,k} \equiv \Lambda_{l'k}^N$.

Appendix F

BRUCE and KYLIE Command Files

F.1 Basic Syntax

The programs BRUCE and KYLIE, discussed in §7.2 and §7.3 respectively, are both controlled by user-supplied command files. These ASCII text files specify the stellar, pulsation and spectroscopic parameters to be used when the programs are run.

The syntax used in the files is the same for both BRUCE and KYLIE, and consists of one or more commands of the form

```
#<command> { <parswitch> <parswitch> ... }
```

where <command> is a token which specifies which particular aspect of the modelling is being controlled. Note that the spaces surrounding the braces *are* significant. The <parswitch> tokens, of which there can be one or more, have two forms; the first of these,

```
<parswitch> = <parname>:<parvalue>
```

specifies that the parameter <parname> should be assigned the numeric value <parvalue>. The second form,

```
<parswitch> = <switch>
```

specifies that some perturbation or modification specified by <switch> should be 'switched on'

The format of the files is case-insensitive, and carriage-returns are taken to be equivalent to whitespace. Comments may be included in the files by placing a % character anywhere on a line; all text following this character is discarded when the files are read. The ! character is used in a similar manner, but the comment text which it introduces is written to standard output rather than being completely discarded.

The following two sections describe the commands and parameters defined within this syntax for BRUCE and KYLIE.

F.2 BRUCE Commands

There are four basic commands used by BRUCE to define model characteristics, each with their own set of parameters. Some of these parameters are mutually exclusive, and others are mutually inclusive; they are summarized below. Parameters which must be specified are marked in boldface.

The `#stellar` Command

This command specifies the basic stellar parameters of the star, which are used to construct the equilibrium surface grid discussed in §7.2.2. Only one `#stellar` command may appear in the command file; the relevant parameters are as follows:

`polar_radius:R` — Sets the polar radius to R $R_\odot$.

`polar_temperature:T` — Sets the polar to T K.

`polar_log_gravity:g` — Sets the polar logarithmic gravity to g cgs dex.

`stellar_mass:M` — Sets the mass to M $M_\odot$.

`equatorial_velocity:v` — Sets the equatorial rotation velocity to V km s^{-1}.

`polar_inclination:i` — Sets the inclination of the polar axis to i degrees.

`zeipel_beta:b` — Sets the gravity-darkening coefficient to b. The default is 0.25.

Note: the `polar_log_gravity` and `stellar_mass` parameters are mutually exclusive; they provide alternative methods of specifying the polar gravity.

The `#fields` Command

This command specifies the overall characteristics of all perturbation fields defined in the models. Only one `#fields` command may appear in the command file; the relevant parameters are as follows:

`number_of_fields:n` — Sets the number of separate time-points at which perturbation fields are calculated to n.

`dump_filestub:<file>` — Sets the file-stub for all output files to `<file>`. All output files will have the filename `<file>`nnn, where nnn is a 3-digit number with leading zeros which indexes the files.

`matrix_dimension:N` — Sets the dimension of the matrices used in the ST technique to N. If this parameter is not specified, single spherical harmonics are used instead of the rotationally-modified basis states $|\lambda_{l_j,m}\rangle$.

`normal_fields` — If this switch is present, 'radial' velocity fields are directed along the local surface normal vector; otherwise, they are directed along the local radial vector.

`temperature_effects` — If this switch is present, temperature perturbations are included; otherwise, no such perturbations are applied.

`area_effects` — If this switch is present, surface area perturbations are included; otherwise, no such perturbations are applied.

`normal_effects` — If this switch is present, surface normal perturbations are included; otherwise, no such perturbations are applied.

`horizontal_velocity_fields` — If this switch is included, horizontal velocity perturbations are included; otherwise, no such perturbations are applied.

`physical_amplitudes` — If this switch is included, all a amplitude specifications in the `#mode` command are taken as physical amplitudes $V_{\max}$; otherwise, they are taken as mathematical amplitudes V_0.

Note: whilst radial velocity fields are always included in calculations, horizontal velocity fields will only be incorporated if the `horizontal_velocity_fields` switch is present.

The #mode Command

This command specifies the properties a pulsation mode present in the model. One or more `#mode` commands may appear in the command file, up to a limit of 999; the relevant parameters are as follows:

`l_value``:l` — Sets the harmonic degree of the mode to `l`.

`m_value``:m` — Sets the azimuthal order of the mode to `m`.

`velocity_amplitude``:V` — Sets the velocity amplitude of the mode to `V` km s^{-1}. The meaning of this amplitude depends on whether the `physical_amplitudes` switch is present in the `#fields` command.

`corotating_period``:P` — Sets the pulsation period in the co-rotating frame to `P` hours.

`observers_period``:P` — Sets the pulsation period in the observer's frame to `P` hours.

`period_from_nu``:n` — Sets the pulsation period to have a value consistent with $\nu =$ `n`.

`initial_phase`$:\phi$ — Sets the initial phase of the mode to ϕ degrees

`na_amplitude_shift:`ΔT — Sets the non-adiabatic temperature perturbation scaling factor to ΔT.

`na_phase_shift:`ψ — Sets the non-adiabatic temperature perturbation phase shift to ψ.

Note: The `corotating_period` , `observers_period` and `period_from_nu` parameters are mutually exclusive; they provide alternative methods of specifying the pulsation period.

The `#timings` Command

This command specifies the time interval over which calculations are to be performed. Only one `#timings` command may appear in the command file; the relevant parameters are as follows:

`start_time:``t` — Sets the start time of the calculations to `t` hours.

`finish_time:``t` — Sets the finish time of the calculations to `t` hours.

`use_mode_parameter:``n` — Sets the start time of the calculations to 0 hours, and the finish time to the observer's period Π of the nth mode defined; there must therefore be at least `n` `#mode` commands in the command file.

Note: The third of these parameters is mutually exclusive with the first two; they provide alternative methods of specifying the modelling time interval.

F.3 KYLIE Commands

There are three basic commands used by BRUCE to define spectral synthesis characteristics, each with their own set of parameters; they are summarized below. Parameters which must be specified are marked in boldface.

The `#fields` Command

This command is equivalent to the BRUCE `#fields` command, and specifies which dump files produced by BRUCE to read in. Only one `#fields` command may appear in the command file; the relevant parameters are as follows:

`number_of_fields:``n` — Sets the number of separate time-points at which spectra are calculated to `n`. This must be the same as the corresponding parameter used by BRUCE.

`dump_filestub:``<file>` — Sets the file-stub for all input and output files to `<file>`; this must be the same as the corresponding parameter used by BRUCE. All output files will have the filename `<file>nnn.sdf`, where `nnn` is a 3-digit number with leading zeros which indexes the files.

`limb_u_override:u` — Specifies that the limb-darkening inherent to the intensity spectra is to be over-ridden by using a limb-darkening with a coefficient `u`.

The `#waveband` Command

This command specifies a wavelength region over which spectra are to be synthesized. As many `#waveband` commands as are needed may appear in the command file; the relevant parameters are as follows:

`start_wavelength:l` — Sets the start wavelength of the region to `l` Å.

`finish_wavelength:l` — Sets the finish wavelength of the region to `l` Å.

`wavelength_resolution:r` — Sets the wavelength-spacing of points in the region to `r` Å.

The `#wavepoint` Command

This command specifies an isolated wavelength point at which spectra are to be calculated. As many `#wavepoint` commands as are needed may appear in the command file; the relevant parameter is as follows:

`wavelength:l` — Sets the wavelength of the point to `l` Å.

Appendix G

List of Symbols

A	Schwarzchild discriminant; $(= -\frac{1}{\Gamma_1}\frac{d\ln p}{dr} + \frac{d\ln \rho}{dr})$
A	pulsation amplitude defined in equation (6.70)
$A^\star$	dimensionless Schwarzchild discriminant; $(= -rA)$
$a_{\mathrm{sph},l}$	spheroidal pulsation amplitude defined in equation (6.13)
$a_{\mathrm{tor},l+1}$	toroidal pulsation amplitude defined in equation (6.14)
$a_{\mathrm{tor},l-1}$	toroidal pulsation amplitude defined in equation (6.15)
$a^{(0)}$	pulsation amplitude defined after equation (6.15)
$a^{(1)}$	pulsation amplitude defined after equation (6.15)
$\mathbf{B}$	eigenvector matrix of coupling matrix $\mathbf{W}$
$\mathbf{b}$	boundary condition matrix defined in equation (3.29)
$\mathbf{C}$	matrix defined in equations (6.31) and (6.32)
$C_{n,l}$	Ledoux rotational splitting constant defined after equation (6.9)
c	adiabatic sound speed; $(= \sqrt{\Gamma_1 p/\rho})$
c	generalized specific heat in polytropic mixing
c_p	specific heat at constant pressure
c_1	dimensionless structure variable; $[= (r/R)^3/(M_r/M)]$
$\mathbf{D}$	eigenvalue matrix of coupling matrix $\mathbf{W}$
$\mathcal{D}$	Castor discriminant defined in equation (5.9)
$d\mathbf{A}$	vector surface area element
dA	surface area element; $(= \lvert dA\rvert)$
$\det(\mathbf{X})$	determinant of general matrix $\mathbf{X}$
dQ	heat transferred in polytropic mixing
E_W	energy of pulsation defined in equation (5.11)

$\mathbf{e}_r$	unit vector in polar radial direction
$\mathbf{e}_x$	unit vector in cartesian x direction
$\mathbf{e}_y$	unit vector in cartesian y direction
$\mathbf{e}_z$	unit vector in cartesian z direction
$\mathbf{e}_\theta$	unit vector in polar θ direction
$\mathbf{e}_\phi$	unit vector in polar ϕ direction
$F(l_j)$	function defined in equation (C.22)
G	gravitational constant; $(= 6.67 \times 10^{-8}$ dyn cm^2 g$^{-2})$
g	gravitational acceleration
$\mathbf{H}$	column vector defined in equation (6.16)
$\mathbf{h_j}$	horizontal basis column vector defined in equation (6.67)
$\mathbf{I}$	identity (unit) matrix
I	number of equations used in Henyey method
$\Im$	imaginary part
i	imaginary unit; $(= \sqrt{-1})$
i	inclination of stellar polar axis to the line-of-sight
J_l^m	function defined in equation (6.33)
$\mathbf{K}$	matrix defined in equations (6.31) and (6.32)
K	number of eigenvalues used in Henyey method
k	'amplitude' of horizontal velocity fields; $(= 1/\omega_c^2)$
k_j	$= \lvert m\rvert + 2(j-1)$
L	stellar luminosity
L	number of boundary conditions used in Henyey method; $(= I + K)$
L_I	number of inner boundary conditions used in Henyey method
L_l	Lamb frequency; $\{= \frac{[l(l+1)]^{1/2}c}{r}\}$
L_r	luminosity at radius r
$\mathbf{L_0}$	matrix defined in equation (6.30)
$\mathbf{L_1}$	matrix defined in equation (6.30)
$L_\odot$	solar luminosity; $(= 3.780 \times 10^{33}$ erg s$^{-1})$;
l	harmonic degree of spherical harmonic $Y_l^m(\theta, \phi)$
l_j	$= \lvert m\rvert + 2(j-1)$ for even-π modes, $= \lvert m\rvert + 2(j-1) + 1$ for odd-π modes
$\tilde{l}_j$	rotationally-modified equivalent of l_j defined in equation (6.73)
$\lvert l_j, m\rangle$	angular basis function for non-rotating star; $(= Y_{l_j}^m)$

l_s	starting value of l used in an EVOLVE development
M	stellar mass
M_r	mass within the radius r
$\mathbf{M_0}$	matrix defined in equation (6.34)
$\mathbf{M_1}$	matrix defined in equation (6.34)
$\mathbf{M_+}$	matrix defined after equation (6.34)
$\mathbf{M_-}$	matrix defined after equation (6.34)
$M_\odot$	solar mass; ($= 1.985 \times 10^{33}$ g)
m	azimuthal order of spherical harmonic $Y_l^m(\theta, \phi)$
N	Brunt-Väisälä frequency; $\{= [g(\frac{1}{\Gamma_1}\frac{d\ln p}{dr} - \frac{d\ln \rho}{dr})]^{1/2}\}$
N	dimension of matrices and vectors used in Chapter 6
$N_{\rm eq}$	number of points around equator of equilibrium surface grid
N_l^m	spherical harmonic normalization function introduced in equation (6.11)
n_j	$= \|m\| + 1 + 2(j-1)$ for even-π modes, $= \|m\| + 2(j-1)$ for odd-π modes
n	radial order of pulsation mode (number of radial nodes)
$\hat{\mathbf{n}}$	surface normal vector
$\bar{n}$	Cowling mode label; $(n_p - n_g)$
n_g	number of radial nodes in g-mode zone
$\|n_j, m\rangle$	angular basis function for non-rotating star; $(= Y_{n_j}^m)$
$\hat{\mathbf{n}}_o$	vector directed towards observer
n_p	number of radial nodes in p-mode zone
$P_l(z)$	Legendre polynomial
$P_l^m(z)$	associated Legendre polynomial
p	pressure
$\mathbf{Q}$	horizontal basis transformation matrix defined in equation (6.80)
$\mathbf{R}$	toroidal basis transformation matrix defined in equations (6.81) and (6.82)
$\mathbf{R}$	position vector of stellar surface
R	stellar radius
$\Re$	real part
$R_\odot$	solar radius; ($= 6.951 \times 10^{10}$ cm)
$\mathbf{r}$	position vector
r	radius in in spherical polar coordinates (r, θ, ϕ)
r_c	critical radius of wind

r_s	sonic radius of wind
S	specific entropy
$\mathcal{S}$	smoothness function defined in equation (6.99)
$\mathbf{T}$	column vector defined in equation (6.16)
T	temperature
$\mathbf{t_j}$	toroidal basis column vector defined in equation (6.68)
U	dimensionless structure variable; $(= \frac{d\ln M_r}{d\ln r})$
u	limb-darkening coefficient defined in equation (7.20)
V	dimensionless structure variable; $(= \frac{d\ln p}{d\ln r})$
V_g	dimensionless structure variable; $(= \Gamma_1^{-1}\frac{d\ln p}{d\ln r})$
$V_{\max}$	maximum pulsation velocity over the stellar surface
V_0	pulsation velocity amplitude
$\mathbf{v}$	velocity vector
$v_{\rm eq}$	equatorial rotation velocity
$\mathbf{v}_h$	velocity in horizontal direction
$v^{\rm phase}$	azimuthal phase velocity of pulsation waves
v_r	velocity in radial direction
$\mathbf{v}_t$	total velocity vector
v_∞	terminal velocity of wind
$\mathbf{W}$	coupling matrix defined in equation (6.43)
W	work integral defined in equation (5.10)
$\mathbf{x}$	generalized matrix eigenvector
x	fractional radius variable; $(= r/R)$
$\mathbf{Y_i}(i = 1, 2)$	column vector defined in equation (6.16)
$Y_l^m(\theta, \phi)$	spherical harmonic
$y_i(i = 1, \ldots, 4)$	dimensionless pulsation variable defined in equations (2.44)–(2.47)
$\mathbf{Z_i}(i = 1, \ldots, 4)$	column vector defined in equations (6.49)–(6.55)
α	independent variable in solution of Lane-Emden equation
α	coefficient used in fitting *CoStar* models with polytropes
α	thermodynamic coefficient; $[= (\frac{d\ln\rho}{d\ln p})_T]$
β	gravity-darkening coefficient defined in equation (7.8)
β	coefficient used in fitting *CoStar* models with polytropes
Γ_1	adiabatic exponent; $[= (\frac{\partial\ln p}{\partial\ln\rho})_S]$

Γ_2	adiabatic exponent; $\{= 1/[1 - (\frac{\partial \ln T}{\partial \ln p})_S]\}$
Γ_3	adiabatic exponent; $[= (\frac{\partial \ln T}{\partial \ln \rho})_S]$
γ	discriminant for wave leakage defined in equation (3.33)
Δ_T	non-adiabatic scaling factor introduced in equation (7.12)
δ	thermodynamic coefficient; $[= -(\frac{\partial \ln \rho}{\partial \ln T})_p]$
ϵ	nuclear energy generation rate
ϵ_p	nuclear energy generation rate pressure derivative; $[= (\frac{\partial \ln \epsilon}{\partial \ln p})_T]$
ϵ_T	nuclear energy generation rate temperature derivative; $[= (\frac{\partial \ln \epsilon}{\partial \ln T})_p]$
η	polytropic index
η_e	effective polytropic index at surface
$\|\eta_{l_j,m}\rangle$	horizontal angular basis function defined in equation (6.74)
θ	polar angle in spherical polar coordinates (r, θ, ϕ)
ϑ	Lane-Emden function
$\tilde{\vartheta}$	Derivative of Lane-Emden function; $(= -\alpha^2 \frac{d\vartheta}{d\alpha})$
ι	angle between observer-directed axis and rotation axis
κ	opacity
κ_T	opacity pressure derivative; $[= (\frac{\partial \ln \kappa}{\partial \ln p})_T]$
κ_T	opacity temperature derivative; $[= (\frac{\partial \ln \kappa}{\partial \ln T})_p]$
$\mathbf{\Lambda}$	matrix defined in equation (6.30)
$\Lambda(l)$	$= l(l+1)$
λ	generalized matrix eigenvalue
$\lambda_i (i = 1, 2)$	eigenvalue of boundary matrix defined in equations (3.30)–(3.31)
$\lambda_{l_j,m}$	eigenvector of coupling matrix $\mathbf{W}$
$\|\lambda_{l_j,m}\rangle$	radial angular basis function defined in equation (6.64)
$\|\lambda_{n_j,m}\rangle$	radial angular basis function defined in equation (6.64)
$\lambda_\pm$	eigenvalue of boundary matrix defined in equation (3.32)
μ	angle parameter; $(= \hat{\mathbf{n}} \cdot \hat{\mathbf{n}}_o)$
ν	parameter quantifying size of rotation effects; $(= \Omega/\sigma_c = \hat{\Omega}/\omega_c)$
$\nu_-^{l_j}$	singular value of ν (< 0) where $\lambda_{l_j,m}^{-1} \to \infty$
$\nu_{l_j}^+$	singular value of ν (> 0) where $\lambda_{l_j,m} \to \infty$
$\nu_{l_j}^-$	singular value of ν (< 0) where $\lambda_{l_j,m} \to \infty$
$\Xi(\nu')$	number of $\lambda_{l_j,m}^{-1} \to \infty$ singularities between $\nu = \nu'$ and $\nu = 0$
$\boldsymbol{\xi}$	displacement vector

$\boldsymbol{\xi}_h$	displacement in horizontal direction
ξ_r	displacement in radial direction
ξ_x	displacement in cartesian x direction
ξ_y	displacement in cartesian y direction
ξ_z	displacement in cartesian z direction
ξ_θ	displacement in polar θ direction
ξ_ϕ	displacement in polar ϕ direction
Π	pulsation period in inertial frame
Π_c	pulsation period in co-rotating frame
π	parity of angular function through the equator
ρ	density
σ	pulsation frequency in inertial frame
σ_c	pulsation frequency in co-rotating frame
ς	correction factor introduced in equation (6.90)
$\tau_{\rm dyn}$	dynamical time-scale; $(= \sqrt{R^3/GM})$
$\tau_{\rm grow}$	pulsation growth rate defined in equation (5.12)
$\tau_{\rm th}$	thermal time-scale; $(= 4\pi r^3 \rho c_p T/L_r)$
$\lvert\tau_{l_j,m}\rangle$	toroidal angular basis function defined in equation (6.75)
$\boldsymbol{\Phi}$	angular basis vector defined in equation (6.18)
Φ	gravitational potential
$\Phi_{\rm eff}$	effective gravitational potential in rotating star
ϕ	azimuthal angle in spherical polar coordinates (r, θ, ϕ)
$\boldsymbol{\Psi}$	angular basis vector defined in equation (6.61)
ψ	non-adiabatic phase shift introduced in equation (7.12)
$\boldsymbol{\Omega}$	angular rotation frequency vector
Ω	angular rotation frequency; $[= \lvert\boldsymbol{\Omega}\rvert]$
$\hat{\Omega}$	dimensionless angular rotation frequency; $(= \Omega^2 R^3/GM)$
ω	dimensionless pulsation frequency in inertial frame; $(= \sigma^2 R^3/GM)$
ω_c	dimensionless pulsation frequency in co-rotating frame; $(= \sigma_c^2 R^3/GM)$
ω_{c_1}	lower critical dimensionless frequency for wave leakage
ω_{c_2}	upper critical dimensionless frequency for wave leakage
ω_t	transition frequency at which non-adiabatic effects become appreciable
$\boldsymbol{\aleph}$	inverse of coupling matrix $\mathbf{W}$

∇	temperature gradient; $(= \frac{d\ln T}{d\ln p})$
$\nabla_{\rm ad}$	adiabatic temperature gradient; $[= (\frac{\partial \ln T}{\partial \ln p})_S]$
∇_{M_r}	mass gradient; $(= \frac{d\ln M_r}{d\ln p})$
∇_r	reciprocal pressure scale height; $(= \frac{d\ln r}{d\ln p})$
∇_μ	mean molecular weight gradient; $(= \frac{d\ln \mu}{d\ln p})$
~	matrix transpose; *e.g.*, $\tilde{\mathbf{W}}$, $\tilde{\mathbf{B}}$
prefix Δ	increment in some quantity; *e.g.*, Δx, $\Delta\sigma$
prefix δ	Lagrangian perturbation; *e.g.*, δp, δT
suffix $'$	Eulerian perturbation; *e.g.*, p', T'
suffix †	matrix/column vector associated with opposite-π; *e.g.*, $\mathbf{W}^\dagger$, $\mathbf{\Phi}^\dagger$
subscript p	value at stellar pole
subscript θ	value at colatitude θ